Scattering of SH wave by surface depression / convex in density inhomogeneous media

POLITECNICO
DI TORINO

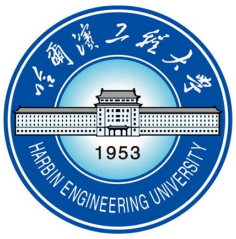

哈爾濱工程大學
HARBIN ENGINEERING UNIVERSITY

Xinzhu Li

Scuola di Dottorato
Department of Mechanical and Aerospace Engineering
Politecnico di Torino
Department of Aerospace and Civil Engineering
Harbin Engineering Univesity

Supervisors:
Prof. Erasmo Carrera
Prof. Zailin Yang

July 2023

...

Declaration

I hereby declare that, the contents and organization of this dissertation constitute my own original work and does not compromise in any way the rights of third parties, including those relating to the security of personal data.

Xinzhu Li
July 2023

Acknowledgements

First and foremost, I would like to extend my deepest gratitude to my advisors and supervisors, Prof. Zailin Yang and Prof. Erasmo Carrera for their supervision during my Ph.D. career. Prof. Zailin Yang's priceless insight and the passion and dedication he put into his work have inspired me in my whole research activities. He provided a constant help during each step of my research. I would like to thank my colleagues in the 5005 office, Guanxixi Jiang, Cheng Sun, Yunqiu Song, Minghe Li, and so on. They provided helpful support both in research activities and study life.

During my joint training at the Politicnico di Torino, I would like to appreciate to Prof. Erasmo Carrera for his guidance on my research. I sincerely appreciate his helping me throughout of my research. I would like to thank Prof. Alfonso for his invaluable help during my stay at PoliTo. I am also express my gratitude to MUL2 group, especially Dr. Matteo Filipi and Dr. Rodolfo Azzara.

I would also like to thank my parents for their mental and support of my Ph.D. career throughout, their inspiration and encouragement.

Finally, I would like to acknowledge the funding provided by China Scholarship Council (No.202006680033).

Abstract

Elastic wave theory has been widely applied in many engineering fields. Meanwhile, with the development of material science, designing and producing composite materials with wave propagation properties becomes possible which is not easily achieved by traditional materials, which makes the research of wave propagation in inhomogeneous media a hot issue in the field of theory and engineering. Moreover, defects and structures with depression or convex on the surface are very common in natural media and artificial materials, while local defects or structures often cause wave scattering and affect wave energy distribution. Excessive aggregation of forces often leads to increased deformation or stress concentration for material failure. Therefor investigating the scattering by surface depression or convex in inhomogeneous media is of theoretical significance and practical engineering valueace. Based on the elastic wave theory, this thesis researches elastic waves scattering by surface depression and convex on the surface of the radially continuous inhomogeneous media with variable wave velocity and density by using the complex function method and emphatically analyzes the influence of the existence of the depression or convex on the surface and internal displacement distribution of the inhomogeneous media.

In this thesis, the complex function method is employs to transform the wave equation of the radial inhomogeneous media with density, and the standard Helmholtz equation that is available directly solved analytically is acquired, thus the expressions of the incident wave field and the scattering wave field in the semi-infinite space could be obtained. Meanwhile, the scattering wave field expression of SH wave in the semi-infinite space from the surface semi-cylindrical depression is ably constructed. By calculating the surface and inside displacement amplitude distribution under the action of various parameters, the influence of various parameters on the displacement distribution is discussed, and the surface depression amplification effect on the displacement distribution under the influence of inhomogeneous parameters is emphatically analyzed.

Considering the influence of surface convex on the dynamic response, this thesis investigates scattering SH wave by the surface convex and surface convex with cylindrical cavity in a density radially inhomogeneous media. The research region is divided into suitable sub-regions which could be applied to construct wave field expressions by utilizing the region-

matching technique (RMT) and the auxiliary boundary. Based on the surface depression scattering problem, the wave field expressions in each sub-region are constructed. Through the boundary conditions at the auxiliary boundary and the free boundary, the wave field expression in the whole research area is solved. The distribution of displacement amplitude and dynamic stress concentration coefficient under the action of various parameters are given. The influence of surface convex on the distribution of displacement amplitude and dynamic stress concentration coefficient (DSCF) under different inhomogeneous parameters is mainly analyzed.

Subsequently, the effect of research region range on the displacement amplitude of the surface under elastic wave incidence is considered, and the dynamic response to SH waves is demonstrates for two forms of density inhomogeneous wedge with vertex angle as cusp and cylindrical depression. The vertex angle is taken to be in the range from 0 to 2π , which can describe a variety of region forms. Based on the acquired standard wave governing equations, the analytical solution of the free wave field expressions in the inhomogeneous wedge space is proposed based on the free boundary conditions at both boundaries and the Sommerfeld radiation conditions. Then, the scattering wave field expressions in the wedge region are constructed based on the previous research of surface depressions. The effects of inhomogeneous parameters on the displacement amplitudes inside the surface and wedge regions are calculated and discussed for the forms of cusp and cylindrical depressions at the vertex angle, respectively.

In addition, the finite element method (FEM) based on the Carrera Unified Formulation (CUF) framework is extended to the analysis and application of elastic wave problems in three-dimensional models in semi-infinite space. The Fortran program self-compiled by MUL2 is expanded to complete the establishment of artificial boundary, input of external waves, and research on wave propagation in layered media.

Table of contents

List of figures

List of tables

Chapter 1

Introduction

1.1 Background

Elastodynamics, as an important component of solid mechanics, originated from the interpretation of light wave phenomena. Its main research content is the dynamic response of elastic media under external loads. Generally, there are two forms of wave and vibration solutions, as the propagation of elastic waves and the vibration of elastic bodies. Wave and vibration have the same basic governing equations, and the difference between the two forms is caused by the different initial and boundary conditions of the elastic body. The research on elastodynamics can be traced back to the 17th century. With Hooke's discovery of the relationship between deformation and restoring force in elastic bodies and the establishment of the three laws of Newton's mechanics, the establishment of vibration equations in beams and plates by scholars such as Germain, Euler, Bernoulli, and Timoshenko has promoted the development of vibration mechanics.

Retrospect on the development of elastic wave propagation is traced back to the early 19th century when Navier established the general equations of equilibrium and motion for elastic bodies, and the research on elastic waves began. Possion decomposed the displacement into two parts: irrotational and dissipative, and obtains the solution of the wave equation. It also discussed issues related to initial values. In the mid-19th century, the mathematical theory of elastic wave propagation matured. Lamé proposed the concepts of scalar potential and vector potential. Stocks proved that longitudinal waves are expansion waves, and shear waves are shear waves. By the end of the 19th century, Rayleigh given the scattering theorem and the wave scattering solution for a finite spaced, which was an important achievement. Elastic wave scattering had become an important research topic in elastodynamics. In the early 20th century, scholars such as Love, Stonely, and Lamb conducted some research on the wave problem at the interface, as well as the wave problem caused by the action of line sources and

point sources. Thus, the theory of wave problems is established and solutions are obtained, making elastic wave problems a hot research field in geophysics. Since the 20th century, with the gradual improvement of elastic wave theory, classic works on wave theory have emerged [2, 54, 130], and the research of elastic wave theory in the engineering field has become active.

1.1.1 Application of elastic wave theory

Elastic wave theory is widely applied in nondestructive testing of structures and materials, geophysical exploration, and acoustics. In the related engineering field, the study of elastic wave propagation characteristic was paid much attention if the media has defects or structures. For example, the propagation characteristics in materials containing cracks or other defects are employed as the basic principle of ultrasonic nondestructive testing techniques and structural health testing to satisfied the need for safety inspection of large structures or components subjected to external loads during assembly or service[3, 34, 53]. SH waves have less energy loss than other types of waves, so they were used in nondestructive testing applications from the early research in infinite space composite board [15] to the current research in more complex interfaces and materials based on SH guided waves [71, 132]. Ultrasonic detection has a scanning speed block, good resolution, and detection ability used in the field, according to the information carried by the ultrasonic detection, obtain the crack location, size, direction, and other characteristic parameters [110]. Therefore, provides a diversified theoretical basis for ultrasonic detection and reconstruction after damage by investigating the scattering of internal and surface defects with different wave forms [45].

Meanwhile, the process of seismic wave propagation is approximated as the process of wave propagation in elastic media, so the elastic wave theory was widely applied in the field of earthquake engineering. Based on the scattering of elastic waves, many scholars conducted a large number of researches on seismic waves scattering by underground structure, local topography and geological conditions, which confirmed that the structure, topography and geological conditions have a relatively obvious influence on ground motion. These achievements provided the corresponding theory for seismic engineering design. Among them, the plane shear wave (SH wave) is not coupled with P and SV wave when it incident in space, and the damage generated at the interface is relatively strong, so in the process of analytical solution, SH wave is often taken as the research object. For instance, in terms of topography, Trifunac [159] first proposed the analytical solution for the scattering of SH wave by semi-cylindrical canyon. It was the research target of many scholars to make employ of the propagation characteristic of elastic wave to conduct geophysical exploration, to conduct earthquake disaster early warning according to the simulation data of seismic

wave, and to improve the earthquake early warning system, [84]. The study on the interaction between underground media (soil mass as the main research object) and ground structure under dynamic load was a hot topic in the field of earthquake engineering[108, 178, 205].

In addition, in the field of civil engineering, due to the demand of urbanization construction rock site blasting, directional blasting of adjacent buildings, aboveground and underground construction of high-rise buildings will cause the elastic wave interaction between the underground media and adjacent buildings [43, 107]. Therefore, the interaction between adjacent buildings and geological conditions under the action of elastic waves was widely studied in vibration isolation of civil engineering.

Furthermore, elastic wave theory also has important applications in the field of acoustics. At present, as a kind of material with special physical properties, new acoustic functional materials realize the regulation of sound wave and elastic wave within a certain scale [66, 24], so as to achieve sound insulation and noise reduction, directional transmission [28] and stealth [209] and other purposes. By setting a series of functional primitives on the surface of the media, some functional controls of sound wave and electromagnetic wave can be realized. However, due to the coupling of P-wave and S-wave in solid media, and the speed of the two wave forms is different, the research of elastic wave regulation is still very limited.

1.1.2 Wave problems in inhomogeneous media

The parameters of inhomogeneous media affect the path, velocity, and frequency of wave propagation, thereby affecting the propagation process of elastic waves to a certain extent. This makes it of important theoretical significance and application prospects to investigate the propagation characteristics of elastic waves in different media, conduct elastic wave regulation and material selection, and analyze the material properties of media. In traditional theoretical research, in order to simplify the problem, it is often assumed that the media is homogeneous and isotropic. On this assumption, some elastic wave propagation characteristics are obtained. However, media in nature often exist in inhomogeneous forms, such as air, ocean, soil, etc. In some studies, using homogeneous media forms for analysis may lead to deviations in results. The research on the influence of the inhomogeneity of natural media on the wave propagation characteristics included early research on the propagation features of light waves in air with refractive index, atmospheric pressure, or sound velocity varying with depth, and the impact of soil stiffness varying with depth on the wave response. In current research, wave propagation in various natural media is discussed based on the physical parameters of the media detected and the approximate functions that correspond to the changing characteristics of the media.

On the other hand, with the continuous development of material science, complex materials continue to emerge, such as phononic crystals, micro and nano materials, and the improvement of artificial material preparation technology, allowing the design and product of materials with special characteristics. In order to break through the functional limitations of traditional materials and realize that elastic wave propagation have specific characteristics, such as negative refraction[29, 131], spontaneous emission control[125], and anomalous tunneling effects [145], bringing new topics to the research of elastic wave propagation in these materials. By determining an appropriate media inhomogeneous function to design a continuous material cladding layer, which is used to achieve a smooth transition of the dielectric parameters of the structure and external materials required for stealth, and to eliminate the dielectric fault between the structure and external materials, the goal of structural non reflection and stealth would be achieved. Realizing dynamic and intelligent regulation of elastic waves was also a key research issue in the field of elastic wave theory, and the emergence of artificial materials also brought opportunities to this goal. Adjust the inhomogeneous area layout and parameter settings of artificial materials to achieve elastic wave propagation according to a predetermined path, wave velocity control, and energy redistribution, meeting the requirements for vibration reduction and isolation, structural stealth, and other wave characteristics in engineering. The inhomogeneous media could be seen as the characteristics of complex or artificial materials. Investigating the propagation features of elastic waves in inhomogeneous media provides a corresponding theoretical basis for applying elastic waves and analyzing material properties.

1.2 Research progress in elastic wave scattering

In natural media, artificial materials, and engineering structures, media containing defects (such as internal cavities, cracks), surface depressions, convexities, and internal structures (such as inclusions, linings) are very common. When elastic waves propagate to the location of a defect or internal structures along the incident direction, the propagation path will be disturbed, and secondary wave sources will appear at that location, thereby affecting the wave energy distribution. Excessive accumulation of forces often leads to increased deformation or stress concentration, leading to damage to the material or structure. Therefore, the scattering of elastic waves, especially the scattering of elastic waves by simple forms of defects or internal structures, was always a concern of scholars. This type of wave scattering problem is available to be solved by analytical methods to analyze and understand the physical significance, as well as to analyze more complex scattering situations in the model. The study of elastic wave scattering begins with acoustic waves. Rayleigh utilized the

wave function expansion method to study the scattering of acoustic waves by rigid spherical inclusions. Subsequently, Sezawa based on special function to provide solutions to the scattering problem of spherical, cylindrical, and elliptical cylinders in an infinite domain under P-wave incidence. Later, with the rise of the engineering field in the 1950s, the scattering of elastic waves by internal structures and defects received more attention. Many scholars conducted many researches on the scattering of elastic waves by simple cavities such as cylindrical and spherical shapes, as well as inclusions in infinite fluids and solids. The achievements achieved so far deepened the theoretical understanding of the impact of internal structures and defects on elastic wave scattering, and also promoted relevant engineering practices.

1.2.1 Research progress on scattering problems within media

In the process of research in recent decades, scholars were deeply demonstrating scattering problems and gradually mature research methods, which complicate the research model and make it more close to the practical application. The research of elastic wave scattering by in-plane defects and internal structures can be divided into two main the study of the complexity of the media and the complexity of the boundary between defects and internal structures. The complexity of the media mainly includes the complexity of the media region, the physical properties of the media and the internal structures.

In the process of the research of media complexity, the first is the complexity of the media region. The research area develops from the scattering of internal structures and defects in the infinite space to the semi-infinite space and the angular space. Lee et al.[82] took the lead in using the mirror method to satisfy the boundary conditions of the free stress at the horizontal free surface in the semi-infinite space, constructed the expression of the scattering wave generated by the cylindrical cavity, and gave the analytical solution for the scattering of SH wave by the cylindrical cavity in the semi-infinite space, extending the study of the scattering problem from the infinite space to the semi-infinite space. It is more close to the practical application model of engineering, and the mirror method is still widely employed in dealing with regional boundary problems, which lays a foundation for the follow-up research on the scope of the region. With the help of mirror image method, Green function and special function, the scattering of cavities, inclusions and lining structures in the semi-infinite space and angular space [68] to different elastic waves (P wave, SV wave, SH wave) attracted the attention of many scholars [67, 74]. Then, based on the great arc approximation method, the defect scattering problem in the semi-infinite space of cylindrical arc and parabola boundary was discussed [79]. Meanwhile, Liu [93, 94] extended the complex function method to the wave wave problem. By using the conformal mapping transformation in the complex

function method, the complex boundary space on the plane is mapped to the corresponding region on the complex plane according to the appropriate mapping function, so the complex boundary problem can be solved. The superiority of complex function method expands its application area. It is available to conveniently solve the scattering problem caused by cylindrical cavity under SH wave incident and scattering problem of arbitrary cavity in anisotropic media. Moreover, the complex function method providing a simplify path for the transformation relationship between multiple coordinate systems in the model and provide convenient analytical solution for scattering problems with multiple scatters in the media. In combination with Green function, complex function and wave function expansion method, Liu investigated the scattering of SH wave by cylindrical cavity in wedge region [96]. For finite space, such as the scattering of SH waves by cylindrical cavities in the plate, Hayir [62] also analyzed.

During this period, much attention was paid to the scattering of defects and internal structures in different media. For example, in the research of scattering in porous media, since Biot established the porous media model, the research of wave propagation in porous media was gradually carried out in the past few decades. In recent years, the continuous development of the solving theory of porous medium model (saturated porous elastic media, unsaturated porous elastic media, etc.) makes the study of wave in porous media become a hot topic [36, 156, 186, 185]. Based on the complex function method, Wang [170] proposed a method for solving the scattering of plane waves by arbitrary shape cavities in porous media. The dynamic stress response of cylindrical cavity in saturated soil under incident wave was demonstrated by using wave function expansion and boundary integral method.[183]. The anisotropy of media is also reflected in commonly used materials, such as concrete, wood, etc., and the research on the fluctuation in the characteristics of such media was continuing. The influence of anisotropy of media on anisoplast, defect or other structure resulting in elastic wave scattering and its solution method were extensively studied [5, 14, 42, 44, 76, 109, 144].

On this basis, the physical properties of internal structures in the research area were also paid attention to. Smerzini [146] investigated the response of the arbitrary rigid packed inclusion to plane wave and cylindrical wave. According to the wave function expansion method, Bostrom [16] gave the anisotropic hole to solve the problem of elastic wave scattering . Based on the proposed equivalent transformation relation, Wang et al. investigated the effect of inhomogeneous lining on elastic wave scattering [171]. Research on elastic wave scattering at nanoscale is also being carried out. Ghanei [52] demonstrated the dynamic response of circular nanoinclusion to P and SV wave scattering. In addition, many achievements were made in the research of elastic wave scattering in piezoelectric, layered, and layered piezoelectric media with functions. In earlier researches, a series of analytical methods

were applied to study the related wave problems in piezoelectric and layer media. For more complex cases, semi-analytical or numerical methods provide a way to solve such problems. For example, transfer matrix method was proposed by Thomson and applied in the wave problem of layered media [157], this method is still one of the commonly used methods to solve the wave problem of layered media, based on this method to solve and analyze the elastic wave scattering problem of circular holes, lining and other heterogeneous bodies [151]. In recent, more and more scholars pay attention to the elastic wave scattering problem in complex media such as composite materials and heterogeneous media [103].

In the study of the complexity of internal structure and defect models, the scattering of elastic waves by single circular and elliptical cylindrical, cavity, lining, and inclusion is developed to the interaction of multiple internal structures and the scattering waves by complex boundaries such as semi-cylindrical and square. By using the mirror image principle and Graf's addition theorem, Balenda [10] researched the dynamic response of two linings under SH wave incidence and gave the relevant analytical solution. Yuan [195] extended Graf's addition theorem and constructed the formula for cylindrical coordinate wave function in global transformation, which solved the limitation of Graf's addition theorem in scattering problem and made the theorem more widely applied in these problem. Based on this method, Lee [80] used the weighted residual method in the process of solving the problem of scattering plane SH waves by arbitrary holes (ellipse and square for example) . In addition, the application of the complex function method in the wave problem is proposed, using the complex function in the convenience of transformation between multiple coordinate systems, a series of studies were made on the elastic wave scattering problem in the case of multiple internal structures combinations [135]. After the region-matching technique (RMT) is introduced into this kind of problem, the complex boundary is partitioned by auxiliary boundary, which is divided into regular and solvable simple boundary, and the corresponding boundary conditions are satisfied at the auxiliary boundary to obtain the final result. According to RMT, the analytical solution of elastic wave scattering by many complex boundaries was solved. For example, Tsaur [164] deduced the series solution of truncated cylindrical cavity scattering problem when SH wave incident, Gao [47] established the solution method for horseshoe cavity scattering problem. Liu [101] gave an analytical solution to the scattering problem of square cavity, Zhang [202] analyzed the scattering problem of semicircular lining with straight boundary, Liu [100] explored the scattering situation of SH wave around the slope in the variable slope wedge area.

With the gradual progress of numerical methods, combined with the engineering needs, it was widely used in the research of solving more complex models in engineering practice. For example, based on the finite element method, the dynamic response of an arched square lined

tunnel under P wave incident, an irregularly arched lined tunnel under P wave incident, a three-dimensional column group under SV wave incident, [117] and some practical models to seismic wave scattering are investigated. Meanwhile, other numerical methods were applied to elastic wave scattering problems. For example, the boundary element method is used to simulate the advantages of more concise and accurate boundary. The scattering problem caused by single or multiple linings in the semi-infinite space and the arbitrary wedge of the top angle is effectively simulated[64, 105, 128]. Wave scattering by a triangular projection with a horseshoe lining is studied [106], the influence of the relative position between the horseshoe lining and the triangular projection on the dynamic response is analyzed and so on.

1.2.2 Research progress on wave scattering by surface depression and convex

The investigation for the influence of surface or interface depression, convex, and structures on wave propagation is of great significance in both theory and practical engineering applications. In the analytical method, the scattering of elastic waves by simple depression boundary is taken as the research basis, based on which the complex depression and convex boundary could be detected later. Retrospected the research on elastic wave scattering by surface defects or structures, Trifunac [159] based on wave function expansion method to construct scattering wave expression by applying the free stress condition of semi-cylindrical depression boundary and Hankel function to express the property of diverging wave, and gave the analytical solution of SH wave scattering by two-dimensional semi-cylindrical depression. Using elliptic coordinate system and Mathieu function, Wong [179, 180] gave the analytical solution of SH wave scattering by semi-elliptic depression and analyzed the influence of each parameter on surface displacement. With the application of Green function, complex function, Graf's addition theorem and other analytical solutions to wave problems, the analytical results of elastic wave scattering by surface depression were developed rapidly, solving the problem of elastic wave scattering by arc depression [60, 78, 92, 184, 196]. In addition, according to the free wave field constructed by Sanchez [152] in the wedge space, Lee [81] gave the solution for the scattering of SH wave by circular arc depression at the vertex.

In recent years, due to the needs of engineering background and the gradual improvement of analytical methods, more achievements were obtained in the research of elastic wave scattering in more depression boundaries and different media surface depressions. Liu [89] derived the analytical solution of the scattering of planar P waves in the two-layer cylindrical arc alluvial valley based on the series expansion method, and analyzed the

influence of parameters of each layer on the scattering with this solution. Liang [175–177] gave a solution to the scattering problem of P wave, SV wave and SH wave in cylindrical arc sedimentary depression by using the great arc hypothesis. Then, the method of RMT enables scholars to break through the limitation of arc depression boundary, and obtain the corresponding subregion of constructible wave field through reasonable regional division of complex boundary. Graf's addition theorem is employed to complete coordinate conversion, and finally, the solution is carried out according to auxiliary boundary conditions. Based on this method, a large number of analytical studies were carried out on the wave scattering by surface depressions with straight boundaries. Tsaur [160, 166] applied the RMT method to derive series solutions for SH wave scattering by symmetric deep V and shallow V-shaped depression. Based on the analytical solution of semi-cylindrical depression, and according to the suitable partition fit, the scattering problem of fan shape, truncated semicircle, semicircle containing sedimentary layer, U shape, symmetrical tridacidal depression and so on complex depression boundary is given [22, 48, 161, 163, 198, 199]. The SH wave scattering by elliptic depression at the vertex angle of rectangular space is studied by applying Green function [165]. Qi [133] utilized Mathieu function addition theorem and multi-elliptic coordinate system to give an analytical expression for asymmetric semi-elliptic depression. It can be seen that the analytical solution of elastic wave scattering by semi-cylindrical depression is the foundation of the research on elastic wave scattering analysis by depression boundary.

Furthermore, the scattering of elastic wave by surface depression is demonstrated by numerical method. In order to satisfied engineering applications, it is always an important research topic to solve the problem of irregular depression boundary or complex media surface depression. Since the early days, some scholars made application of the advantages of the boundary element method (BEM) at the boundary to simulate the scattering of SH wave by two-dimensional arbitrary depression and the combination boundary of depression and convex in the frequency domain and time domain[41, 153, 154]. The finite element method (FEM) is also applied to the simulation of wave problems. By coupling the wave equation in differential form with discrete domain, the node or element solution are utilized to approximate the solution of the differential equation. This process has clear physical meaning, and is available in mathematical derivation and program implementation[116, 147]. Therefore, finite element method has a long history of development and discuss in the wave problem. In the process of using FEM to investigate the scattering problem of surface depression. Zhang [200] earlier simulated the dynamic response of arbitrary depression under the incidence of seismic waves, and gave a variety of depression boundary simulation results. Kashiba [73] simulated the scattering behavior of Lamb waves from a depression defect in a plate. Casadei [19] investigated the scattering of elastic waves by local defects on

surfaces. At present, the development of finite element method based on the simulation of actual large-scale depression terrain ground motion is more rapid[123].

For analytical research on elastic wave scattering by surface convex boundaries, the analytical solution of SH wave scattering by semicircular convex and the region-matching technique (RMT) presented by Yuan and Men [197] laid the foundation for subsequent exploration on surface convex boundary scattering, providing a solution idea for surface convex boundary researches. In [197], the convex boundary was divided into semi-infinite space with cylindrical arc depression and cylindrical closed region through an auxiliary boundary. After constructing wave field expressions in each region, the solution is solved applying the unified coordinates of the Graf's addition theorem. Therefore, the basis of the analytical solution of the elastic waves scattering problem by surface boundary is still the semi-infinite cylindrical depression problem. Based on RMT, the scattering problem by cylindrical convex and the interaction between surface convex and internal structures is further investigated. For the demonstration of elastic wave scattering by convex boundary with straight boundary, the method of partition is still employed. Meanwhile, the method of complex variable function is introduced to facilitate coordinate transformation between coordinate systems. The fractional Bessel function is used to satisfy the boundary conditions of straight boundary. Thus, the SH wave scattering problem of isosceles triangular convex in semi-infinite space is solved [138]. Then, according to this method, a series of scattering problems, such as double isosceles triangle convex, isosceles triangle convex and circular convex, isosceles triangle convex and internal structures, were solved, and the specific analysis of scattering effect was illustrated[38, 39, 137, 139]. Guo [134] considered the scattering problem of angular domain surfaces with isosceles triangular bumps. In order to further study the surface convex scattering problem, Tsuar [162] proposed the series solution of the cylindrical arc convex scattering problem through the wave function expansion method combined with the RMT, which improved the computational accuracy of the traditional analytical results. For a more complex anisosceles, Lin [91] detected a preliminary analytical result of anisosceles triangle scattering with an obtuse vertex angle .

For a period afterwards, due to the limitations of existing methods on the elastic wave scattering problems by complex convex boundary, many scholars' analytical solutions to scattering by convex boundary mainly focus on the influence of the relative position of internal structures and convex or concave on elastic wave scattering [59, 95], and the scattering by internal structure contained in convex boundaries [88, 85]. However, convex boundary on complex surface is more satisfied actual situation, so it is of practical significance to demonstrate this problems. The multi-region-matching technique (MRMT) proposed by Song [148, 149, 188, 189] broken through this situation. By utilizing the flexibility of the

multilevel partitioning technique, the more complex convex surface boundary is partitioned several times to construct corresponding wave field expressions respectively, and then the complex function method is used to solve the problem in accordance with the convenience of coordinate transformation. And then, the SH wave scattering problem of semi-infinite surface isosceles trapezoidal convex and multistage gradient isosceles triangular convex was demonstrated. Research on convex boundary scattering problems is also being carried out in other engineering fields, such as the analysis of dam by edge waves propagation along the coast [201].

The numerical method is also applied to detect the boundary scattering of convex surfaces in semi-infinite space. The numerical method is utilized to simulate the scattering problems by a more complex convex boundary. With the convenience of boundary element description, BEM is often applied to analyze the scattering problem of convex, depression and internal structures combination [129], and investigate the three-dimensional dynamic response of convex [8], etc. Moreover, FEM and finite difference method (FDM) also have many applications in these scattering problems. Such as, in the field of earthquake engineering, many researches were carried out on the ground motion response of the actual raised boundary (mountain, dam, etc.) [26, 27, 40, 50].

1.3 Research progress in inhomogeneous media

Investigating wave propagation in inhomogeneous media attracted the attention of many scholars, since the large influence of media properties on wave propagation characteristics. The inhomogeneous properties of media are significant both reflected in natural materials and the design of artificial materials. However, the research of wave problems in inhomogeneous media is more complicated, and its solution methods are divided into analytical methods (including semi-analytical methods) and numerical methods. Analytical methods reveal intuitively analyzing the physical significance of the influence of wave propagation properties, while numerical methods provide the possibility to simulate complex situations.

1.3.1 Analytical method

The essence of analytical solution of wave problems in inhomogeneous media is to analytically solve differential equations with variable coefficients, which is usually difficult. However, the analytical method has a clear physical meaning and is fast in calculation. Meanwhile, the analytical solution provides a theoretical foundation for the numerical method and a benchmark for verifying the simulation results. Based on the properties of the me-

dia, employing analytical methods to solve wave problems in inhomogeneous media is divided into two main aspects: the research of layered media and the research of continuous inhomogeneous media.

The research and application development of functionally graded materials (FGM) makes the investigation of the wave problem in them become a hot topic. Early, the inhomogeneous of FGM posed greater difficulties for discussing their kinetic response using analytical methods. The FEM parameters have a more pronounced effect on the scattering caused by defects or internal structures, which tend to cause significant concentrations of dynamic stresses and displacements, thus causing premature destruction of the material in service. Therefore, many scholars divided FGM into layered homogeneous media for the research. And, the wave propagation characteristic is also approximated in the early studies of wave problems in continuously inhomogeneous media by the method of layering and setting the material parameters of each layer as constants to analyze the wave propagation characteristic. Naderi [122] presented an analytical solution for a sector-shaped functional gradient plate under flexural loading. Through the Green function method, Kumar [75] demonstrated the propagation characteristic of shear waves in inhomogeneous layers. Chattopadhyay [23] discussed the propagation of SH waves caused by point sources in transversely isotropic layers.

Moreover, the semi-infinite space with overburden layer approximately simulated the soil layer formed through long-term deposition, which has practical engineering significance in the field of seismic engineering. Exploring the elastic wave propagation characteristic in such media through analytical methods will provide theoretical foundation for engineering. Using the complex variable function and wave function expansion method, combined with the orthodrome assumption, Zhao [206, 207] conducted research and analysis on the dynamic stress around internal structures such as cylindrical cavity in a semi-infinite space with a covering layer under the incidence of SH waves. Based on this assumption, some scholars also considered the scattering problems by depression or convex boundaries on the surface of a media. Liu [97] analyzed the scattering problem of surface depressions with a covering layer under the incidence of SV waves. Gupta [56, 57] applied analytical methods to discuss the propagation laws of torsional surface waves in a inhomogeneous semi-infinite space with a covering layer and Love waves in a inhomogeneous dual porous layer. Chaki [20] deduced the dispersion equation for SH waves with an irregular dielectric layer on a functionally graded piezoelectric layer.

The application of semi-analytical methods provides more avenues for the study of layered problems. Employing the transfer matrix method, Love wave and SH wave propagation in functionally graded piezoelectric media and structure features carried out extensive research

and analysis [37, 46, 49, 72, 127]. Later, Zhang [203] applied the transfer matrix method and the wave function expansion method to investigate the elastic wave scattering by a dielectric surface depression with a single or multiple radial inhomogeneous layer. Rokhlin [142] proposed a stiffness matrix method based on the idea of the transfer matrix method to analyze the wave propagation problem in multi-layer anisotropic media. Chen [25] presented the dispersion behavior of waves in laminated FGM plates based on the developed echo matrix method. Han [61] proposed a semi-analytical method to study the scattering behavior of waves by cylinders in functionally gradient piezoelectric materials. Utilizing the WKB approximation method, Qian [136] discussed the propagation characteristics of Love waves in FGM. Li [87] studied the characteristics of Love waves in layered functionally gradient piezoelectric structures. With the deepening of the research on FGM, more scholars consider the continuous variation of material parameters. Cao [17] solved the Lamb wave problem in FGM plates using the power series method.

Subsequently, in investigation continuous inhomogeneous media, among the factors that affect the properties of the media, such as density and modulus, scholars first pay attention to the variable wave velocity caused by these properties. Changes in wave velocity will lead to changes in the propagation path or characteristics of waves, resulting in differential dynamic responses. Based on the Green function method, Manolis [111] considered the characteristic of plane wave propagation when the wave velocity varies with depth, and presented a solution to the Helmholtz equation under this condition. The vertical variation of medium parameters in accordance with some natural features has engineering significance. Therefore, employing the Green function method, Guzina [58] derived the response of a inhomogeneous elastic semi-infinite space in the vertical direction under a point source. Muravskii [120, 121] demonstrated the time harmonic vibration problem in a semi-infinite space where the shear modulus linearly increases with depth. Subsequently, Manolis [112, 114, 115] presented a series of basic solutions for elastic wave propagation problems in vertical and layered inhomogeneous media, and applied them to numerical methods such as BEM. For other forms of inhomogeneous media, the Green function method was also applied to solve. Watanabe [172] obtained Green function solutions for SH waves in heterogeneous media with power function changes in wave velocity, and Green function solutions for wave number changes in anisotropic heterogeneous media[173]. According to Manolis's solution, Daros [30] proposed the foundation solution for SH waves in anisotropic density inhomogeneous media. In combination with Radon transformation, Rangelov [141] gave a fundamental solution for anisotropic density varying with depth in media. In other analytical methods, Abd [1] applied the Fourier transform method to solve the dispersion equation of Love waves in anisotropic media with inhomogeneous shear modulus. Ting [158] demonstrated an analytical

expression for the anti plane wave problem in a semi-infinite space with inhonogeneous density anisotropy. Meirbekova [118] applied periodic geometric transformation to solve the scattering of plane shear waves by multiple heterogeneous bodies in radially anisotropic inhomogeneous shells.

As complex variable function methods are applied to wave problems, they also provide new ideas for solving wave problems in heterogeneous media. Vrettos [167, 168] solved the wave propagation in inhomogeneous media with shear modulus varying with depth problem utilizing complex function method. Shaw [143] gave the fundamental solution of the generalized Helmholtz equation in variable wave velocity media based on the complex variable function method and conformal mapping. For the scattering of elastic waves in inhomogeneous media, Zhou [208] investigated the dynamic stress concentration around double elliptical cavities in inhomogeneous media with exponential changes in density and modulus applying the complex variable function method. Similarly, the problem of dynamic stress concentration around cylindrical and elliptical cylindrical cavities in a semi-infinite space of exponentially varying inhomogeneous media was solved [51, 102, 103]. Achenbach [4, 11] explored the surface wave situation in a inhomogeneous semi-infinite space where the shear modulus and density vary with depth under different sources. However, in early, only inhomogeneous parameters was preserved, and the wave velocity was simplified to a constant wave velocity for research. In order to continue exploring the scattering of elastic waves by heterogeneous bodies in heterogeneous media under variable wave velocities, Hei [63] combined with the mapping method, proposed the foundation solution of the Helmholtz equation for density inhomogeneous media, and analyzed the dynamic response of cylindrical cavity in inhomogeneous media with density varying with depth to SH wave scattering. Based on this investigation, SH wave scattering by a series of internal structures in inhomogeneous media with varying density was studied [65, 187, 192]. Subsequently, a related research was carried out in varying modulus media, and the distribution of dynamic stress concentration coefficients due to scattering from internal structure within the media was analyzed[193]. Moreover, on the basis of this study, the inhomogeneous media parameters were extended and the relevant solution to the scattering problem related to variable wave velocity under simultaneous modulus and density variations were given in the subsequent exploration. In addition, based on the proposed equivalent transformation relation, Yang [191] proposed another method for the analytical solution of the wave problem in one-dimensional inhomogeneous media. A summary of relevant literature on using analytical methods to solve wave problems in non-uniform media is shown in Table 1.1.

The analytical investigation of inhomogeneous media, most of it focuses on wave scattering by internal structures within the media and the propagation characteristics of waves.

Table 1.1 Summary of main references for researching wave problems in inhomogeneous media by analytical methods

Type		Reference
Analytical method	Layered media	the propagation characteristic of shear waves in inhomogeneous layers [75] propagation of SH waves caused by point sources in layered media[23] wave propagation in anisotropic layered media [142] propagation of Love wave in layered media [136] and structures [87]
		scattering of elastic waves by internal cavities [206, 207] and surface depressions in a semi-infinite space with a covering layer [97] propagation of surface waves in inhomogeneous semi-infinite space with a covering layer [57] scattering of SH waves by surface depressions in layered media with single or multiple covering [203]
	Inhomogeneous media	elastic wave propagation characteristic with wave velocity varying with depth [111] analytical solution of SH wave in medium with power function wave velocity [172] basic solutions of the generalized helmholtz equation in variable wave velocity media [143] Green's function solution to wave problems in density varying media [30, 141, 158] surface wave propagation in media with shear modulus varying with depth [167, 168]
		dynamic stress concentration around cavities in constant wave velocity media with density and shear modulus varying [51, 102, 103] dynamic stress concentration around scattering bodies such as cavities and lining in variable wave velocity media with varying density [63, 65, 187, 192] scattering problem of cavities in variable wave velocity media with changing modulus [193]

However, there are few types of research on the scattering of defects and structures with surface depression or convex, especially in continuously inhomogeneous media.

1.3.2 Numerical method

The numerical method provides an efficient and feasible solution tool for solving complex and heterogeneous media fluctuation problems or practical engineering problems. Based on the basic solution given by Green function method, BEM is applied to the study of inhomogeneous media fluctuation problem. BEM was used to considered wave in continuous inhomogeneous media problems. Leung [83] discussed the dynamic response of internal structures scattering in inhomogeneous media with shear modulus varying with depth. Daors [32] proposed a BEM for SH waves in heterogeneous anisotropic media with the same variation of stiffness and density and carried out crack modeling and stress intensity factor analysis. In the follow-up researches, the propagation characteristics of SH wave under the condition of variable media parameters are discussed based on BEM [31, 33]. Dineva [35] studied the problem of crack scattering in inhomogeneous semi-infinite space with parabolic media parameter. Wei [174] simulated the antiplane wave motion in two continuous inhomogeneous media. Mojtabazadeh [119] proposed the complete formula of BEM for the analysis of transient SH wave scattering in the anisotropic semi-infinite space. BEM was also employed to discuss scattering problems by internal structures and surface defects in layered media. Lee [77] analyzed the scattering of SH wave in anisotropic media with multiple layers of anisotropic anisoplasty. Ba [6] proposed the indirect BEM to investigate the scattering and diffraction by surface depression in multilayer transverse isotropic semi-infinite space, and the dynamic response of local periodic layers under P wave and S wave [7, 9]. Liu [104] further considered the problem of three-dimensional elastic wave scattering in multi-layer semi-infinite space. When BEM is employed to solve the wave problem in inhomogeneous media, it needs to give the foundation solution of the corresponding media parameters, so it is difficult to solve in some complicated cases.

As a widely used numerical method, FEM has experienced many years of development and acquired many research results in the application of inhomogeneous wave problems. FEM is used for numerical calculation of wave problems in layered media, is available to simulate more complex media situations and provide high accuracy simulation results. Sullivan [150] proposed plane strain and axisymmetric finite element formulas for multilayer anisotropic media and viscous damping, which effectively reduced model freedom and calculation time. Yazdi [194] developed a finite element model that considers the fluid saturation continuum in the rigid semi-infinite space under the action of harmonics, which is employed to consider the inhomogeneity of complex geometric boundaries and media. In order to

simulate the parameters of continuous inhomogeneous media, many scholars investigated FEM. For example, based on static problems in inhomogeneous media, inhomogeneous isoparametric element [204] and gradient finite element [70] are proposed. Then, in order to explored dynamic analysis problem in inhomogeneous media, Yang [190] proposed dynamic inhomogeneous isoparametric element format; Chakraborty [21] proposed a spectral layer element for wave propagation in anisotropic inhomogeneous layered media caused by high frequency impact loads. For the finite element solution of models with local shapes or media changes, larger degrees of freedom and calculation cost are often needed, Carrera [18] proposed a finite element method based on the framework of Carrera Unified Formulation (CUF), which proposed path for effectively saving the degree of freedom required by the model, greatly reduce the calculation time. Based on this method, the multi-field coupling mechanics of layered and nonlinear media structures are investigated [12, 126, 140, 181].

Another significant point to solve wave problem in inhomogeneous media in infinite or semi-infinite space by FEM is to set the artificial boundary at the truncation boundary. Most of the commonly applied artificial boundaries, such as Higdon boundary, transmission boundary and viscous-spring boundary, are established based on the parameters of homogeneous media. However, the artificial boundaries based on the parameters of inhomogeneous media with better establishment effect and faster calculation often require the analytical foundation solutions of relevant problems. Currently, the research on artificial boundaries of inhomogeneous media is still in progress. There are related solutions in one- and two-dimensional separable waves.

Other numerical methods, such as the finite difference method, can be used to analyze the propagation characteristics of Love waves in inhomogeneous functionally gradient materials [69]. The scattering problem [155] caused by inhomogeneous media with variable wave velocity and irregular surface defects was studied, as well as the spectral element method (SEM) [55], the meshless methods (MMs) [169], and the combination of different numerical methods [90, 113, Xiao et al.] is employed for investigating wave in inhomogeneous media problems. Similar to the FEM, these methods also necessary to set the artificial boundary to satisfied the radiation condition at the truncated boundary as solving the infinite space wave problem.

From the above research progress introduction, it can be found that the analytical research methods for elastic wave scattering problems in homogeneous media are relatively mature and have rich achievements. Because the variable coefficient wave equation caused by the inhomogeneous media is difficult to solve analytically, the current research work is limited to the SH waves scattering by inclusions such as cavities and lining in the media, and the research on the dynamic response of complex boundary on the surface of inhomogeneous

media is less. Considering that the actual material surface often has irregular boundaries such as defects and structures, this thesis approximates these boundaries to circular or wedge-shaped boundary forms, and studies the displacement and stress situations of these boundaries and nearby areas under SH wave action. From an analytical perspective, this provides a theoretical reference for the damage and failure analysis of inhomogeneous materials. In addition, the analytical solution of the SH wave scattering problem caused by the depression and convex types surface arc-circular boundary can serve as the basis for researching complex boundary problems, providing ideas and inspiration for subsequent more complex analytical research work.

1.4 Outline

Analytical solutions for the scattering of SH waves by surface defects or structures in continuously inhomogeneous media with variable wave velocities are of great significance for both theoretical and practical engineering applications. Therefore, the purpose of this thesis is to investigate SH incident propagation characteristics on the surface depression and convex boundaries in inhomogeneous media with variable wave velocity, in Harbin Engineering University. Meanwhile, during the joint training in Politecnico di Torino, the FEM under the CUF framework is expanded to exploration the elastic wave problem utilizing the CUF method. The dynamic response of the superstructure is analyzed considering the oblique input of elastic waves. The main research content of this article is as follows:

(1) In Chapter 2, based on the elastic wave theory, the wave equation of inhomogeneous media with density and shear modulus varying with coordinate components is derived, and the solution idea is proposed. In order to be able to perform analytical solutions and ensure the variable wave velocity characteristics in the media, this thesis mainly considers inhomogeneous media with radial variations in density and constant shear modulus. The Helmholtz equation with variable coefficients is successfully reduced to standard form by using the complex variable function method and introducing a transformation function.

(2) The scattering of SH waves by a radial inhomogeneous media with a semi-cylindrical depression surface boundary is investigated in Chapter 3, and the expressions of free and scattering wave field are constructed. The validation of the proposed method is verified by comparing the results with existing results by reducing the influence of parameters. By calculating the displacement amplitude results under each parameter, the influence of each parameter on the dynamic response under SH wave incidence is analyzed.

(3) Convex boundaries on the surface of a media also have a significant impact on the scattering of elastic waves. Chapter 4 is mainly detected SH wave scattering by considering

semi-cylindrical convex boundary and semi-cylindrical convex boundary with cylindrical cavity. In order to explore the comparison of the scattering characteristic of SH waves by convex and depression boundary in the same inhomogeneous media, the density radial inhomogeneous media is still employed in this chapter. According to the solved standard Helmholtz equation and the idea of region-matching, the wave field expressions in each region after the model division are constructed, and the displacement and stress boundary conditions are applied at the auxiliary boundary to solve the problem. Taking the parameters closer to the existing result parameter settings, the validation in this chapter is verified through calculation and comparison. The surface and internal displacement amplitudes are calculated under various parameters, and the effects of various parameters on the distribution of dynamic stress concentration coefficients (DSCF) around the cylindrical cavity are analyzed.

(4) Based on the consideration range of the research media, SH waves propagation in the inhomogeneous wedge space is investigated in Chapter 5, and the effect on the dynamic response is considered for both the cases of the wedge domain with cusps and circular depressions. The inhomogeneous media parameters are still in the form of density variation along the radial direction under the condition of retaining the variable wave velocity, and the results are analyzed in comparison with the first two problems. From the governing equations obtained after the transformation, the expressions for the free wave field, as the incident and reflected waves, in the density radial inhomogeneous wedge space are derived for the cylindrical depression scattering problem, while the expressions for SH wave scattering wave field in the wedge space are constructed. The wedge vertex angle takes the value range from 0 to 2π, which can correspond to a variety of regional boundary forms. The validation in this chapter verified by setting the media parameters to calculate and compare with the existing results for similar cases. Then the displacement distribution on the surface and inside of the wedge space is calculated and the effect of each parameter on the displacement distribution is discussed.

(5) FEM often requires more degrees of freedom and computational time when simulating the dynamic response of large-scale models under elastic wave input. During the joint training period, FEM based on the CUF framework effectively reduces the advantages of the finite element model's degrees of freedom and calculation time. In Chapter 6, by establishing the viscous-spring artificial boundary, the method is applied to the calculation model with truncated boundaries. This process is implemented using the MUL2 team's self-developed Fortran code. The validation of artificial boundary is verified applying the classical Lamb problem. Subsequently, the input process of external waves oblique incident and external waves in layered media is completed, and the dynamic response of external waves under oblique incident in various underground media with upper structures is considered, with

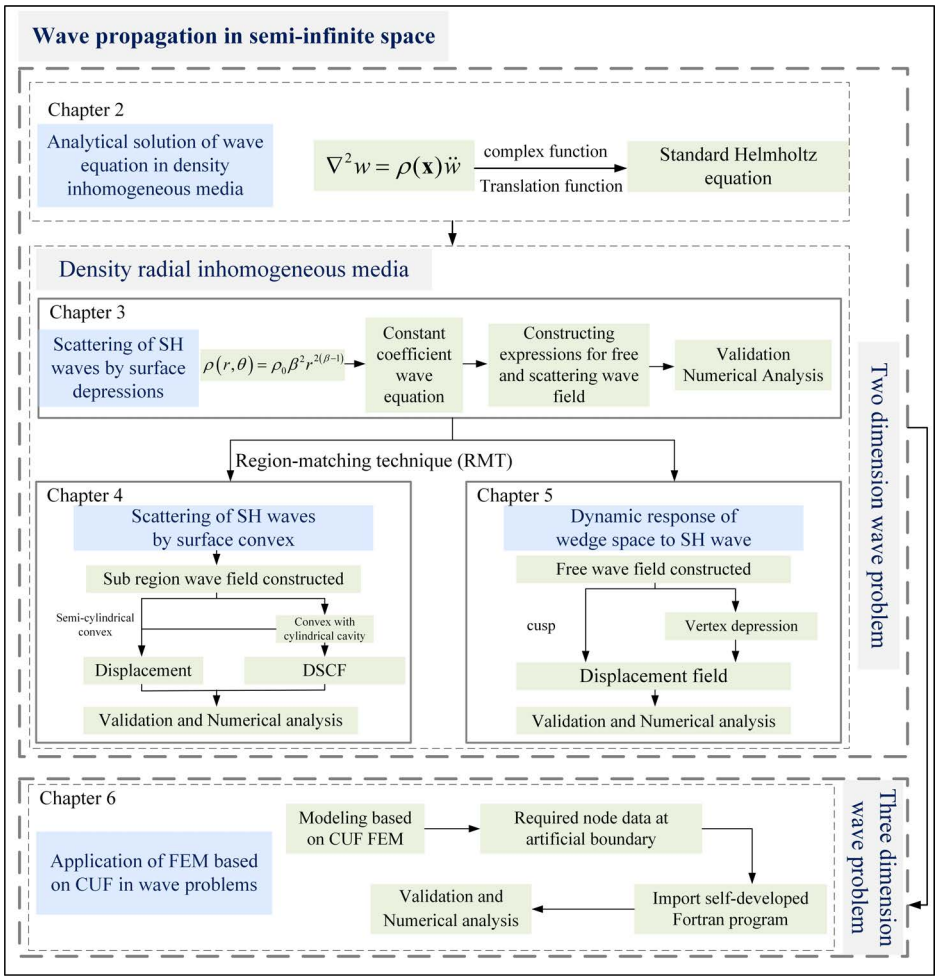

Fig. 1.1 Structure diagram of this thesis

emphasis on the influence of incident angle. Fig. 1.1 shows the structural relationship of each chapter.

Chapter 2

Theory of analytical methods for wave propagation in inhomogeneous media

The research of traditional elastic wave problems is more based on the assumption of isotropic media, under which the solution of the equation is only applicable to discussing the elastic waves propagation characteristic in isotropic media. For complex media, such as anisotropic media, inhomogeneous media, porous media, etc., it is necessary to further expand the original theory to analytically solve related problems.

2.1 Wave equation in inhomogeneous media

2.1.1 Establishment of equation of motion

For an elastomer with a volume of V and a surface area of S, let its density be ρ and its physical strength be f_i (excluding inertial force), the dynamic governing equation can be obtained through Gauss formula

$$\sigma_{ij,j} + \rho f_i = \rho \ddot{u}_i \tag{2.1}$$

$$\varepsilon_{ij} = \frac{1}{2}\left(u_{i,j} + u_{j.i}\right) \tag{2.2}$$

$$\sigma_{ij} = \lambda \varepsilon_{kk} \delta_{ij} + 2\mu \varepsilon_{ij} \tag{2.3}$$

where u_i, ρf_i, ε_{ij} and σ_{ij} represents displacement, physical force for unit volume, strain, and stress, respectively. λ and μ are Lame constants. In addition, ε_{kk} is the expansion coefficient. For two-dimensional problems, the range of the lower subscript is from 1 to 2, δ_{ij} represents the Kronecker symbol. Collate the above equations to obtain the displacement equation of

elastodynamic motion

$$(\lambda+\mu)\,u_{j,ji}+\mu u_{i,jj}+\rho f_i=\rho\ddot{u}_i \tag{2.4}$$

2.1.2 Derivation of wave equation in inhomogeneous media

If the continuous elastic body is a inhomogeneous media, the material parameters are related to the coordinate components, such as $\lambda=\lambda(\mathbf{x})$, $\mu=\mu(\mathbf{x})$, $\rho=\rho(\mathbf{x})$. By introducing the vector operator Eq. (2.4), it can be written as

$$(\lambda(\mathbf{x})+\mu(\mathbf{x}))\,\nabla\nabla\cdot\mathbf{u}+\mu(\mathbf{x})\,\nabla^2\mathbf{u}+\rho(\mathbf{x})\,\mathbf{f}=\rho(\mathbf{x})\,\ddot{\mathbf{u}} \tag{2.5}$$

where ∇ is Laplace operator.

In order to rewrite Eq. (2.5) into a suitable solution form that does not involve material parameter derivatives, the following transformation is established for the displacement vector $\mathbf{u}$

$$\mathbf{u}(\mathbf{x},t)=P(\mathbf{x})\,\mathbf{U}(\mathbf{x},t) \tag{2.6}$$

where the exact form of the function $P(\mathbf{x})$ is yet to be determined.

The derivative of u_i relative to spatial coordinates is as follows

$$\mathbf{u}_{i,j}=P\mathbf{U}_{i,j}+P_{,j}\mathbf{U}_i \tag{2.7}$$

$$\mathbf{u}_{i,jj}=P\mathbf{U}_{i,jj}+2P_{,j}\mathbf{U}_{i,j}+P_{,jj}\mathbf{U}_i \tag{2.8}$$

$$\mathbf{u}_{j,ij}=P\mathbf{U}_{j,ij}+P_{,j}\mathbf{U}_{j,i}+P_{,i}\mathbf{U}_{j,j}+P_{,ij}\mathbf{U}_j \tag{2.9}$$

Bring Eqs. 2.7 and (2.8) into Eq. (2.5) to obtain the transformed displacement vector $\mathbf{U}$. The equation is as follows

$$\begin{gathered}(\lambda+\mu)\,P\mathbf{U}_{j,ij}+\mu P\mathbf{U}_{i,jj}+\left(2\mu P_{,j}+\mu_{,j}P\right)\mathbf{U}_{i,j}\\+\left(\lambda P_{,j}+\mu P_{,j}+\mu_{,j}P\right)\mathbf{U}_{j,i}+\left(\lambda P_{,i}+\lambda_{,i}P+\mu P_{,i}\right)\mathbf{U}_{j,j}\\+\left(\mu P_{,jj}+\mu_{,j}P_{,j}\right)\mathbf{U}_i+\left(\lambda P_{,ij}+\lambda_{,i}P_{,j}+\mu P_{,ij}+\mu_{,j}P_{,i}\right)\mathbf{U}_j\\+\rho\mathsf{f}_i=\rho P\ddot{\mathbf{U}}_i\end{gathered} \tag{2.10}$$

From the above equation, an accurate form of the function $P(\mathbf{x})$ can be constructed, thereby simplifying Eq. (2.10) into mutually independent wave equations. Further sorting out and transforming the simplified wave equations can yield analytical solutions to the corresponding equations.

In this thesis, we mainly research inhomogeneous media with varying density, $\lambda(\mathbf{x})$, $\mu(\mathbf{x})$ are constants, so we directly bring them into Eq. (2.1) for simplification

$$(\lambda+\mu)\nabla\nabla\cdot\mathbf{u}+\mu\nabla^2\mathbf{u}+\rho(\mathbf{x})\mathbf{f}_i=\rho(\mathbf{x})\ddot{\mathbf{u}}_i \tag{2.11}$$

Since only density is a function in the equation, the usual displacement decomposition can be introduced, and the displacement vector **u**can be expressed as the sum of two vector fields

$$\mathbf{u}(\mathbf{x},t)=\phi(\mathbf{x},t)+\varphi(\mathbf{x},t) \tag{2.12}$$

where ϕ and φ represent scalar and vector displacement potentials, respectively, while satisfying the following relationships $\nabla\wedge\phi=0$, $\nabla\cdot\varphi=0$.

Taking the above decomposition into governing equation Eq. (2.11), ignoring physical strength

$$(\lambda+2\mu)\nabla^2\phi+\mu\nabla^2\varphi=\rho(\mathbf{x})\ddot{\phi}+\rho(\mathbf{x})\ddot{\varphi} \tag{2.13}$$

If each wave equation is independent of each other, we can obtain

$$\nabla^2\phi=\frac{1}{c_p^2}\ddot{\phi} \tag{2.14}$$

$$\nabla^2\varphi=\frac{1}{c_s^2}\ddot{\varphi} \tag{2.15}$$

where $c_p=\sqrt{(\lambda+2\mu)/\rho(\mathbf{x})}$, $c_s=\sqrt{\mu/\rho(\mathbf{x})}$ represent the longitudinal wave velocity and the transverse wave velocity, respectively. Under the condition of simple harmonic time, the following Helmholtz equation can be obtained

$$\nabla^2\phi+k_p^2\phi=0 \tag{2.16}$$

$$\nabla^2\varphi+k_s^2\varphi=0 \tag{2.17}$$

where $k_p=\omega/c_p$, $k_s=\omega/c_s$ represents the longitudinal wave number and the transverse wave number, respectively.

2.2 Basic solution of wave equation in density inhomogeneous media

2.2.1 Standardization of wave equation in density inhomogeneous media

The two-dimensional wave equation includes the basic concept of elastic wave propagation, so it can reflect the basic propagation characteristic of elastic wave problems and is the basis for exploring elastic wave problems. This section takes the two-dimensional wave problem as an example. Under the condition of simple harmonic time, the two-dimensional density inhomogeneous wave equation can be expressed as a constant form in the Cartesian coordinate system

$$\frac{\partial^2 w}{\partial x^2}+\frac{\partial^2 w}{\partial y^2}+k^2(x,y)=0 \tag{2.18}$$

Eq. (2.18) is a Helmholtz equation with variable coefficients, which is currently difficult to directly solve analytically. To solve the equation is transformed into a standard Helmholtz equation, and the transformed solvable equation is solved to obtain an analytical solution to the original equation. Firstly, based on the theory of complex variable functions, the wave equation can be transformed into a complex field by introducing complex variables $z=x+\mathrm{i}y$, $\bar{z}=x-\mathrm{i}y$

$$\frac{\partial^2 w}{\partial z\partial \bar{z}}+\frac{1}{4}k^2(z,\bar{z})\,w=0 \tag{2.19}$$

Secondly, continue to introduce the variable (ξ_1,ξ_2), and set the function $\zeta=\zeta(z)=\xi_1+\mathrm{i}\xi_2$ is an analytic function of complex variable z, then Eq. (2.19) is converted to

$$\frac{\partial^2 w}{\partial \xi_1^2}+\frac{\partial^2 w}{\partial \xi_2^2}+\frac{1}{4}\left|\frac{dz}{d\zeta}\right|^2 k^2(\xi_1,\xi_2)\,w=0 \tag{2.20}$$

where $|dz/d\zeta|^2$ is the determinant of a transformation matrix between the coordinate system (x,y) and (ξ_1,ξ_2). This matrix is called the Jacobian matrix $J(x,y;\xi_1,\xi_2)$ in computational mechanics, and its determinant is called the Jacobian matrix $|J(x,y;\xi_1,\xi_2)|$. Therefore,

$$J(x,y;\xi_1,\xi_2)=\frac{\partial(x,y)}{\partial(\xi_1,\xi_2)}=\begin{bmatrix}\partial x/\partial\xi_1 & \partial x/\partial\xi_2\\ \partial y/\partial\xi_1 & \partial y/\partial\xi_2\end{bmatrix} \tag{2.21}$$

$$|J(x,y;\xi_1,\xi_2)|=(\partial x/\partial\xi_1)(\partial y/\partial\xi_2)-(\partial x/\partial\xi_2)(\partial y/\partial\xi_1) \tag{2.22}$$

To ensure that $\zeta(z)$ is a parsing function of z, and $d\zeta/dz$ is unique, it needs to satisfy $J(x,y;\xi_1,\xi_2)\neq 0$. According to the Kohlmann condition $\partial x/\partial\xi_1 = \partial y/\partial\xi_2, \partial x/\partial\xi_2 = -\partial y/\partial\xi_1$, Eq. (2.22) can be rewritten to

$$|J(x,y;\xi_1,\xi_2)| = \left(\frac{\partial\xi_1}{\partial x}\right)^2 + \left(\frac{\partial\xi_2}{\partial y}\right)^2 \tag{2.23}$$

For using the Green's function or separation variable method to solve the equation, in order to make the two-dimensional Helmholtz equation separable and have a separation form of $w = F(\xi_1)G(\xi_2)$, the following conditions must be satisfied

$$\frac{\partial^2}{\partial\xi_1\partial\xi_2}\left[\left|\frac{dz}{d\zeta}\right|^2\right] = 0 \tag{2.24}$$

The governing differential equation used to establish a coordinate system for separating Helmholtz equations is

$$\frac{d^2}{d\zeta^2}\left(\frac{dz}{d\zeta}\right) = \chi\left(\frac{dz}{d\zeta}\right) \tag{2.25}$$

where χ is a constant.

According to Eq. (2.21), the wave number k is expressed as

$$k^2(z,\bar{z}) = \frac{\partial(\xi_1(x,y),\xi_2(x,y))}{\partial(x,y)} = k_0^2\left|\frac{d\zeta}{dz}\right|^2 \tag{2.26}$$

where k_0 is the reference wave number, $k_0 = \omega_0/c_0$, c_0 is the corresponding reference wave velocity.

Bringing Eq. (2.26) into Eq. (2.20) yields the standard Helmholtz equation

$$\frac{\partial^2 w}{\partial\xi_1^2} + \frac{\partial^2 w}{\partial\xi_2^2} + \frac{1}{4}k_0^2 w = 0 \tag{2.27}$$

The standardization process of variable coefficient partial differential equations in this section is essentially a process of converting a two-dimensional coordinate system $(x,y)$to another two-dimensional coordinate system (ξ_1,ξ_2). The converted coordinate system can be represented as $\xi_1(x,y)$and $\xi_2(x,y)$, the conversion relationship between two coordinate systems can be determined through the complex variable function $\zeta = \zeta(z) = \xi_1 + i(\xi_2)$ given. Moreover, this complex variable function must be an analytic function of the complex variable function $z = x + \mathrm{i}y$. The partial differential equation between two complex variable functions can be expressed as $\partial/\partial z = (d\zeta/dz)/(\partial/\partial\zeta\ )$ and $\partial/\partial\bar{z} = \left(d\bar{\zeta}/d\bar{z}\right)/\left(\partial/\partial\bar{\zeta}\right)$.

2.2.2 Solution of wave equation in density inhomogeneous media

A two-dimensional density inhomogeneous continuous medium with a density of $\rho(x,y)$ and a constant elastic modulus. In the case of time harmonic, the basic equation for controlling the free propagation of waves is one with a variable coefficient, as a variable wave number of $k(x,y)=\omega/c$ Helmholtz equation, where c represents $\sqrt{(\lambda+2\mu)/\rho}$; or $\sqrt{\mu/\rho}$;. The equation can be expressed as

$$\nabla^2 w + k^2(x,y)\, w = 0 \tag{2.28}$$

Stress component form

According to the previous section, this equation can be written in the form of Eq. (2.27) by introducing variables. In order to determine the unique solution of the displacement field for a given stress boundary condition in subsequent research, this section provides the expression of the stress component in the corresponding coordinate system. In the complex plane z, the corresponding stress component can be expressed as

$$\tau_{xz} = \mu\left(\frac{\partial w}{\partial z} + \frac{\partial w}{\partial \bar{z}}\right) \tag{2.29}$$

$$\tau_{yz} = \mathrm{i}\mu\left(\frac{\partial w}{\partial z} - \frac{\partial w}{\partial \bar{z}}\right) \tag{2.30}$$

In cylindrical coordinate by using $z = re^{\mathrm{i}\theta}$, the above equations can be rewritten into radial and circumferential stress forms

$$\tau_{rz} = \mu\left(\frac{\partial w}{\partial z}e^{\mathrm{i}\theta} + \frac{\partial w}{\partial \bar{z}}e^{-\mathrm{i}\theta}\right) \tag{2.31}$$

$$\tau_{\theta z} = i\mu\left(\frac{\partial w}{\partial z}e^{\mathrm{i}\theta} - \frac{\partial w}{\partial \bar{z}}e^{-\mathrm{i}\theta}\right) \tag{2.32}$$

Introduce a coordinate variable ξ_i and parsing function $\zeta = \zeta(z) = \xi_1 + \mathrm{i}\xi_2$, which can ultimately convert the Helmholtz equation with variable coefficients into a standard Helmholtz equation, as Eq. (2.27). The key step here is to specify the spatial variation of the Jacobian matrix $|J(x,y;\xi_1,\xi_2)|$, which offsets the spatial variation of the wave number

$$k^2(x,y;\xi_1,\xi_2) = k_0^2 |ds/dz\,|^2 = k_0^2 |J(x,y;\xi_1,\xi_2)|^{-2} \tag{2.33}$$

According to the above formulation, it can be deduced that the applicable density form distribution is

$$\rho(x,y) = \rho_0 |J(x,y;\xi_1,\xi_2)|^{-1} \tag{2.34}$$

In this way, the form of the solution to Eq. (2.28) depends on the selected density distribution form of the inhomogeneous medium that satisfies the above conditions.

In the form of Eq. (2.27), based on Eqs. (2.31) and (2.32) and the coordinate transformation function $\zeta = \zeta(z) = \xi_1 + \mathrm{i}\xi_2$, the corresponding stress component expression in the ζ plane can be obtained

$$\tau_{rz} = \mu \left[\frac{\partial \varphi}{\partial \zeta} \zeta'(z) e^{\mathrm{i}\theta} + \frac{\partial \varphi}{\partial \bar{\zeta}} \bar{\zeta}'(\bar{z}) e^{-\mathrm{i}\theta} \right] \tag{2.35}$$

$$\tau_{\theta z} = \mathrm{i}\mu \left[\frac{\partial \varphi}{\partial \zeta} \zeta'(z) e^{\mathrm{i}\theta} - \frac{\partial \varphi}{\partial \bar{\zeta}} \bar{\zeta}'(\bar{z}) e^{-\mathrm{i}\theta} \right] \tag{2.36}$$

Solution based on separation of variables

The analytical solution of the Helmholtz equation can be obtained by using the separation of variables method, Green's function method, energy method, etc. In this thesis, the wave function expansion solution of the separation of variables method is used. Under polar coordinates (r,θ), $r = \sqrt{(\xi_1^2 + \xi_2^2)} = |\zeta|$, $\theta = \tan^{-1}(\xi_2/\xi_1)$, Eq. (2.28) can be converted to

$$\frac{\partial^2 w}{\partial r^2} + \frac{1}{r}\frac{\partial w}{\partial r} + \frac{1}{r^2}\frac{\partial^2 w}{\partial \theta^2} + {k_0}^2 w = 0 \tag{2.37}$$

Based on the following separated variable form

$$w(r,\theta,z) = R(r)\Theta(\theta) \tag{2.38}$$

Substituting the above equation into Eq. (2.37) has

$$\Theta\frac{d^2R}{dr^2} + \frac{\Theta}{r}\frac{dR}{dr} + \frac{R}{r^2}\frac{d^2\Theta}{d\theta^2} + k_0^2 R\Theta = 0 \tag{2.39}$$

Simplify the equation and introduce the constant λ to decompose the equation into

$$\Theta + \lambda\Theta = 0 \tag{2.40}$$

$$r^2\frac{d^2R}{dr^2} + r\frac{dR}{dr} + \left(k_0^2 r^2 - \lambda\right) R \tag{2.41}$$

The eigenfunction of Eq. (2.40) is

$$\Theta(\theta) = A\cos\sqrt{\lambda}\theta + B\sin\sqrt{\lambda}\theta \tag{2.42}$$

where in the process of solving wave problems, the constant λ can be calculated based on stress boundary conditions, which is generally an array of n terms. To facilitate subsequent representations, let $\lambda = n^2$, A, B are unknown coefficients to be determined.

Eq. (2.41) is a Bessel equation of order n, and the form of its solution can be written as follows

$$R(r) = J_n(k_0 r) \tag{2.43}$$

Then, according to the form of the solution shown in Eq. (2.42) and (2.43), the return Eq. (2.38) has

$$w(r,\theta) = \sum_{n=0}^{\infty} A_n J_n(k_0 r)\cos n\theta + B_n J_n(k_0 r)\sin n\theta \tag{2.44}$$

In the ζ coordinate system

$$\begin{aligned} w(r,\theta) = \sum_{n=0}^{\infty} & A_n J_n(k_0|\zeta|)\left\{\left(\frac{\zeta}{|\zeta|}\right)^n + \left(\frac{\zeta}{|\zeta|}\right)^{-n}\right\} \\ & + B_n J_n(k_0|\zeta|)\left\{\left(\frac{\zeta}{|\zeta|}\right)^n - \left(\frac{\zeta}{|\zeta|}\right)^{-n}\right\} \end{aligned} \tag{2.45}$$

where the unknown coefficient to be determined is A_n, B_n can be obtained by substituting boundary conditions.

2.3 Summary

This chapter first introduces the kinematic governing equations of elastomers in detail, and then derives the general form of the governing equations for inhomogeneous media. Taking a two-dimensional density inhomogeneous media as an example, the corresponding wave equation is given. Based on the theory of complex variable functions, the process of converting variable coefficient partial differential equations into standard Helmholtz equations is presented in detail. Meanwhile, the stress component forms in each plane are given. By using the wave function expansion method, the fundamental solution of the wave equation in inhomogeneous media is established.

Chapter 3

Scattering of SH waves by a semi-cylindrical depression in inhomogeneous media

Traditional homogeneous materials are no longer satisfied the demand of engineering application with the engineering demand constantly updated. Designable functionality inhomogeneous materials have been widely researched and applied with the continuous development of materials science, meanwhile, the propagation characteristics of elastic waves in the inhomogeneous media are also concerned. Investigating the propagation of the elastic waves in inhomogeneous media is necessary to analyze the dynamic responses of natural and artificial materials. The scattering of elastic waves on the material surface plays an important role in many engineering applications, such as soil exploration, nondestructive testing, and earthquake engineering. The scattering of SH waves by a semi-cylindrical depression can be regarded as the research foundation of the effect of surface shapes on elastic wave scattering, and therefore is of theoretical and practical engineering significance to investigate.

3.1 Model and governing equation

3.1.1 Model establishment

The scattering of SH waves by semi-cylindrical depression on the surface of inhomogeneous media is the main research content of this chapter, a semi-infinite mechanical model was established, as shown in Fig.3.1. There are many factors affecting the assumption of material parameters in inhomogeneous media. The focus of consideration is the variable wave velocity due to the inhomogeneous media, as researching the propagation characteristic of elastic

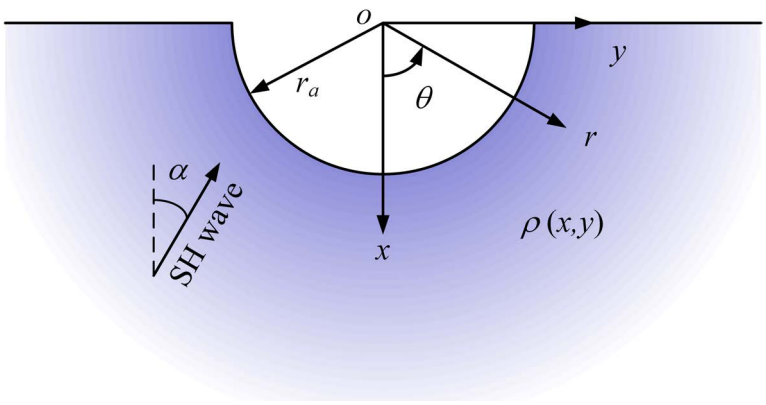

Fig. 3.1 Model for scattering SH wave by a surface semi-cylindrical depression in density inhomogeneous media.

waves in the inhomogeneous media. Therefore, in order to ensure that the wave velocity various with the spatial coordinates, the model media parameters are in the form of density $\rho(x,y)$ varying with the spatial coordinates and elastic modulus μ is constant. The radius of the semi-cylindrical depression in this model is r_a, and the origin of the coordinates of the Cartesian coordinate system is located at the center of the semi-cylindrical. The x-axis is vertically down, the y-axis is horizontally to the right, and the SH wave is incident at an angle α to the x-axis.

3.1.2 Solution of governing equation

According to the model and the form of boundary conditions, the polar coordinate system was used to establish the equation. The density of the inhomogeneous media $\rho(r,\theta)$ varies with the coordinates in the following form, and satisfy the condition that Eq. (2.34).

$$\rho(r,\theta) = \rho_0 \beta^2 r^{2(\beta-1)}, \beta > 0 \tag{3.1}$$

where ρ_0 is the reference density of the media, β is the inhomogeneous parameter, represents the various of density radial inhomogeneous media. The media density is proportional to β in the case of radius is r, The density of media increases with the deepening of the radius r, when $\beta > 1$. The density of media decreases with the deepening of the radius r, when $\beta < 1$. In particular, $\rho(r,\theta) = \rho_0$ as $\beta = 1$, which means homogeneous media situation. According to the above formalism, $c = \sqrt{\rho_0 \beta^2 r^{2(\beta-1)}/\mu} = \beta r^{(\beta-1)} \sqrt{\rho_0/\mu}$.

According to the density form set, the corresponding wave number form can be obtained as following by bringing it into Eq. (2.33).

$$k(r,\theta) = k_0 \beta r^{\beta-1}, \beta > 0 \tag{3.2}$$

where k_0 is the reference wave number.

The governing equation of the two-dimensional density inhomogeneous plane SH wave in cylindrical coordinates can be written as:

$$r^2 \frac{\partial^2 w}{\partial r^2} + r \frac{\partial w}{\partial r} + \frac{\partial^2 w}{\partial \theta^2} + r^2 k^2(r,\theta) u = 0 \tag{3.3}$$

Bring Eq. (3.2) into

$$\frac{\partial^2 w}{\partial r^2} + \frac{1}{r}\frac{\partial w}{\partial r} + \frac{1}{r^2}\frac{\partial^2 w}{\partial \theta^2} + k_0^2 \beta^2 r^{2(\beta-1)} w = 0 \tag{3.4}$$

According to the transformation method in the previous chapter, complex variables are introduced, z and $\bar{z}$ are equal to $re^{\mathrm{i}\theta}$ and $re^{-\mathrm{i}\theta}$, respectively. The Eq. (3.4) is transformed into:

$$\frac{\partial^2 w}{\partial z \partial \bar{z}} + \frac{1}{4}\beta^2 (z\bar{z})^{\beta} k_0^2 w = 0 \tag{3.5}$$

According to the transformation method in the section 2.2.2, variate ξ_i are introduced, hence ζ, $\zeta(z)$ and $\xi_1 + \mathrm{i}\xi_2$ are equal. The transformation form can be derived from Eq. (2.26) and Eq. (3.1)

$$\zeta = z^{\beta}, \ \bar{\zeta} = \bar{z}^{\beta} \tag{3.6}$$

Then Eq. (3.5) can be transformed into the standard Helmholtz equation:

$$\frac{\partial^2 w}{\partial \zeta \partial \bar{\zeta}} + \frac{1}{4} k_0^2 w = 0 \tag{3.7}$$

This equation is the standard Helmholtz equation, and there is no variable coefficient before the function term. Thus, this equation can be solved analytically using the separation variable method in the section 2.2.

3.2 Wave field in the region

3.2.1 Displacement field expression

In this model, the total wave field w in the inhomogeneous semi-infinite space can be composed of free wave field $w^{(f)}$ and scattering wave field $w^{(s)}$:

$$w = w^{(f)} + w^{(s)} \tag{3.8}$$

With SH wave incident at an angle α to the x-axis, based on the symmetry of the inhomogeneous media and the model used in this chapter, the incident wave in the ζ plane can be written as:

$$w^{(i)} = w_0 \exp\left[\mathrm{i}k_0\left(-\zeta e^{\mathrm{i}\alpha} - \bar{\zeta} e^{-\mathrm{i}\alpha}\right)/2\right] \tag{3.9}$$

where w_0 is the displacement amplitude of the incident wave.

The problem of inhomogeneous semi-infinite space is demonstrated in this chapter, so the incident wave will produce a reflected wave at the horizontal boundary of the semi-infinite space, and the reflecting wave can be expressed as:

$$w^{(r)} = w_0 \exp\left[\mathrm{i}k_0\left(\zeta e^{-\mathrm{i}\alpha} + \bar{\zeta} e^{\mathrm{i}\alpha}\right)/2\right] \tag{3.10}$$

The free wave field $w^{(f)}$ in the semi-infinite space is the superposition of the incident wave field $w^{(i)}$ and the reflected wave field $w^{(r)}$:

$$w^{(f)} = w^{(i)} + w^{(r)} \tag{3.11}$$

The expression of the free wave field satisfies the stress free condition at the horizontal boundary on both sides of the semi-infinite domain, and it is expanded into the form of cylindrical wave:

$$\begin{aligned} w^{(f)} = & \sum_{n=0}^{\infty} (-1)^n \varepsilon_n w_0 J_{2n/\beta}\left(k_0|\zeta|\right)\cos 2n\alpha \cdot \left\{\left(\frac{\zeta}{|\zeta|}\right)^{2n/\beta} + \left(\frac{\zeta}{|\zeta|}\right)^{-2n/\beta}\right\} \\ & + 2\sum_{n=0}^{\infty} (-1)^n w_0 J_{(2n+1)/\beta}\left(k_0|\zeta|\right)\sin\left(2n+1\right)\alpha \\ & \cdot \left\{\left(\frac{\zeta}{|\zeta|}\right)^{(2n+1)/\beta} - \left(\frac{\zeta}{|\zeta|}\right)^{-(2n+1)/\beta}\right\} \end{aligned} \tag{3.12}$$

where $J_n(\cdot)$ is Bessel function of order n, $\varepsilon_n = \begin{cases} 1, & n=0 \\ 2, & n>0 \end{cases}$

There will be corresponding scattering wave field due to the defect of semi-cylindrical depression at the horizontal interface of semi-infinite space, since the incident wave reaches the boundary of the semi-cylindrical depression. Therefore, it is necessary to construct the scattering wave field satisfying the governing equation of the inhomogeneous media, according to the standardized Helmholtz equation.

In order to ensure the existence of a unique solution of the constructed wave field, the Sommerfeld radiation condition should be satisfied, and the scattering wave field can be expressed as:

$$\begin{aligned} w^{(s)}\left(\zeta,\bar{\zeta}\right) = w_0 \sum_{n=0}^{\infty} \Bigg\{ & A_n{}^{(1)} H^{(1)}_{2n/\beta}\left(k_0|\zeta|\right)\left[\left(\frac{\zeta}{|\zeta|}\right)^{2n/\beta} + \left(\frac{\zeta}{|\zeta|}\right)^{-2n/\beta}\right] \\ & + A_n{}^{(2)} H^{(1)}_{(2n+1)/\beta}\left(k_0|\zeta|\right)\left[\left(\frac{\zeta}{|\zeta|}\right)^{(2n+1)/\beta} - \left(\frac{\zeta}{|\zeta|}\right)^{-(2n+1)/\beta}\right] \Bigg\} \end{aligned} \tag{3.13}$$

where $H_n^{(1)}(\cdot)$ is the first Hankel function of order n, $A_n^{(1)}$ and $A_n^{(2)}$ are the unknown coefficient to be solved. The unknown coefficient can be solved by boundary conditions, and then the final wave field expression can be obtained.

3.2.2 Stress field expression

In order to obtain the wave field, the stress boundary conditions should be used at the semi-cylindrical depression boundary to solve the unknown coefficients in the scattering wave.

Therefore, it is necessary to give the stress expression forms corresponding to the free wave field and the scattering wave field. According to Eqs. 2.35 and 2.36 and the transformation form Eq. (3.6), there is:

$$\tau_{rz} = \beta\mu\left(\frac{\partial w}{\partial\zeta} z^{\beta-1} e^{\mathrm{i}\theta} + \frac{\partial w}{\partial\bar{\zeta}} \bar{z}^{\beta-1} e^{-\mathrm{i}\theta}\right) \tag{3.14}$$

$$\tau_{\theta z} = \mathrm{i}\beta\mu\left(\frac{\partial w}{\partial\zeta} z^{\beta-1} e^{\mathrm{i}\theta} - \frac{\partial w}{\partial\bar{\zeta}} \bar{z}^{\beta-1} e^{-\mathrm{i}\theta}\right) \tag{3.15}$$

The expression of the free wave field Eq. (3.11) brings into the above equation, and the expression of the stress field is as follows:

$$\begin{aligned}\tau_{rz}^{(f)} = \frac{\beta\mu k_0 w_0}{2}\Bigg[&\sum_{n=0}^{\infty}(-1)^n\varepsilon_n P_{2n/\beta}\ (\zeta)\cos 2n\alpha \\ &+2\sum_{n=0}^{\infty}(-1)^n Q_{(2n+1)/\beta}\ (\zeta)\sin(2n+1)\alpha\Bigg]\end{aligned} \tag{3.16}$$

$$\begin{aligned}\tau_{\theta z}^{(f)} = \frac{\mathrm{i}\beta\mu k_0 w_0}{2}\Bigg[&\sum_{n=0}^{\infty}(-1)^n\varepsilon_n P_{2n/\beta}\ (\zeta)\cos 2n\alpha \\ &-2\sum_{n=0}^{\infty}(-1)^n Q_{(2n+1)/\beta}\ (\zeta)\sin(2n+1)\alpha\Bigg]\end{aligned} \tag{3.17}$$

where

$$\begin{aligned}P_t(s) = {} & J_{t-1}(k_0|s|)\left[\frac{s}{|s|}\right]^{t-1} z^{\beta-1}e^{\mathrm{i}\theta} - J_{t+1}(k_0|s|)\left[\frac{s}{|s|}\right]^{-t-1} z^{\beta-1}e^{\mathrm{i}\theta} \\ & + J_{t-1}(k_0|s|)\left[\frac{s}{|s|}\right]^{1-t}\bar{z}^{\beta-1}e^{-\mathrm{i}\theta} - J_{t+1}(k_0|s|)\left[\frac{s}{|s|}\right]^{-t-1}\bar{z}^{\beta-1}e^{-\mathrm{i}\theta}\end{aligned}$$

$$\begin{aligned}Q_t(s) = {} & J_{t-1}(k_0|s|)\left[\frac{s}{|s|}\right]^{t-1} z^{\beta-1}e^{\mathrm{i}\theta} + J_{t+1}(k_0|s|)\left[\frac{s}{|s|}\right]^{-t-1} z^{\beta-1}e^{\mathrm{i}\theta} \\ & - J_{t-1}(k_0|s|)\left[\frac{s}{|s|}\right]^{1-t}\bar{z}^{\beta-1}e^{-\mathrm{i}\theta} - J_{t+1}(k_0|s|)\left[\frac{s}{|s|}\right]^{-t-1}\bar{z}^{\beta-1}e^{-\mathrm{i}\theta}\end{aligned}$$

Based on the scattering wave field expression Eq. (3.12), the corresponding stress field is given as:

$$\tau_{rz}^{(s)} = \frac{\beta\mu k_0 w_0}{2}\sum_{n=0}^{\infty}\left[A_n^{(1)}U_{2n/\beta}\ (\zeta) + A_n^{(2)}V_{(2n+1)/\beta}\ (\zeta)\right] \tag{3.18}$$

$$\tau_{\theta z}^{(s)} = \frac{\mathrm{i}\beta\mu k_0 w_0}{2}\sum_{n=0}^{\infty}\left[A_n^{(1)}U_{2n/\beta}\ (\zeta) - A_n^{(2)}V_{(2n+1)/\beta}\ (\zeta)\right] \tag{3.19}$$

where

$$\begin{aligned}U_t(s) = {} & H_{t-1}^{(1)}(k_0|s|)\left[\frac{s}{|s|}\right]^{t-1} z^{\beta-1}e^{\mathrm{i}\theta} - H_{t+1}^{(1)}(k_0|s|)\left[\frac{s}{|s|}\right]^{-t-1} z^{\beta-1}e^{\mathrm{i}\theta} \\ & + H_{t-1}^{(1)}(k_0|s|)\left[\frac{s}{|s|}\right]^{1-t}\bar{z}^{\beta-1}e^{-\mathrm{i}\theta} - H_{t+1}^{(1)}(k_0|s|)\left[\frac{s}{|s|}\right]^{-t-1}\bar{z}^{\beta-1}e^{-\mathrm{i}\theta}\end{aligned}$$

$$V_t(s) = H_{t-1}^{(1)}(k_0|s|)\left[\frac{s}{|s|}\right]^{t-1} z^{\beta-1}e^{\mathrm{i}\theta} + H_{t+1}^{(1)}(k_0|s|)\left[\frac{s}{|s|}\right]^{-t-1} z^{\beta-1}e^{\mathrm{i}\theta}$$
$$- H_{t-1}^{(1)}(k_0|s|)\left[\frac{s}{|s|}\right]^{1-t} \bar{z}^{\beta-1}e^{-\mathrm{i}\theta} - H_{t+1}^{(1)}(k_0|s|)\left[\frac{s}{|s|}\right]^{-t-1} \bar{z}^{\beta-1}e^{-\mathrm{i}\theta}$$

3.3 Boundary conditions and equations solving

3.3.1 Boundary conditions

The stress free condition of the model in this chapter has been automatically satisfied at the horizontal boundary when constructing the free wave field. The stress free condition needs to be satisfied at the boundary of the semi-cylindrical depression, that is:

$$\tau_{rz}^{(f)} + \tau_{rz}^{(s)} = 0,\ r = r_a \tag{3.20}$$

Plugging the Eqs. (3.15)-(3.18) into the boundary conditions Eq. (3.19),

$$\begin{cases} \sum_{n=0}^{\infty} A_n^{(1)} E_{2n} = -\sum_{n=0}^{\infty} F_{2n} \\ \sum_{n=0}^{\infty} A_n^{(2)} E_{2n+1} = -\sum_{n=0}^{\infty} F_{2n+1} \end{cases} \tag{3.21}$$

where $E_{2n} = U_{2n/\beta}(\zeta)$, $\quad E_{2n+1} = V_{(2n+1)/\beta}(\zeta)$,
$F_{2n} = (-1)^n \varepsilon_n \cos 2n\alpha \cdot P_{2n/\beta}$, $\quad F_{2n+1} = 2(-1)^n \sin(2n+1)\alpha \cdot Q_{(2n+1)/\beta}$.

3.3.2 Solution of wave motion equation

There are many methods to solve above infinite algebraic equations, while different methods bring slightly different accuracy and computational cost, such as convergence results can be obtained quickly at high frequencies. At present, solving infinite equations with high precision is still a direction of mathematical research. The Fourier series expansion method is used to solve the above infinite algebraic equations in this work. This method is widely used in solving the infinite algebraic equations with well convergence and calculation speed. Multiply both sides of the equation by $e^{-\mathrm{i}m\theta}$ and integrate from $-\pi/2$ to $\pi/2$, the equation

can be expanded into the following form:

$$\begin{cases} \sum_{n=0}^{\infty} E_{mn}^{(1)} A_n^{(1)} = -\sum_{n=0}^{\infty} F_{mn}^{(1)} \\ \sum_{n=0}^{\infty} E_{mn}^{(2)} A_n^{(2)} = -\sum_{n=0}^{\infty} F_{mn}^{(2)} \end{cases} \tag{3.22}$$

where $E_{mn}^{(1)} = \int_{-\frac{\pi}{2}}^{\frac{\pi}{2}} E_{2n} e^{-\mathrm{i}m\theta} d\theta$, $E_{mn}^{(2)} = \int_{-\frac{\pi}{2}}^{\frac{\pi}{2}} E_{2n+1}(\zeta) e^{-\mathrm{i}m\theta} d\theta$,
$F_{mn}^{(1)} = \int_{-\frac{\pi}{2}}^{\frac{\pi}{2}} F_{2n} e^{-\mathrm{i}m\theta} d\theta$, $F_{mn}^{(1)} = \int_{-\frac{\pi}{2}}^{\frac{\pi}{2}} F_{2n+1} e^{-\mathrm{i}m\theta} d\theta$.

3.4 Examples analysis

Dimensionless frequency η is defined for presentation.

$$\eta = 2r_a/\lambda \ = k_0 r_a/\pi \tag{3.23}$$

where λ is the wavelength. The dimensionless frequency η can be used to represent the magnitude of the wave number and the ratio of wavelengths in the span domain of the depression.

The displacement amplitude $|w|$ can be calculated by the following formula:

$$|w| = \sqrt{[\mathrm{Re}(w)]^2 + [\mathrm{Im}(w)]^2} \tag{3.24}$$

3.4.1 Convergence analysis

This research requires to truncate the infinite series in order to obtain the corresponding numerical results, since the series expansion method is used to solve the infinite system of equations. Two typical positions, point 1 $(0,-1.5)$ and point 2 $(1,0)$, are chosen to analyze the convergence of the free and scattering wave fields, as shown in Fig. 3.2. The dimensionless frequency $\eta = 1.5$ incident angle $\alpha = 90°$, inhomogeneous parameters $\beta = 0.5$ and $\beta = 1.5$ are set in order to satisfy the convergence requirements of all examples in this section. Truncating terms $N = m = n$ are considered to build the standard solution matrix. The results of the free wave field and the scattering wave field can already converge, as truncation terms reaches 5 in Fig. 3.2. Therefore, the stability and reliability of the numerical results have been ensured through a large number of convergence analyses. The convergence requirement can be satisfied if m and n are taken to be 15 for the subsequent examples.

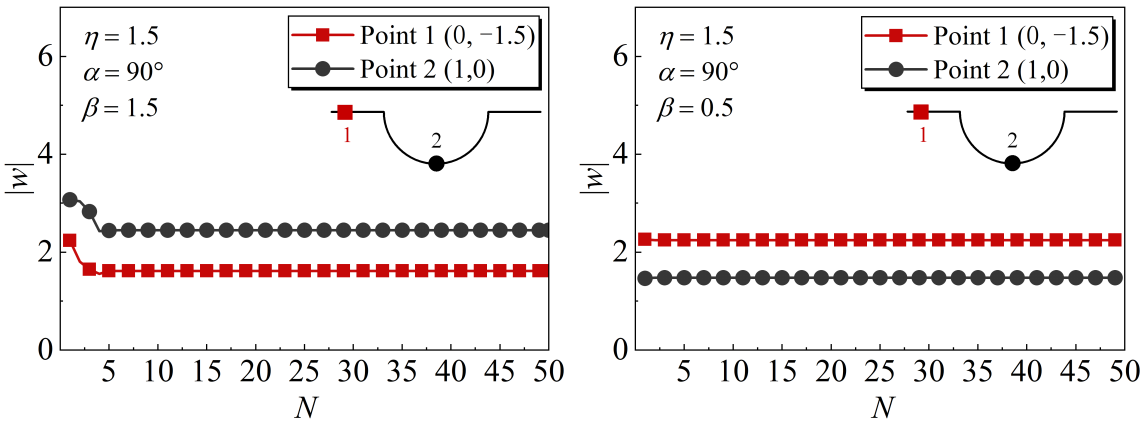

(a) $\beta = 1.5$ (b) $\beta = 0.5$

Fig. 3.2 Convergence analysis of five typical position displacement amplitudes increasing with truncation term N

3.4.2 Validation

In order to verify the validation of the obtained standardized Helmholtz equation and the constructed scattering wave field in this chapter, the present results is compared with the previous work. The horizontal axis represents the relative position coordinates of the semi-cylindrical depression and the horizontal boundary, where $[-3,-1)$ and $(1,\ 3]$ represents the horizontal boundary and $[-1,\ 1]$ represents the semi-circular depression, in Fig. 3.3. The dimensionless frequency η is set to 1.25. The inhomogeneous parameter β is set to 0.999 in order to ensure that the media still has certain inhomogeneous and approaches the homogeneous media, and the results of four incident angles are calculated and compared with those of the existing result, given in Fig. 3.3(a). Fig. 3.3(b) illustrates the displacement of the six observation points selected at the same position as in the reference as changing with the dimensionless frequency under horizontal incident. Fig. 3.3 dedicates that the calculation results are basically consistent with the results of Trifunac [159], thus verifying the validation of the method used in this section. Meanwhile, two sets of inhomogeneous parameters (β= 0.94, 0.96, 0.98 and β= 1.02, 1.04, 1.06), which approximate the homogeneous media, were used for calculation under horizontal and vertical incident with the dimensionless frequencies were 1.25 and 0.75, respectively, are shown in Fig. 3.4. The corresponding displacement is basically consistent with the results of the existing homogeneous media, when the value of the inhomogeneous parameter is close to 1, and the overall trend is consistent. This trend is reasonable in theory and further verifies the validation of the normalized and constructed wave field expressions.

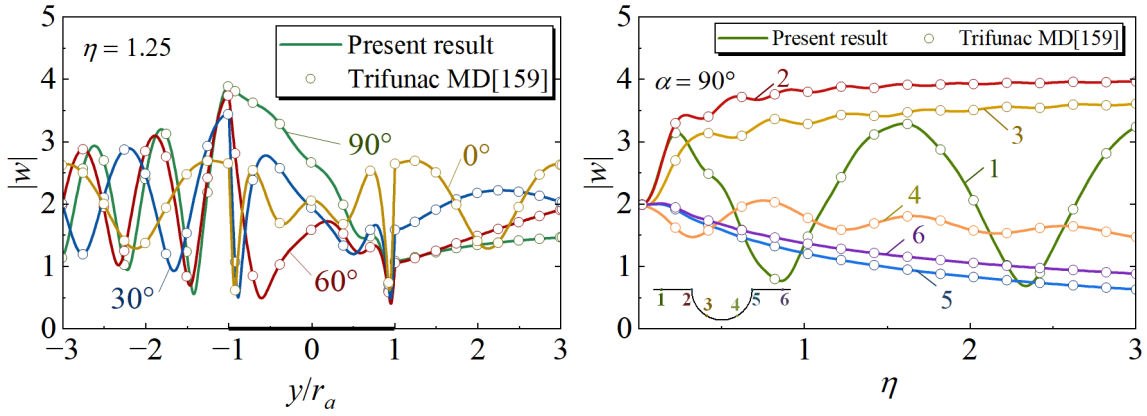

(a) $\eta = 1.25$ (b) $\alpha = 90°$

Fig. 3.3 Results of approximately homogeneous medium for comparison with the existing displacement results

3.4.3 Numerical Discussion

In this section, a series of numerical examples are carried out to explore the influence of inhomogeneous media on the propagation of elastic waves in the semi-infinite space and whether the amplification effect of surface depression on SH waves still holds. The first group of examples gives the displacement amplitudes of four different incident angles from the left at the dimensionless frequency η is 1.5 and the inhomogeneous parameters are 0.5, 0.75, 1.25 and 1.5, as shown in Fig. 3.5.

The displacement amplitude and the vibration frequency is proportional to inhomogeneous parameter, and the maximum displacement amplitude generally appears near the intersection of the horizontal boundary and depression. Notable is, under horizontal incident, the displacement amplitude of left side plane boundary at $\beta < 1$ is greater than $\beta > 1$, as shown in Fig. 3.5 (d). Due to the same radius, the media density at $\beta < 1$ is less than at $\beta > 1$. Therefore, horizontal incident at the same position, the displacement amplitude with small media density is slightly larger than that with large media density. However, this situation will change with the various incident angle in inhomogeneous media, the displacement on the left side of the semi-cylindrical depression still proportion in β. From the comparison of the four below figures that the inhomogeneous parameters have a great influence on the displacement distribution in different locations under different incident angles. The displacement amplitudes of different inhomogeneous parameters at the horizontal boundary are greatly different when the incident angle is less than 60°, while different inhomogeneous parameters have great influence on the displacement amplitudes at the depression as $\alpha > 60°$.

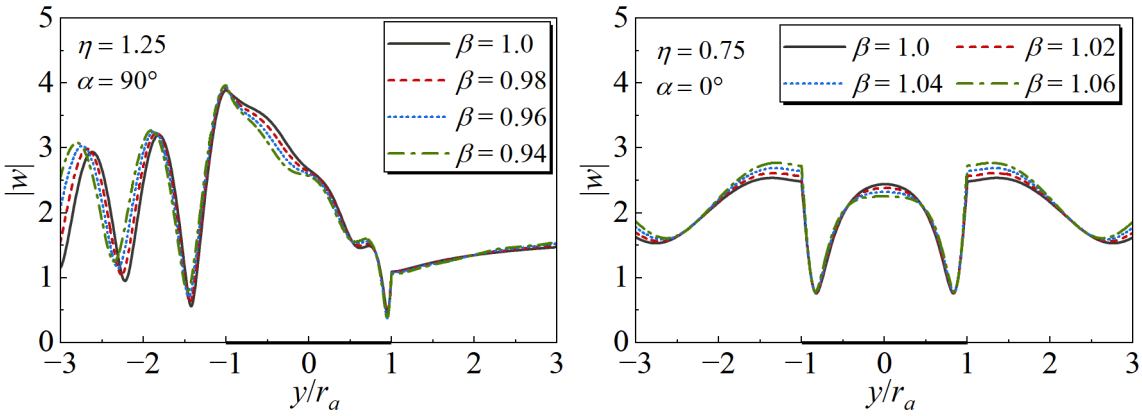

(a) $\eta = 1.25$ (b) $\eta = 0.75$

Fig. 3.4 Displacement distribution corresponding to different inhomogeneous parameters

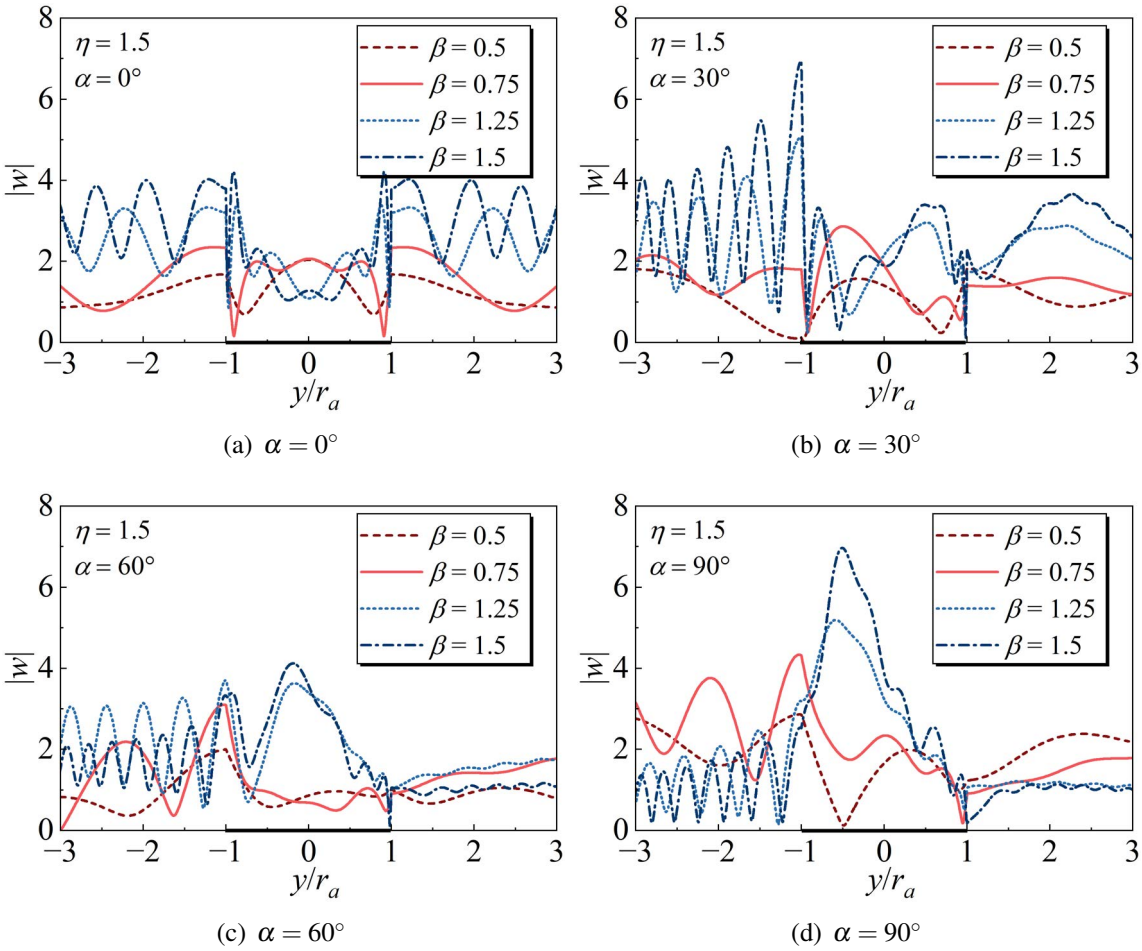

(a) $\alpha = 0°$ (b) $\alpha = 30°$

(c) $\alpha = 60°$ (d) $\alpha = 90°$

Fig. 3.5 Displacement amplitude with inhomogeneous parameter at dimensionless frequency $\eta = 1.5$

According to the results of the previous set of examples, the inhomogeneous parameters of 0.75 and 1.25 were selected as the values of the subsequent examples for the convenience of observation. The influence of inhomogeneous parameters on the surface displacement is further explored, and the results of a set of homogeneous result were adjunction for comparative analysis. Figs. 3.6 and 3.7 indicate the displacement amplitude at four incident angles with dimensionless frequencies $\eta = 0.75, 1.25$, $\beta = 0.75, 1.0, 1.25$, respectively. The displacement amplitude in inhomogeneous media can be observed more intuitively by introducing the results of homogeneous media. The displacement of the left side of the semi-cylindrical depression in the two sets of dimensionless parameter examples still indicates inversely proportional of density under horizontal incident, as shown in Figs. 3.6 (a) and 3.7 (a). At $\eta = 1.25$, the displacement amplitude at the junction of the depression and horizontal boundary is almost zero, which means, the displacement has a sudden change at this point. This phenomenon is also conformed with the characteristic that boundary between the horizontal and depression is prone to failure, and with dimensionless frequency rises, the displacement amplitude near the junction boundary is more obvious. Compared with the displacement amplitude results of the homogeneous media in the two sets of examples, the value and vibration of displacement amplitude with position change are basically smaller in the case of inhomogeneous media, at $\beta < 1$. While $\beta > 1$, it is larger than the homogeneous media, and the special case is the horizontal incident. The displacement amplitude of the depression surface increases obviously under $\beta > 1$, and decreases obviously if $\beta < 1$. At 60° and 90° incident, the displacement amplitude of the semi-cylindrical depression indicates large vibrations, while at incidence angle is 0° and 30°, the displacement of the horizontal boundary displays large variation.

As the incident angle changes from 0° to 90°, compared with the displacement amplitude in the homogeneous case, the influence of the displacement amplitude on the corresponding side of the wave surface increases first and then decreases as $\beta > 1$. Otherwise, if $\beta < 1$, it first decreases and then increases. With the dimensionless frequency η from Fig. 3.6 to Fig. 3.7, the displacement amplitude advanced and the vibration intensified. At vertical and 30° incident, for both sets of dimensionless frequencies, the position where the maximum displacement occurs moves from the lowest point of the depression to the junction with inhomogeneous parameters increasing. Under horizontal and 60° incident, the surface displacement of the horizontal boundary on the right side of the depression finally basically stabilized at an amplitude of about 1.

In order to explore the amplification effect of semi-cylindrical depression in density inhomogeneous media on the displacement amplitude, five observation points with different incident angles under $\beta = 1.25, 0.75$, respectively, are presented in Fig. 3.8 and Fig. 3.9.

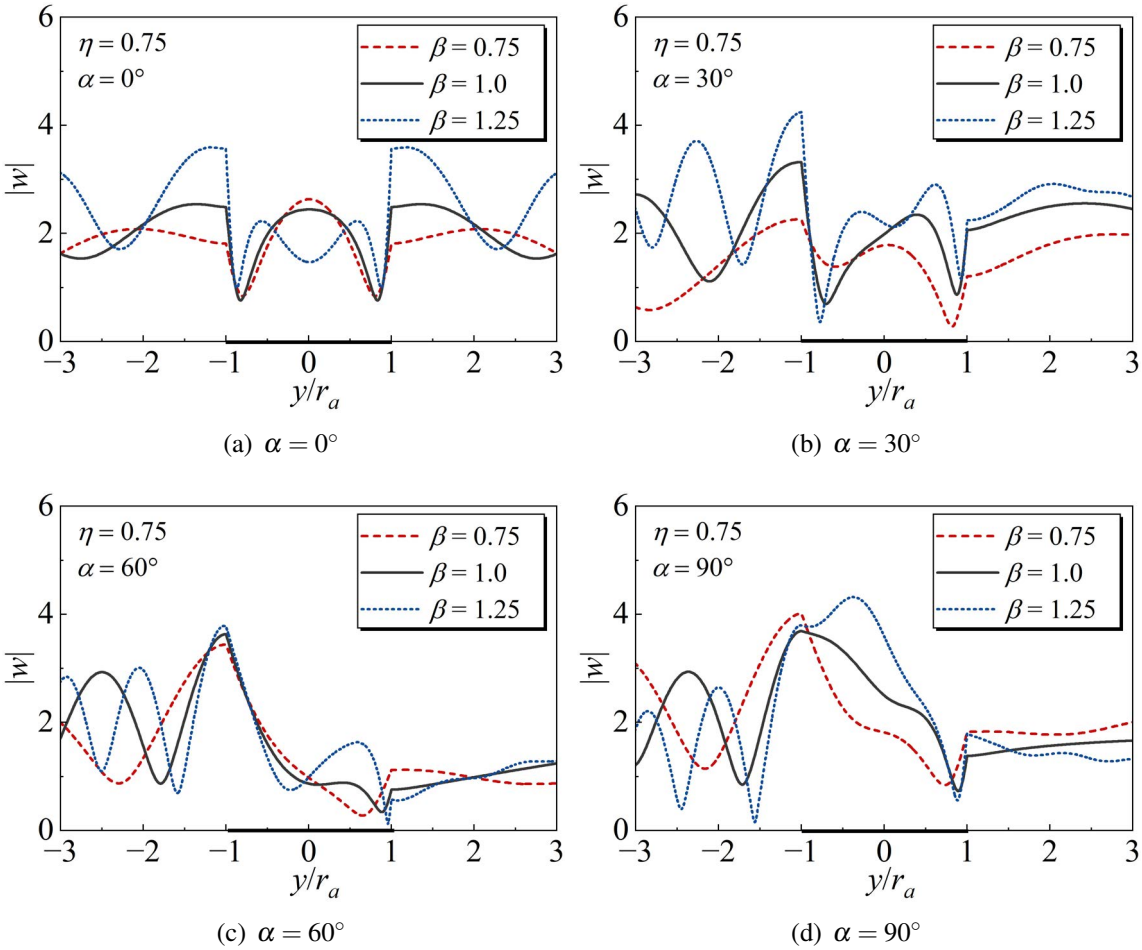

Fig. 3.6 Displacement amplitude with inhomogeneous parameter at dimensionless frequency $\eta = 0.75$

The amplification effect of surface depression in density inhomogeneous media on displacement amplitude is not more than 2 times, under the SH wave incident with $\beta = 1.25$ and $\eta < 3$. This amplification effect is higher than the 1.5 times amplification effect in homogeneous medium, as shown in Fig. 3.8(a). Although the amplification effect of point 3 shows vibration mode at vertical incident, the overall amplification effect is 0.5 times, and the amplification effect increases to 2 times with incident angle growing. For point 2, as the junction point between the depression and the horizontal boundary, the amplification effect is not proportion in incident angle as the incident angle varying from vertical to horizontal. However, the amplification effect reaches to 2.5 times at $\alpha = 30°$, in Fig. 3.8(b), and is not more than 2 times at the other incident angles. The amplification effect is always in the form of vibration and not greater than 2, which is also higher than the homogeneous case at point 1. Fig. 3.8(d) illustrates that although the amplification effect is in the form of vibration, it

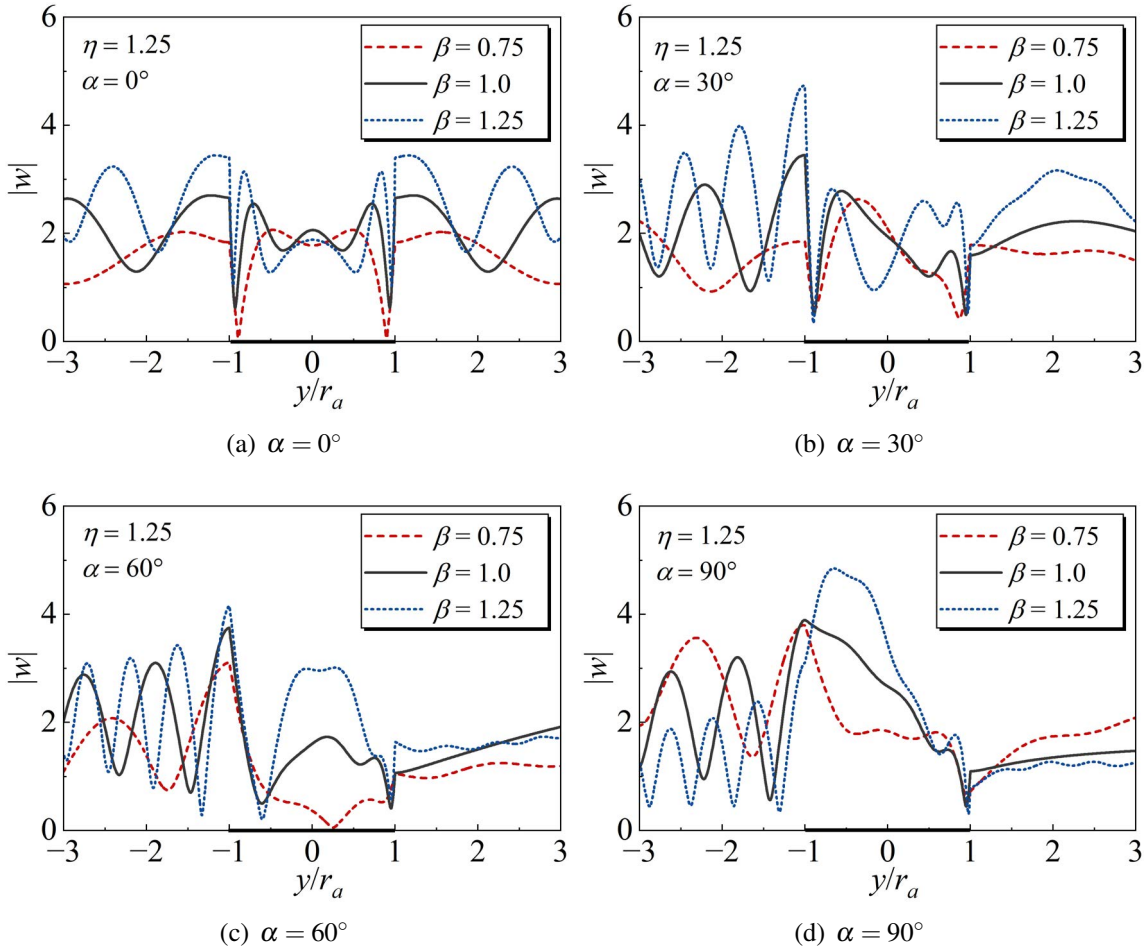

Fig. 3.7 Displacement amplitude with inhomogeneous parameter at dimensionless frequency $\eta = 1.25$

gradually reaches 0.5 times with the dimensionless frequency rising at the horizontal incident of points 1,4 and 5. The amplification effect of points of the back wave surface, as points 4 and 5, reaches the maximum under horizontal and vertical incident, and weakens under oblique incident.

Fig. 3.9 displays the amplification effect is weakened as a whole, and its amplification is basically no more than 1.5 times, when the inhomogeneous parameter is 0.75. Point 3 amplification is obviously different from that of the previous set of examples. As it amplification is inversely proportional of incident angle. Especially, it almost approaches to no amplification at horizontal incident. However, the displacement of points 1 and 2 increases sharply to 2.5 times under horizontal incident, from Fig.3.9 (d). Point 2 amplification effect begins to increase with the ascender of dimensionless frequency, as $\eta > 0.5$. However, the amplification effect will take the form of vibration as the dimensionless frequency variation at

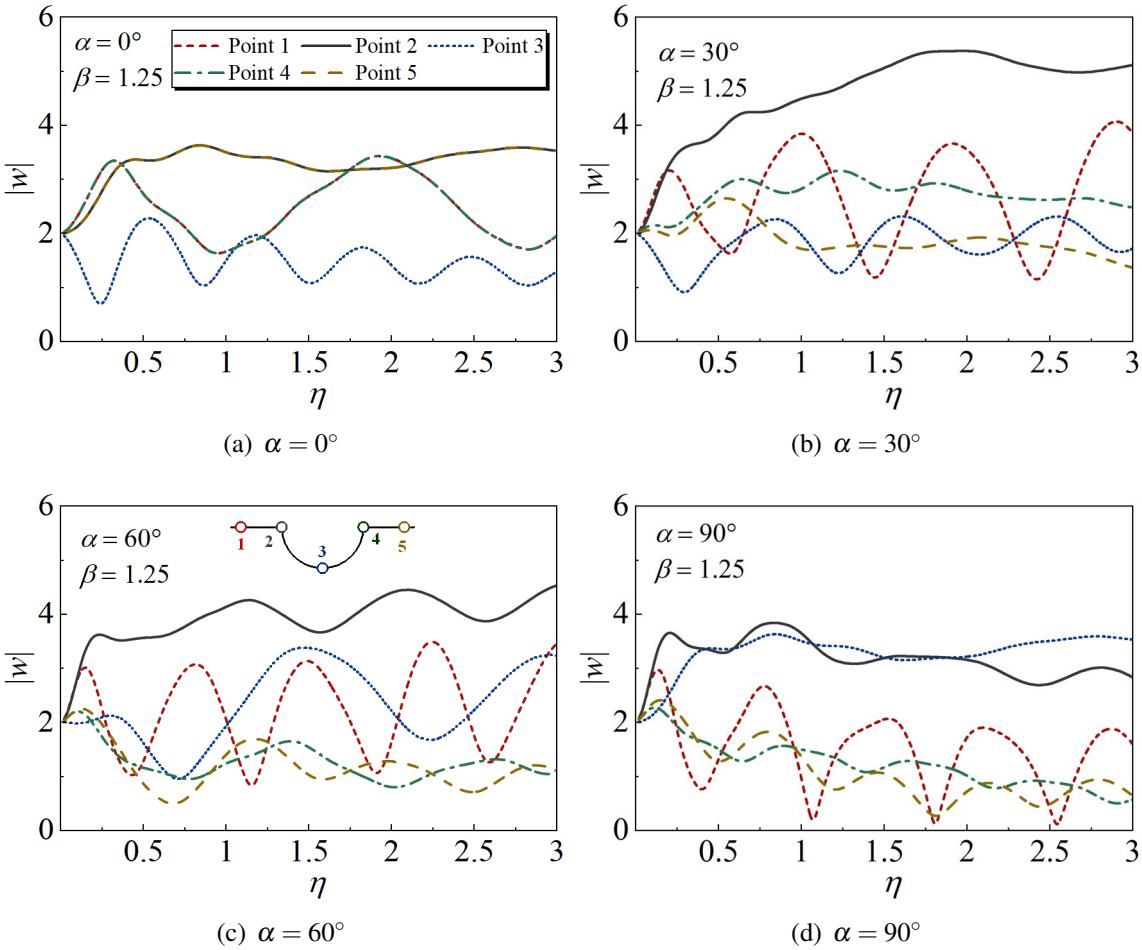

Fig. 3.8 Displacement amplitude of five selection observation points under inhomogeneous parameter $\beta = 1.25$

other points. Points 4 and 5 present the same effect as the previous set of examples, and still the horizontal and vertical incident have the largest effect. In general, the amplification effect of semi-cylindrical depression on displacement amplitude is weaker than that in homogeneous media in this kind of density inhomogeneous media. The most obvious amplification effect is observed at 30° incident for $\beta > 1$ and at vertical incident for $\beta < 1$.

In order to further explore the influence of surface depression on the displacement amplitude in inhomogeneous media with different parameters. Meanwhile, in order to more clearly explain the surface amplification of the depression boundary, the displacement amplification factor w^* is defined:

$$w^* = \frac{|w|}{\bar{w}} \tag{3.25}$$

where, $\bar{w}$ is the homogeneous surface displacement amplitude under quasi-static conditions.

Table 3.1 Displacement amplification coefficients under different incident angles with four inhomogeneous parameters

		$\beta = 0.5$							$\beta = 0.75$						
α	η / point	0.01	0.5	1	1.5	2	2.5	3	0.01	0.5	1	1.5	2	2.5	3
0°	1,6	1.00	0.84	0.67	0.57	0.49	0.49	0.65	1.00	0.86	0.84	0.95	1.07	1.00	0.89
	2,5	1.00	0.85	0.72	0.64	0.58	0.49	0.36	1.00	0.88	0.85	0.93	0.97	0.86	0.76
	3	1.00	0.85	0.70	0.58	0.54	0.68	1.01	1.00	0.83	0.58	0.53	1.01	1.37	1.35
30°	1	1.00	0.85	0.83	0.95	0.93	0.76	0.54	1.00	0.95	1.17	1.13	0.89	0.67	0.66
	2	1.00	0.86	0.83	0.96	1.02	0.96	0.79	1.00	0.95	1.19	1.31	1.24	1.09	1.06
	3	1.00	0.85	0.71	0.60	0.54	0.57	0.72	1.00	0.84	0.64	0.53	0.71	0.94	0.99
	4	1.00	0.85	0.64	0.35	0.11	0.06	0.26	1.00	0.85	0.58	0.43	0.49	0.65	0.82
	5	1.00	0.83	0.57	0.28	0.15	0.26	0.45	1.00	0.83	0.59	0.56	0.77	0.93	0.95
60°	1	1.00	0.86	0.96	1.23	1.23	1.04	0.87	1.00	1.04	1.39	1.17	0.91	0.55	0.38
	2	1.00	0.87	0.92	1.19	1.31	1.32	1.37	1.00	1.02	1.43	1.53	1.61	1.74	1.69
	3	1.00	0.85	0.71	0.63	0.56	0.46	0.27	1.00	0.87	0.78	0.75	0.65	0.41	0.17
	4	1.00	0.84	0.60	0.25	0.28	0.56	0.78	1.00	0.85	0.59	0.47	0.54	0.56	0.55
	5	1.00	0.83	0.55	0.37	0.52	0.63	0.60	1.00	0.85	0.69	0.64	0.58	0.45	0.41
90°	1	1.00	0.87	1.01	1.34	1.33	1.18	1.13	1.00	1.08	1.45	1.18	1.00	0.55	0.85
	2	1.00	0.87	0.95	1.28	1.42	1.47	1.65	1.00	1.05	1.52	1.61	1.82	2.03	1.91
	3	1.00	0.85	0.72	0.64	0.58	0.49	0.36	1.00	0.88	0.85	0.93	0.97	0.86	0.76
	4	1.00	0.84	0.59	0.27	0.43	0.78	1.05	1.00	0.86	0.66	0.67	0.86	0.90	0.78
	5	1.00	0.82	0.56	0.47	0.69	0.86	0.90	1.00	0.86	0.80	0.86	0.90	0.89	0.94

Continued Table 3.1 Displacement amplification coefficients under different incident angles with four inhomogeneous parameters

		$\beta = 0.5$							$\beta = 0.75$						
α	point \ η	0.01	0.5	1	1.5	2	2.5	3	0.01	0.5	1	1.5	2	2.5	3
0°	1,6	1.00	1.33	1.68	1.41	1.19	0.98	0.82	1.00	1.73	1.85	1.39	1.04	1.05	1.41
	2,5	1.00	1.17	1.56	1.68	1.70	1.81	1.78	1.00	1.42	1.90	2.03	2.20	2.22	2.19
	3	1.00	0.56	0.58	1.11	1.03	0.61	0.65	1.00	0.37	0.79	1.00	0.62	0.50	0.79
30°	1	1.00	1.53	1.34	0.93	0.94	1.59	1.90	1.00	1.73	1.13	1.23	2.15	2.06	1.15
	2	1.00	1.49	1.81	1.90	2.11	2.13	2.22	1.00	1.80	2.11	2.40	2.47	2.53	2.62
	3	1.00	0.70	0.47	0.78	0.98	1.12	1.06	1.00	0.58	0.53	0.84	1.03	1.00	0.67
	4	1.00	1.00	1.06	1.29	1.28	1.05	0.88	1.00	1.18	1.46	1.62	1.35	1.02	0.81
	5	1.00	1.06	1.15	1.37	1.50	1.42	1.38	1.00	1.25	1.39	1.67	1.68	1.64	1.85
60°	1	1.00	1.51	0.77	0.57	1.18	1.54	1.23	1.00	1.35	0.45	1.10	1.33	0.61	0.82
	2	1.00	1.71	1.77	1.78	1.81	1.93	2.04	1.00	1.95	1.82	1.72	1.83	2.08	2.30
	3	1.00	1.00	1.06	0.86	0.54	0.56	0.88	1.00	1.11	1.10	0.74	0.56	0.92	1.37
	4	1.00	1.12	0.84	0.48	0.26	0.35	0.63	1.00	1.29	0.84	0.33	0.31	0.84	1.18
	5	1.00	1.06	0.74	0.59	0.53	0.48	0.59	1.00	1.06	0.68	0.58	0.37	0.48	0.61
90°	1	1.00	1.46	0.56	0.57	1.04	1.33	0.76	1.00	1.17	0.36	0.80	1.13	0.35	0.90
	2	1.00	1.77	1.71	1.66	1.75	1.92	1.87	1.00	1.95	1.60	1.49	1.86	1.91	1.61
	3	1.00	1.17	1.56	1.68	1.70	1.81	1.78	1.00	1.42	1.90	2.03	2.20	2.22	2.19
	4	1.00	1.21	0.96	0.65	0.77	0.91	0.77	1.00	1.38	0.81	0.69	1.10	0.97	0.39
	5	1.00	1.11	0.88	0.77	0.64	0.75	0.77	1.00	1.08	0.80	0.57	0.77	0.82	0.78

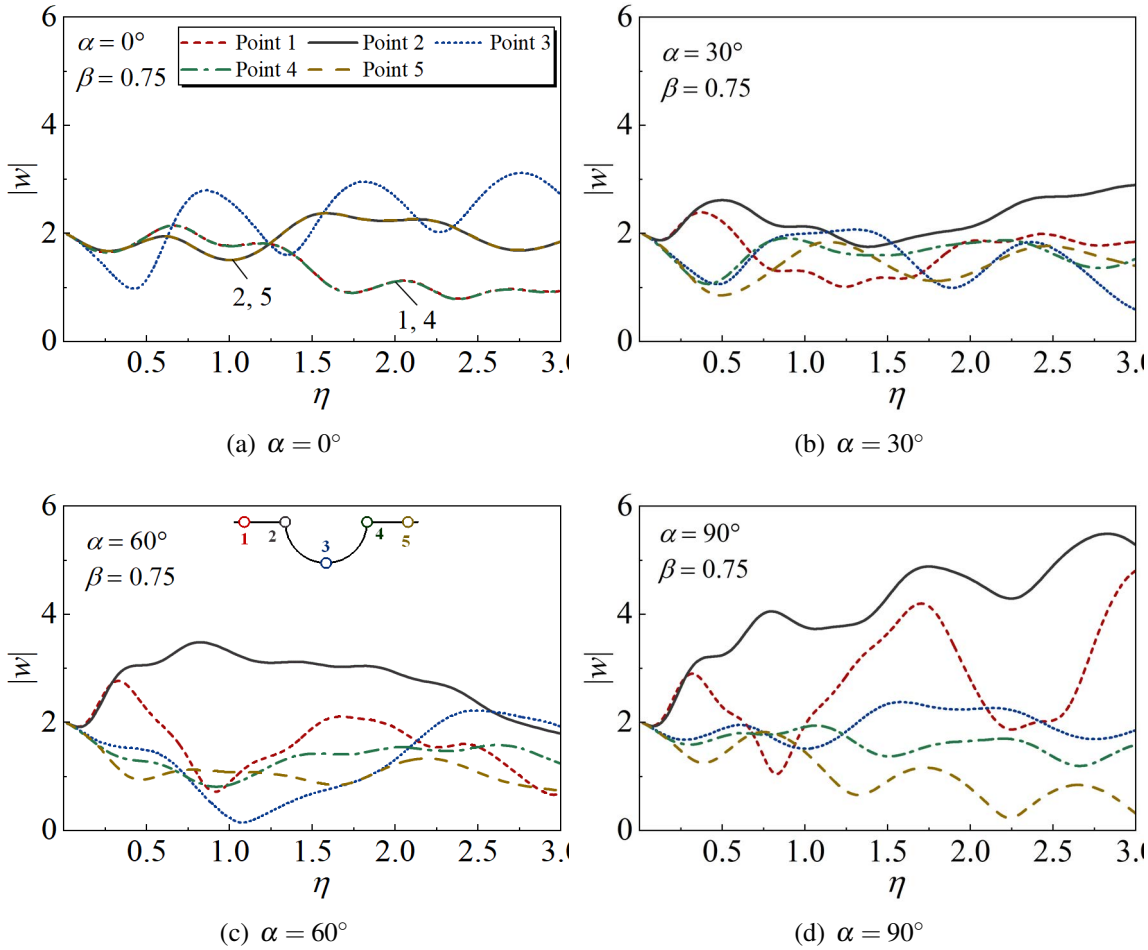

Fig. 3.9 Displacement amplitude of five selection observation points under inhomogeneous parameter $\beta = 0.75$

It can be seen more clearly from the table that with inhomogeneous parameter increasing, the amplification effect of the depression gradually aggravates. Which illustrates that surface depression has a significant effect on the displacement for observation point 2under all parameters. Compared with the amplification by the interface depression in homogeneous media in literature [4], the amplification effect is weakened as $\beta < 1$ while is increased as $\beta > 1$. And the maximum amplification effect of point 2 has reached 1.3 times for $\beta = 1.5$. In particular, for the four inhomogeneous parameters, the amplifying effect is consistent for point 3 under vertical incident and point 2, 5 under horizontal incident. The displacement amplification coefficients of points 1 and 5 is inversely proportional of dimensionless frequency with vertical incident. However, the above phenomenon is observed for points 2 and 4 when $\beta < 1$ and vertical incident. Consequently, considering horizontal cases, w^* of point 3 decreases as $\beta < 1$, and increases as $\beta > 1$. At the same time, w^* of points 3,

4, and 5 vary very little under the inhomogeneous parameter of 0.75. This means that the displacement amplitude hardly changes as a function of the dimensionless frequency under this condition. The inhomogeneous parameters as well as the surface depression have little effect on the displacement amplitude in the quasi-static case. Meanwhile, for $\beta < 1$ the maximum of displacement amplification occurs at vertical incident, for $\beta > 1$ the maximum of displacement amplification occurs at 30° oblique incident.

In order to clearly observe the distribution of the surface displacement amplitude of the depression and the horizontal boundary, Fig. 3.10 and 3.11 illustrate the surface displacement amplitude distribution at $\beta = 0.75, 1.25$ respectively. The displacement amplitude increases as a whole and vibrations more obviously with dimensionless frequency as the incident angle various from vertical to horizontal, as shown in the figure. The point of maximum displacement amplitude appears at the low point of the depression as $\beta < 1$, given in Figs. 3.10 (a) and 3.11 (a) under vertical incident. While the point of maximum displacement amplitude appears at the junction as $\beta > 1$. The point of maximum displacement amplitude appeared at the junction of the depression and the left horizontal boundary for both oblique and horizontal incident. And the position of the maximum displacement amplitude point moves from the junction at left side to the horizontal boundary under horizontal incident. The maximum points also advanced with the growth of dimensionless frequency. The displacement amplitude at the horizontal boundary is significantly inversely proportional of inhomogeneous parameters, especially in the direction of the left wave front at the horizontal incident. It increases the displacement amplitude as oblique incident. The back wave surface at the dimensionless frequency over 3 and $\beta > 1$, appears a region with displacement almost zero, from Fig. 3.11(d). In the two sets of surface displacement amplitude, the maximum value of the displacement is inversely proportional of inhomogeneous parameter, the surface displacement amplitude is more prone to abrupt changes in large inhomogeneous parameters.

The above example gives the effect of inhomogeneous parameters and surface depression in inhomogeneous media on the surface displacement amplitude. Then we explore the effect of inhomogeneous parameters on the distribution of internal displacement amplitude. Figs. 3.12-3.14 demonstrate the displacement amplitude distribution in the semi-infinite space with dimensionless frequency $\eta = 1.5$, and the inhomogeneous parameters are 0.75, 1.0 and 1.25 respectively.

By comparing the three sets of figures, the displacement amplitude distribution in the inhomogeneous semi-infinite space has a certain similar characteristic with the internal displacement amplitude distribution in the homogeneous case (Fig. 3.12). The included angle between the connecting line and the x-axis of the position where the larger internal displacement amplitude occurs under the three inhomogeneous parameters is about 45°,

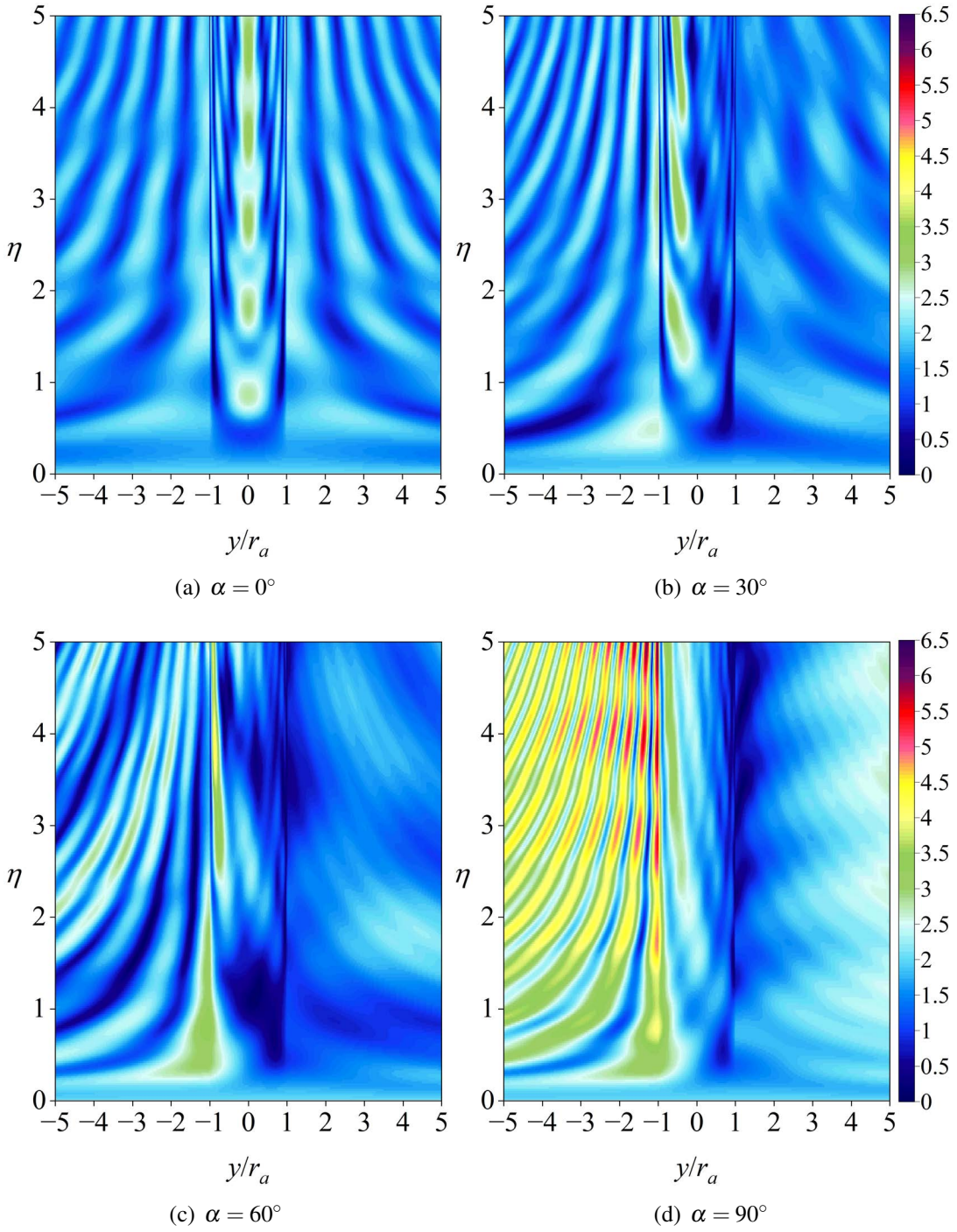

(a) $\alpha = 0°$ (b) $\alpha = 30°$

(c) $\alpha = 60°$ (d) $\alpha = 90°$

Fig. 3.10 Spectral variations in surface displacement amplitude with inhomogeneous parameter $\beta = 0.75$

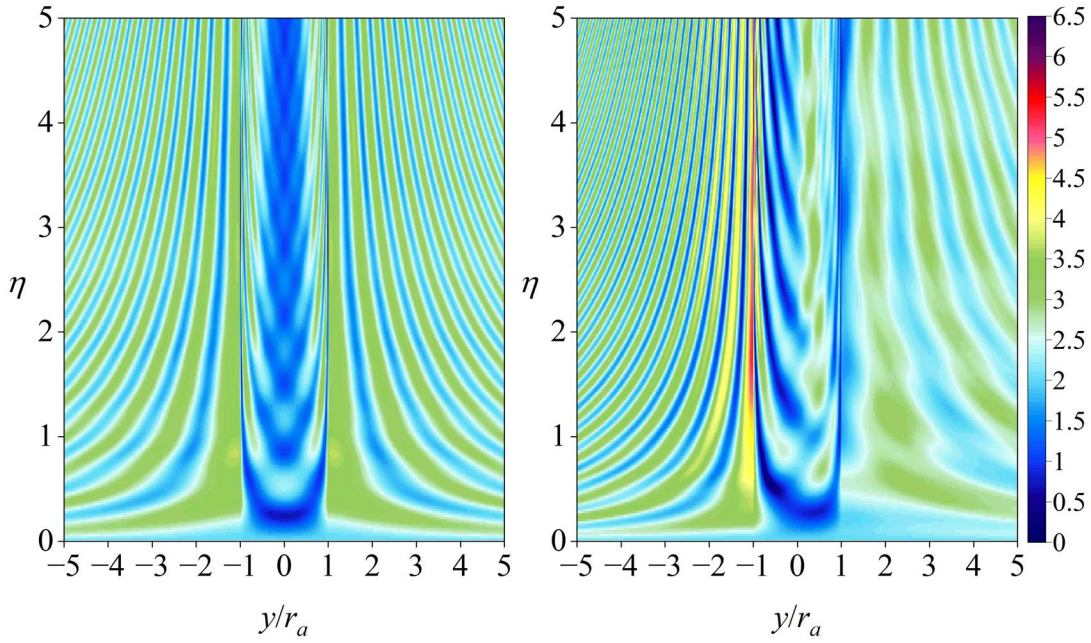

(a) $\alpha = 0°$ (b) $\alpha = 30°$

(c) $\alpha = 60°$ (d) $\alpha = 90°$

Fig. 3.11 Spectral variations in surface displacement amplitude with inhomogeneous parameter $\beta = 1.25$

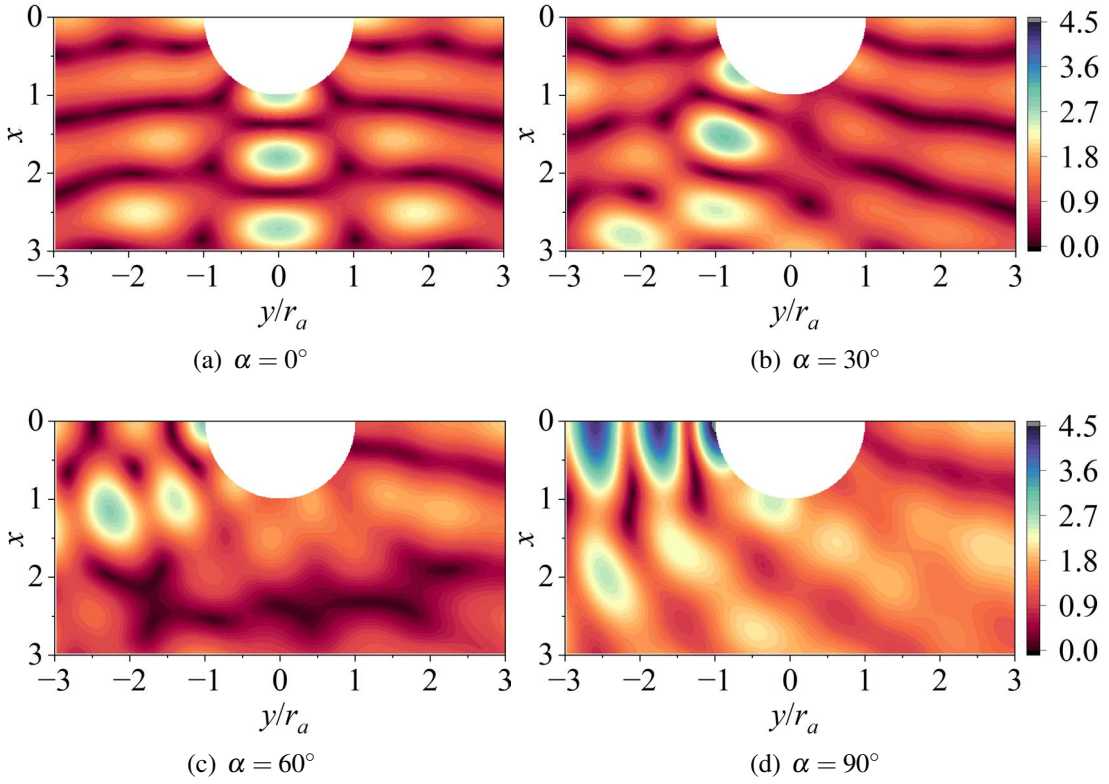

(a) $\alpha = 0°$ (b) $\alpha = 30°$

(c) $\alpha = 60°$ (d) $\alpha = 90°$

Fig. 3.12 Distribution of internal displacement under inhomogeneous parameter $\beta = 0.75$

as shown in Figs. 3.12(a), 3.13(a) and 3.14(a). And the values slightly increase with the ascender of β, and the number of locations with large values increases, which means, the vibration is aggravated. The inhomogeneous parameters have a certain influence on the internal displacement amplitude distribution. While, under the vertical incident, there is no large displacement amplitude at the bottom of the depression if $\beta > 1$, and the displacement amplitude in the area near the bottom of the depression is in a small state. In the case of 30° oblique incident, as in the three groups figure (b), the maximum point of the displacement amplitude all appears at the intersection point between the depression and the left side of the horizontal boundary as $\beta > 1$, while the maximum point appears on the surface of the depression as $\beta < 1$. Moreover, at $\beta = 1.25$, the displacement amplitude inside the wave face declines along the positive direction of the x-axis, and some large areas occur directly below the depression.

However, the internal displacement amplitude distribution decreases along the positive x-axis under the situation of homogeneous and inhomogeneous parameters are 1.25 and 0.75. For horizontal incident, such as the three groups figure (d), the distribution of internal displacement amplitude indicates a circular distribution along the depression boundary of the

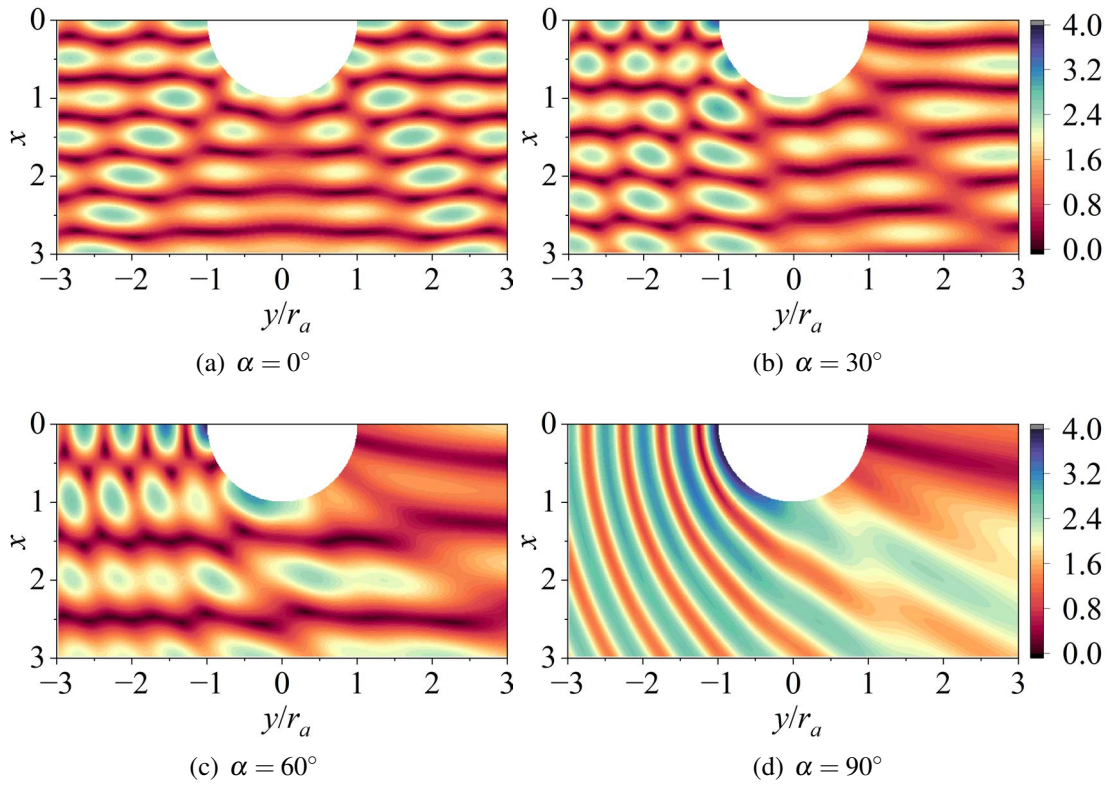

(a) $\alpha = 0°$ (b) $\alpha = 30°$

(c) $\alpha = 60°$ (d) $\alpha = 90°$

Fig. 3.13 Distribution of internal displacement under inhomogeneous parameter $\beta = 1.0$

wave face, and the point of maximum displacement amplitude moves from the left junction and the horizontal boundary to the bottom of the depression surface with inhomogeneous parameter growing. As $\beta > 1$, the displacement amplitude at the left horizontal boundary is also small, while the internal displacement amplitude with the ascender if x coordinate then increase when the angle with the x-axis is approximately $60°$. As $\beta < 1$, the internal displacement amplitude decreases rapidly along the positive direction of the x-axis. In a homogeneous media, the internal displacement presents a relatively stable distribution along the positive x-axis. There still is a distribution region with small displacement amplitude for all three inhomogeneous parameters near the right horizontal boundary under horizontal incident.

3.5 Summary

This chapter mainly solves the scattering problem of SH wave by a semi-cylindrical depression in density radial inhomogeneous media. The governing equation is transformed into the standard Helmholtz equation through the complex function method and auxiliary function,

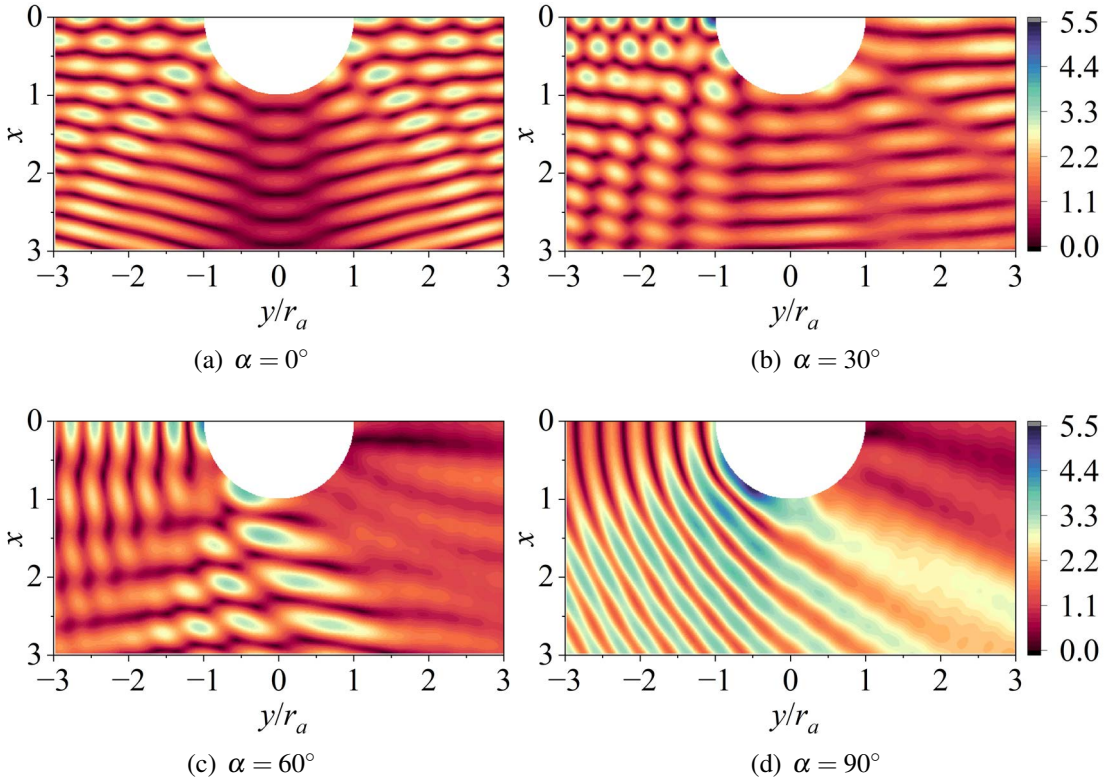

(a) $\alpha = 0°$ (b) $\alpha = 30°$

(c) $\alpha = 60°$ (d) $\alpha = 90°$

Fig. 3.14 Distribution of internal displacement under inhomogeneous parameter $\beta = 1.25$

and the expressions of the free wave field and the scattering wave field in the model are constructed. The unknown coefficients in the constructed wave field expression are obtained by using Fourier series expansion through the boundary conditions, so as to acquire the whole wave field expression form. The validation of the method used in this chapter and the construction of the wave field expression are verified through convergence analysis and comparison with the existing results. Furthermore, the effects of different inhomogeneous parameters, incident angles and dimensionless frequencies on SH wave scattering were calculated, and the effects of these parameters and the surface depression in inhomogeneous media on SH wave scattering were analyzed.

Chapter 4

Scattering of SH wave by surface convex in inhomogeneous media

The scattering of elastic waves by the surface convex has always been the focus of many scholars. The surface boundary will lead to the elastic wave reflection, resulting in the irregular distribution of energy, and the surface displacement in some areas will increase significantly. In the past few decades, a large number of researches have been carried out on wave scattering problems caused by convex boundaries such as semi-cylindrical, triangle, trapezoid and complex slope in homogeneous media. The development of material design science provides technical support for the realization of elastic wave regulation. Moreover, it also attracts more attention to the wave problem in complex media. The wave propagation characteristic at the interface between complex media and homogeneous media as well as in complex media has been discussed. However, there is still a lot of research space for the scattering of elastic waves by surface defects in complex media. As a typical analytical model, the semi-cylindrical depression or convex surface has attracted much attention. Therefore, this chapter researches the scattering of SH waves by the surface semi-cylindrical convex in inhomogeneous media.

4.1 Scattering of SH waves by surface semi-cylindrical convex in density inhomogeneous media

First of all, this section investigates the scattering of SH wave by the surface semi-cylindrical convex in density inhomogeneous media and discusses it with the semi-cylindrical convex model. Semi-cylindrical boundary is a relatively simple form of convex, and the research of

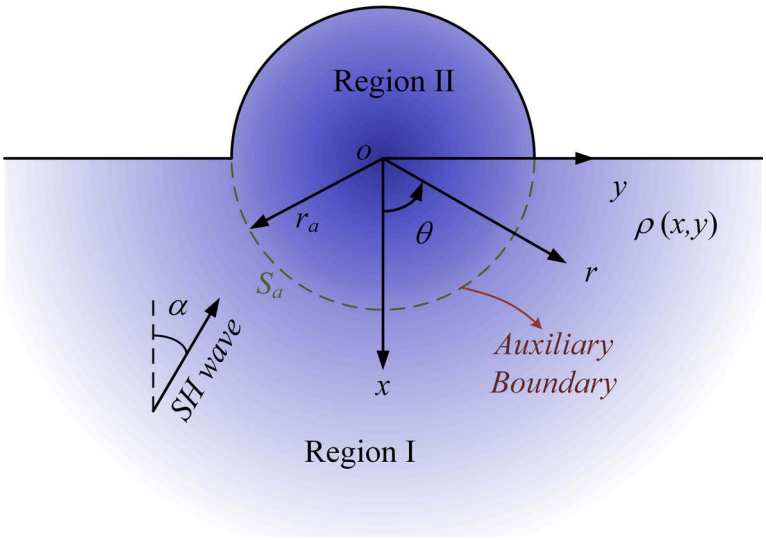

Fig. 4.1 Model for scattering SH wave by a semi-cylindrical convex in density inhomogeneous media

this model can provide the corresponding theoretical basis for the subsequent more complex models.

4.1.1 Model and wave equation

The model of a semi-cylindrical convex on the surface in density radially inhomogeneous half space under SH waves incident is shown in Fig. 4.1. The coordinate origin o is set at the center of semi-cylindrical convex with a radius of r_a. The x-axis is vertically downward and the y-axis is horizontally right. In order to divide the model into two regions, the auxiliary boundary S_a is introduced. Region I is a semi-infinite space with semi-cylindrical boundary, and Region II is a closed cylindrical region with boundary S_a and L. The function of density along the radius is still selected in the same form as in section 3.1.2:

$$\rho(r,\theta) = \rho_0 \beta^2 r^{2(\beta-1)}, \quad \beta > 0 \tag{4.1}$$

The meaning of each parameter is the same as that of section 3.1.2. Therefore, the solving process of the control equation of the problem is the same as that of section 3.1.2. Finally, the dynamic control equation of the inhomogeneous media with the density radially varies as the above function is transformed into:

$$\frac{\partial^2 w}{\partial \xi_1^2} + \frac{\partial^2 w}{\partial \xi_2^2} + \frac{1}{4} k_0^2 w = 0 \tag{4.2}$$

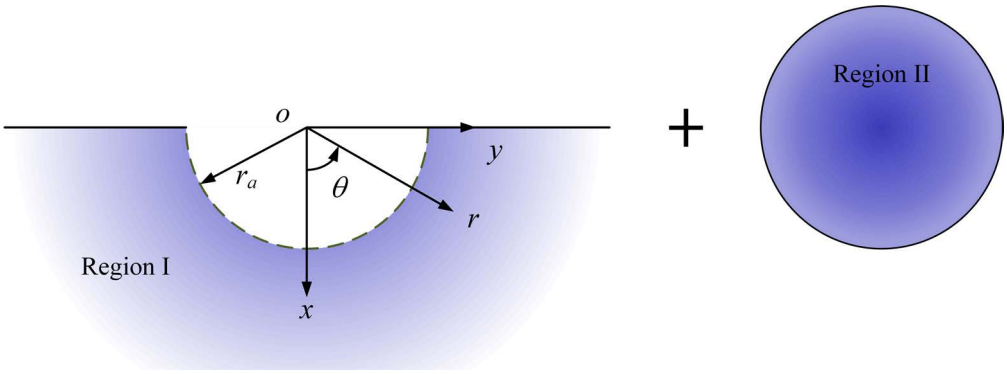

Fig. 4.2 Schematic of semi-cylindrical convex model division

4.1.2 Displacement field expression in each region

In the problem of elastic wave with surface convex boundary in semi-infinite space, the whole region is usually divided into several constructional regions by auxiliary boundary by using region matching technique (RMT). After the wave field expressions satisfying their boundary conditions are constructed in each region, the corresponding boundary conditions are satisfied at the auxiliary boundary. Then the unknown coefficients to be solved for each expression are obtained. Finally, the wave field in each region is available to be obtained, and the problem will be solved. The whole region can be divided into a semi-infinite space with a semi-cylindrical depression on the surface (Region I) and a closed cylindrical region (Region II), from Fig. 4.2. When constructing the wave field, the free wave field in Region I, the scattering field generated by the semi-cylindrical depression and the standing wave field in Region II are constructed respectively.

Displacement field expression in Region I

Region I can be seen as a semi-cylindrical depression on the surface in an inhomogeneous semi-infinite space. Under SH wave incident with the angle α, there is a free wave field $w^{(f)}$ and a scattering field $w^{(s)}$ generated by the semi-cylindrical depression in Region I. The free wave field $w^{(f)}$ can be expressed as:

$$\begin{aligned} w^{(f)} = & \sum_{n=0}^{\infty} (-1)^n \varepsilon_n J_{2n/\beta}\left(k_0|\zeta|\right) cos2n\alpha \cdot \left\{ \left(\frac{\zeta}{|\zeta|}\right)^{2n/\beta} + \left(\frac{\zeta}{|\zeta|}\right)^{-2n/\beta} \right\} \\ & + 2\sum_{n=0}^{\infty} (-1)^n J_{(2n+1)/\beta}\left(k_0|\zeta|\right) \sin\left(2n+1\right)\alpha \\ & \cdot \left\{ \left(\frac{\zeta}{|\zeta|}\right)^{(2n+1)/\beta} - \left(\frac{\zeta}{|\zeta|}\right)^{-(2n+1)/\beta} \right\} \end{aligned} \tag{4.3}$$

The scattered wave $w^{(s)}$ generated by depression boudary:

$$\begin{aligned} w^{(s)}\left(\zeta,\bar{\zeta}\right) = w_0 \sum_{n=0}^{\infty} \Bigg\{ & A_n H^{(1)}_{2n/\beta}\left(k_0\left|\zeta\right|\right)\left[\left(\frac{\zeta}{|\zeta|}\right)^{2n/\beta} + \left(\frac{\zeta}{|\zeta|}\right)^{-2n/\beta}\right] \\ & + B_n H^{(1)}_{(2n+1)/\beta}\left(k_0\left|\zeta\right|\right)\left[\left(\frac{\zeta}{|\zeta|}\right)^{(2n+1)/\beta} - \left(\frac{\zeta}{|\zeta|}\right)^{-(2n+1)/\beta}\right]\Bigg\} \end{aligned} \tag{4.4}$$

where A_n, B_n are unknown coefficients to be solved. Then, the total wave field in Region I can be obtained:

$$w_1 = w^{(f)} + w^{(s)} \tag{4.5}$$

Displacement field expression in Region II

The wave field in Region II can be regarded as the cohesive wave generated by the boundary S_a and L. When constructing the wave field form, the stress free condition of the upper semi-cylindrical convex part should be satisfied while satisfying Eq.4.2. The form of Bessel function construction is as follows:

$$\begin{aligned} w_2\left(\zeta,\bar{\zeta}\right) = & \sum_{n=0}^{\infty} C_n J_{2n/\beta}\left(k_0\left|\zeta\right|\right)\left[\left(\frac{\zeta}{\bar{\zeta}}\right)^{2n/\beta} + \left(\frac{\zeta}{\bar{\zeta}}\right)^{-2n/\beta}\right] \\ & + \sum_{n=0}^{\infty} D_n J_{(2n+1)/\beta}\left(k_0\left|\zeta\right|\right)\left[\left(\frac{\zeta}{\bar{\zeta}}\right)^{(2n+1)/\beta} - \left(\frac{\zeta}{\bar{\zeta}}\right)^{-(2n+1)/\beta}\right] \\ & + \sum_{n=0}^{\infty} E_n J_{(2n+1)/\beta}\left(k_0\left|\zeta\right|\right)\left[\left(\frac{\zeta}{\bar{\zeta}}\right)^{(2n+1)/\beta} + \left(\frac{\zeta}{\bar{\zeta}}\right)^{-(2n+1)/\beta}\right] \\ & + \sum_{n=1}^{\infty} F_n J_{(2n+1)/\beta}\left(k_0\left|\zeta\right|\right)\left[\left(\frac{\zeta}{\bar{\zeta}}\right)^{2n/\beta} - \left(\frac{\zeta}{\bar{\zeta}}\right)^{-2n/\beta}\right] \end{aligned} \tag{4.6}$$

where C_n, D_n, E_n, F_n are unknown coefficients to be solved.

4.1.3 Stress field expression in each region

According to Eqs. (2.35) and (2.36) , the stress field expressions in each region can be obtained by substituting the wave field expressions in the two regions. The stress field in

Region I can be expressed as:

$$\begin{aligned}\tau_{rz}^{(1)} = \frac{\beta\mu k_0 w_0}{2}\Bigg[&\sum_{n=0}^{\infty}(-1)^n\varepsilon_n P_{2n/\beta}\ (\zeta)\cos 2n\alpha \\ &+\sum_{n=0}^{\infty}(-1)^n Q_{(2n+1)/\beta}\ (\zeta)\sin(2n+1)\alpha \\ &+\sum_{n=0}^{\infty}A_n U_{2n/\beta}\ (\zeta)+\sum_{n=0}^{\infty}B_n V_{(2n+1)/\beta}\ (\zeta)\Bigg]\end{aligned} \tag{4.7}$$

$$\begin{aligned}\tau_{\theta z}^{(1)} = \frac{\mathrm{i}\beta\mu k_0 w_0}{2}\Bigg[&\sum_{n=0}^{\infty}(-1)^n\varepsilon_n P_{2n/\beta}\ (\zeta)\cos 2n\alpha \\ &-\sum_{n=0}^{\infty}(-1)^n Q_{(2n+1)/\beta}\ (\zeta)\sin(2n+1)\alpha \\ &+\sum_{n=0}^{\infty}A_n U_{2n/\beta}\ (\zeta)-\sum_{n=0}^{\infty}B_n V_{(2n+1)/\beta}\ (\zeta)\Bigg]\end{aligned} \tag{4.8}$$

where

$$\begin{aligned}P_t(s) = {} & J_{t-1}(k_0|s|)\left[\frac{s}{|s|}\right]^{t-1} z^{\beta-1}e^{\mathrm{i}\theta} - J_{t+1}(k_0|s|)\left[\frac{s}{|s|}\right]^{-t-1} z^{\beta-1}e^{\mathrm{i}\theta} \\ & + J_{t-1}(k_0|s|)\left[\frac{s}{|s|}\right]^{1-t}\bar{z}^{\beta-1}e^{-\mathrm{i}\theta} - J_{t+1}(k_0|s|)\left[\frac{s}{|s|}\right]^{-t-1}\bar{z}^{\beta-1}e^{-\mathrm{i}\theta}\end{aligned}$$

$$\begin{aligned}Q_t(s) = {} & J_{t-1}(k_0|s|)\left[\frac{s}{|s|}\right]^{t-1} z^{\beta-1}e^{\mathrm{i}\theta} + J_{t+1}(k_0|s|)\left[\frac{s}{|s|}\right]^{-t-1} z^{\beta-1}e^{\mathrm{i}\theta} \\ & - J_{t-1}(k_0|s|)\left[\frac{s}{|s|}\right]^{1-t}\bar{z}^{\beta-1}e^{-\mathrm{i}\theta} - J_{t+1}(k_0|s|)\left[\frac{s}{|s|}\right]^{-t-1}\bar{z}^{\beta-1}e^{-\mathrm{i}\theta}\end{aligned}$$

$$\begin{aligned}U_t(s) = {} & H_{t-1}^{(1)}(k_0|s|)\left[\frac{s}{|s|}\right]^{t-1} z^{\beta-1}e^{\mathrm{i}\theta} - H_{t+1}^{(1)}(k_0|s|)\left[\frac{s}{|s|}\right]^{-t-1} z^{\beta-1}e^{\mathrm{i}\theta} \\ & + H_{t-1}^{(1)}(k_0|s|)\left[\frac{s}{|s|}\right]^{1-t}\bar{z}^{\beta-1}e^{-\mathrm{i}\theta} - H_{t+1}^{(1)}(k_0|s|)\left[\frac{s}{|s|}\right]^{-t-1}\bar{z}^{\beta-1}e^{-\mathrm{i}\theta}\end{aligned}$$

$$\begin{aligned}V_t(s) = {} & H_{t-1}^{(1)}(k_0|s|)\left[\frac{s}{|s|}\right]^{t-1} z^{\beta-1}e^{\mathrm{i}\theta} + H_{t+1}^{(1)}(k_0|s|)\left[\frac{s}{|s|}\right]^{-t-1} z^{\beta-1}e^{\mathrm{i}\theta} \\ & - H_{t-1}^{(1)}(k_0|s|)\left[\frac{s}{|s|}\right]^{1-t}\bar{z}^{\beta-1}e^{-\mathrm{i}\theta} - H_{t+1}^{(1)}(k_0|s|)\left[\frac{s}{|s|}\right]^{-t-1}\bar{z}^{\beta-1}e^{-\mathrm{i}\theta}\end{aligned}$$

The stress field in Region II is:

$$\begin{aligned}\tau_{rz}^{(2)} = \frac{\beta\mu k_0 w_0}{2}\sum_{n=0}^{\infty}\big[&C_n P_{2n/\beta}\ (\zeta) + D_n Q_{(2n+1)/\beta}\ (\zeta) \\ &+E_n P_{(2n+1)/\beta}\ (\zeta) + F_n Q_{2n/\beta}\ (\zeta)\big]\end{aligned} \tag{4.9}$$

$$\begin{aligned}\tau_{\theta z}^{(2)} = \frac{i\beta\mu k_0 w_0}{2}\sum_{n=0}^{\infty}\big[&C_n P_{2n/\beta}\ (\zeta) - D_n Q_{(2n+1)/\beta}\ (\zeta) \\ &+E_n P_{(2n+1)/\beta}\ (\zeta) - F_n Q_{2n/\beta}\ (\zeta)\big]\end{aligned} \tag{4.10}$$

4.1.4 Boundary conditions and solutions

Since the original surface convex in semi-infinite space is divided into two solution regions. The stress and displacement continuity conditions should be satisfied at the auxiliary boundary S_a:

$$w_1 = w_2, \qquad r = r_a, \qquad -\pi/2 \le \theta \le \pi/2 \tag{4.11}$$

$$\tau_{rz}^{(1)} = \tau_{rz}^{(2)}, \qquad r = r_a, \qquad -\pi/2 \le \theta \le \pi/2 \tag{4.12}$$

Stress free condition of semicircular convex:

$$\tau_{rz}^{(2)} = 0,\ r = r_a,\ \pi/2 \le \theta \le 3\pi/2 \tag{4.13}$$

In order to solve the equation and obtain the unknown coefficients in the wave field expression, multiply $e^{-\mathrm{i}m\theta}$ and integrate the two ends of Eqs. (4.11)-(4.13) to obtain the following two sets of infinite algebraic equations:

$$\begin{cases} \sum\limits_{n=0}^{\infty} C_n \beta_{mn}^{(1)} + \sum\limits_{n=0}^{\infty} E_n \lambda_{mn}^{(1)} = 0 \\ -\sum\limits_{n=0}^{\infty} A_n \beta_{mn}^{(2)} + \sum\limits_{n=0}^{\infty} C_n \lambda_{mn}^{(2)} + \sum\limits_{n=0}^{\infty} E_n \varphi_{mn}^{(2)} = \sum\limits_{n=0}^{\infty} \varsigma_{mn}^{(2)} \qquad m = 1,2,3,..., \\ -\sum\limits_{n=0}^{\infty} A_n \beta_{mn}^{(3)} + \sum\limits_{n=0}^{\infty} C_n \lambda_{mn}^{(3)} + \sum\limits_{n=0}^{\infty} E_n \varphi_{mn}^{(3)} = \sum\limits_{n=0}^{\infty} \varsigma_{mn}^{(3)} \end{cases} \tag{4.14}$$

$$\begin{cases} \sum\limits_{n=0}^{\infty} D_n \beta_{mn}^{(4)} + \sum\limits_{n=0}^{\infty} F_n \lambda_{mn}^{(4)} = 0 \\ -\sum\limits_{n=0}^{\infty} B_n \beta_{mn}^{(5)} + \sum\limits_{n=0}^{\infty} D_n \lambda_{mn}^{(5)} + \sum\limits_{n=0}^{\infty} F_n \varphi_{mn}^{(5)} = \sum\limits_{n=0}^{\infty} \varsigma_{mn}^{(5)} \qquad m = 1,2,3,..., \\ -\sum\limits_{n=0}^{\infty} B_n \beta_{mn}^{(6)} + \sum\limits_{n=0}^{\infty} D_n \lambda_{mn}^{(6)} + \sum\limits_{n=0}^{\infty} F_n \varphi_{mn}^{(6)} = \sum\limits_{n=0}^{\infty} \varsigma_{mn}^{(6)} \end{cases} \tag{4.15}$$

where $\beta_{mn}^{(\cdot)}$, $\lambda_{mn}^{(\cdot)}$, $\varphi_{mn}^{(\cdot)}$, $\varsigma_{mn}^{(\cdot)}$are the corresponding expressions expanded by Fourier series.

$$\begin{cases} \beta_{mn}^{(1)} = \int_{\pi/2}^{3\pi/2} P_{2n/\beta}\ (\zeta)\, \mathrm{e}^{-2m\mathrm{i}\theta} d\theta \\ \lambda_{mn}^{(1)} = \int_{\pi/2}^{3\pi/2} P_{(2n+1)/\beta}\ (\zeta)\, \mathrm{e}^{-2m\mathrm{i}\theta} d\theta \end{cases}$$

$$\begin{cases} \beta_{mn}^{(2)} = \int_{-\pi/2}^{\pi/2} H_{2n/\beta}^{(1)}\ (k|\zeta|) \left[(\zeta/|\zeta|)^{2n/\beta} + (\zeta/|\zeta|)^{-2n/\beta} \right] \mathrm{e}^{-2m\mathrm{i}\theta} d\theta \\ \lambda_{mn}^{(2)} = \int_{-\pi/2}^{\pi/2} J_{2n/\beta}\ (k|\zeta|) \left[(\zeta/|\zeta|)^{2n/\beta} + (\zeta/|\zeta|)^{-2n/\beta} \right] \mathrm{e}^{-2m\mathrm{i}\theta} d\theta \\ \varphi_{mn}^{(2)} = \int_{-\pi/2}^{\pi/2} J_{(2n+1)/\beta}\ (k|\zeta|) \left[(\zeta/|\zeta|)^{(2n+1)/\beta} + (\zeta/|\zeta|)^{-(2n+1)/\beta} \right] \mathrm{e}^{-2m\mathrm{i}\theta} d\theta \\ \zeta_{mn}^{(2)} = \int_{-\pi/2}^{\pi/2} (-1)^n \varepsilon_n J_{2n/\beta}\ (k|\zeta|) \cos 2n\alpha \left[(\zeta/|\zeta|)^{2n/\beta} + (\zeta/|\zeta|)^{-2n/\beta} \right] \mathrm{e}^{-2m\mathrm{i}\theta} d\theta \end{cases}$$

$$\begin{cases} \beta_{mn}^{(3)} = \int_{-\pi/2}^{\pi/2} U_{2n/\beta}\ (\zeta)\, \mathrm{e}^{-2m\mathrm{i}\theta} d\theta \\ \lambda_{mn}^{(3)} = \int_{-\pi/2}^{\pi/2} P_{2n/\beta}\ (\zeta)\, \mathrm{e}^{-2m\mathrm{i}\theta} d\theta \\ \varphi_{mn}^{(3)} = \int_{-\pi/2}^{\pi/2} P_{(2n+1)/\beta}\ (\zeta)\, \mathrm{e}^{-2m\mathrm{i}\theta} d\theta \\ \zeta_{mn}^{(3)} = \int_{-\pi/2}^{\pi/2} (-1)^n \varepsilon_n P_{2n/\beta}\ (\zeta) \cos 2n\alpha \mathrm{e}^{-2m\mathrm{i}\theta} d\theta \end{cases}$$

$$\begin{cases} \beta_{mn}^{(4)} = \int_{\pi/2}^{3\pi/2} Q_{(2n+1)/\beta}\ (\zeta)\, \mathrm{e}^{-(2m+1)\mathrm{i}\theta} d\theta \\ \lambda_{mn}^{(4)} = \int_{\pi/2}^{3\pi/2} Q_{2n/\beta}\ (\zeta)\, \mathrm{e}^{-(2m+1)\mathrm{i}\theta} d\theta \end{cases}$$

$$\begin{cases} \beta_{mn}^{(5)} = \int_{-\pi/2}^{\pi/2} H_{(2n+1)/\beta}^{(1)}(k|\zeta|)\left[(\zeta/|\zeta|)^{(2n+1)/\beta} - (\zeta/|\zeta|)^{-(2n+1)/\beta}\right] \mathrm{e}^{-(2m+1)\mathrm{i}\theta} d\theta \\ \lambda_{mn}^{(5)} = \int_{-\pi/2}^{\pi/2} J_{(2n+1)/\beta}(k|\zeta|)\left[(\zeta/|\zeta|)^{(2n+1)/\beta} - (\zeta/|\zeta|)^{-(2n+1)/\beta}\right] \mathrm{e}^{-(2m+1)\mathrm{i}\theta} d\theta \\ \varphi_{mn}^{(5)} = \int_{-\pi/2}^{\pi/2} J_{2n/\beta}(k|\zeta|)\left[(\zeta/|\zeta|)^{2n/\beta} - (\zeta/|\zeta|)^{-2n/\beta}\right] \mathrm{e}^{-(2m+1)\mathrm{i}\theta} d\theta \\ \zeta_{mn}^{(5)} = \int_{-\pi/2}^{\pi/2} 2(-1)^n J_{(2n+1)/\beta}(k|\zeta|)\sin(2n+1)\alpha\left[(\zeta/|\zeta|)^{(2n+1)/\beta} - (\zeta/|\zeta|)^{-(2n+1)/\beta}\right] \\ \mathrm{e}^{-(2m+1)\mathrm{i}\theta} d\theta \end{cases}$$

$$\begin{cases} \beta_{mn}^{(6)} = \int_{-\pi/2}^{\pi/2} V_{(2n+1)/\beta}(\zeta)\mathrm{e}^{-(2m+1)\mathrm{i}\theta} d\theta \\ \lambda_{mn}^{(6)} = \int_{-\pi/2}^{\pi/2} Q_{(2n+1)/\beta}(\zeta)\mathrm{e}^{-(2m+1)\mathrm{i}\theta} d\theta \\ \varphi_{mn}^{(6)} = \int_{-\pi/2}^{\pi/2} Q_{2n/\beta}(\zeta)\mathrm{e}^{-(2m+1)\mathrm{i}\theta} d\theta \\ \zeta_{mn}^{(6)} = \int_{-\pi/2}^{\pi/2} 2(-1)^n Q_{(2n+1)/\beta}(\zeta)\sin(2n+1)\alpha\mathrm{e}^{-(2m+1)\mathrm{i}\theta} d\theta \end{cases}$$

4.1.5 Convergence analysis

In order to express the relationship between the incident wave length and the model size, and to facilitate the analysis of subsequent examples, the dimensionless frequency η in the form of Eq. (3.23) is still used. The r_a represents the convex radius. The displacement amplitude $|w|$ is shown in Eq. (3.24).

Based on the use of Bessel functions and Fourier series expansion in the process of solving the equation, the equation is transformed into infinite algebraic equations. Therefore, it is necessary to truncate the infinite series and perform convergence analysis when finally obtaining the unknown coefficient. Four typical locations are selected to analyze the convergence of free, scattering and standing wave field. In order to ensure the convergence requirements of all calculation examples in this chapter, dimensionless frequency $\eta = 1.5$, incident angle $\alpha = 90°$, inhomogeneous parameter $\beta = 0.5$ and $\beta = 1.5$ are set, and the truncation term $N = m = n$ is considered to establish the standard solution matrix. According to a large number of convergence calculations as shown in Fig. 4.3. When 10 items are taken, the results have converged. Therefore, in subsequent calculations, taking can ensure the convergence of the results and save calculation time.

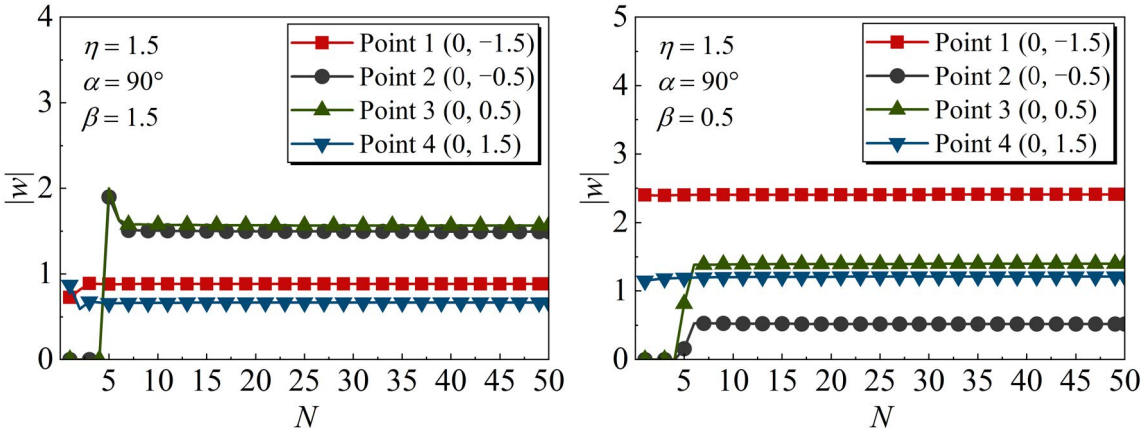

(a) $\beta = 1.5$ (b) $\beta = 0.5$

Fig. 4.3 Convergence analyses of displacement amplitudes at four typical positions with increasing N

4.1.6 Verification

In order to verify validation of the method in this section, two sets of numerical examples are calculated. Fig. 4.4 shows the comparison between the present results in this section and the existed results [162]. Taking inhomogeneous parameters $\beta = 0.99$ for ensuring the existence of inhomogeneous parameters in the formula, and it similarly simulates the situation of homogeneous media. Fig.4.4 (a) shows the surface displacement amplitude under four incident angles with a dimensionless frequency $\eta = 1.0$. Fig.4.4 (b) indicates the displacement amplitude of two observation points with dimensionless changes. From the two figures, it can be seen that the calculated results in this section are in good agreement with the existed results, which can verify the validation of the wave field and calculation method constructed in this section.

Fig. 4.5 gives the displacement amplitude of horizontal and vertical incident at two dimensionless frequencies when the values of two groups of inhomogeneous parameters are approximate to 1.0. Fig. 4.5 (a) presents the result of approaching 1.0 when the dimensionless frequency $\eta = 1.25$, $\beta < 1$. And the calculation result of β approaching 1.0 as the inhomogeneous parameter $\beta > 1$ ($\eta = 0.75$) is shown in Fig. 4.5 (b). The two groups of results indicate a continuous close to the $\beta = 1$, which verifies the continuity of calculation results and thus reflects the validation of method.

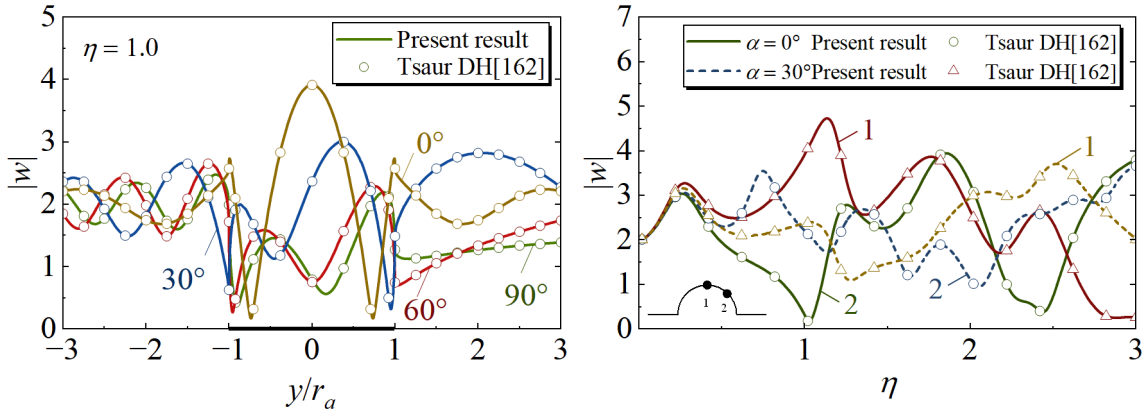

(a) $\eta = 1.0$ (b) Two observision point

Fig. 4.4 Results of approximately homogeneous medium for comparison with the existed displacement results

4.1.7 Numerical results and discussion

In order to explore the influence of inhomogeneous media on the displacement amplitude in the semi-infinite space with a surface semi-cylindrical convex under the SH wave incident, the displacement amplitude of five groups of selected inhomogeneous parameters under different incident angles is calculated, as shown in Fig. 4.6. Figs. 4.6 (a)-(d) display the cases with incident angles of 0°, 30°, 60°, and 90°, which means vertical incidence, two kinds of oblique incident, and horizontal incident. Among them, the results under homogeneous conditions are calculated by adding the inhomogeneous parameter $\beta = 1$ for comparison. Owing to the change of inhomogeneous parameters has a great impact on the density of media, the selected parameters have a small change, which is available to clearly observe the variation of displacement amplitude under a similar change of parameters. The abscissa in the figure represents the relative coordinates of the surface position of the model. Since the r_a unit is 1, the coordinates $[-1,1]$ are the convex part. $[-3,-1)$ and $(1,3]$ are the horizontal boundaries.

From Fig. 4.6 (d), the displacement amplitude is inversely proportional of inhomogeneous parameters, especially at the horizontal boundary. While the inhomogeneous parameter reaches 1.4, the surface displacement at the left horizontal boundary, as the wave front, is almost equal to the surface displacement at the right horizontal boundary, as the wave back. However, in the case of vertical incident and oblique incident, as shown in Figs. 4.6 (a)-(c), the displacement amplitude illustrates an increasing trend as the acsender of inhomogeneous parameters, especially in 30° incident. Comparing with the homogeneous media situation, the displacement amplitude under $\beta > 1$ has a significant increase. In vertical incident, given

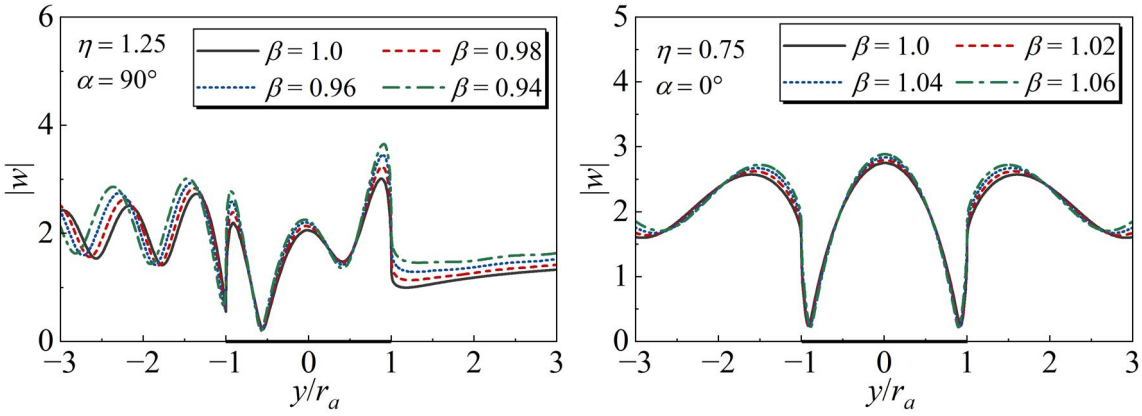

(a) $\eta = 1.25$ (b) $\eta = 0.75$

Fig. 4.5 Displacement distribution corresponding to different inhomogeneous parameters

in Fig. 4.6 (a), the displacement amplitude at the horizontal boundary with $\beta = 0.6, 1.2$ has a significantly vibration with the position various comparing with the displacement amplitude at $\beta = 0.8, 1.4$. Meanwhile, the maximum point of displacement amplitude from the convex crest to the junction of convex and horizontal boundary with inhomogeneous parameter growing.

Set the dimensionless frequency $\eta = 0.75$, and observe the influence of inhomogeneous parameters on displacement amplitude under dimensionless frequency changes, as displayed in Fig. 4.7. Compared with Fig. 4.6 and Fig. 4.7, in vertical incidence and 30° incident, the surface displacement and the vibration frequency with the position are proportional of dimensionless frequency. However, at horizontal and 60° incident, with dimensionless frequency declining, the displacement amplitude increases, and the vibration frequency has no obvious weakening trend. Meanwhile, in horizontal incident and $\eta = 0.75$, the displacement amplitude at the horizontal boundary is weakened by inhomogeneous parameters various. Moreover, under $\eta = 1.25$, the most obvious impact of inhomogeneous parameters on displacement amplitude is 30°, while $\eta = 0.75$, the most obvious impact is 0°, which is the same as the characteristic reflected in the surface depression in the previous chapter. In particular, in Figs. 4.7 (c) and (d), the maximum displacement amplitude under the homogeneous condition is significantly higher than that under the inhomogeneous condition at the horizontal incidence and 60° incident. In Fig. 4.7 (a) of vertical incident, the displacement amplitude is advanced gradually with the growth of inhomogeneous parameters. And the position where the maximum displacement amplitude occurs is at the convex vertex at this dimensionless frequency.

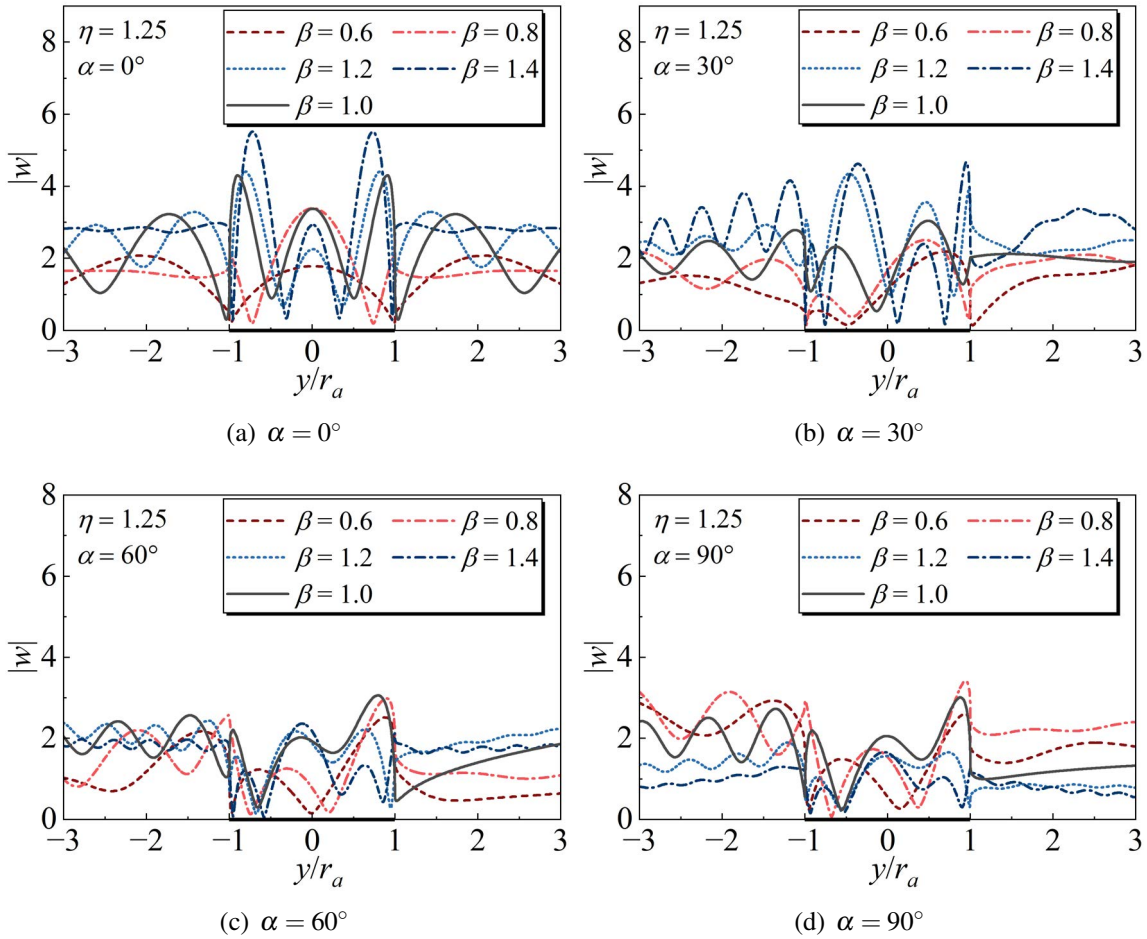

Fig. 4.6 Displacement amplitude with inhomogeneous parameter at dimensionless frequency $\eta = 1.25$

Subsequently, in order to explore the amplification effect of surface convex on displacement amplitude under SH wave incident in inhomogeneous media $\beta = 1.2$ and $\beta = 0.8$, the displacement amplitudes of six typical observation points under four incident angles are calculated, the result are given in Fig. 4.8 and Fig. 4.9 respectively. The coordinates of the six observation points are point 1 $(2, -\pi/2)$, point 2 $(1, -\pi/2)$, point 3 $(1, -5\pi/6)$, point 4 $(1, 5\pi/6)$, point 5 $(1, \pi/2)$, and point 6 $(2, \pi/2)$. From Figs. 4.8 (a)-(d) that under $\beta = 1.2$, the displacement amplitude decreases as the incident angle various from vertical to horizontal. Especially in horizontal incident, the displacement amplitude of all observation points reduces with the growth of dimensionless frequency. It can be considered that under this inhomogeneous parameter, the semi-cylindrical convex has the effect of reducing the displacement amplitude, and the displacement amplitude decreases to about 0.5 times. Point 3 amplifies the displacement amplitude reaches 2.5 times when the incident angle is 30°, and

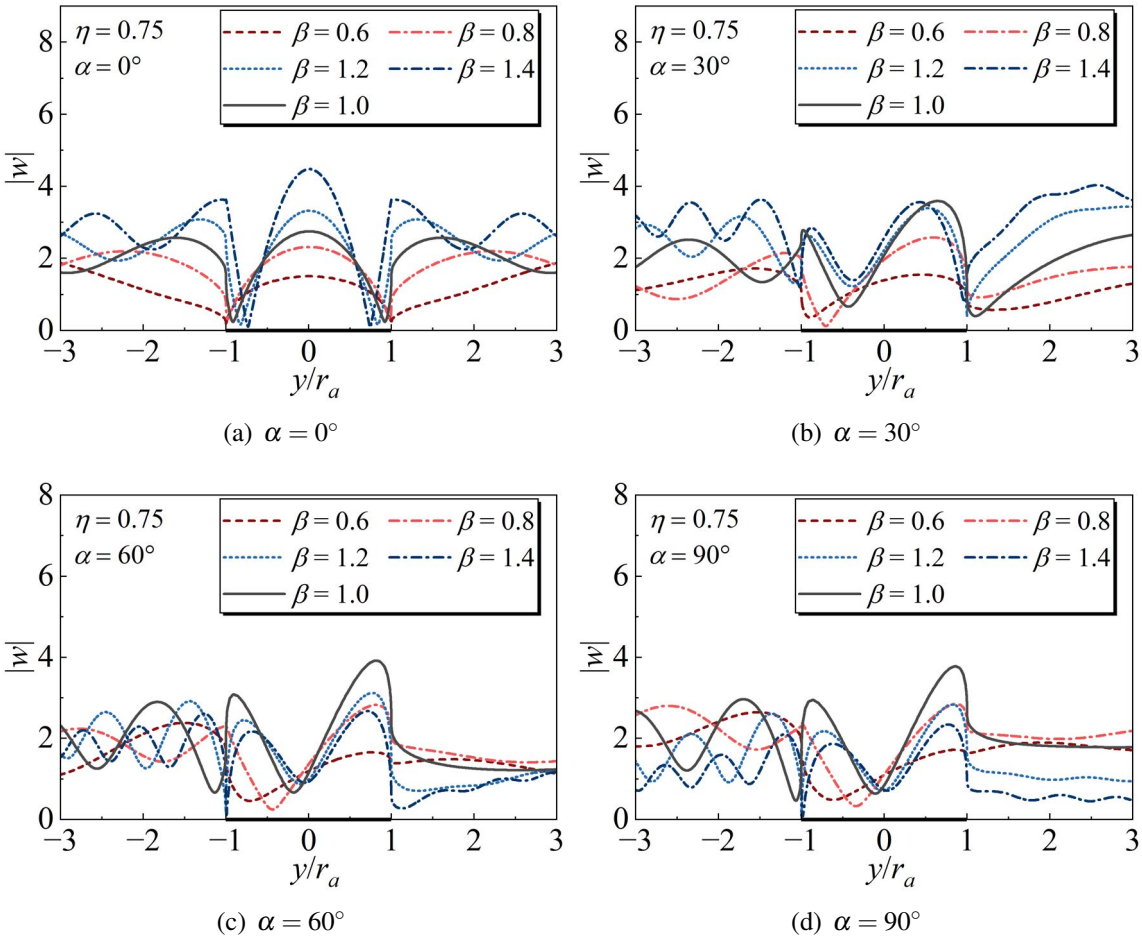

Fig. 4.7 Displacement amplitude with inhomogeneous parameter at dimensionless frequency $\eta = 0.75$

the vibration amplitude is obvious. The amplification effect of points 2 and 5 on displacement demonstrates an vibration mode with the frequency variation, and its amplification factor is 2 times. Points 1 and 6 amplify the displacement amplitude is not more than 1.5 times under incident vertically or obliquely. While point 1 at 60° incident, it tends to be stable with dimensionless frequency increasing. While point 4 is at horizontal and oblique incident of 60°, the amplification effect on displacement amplitude is most obvious if $\eta < 1$. However, with the dimensionless frequency increasing continuously, its amplification effect on displacement amplitude decreases sharply to 0.5 times.

When the inhomogeneous parameter $\beta = 0.8$, the surface convex amplifies the displacement amplitude increasing with the incident angle from vertical to horizontal, as shown in Fig. 4.9. Compared with Fig. 4.8, the amplification effect of surface convex on displacement amplitude tends to decrease with the inhomogeneous parameter declining, except for horizon-

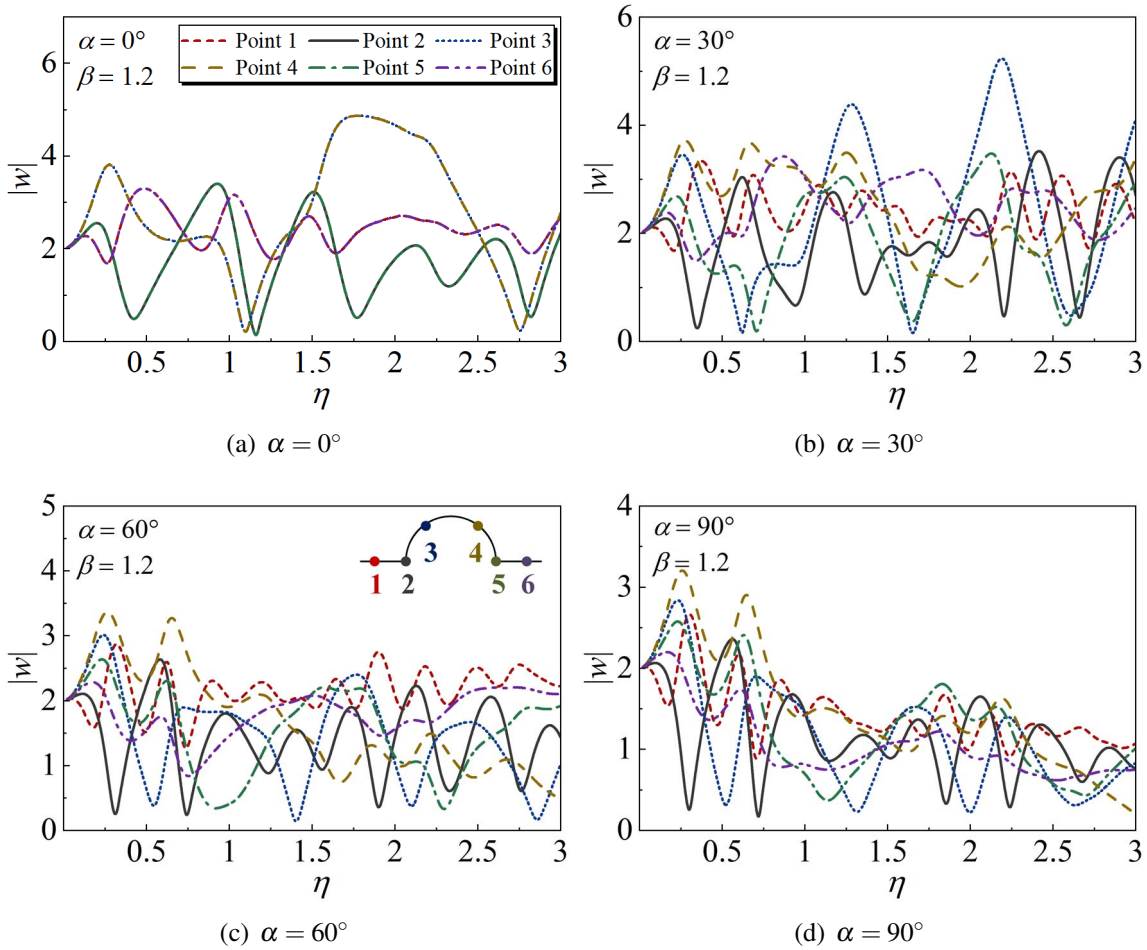

Fig. 4.8 Displacement amplitude of six selection observation points under inhomogeneous parameter $\beta = 1.2$

tal incident. However, in horizontal incident, when the inhomogeneous parameter decreases, the amplification effect increases instead. Especially at point 1, the amplification effect reaches 1.9 times, while at other angles of incidence, the amplification effect is stable within 1.5 times. When the point 4 at 30° incident, the amplification effect is the most obvious and the maximum is 2 times, and with the ascender of dimensionless frequency, it shows a trend of increasing. As points 2 and 3 are incident at different angles, the amplification effect reflected is basically stable at 1.5 times. Meanwhile, the inhomogeneous parameter is 0.8, the phenomenon that the displacement amplitude of point 2 changes with the dimensionless frequency is more obvious than $\beta = 1.2$.

Table 4.1 demonstrates the displacement amplification coefficients of six typical observation points on the surface at multiple frequencies and incident angles. It is observed from the table that in vertical and oblique incident, the observation points of the maximum

Table 4.1 Displacement amplification coefficients under different incident angles with four inhomogeneous parameters

		$\beta = 0.5$							$\beta = 0.75$						
α	point \ η	0.01	0.5	1	1.5	2	2.5	3	0.01	0.5	1	1.5	2	2.5	3
0°	1,6	.001	0.24	0.65	1.02	0.57	0.70	0.84	1.00	0.61	0.82	0.98	0.64	0.55	0.79
	2,5	1.00	0.21	0.14	0.4	0.53	0.34	0.19	1	0.19	0.54	0.34	0.84	0.5.	0.86
	3,4	1.00	0.62	0.8	0.33	0.64	0.07	0.19	1	0.89	1.14	0.64	0.5.	1.12	0.87
30°	1	1.00	0.61	0.45	0.58	1.02	0.78	0.33	1.00	1.08	0.89	0.79	0.74	0.57	0.75
	2	1.00	0.14	0.59	0.19	0.33	0.76	1.02	1	0.26	0.46	0.67	0.29	0.66	1.07
	3	1.00	0.58	0.57	0.14	1.22	0.93	0.34	1	0.75	0.62	0.61	0.92	0.57	0.95
	4	1.00	0.64	0.91	0.48	1.92	0.91	1.02	1	0.95	1.59	1.43	1.76	1.56	1.78
	5	1.00	0.36	0.46	0.13	0.31	0.66	0.61	1	0.50	0.16	0.69	0.63	0.16	0.89
	6	1.00	1.21	0.48	0.77	0.49	0.62	0.34	1	0.34	0.90	1.00	0.86	0.90	0.71
60°	1	1.00	0.90	0.58	0.48	0.49	0.25	0.74	1.00	1.37	1.13	0.42	0.07	0.25	0.58
	2	1.00	0.20	0.92	0.58	0.40	0.31	0.12	1.00	0.51	0.09	0.29	0.63	0.82	0.88
	3	1.00	0.55	0.45	0.53	1.36	0.25	0.10	1.00	0.60	0.84	0.69	0.77	0.36	0.53
	4	1.00	0.66	0.88	0.31	1.06	0.20	0.13	1.00	0.92	1.40	0.91	1.01	0.48	0.46
	5	1.00	0.48	0.87	0.42	0.67	0.32	0.09	1.00	0.70	0.82	0.39	0.20	0.33	0.58
	6	1.00	0.49	0.66	0.19	0.14	0.64	0.89	1.00	0.68	0.38	0.53	0.75	0.89	0.85
90°	1	1.00	1.01	0.84	1.13	0.82	1.18	1.16	1.00	1.47	1.22	0.91	1.77	1.88	1.36
	2	1.00	0.24	1.04	0.86	0.68	0.85	1.07	1.00	0.60	0.37	0.24	0.07	0.39	0.65
	3	1.00	0.54	0.47	0.67	0.92	1.01	0.30	1.00	0.54	0.94	0.51	1.19	0.73	0.50
	4	1.00	0.66	0.85	0.17	0.33	1.06	0.72	1.00	0.90	1.21	0.63	1.25	1.29	0.91
	5	1.00	0.52	1.02	0.68	1.21	1.14	0.90	1.00	0.77	1.05	0.92	0.98	0.76	0.63
	6	1.00	0.59	0.91	0.82	0.77	0.72	0.74	1.00	0.85	0.82	0.68	0.80	0.82	1.06

Continued Table 4.1 Displacement amplification coefficients under different incident angles with four inhomogeneous parameters

		$\beta = 1.25$							$\beta = 1.5$						
α	η / point	0.01	0.5	1	1.5	2	2.5	3	0.01	0.5	1	1.5	2	2.5	3
0°	1,6	1.00	1.71	1.61	1.21	1.39	1.35	1.47	1.00	1.74	1.28	1.70	1.10	1.87	1.50
	2,5	1.00	0.52	1.22	1.57	1.02	1.33	1.77	1	0.92	0.57	0.82	1.18	1.06	1.22
	3,4	1.00	1.24	0.56	1.97	2.48	0.84	1.95	1	1.25	0.35	2.84	1.32	1.13	1.39
30°	1	1.00	1.15	1.49	1.33	1.04	1.36	1.42	1.00	1.51	1.72	1.86	1.49	1.35	1.56
	2	1.00	1.10	0.79	0.99	1.35	0.91	0.27	1.00	1.64	1.51	0.33	1.28	0.94	1.10
	3	1.00	0.69	1.01	0.89	2.11	0.44	2.14	1.00	0.39	2.13	0.53	1.66	1.51	2.15
	4	1.00	1.38	1.51	1.07	0.58	1.30	2.12	1.00	1.67	1.81	0.80	1.58	2.43	1.86
	5	1.00	0.70	1.43	0.62	1.75	0.18	1.34	1.00	0.88	1.72	1.20	0.73	1.47	2.33
	6	1.00	1.03	1.50	1.60	1.02	1.27	1.29	1.00	1.24	1.68	1.82	1.60	1.62	1.61
60°	1	1.00	0.79	0.99	0.95	0.92	1.14	1.18	1.00	1.13	0.79	0.78	0.84	0.77	0.70
	2	1.00	1.18	0.83	0.37	0.91	0.92	0.44	1.00	1.37	0.49	1.02	0.44	0.69	0.6
	3	1.00	0.28	0.91	0.65	0.36	0.75	0.44	1.00	0.38	1.07	0.64	0.52	0.59	0.22
	4	1.00	1.18	0.97	0.58	0.42	0.36	0.20	1.00	1.16	0.71	0.73	0.61	0.50	0.71
	5	1.00	0.93	0.18	1.17	0.44	0.78	0.85	1.00	1.42	1.05	0.19	0.41	0.44	0.66
	6	1.00	0.80	0.75	1.00	0.76	1.04	0.94	1.00	0.85	0.69	0.67	0.64	0.64	0.58
90°	1	1.00	0.74	0.72	0.66	0.61	0.54	0.54	1.00	0.81	0.40	0.44	0.35	0.29	0.28
	2	1.00	1.12	0.60	0.39	0.79	0.47	0.46	1.00	1.18	0.32	0.75	0.25	0.40	0.37
	3	1.00	0.18	0.69	0.59	0.10	0.29	0.28	1.00	0.43	0.72	0.46	0.31	0.45	0.26
	4	1.00	1.07	0.73	0.47	0.56	0.29	0.13	1.00	1.27	0.76	0.25	0.17	0.31	0.51
	5	1.00	0.93	0.25	0.73	0.64	0.20	0.60	1.00	1.11	0.34	0.64	0.24	0.35	0.41
	6	1.00	0.73	0.35	0.51	0.36	0.26	0.36	1.00	0.68	0.23	0.34	0.16	0.21	0.17

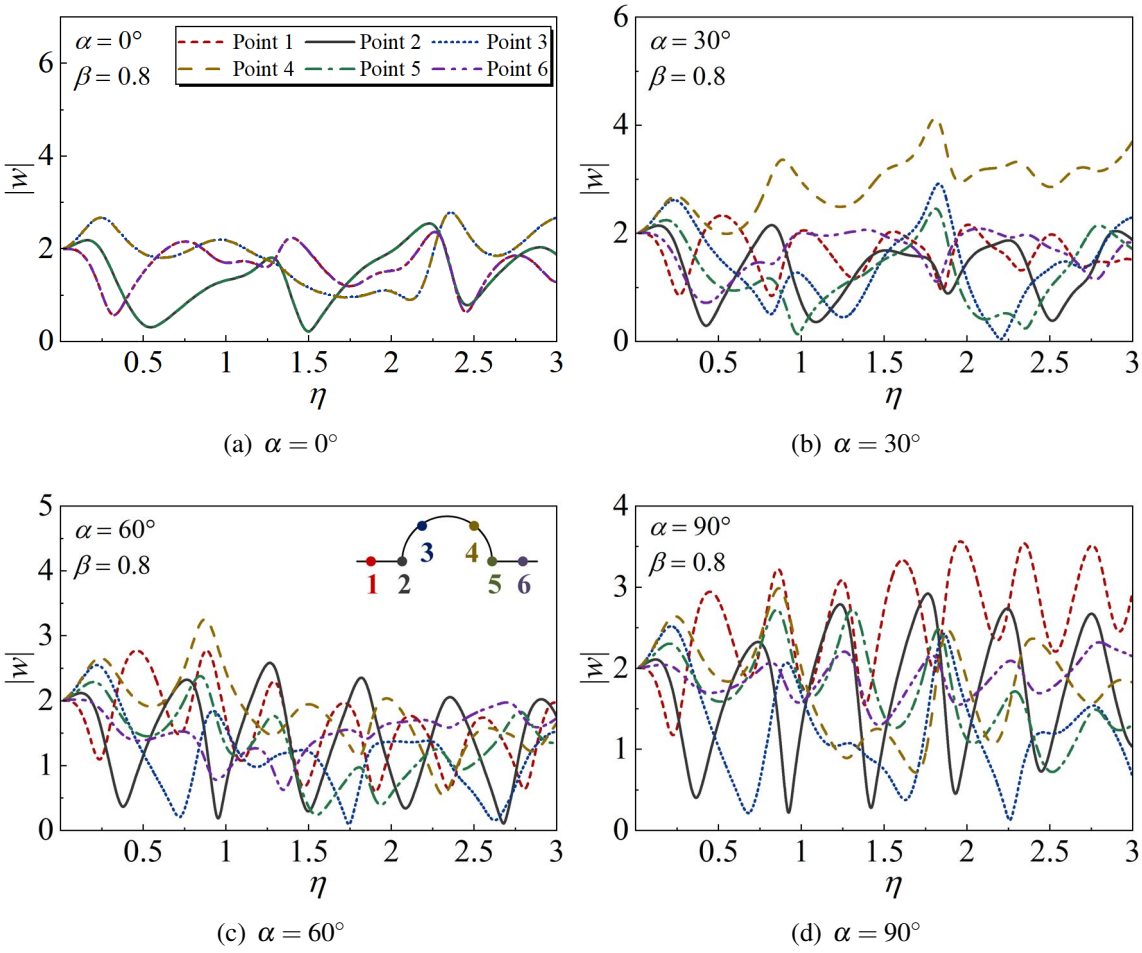

Fig. 4.9 Displacement amplitude of six selection observation points under inhomogeneous parameter $\beta = 0.7$

displacement amplification coefficient are points 3 and 4, which are the observation points on the convex surface, and the amplification coefficient with the ascender of inhomogeneous parameters then increases. However, at horizontal incident, the observation point with the maximum $|w^*|$ appears on the horizontal boundary, and decreases with the inhomogeneous parameters growing. As $\beta > 1$ and 60° incident, $|w^*|$ is inversely proportional to the dimensionless frequency, for horizontal incident, the inversely proportional phenomenon is more obvious. With the comparing of influence of four incident angles on the displacement amplification coefficient, at $\beta < 1$ the maximum value of $|w^*|$ appears at the 30° incident, while at other inhomogeneous parameters it appears at the vertical incident. Meanwhile, from the data in the table that under some parameter conditions, the displacement amplification coefficient is close to 0.1, which means that it has an obvious reduction effect on the displacement, and

the displacement amplitude is close to zero, which will also lead to the obvious vibration of the displacement amplitude with the frequency variation.

Compared with the displacement amplification coefficient in the case of surface depression with the same parameters given in Table 3.1. In addition to the maximum displacement amplification coefficient, the coefficient in the case of surface convex is slightly smaller than surface depression, especially at the horizontal incident situation. And, in the case of surface depression, $|w^*|$ is proportional to the dimensionless frequency, while for the surface convex, this situation is only applicable to the situation of $\beta < 1$. Compared with the minimum value of $|w^*|$, the median value of apparent convex on the surface is smaller. Based on the above results, it can be considered that the amplitude of surface displacement will be weakened to a certain extent when the surface of this type of inhomogeneous media with convex compared with a depression defect.

For clearly observing the displacement amplitude distribution of the convex and its adjacent horizontal surface, the three-dimensional displacement amplitude of its surface is given. Fig.4.10 and Fig.4.11 indicate the three-dimensional displacement amplitude of the surface varying with the dimensionless frequency when the inhomogeneous parameters β are set as 0.75 and 1.25 at four incident angles. Similar to the plan view, the axis y/r_a represents the relative position, $[-1,1]$ is the corresponding position of the convex surface. $[-3,-1)$ and $(1,3]$ is the corresponding position of the horizontal boundary. According to the two groups of figures that the vibration of surface displacement amplitude is significantly intensified when the inhomogeneous parameter increases. And, it can be clearly observed that in vertical incident, as shown in Fig. 4.10 (a) and Fig. 4.11 (a), the maximum value of the surface displacement amplitude of $\beta > 1$ mostly occurs at the junction of the convex and horizontal boundary. However at $\beta < 1$, the maximum value of surface displacement amplitude appears at the top of the depression, and its value is advanced significantly with the growth of dimensionless frequency. But its change is not obvious when the dimensionless frequency is greater than 1.0. Obviously, at 30° incident, as shown in Fig. 4.10 (b) and Fig. 4.11 (b), the position of the maximum point is still similar to that of the vertical incidence. However, when the incident angle varies to 60° , as Fig. 4.10 (c) and Fig. 4.11 (c), the maximum value of the surface displacement amplitude appears near the convex vertex. Under the action of two inhomogeneous parameters, the maximum displacement amplitude has the same result. In case of horizontal incidence, from Fig. 4.10 (d) and Fig. 4.11 (d), it can be clearly observed that at $\beta > 1$, the amplitude of surface displacement decreases significantly with the growth of dimensionless frequency, especially at the horizontal boundary on both sides, and at the right horizontal boundary, the amplitude of surface displacement in some areas is almost zero. At $\beta < 1$, the amplitude of surface displacement with the dimensionless frequency's

ascender then increase, and the displacement on the left side of the horizontal boundary increased more obviously. In particular, under this condition, the maximum displacement amplitude of $\beta = 0.75$ is greater than $\beta = 1.25$. Meanwhile, from two sets of figures that when the dimensionless frequency reaches 2.0, the amplitude of surface displacement will suddenly increase, especially at the horizontal boundary.

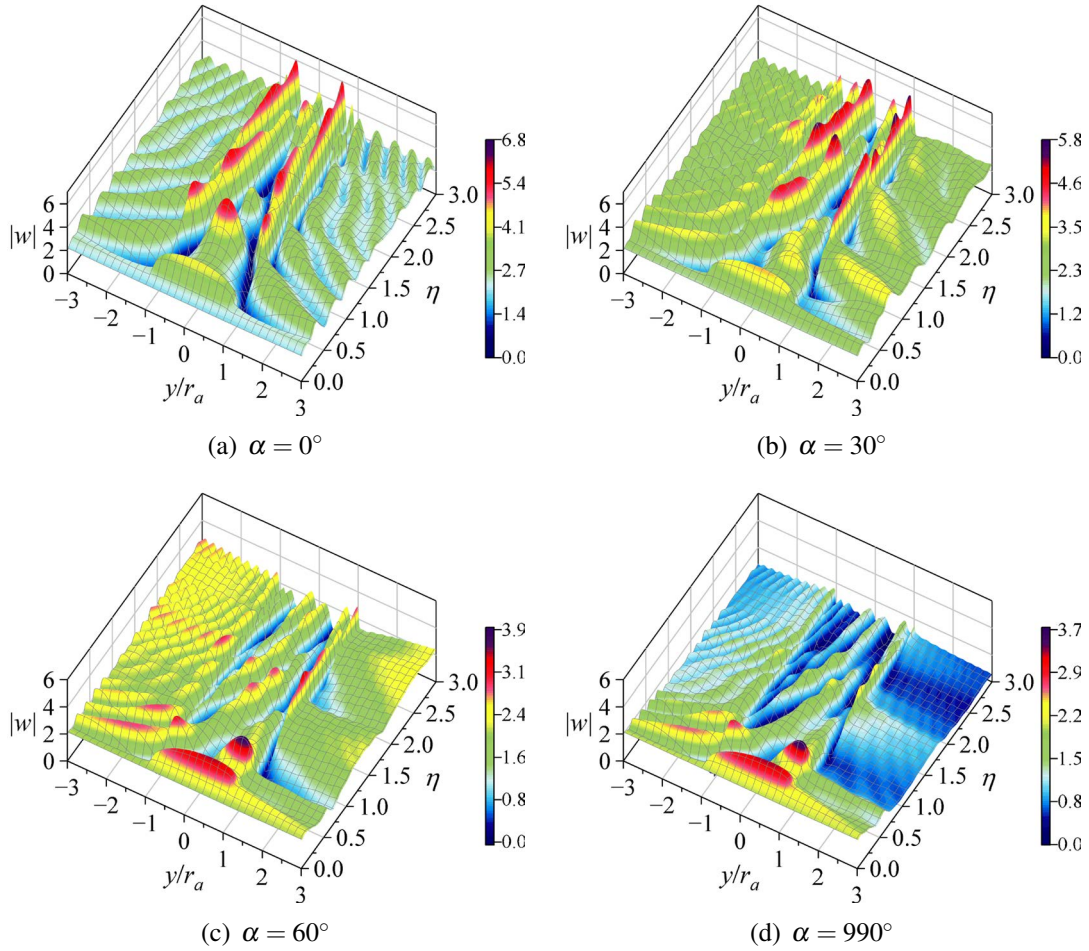

Fig. 4.10 3D surface displacement of inhomogeneous parameter $\beta = 1.25$

Meanwhile, the influence of internal displacement amplitude distribution of semi-cylindrical convex in inhomogeneous media under the inhomogeneous parameters is analyzed and discussed. The results displayed in Figs. 4.12-4.14 can be obtained by calculating the displacement amplitude of the semi-cylindrical convex semi-infinite region of the interface at four incident angles, with the dimensionless frequency of 2.0 and the inhomogeneous parameters β set as 0.75, 1.0 and 1.25 respectively. Among them, when the inhomogeneous parameter is set to 1.0, the homogeneous media can be simulated. From Fig. 4.12, with the incident angle increasing, the maximum point of displacement amplitude is larger than the

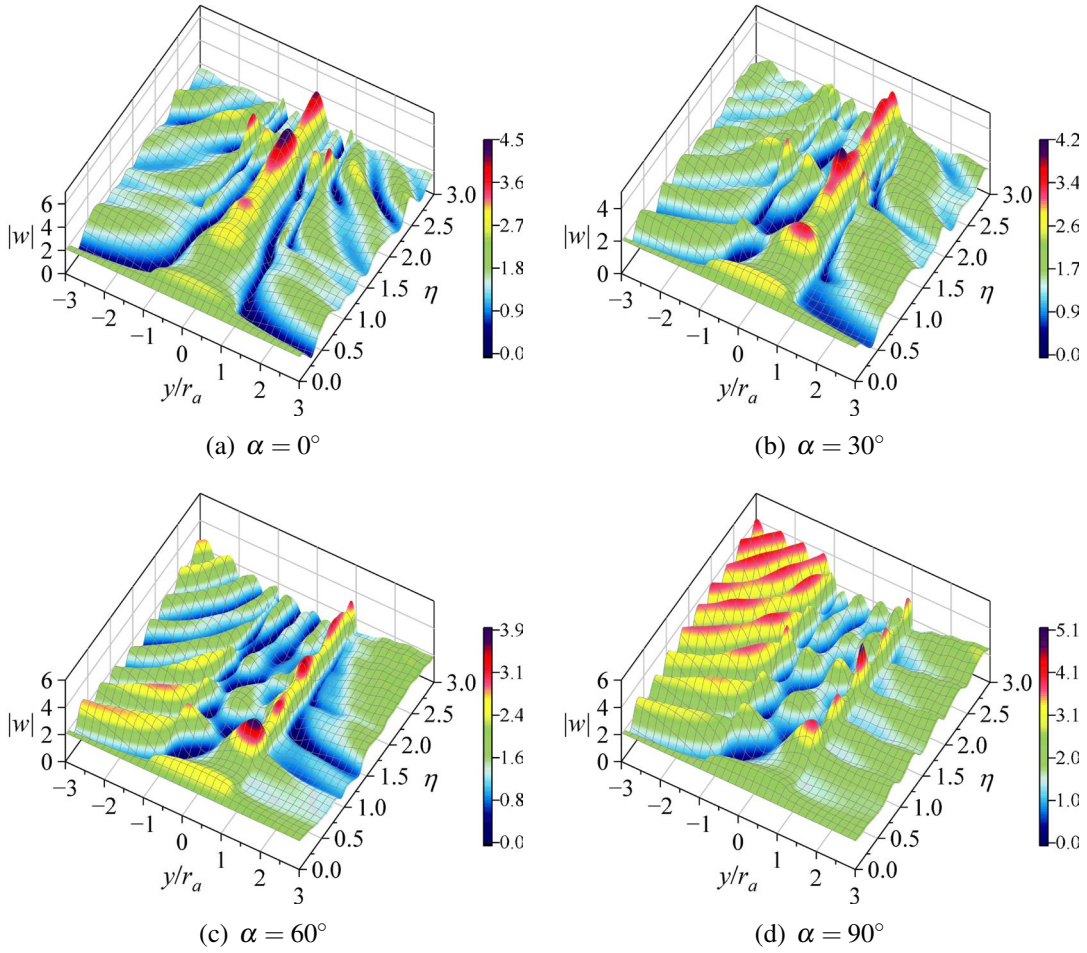

Fig. 4.11 3D surface displacement of inhomogeneous parameter $\beta = 0.75$

surface displacement amplitude from the top of convex to horizontal boundary. These areas with large internal displacement amplitude are connected with the maximum area, and the included angle between the line and the x-axis is close to the incident angle. With horizontal incident, the maximum displacement amplitude appears on the horizontal boundary surface of the wave front and the right side of the convex, and there is an obvious decrease trend along the positive direction of the y/r_a axis. Compared with the concave boundary, it can be found that the maximum displacement amplitude of the convex boundary is located on the side of the back wave surface, while the concave boundary is located on the side of the front wave surface.

In the case of homogeneous media $\beta = 1$, as given in Fig. 4.13, the area with large internal displacement amplitude increases significantly. However, from Fig. 4.13 (d), under horizontal incident although the region with large internal displacement amplitude is almost full of the entire semi-infinite region. But the displacement amplitude in the convex is the smallest of

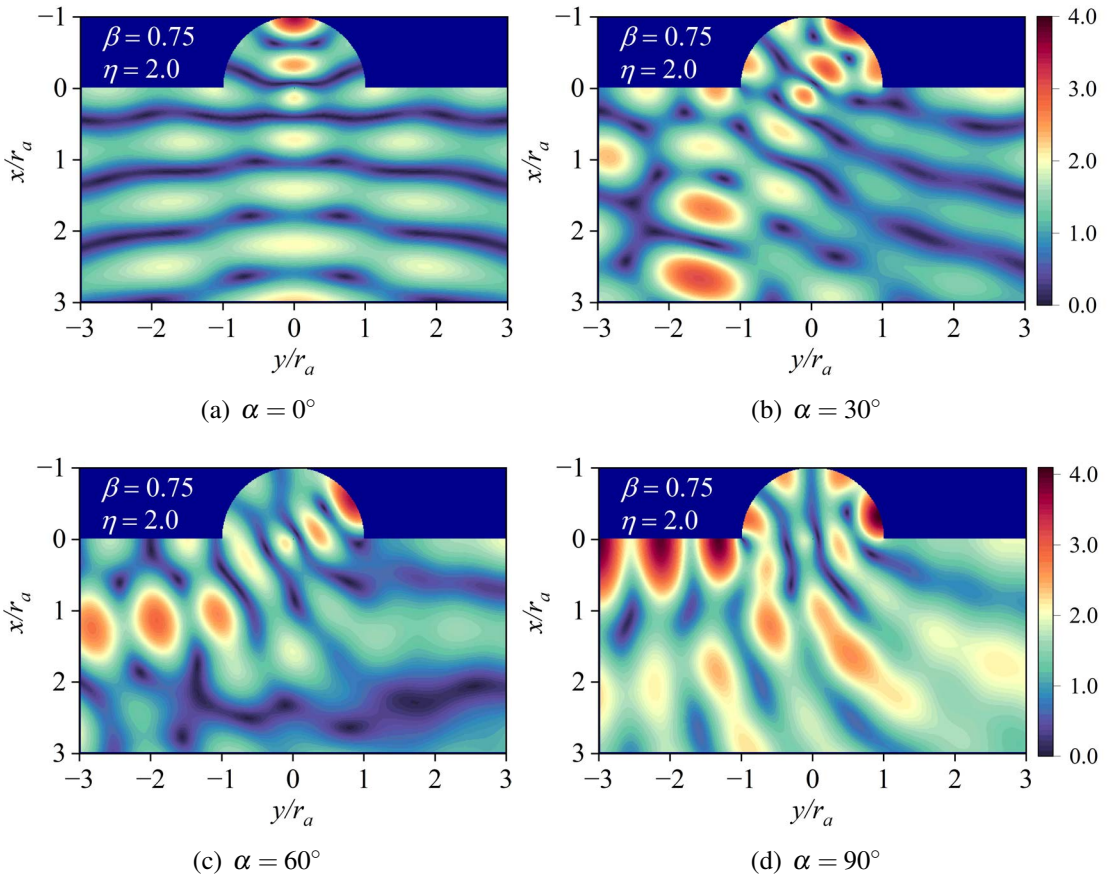

(a) $\alpha = 0°$ (b) $\alpha = 30°$

(c) $\alpha = 60°$ (d) $\alpha = 90°$

Fig. 4.12 Internal displacement amplitude of inhomogeneous parameter $\beta = 0.75$

the four incident angles. With the incident angle increasing, the displacement amplitude reduces significantly. At 60° and horizontal incident, the maximum point of displacement amplitude appears in the region. At 30° and vertical incident, the maximum displacement amplitude appears on the convex surface. Increase the inhomogeneous parameter to 1.25 for calculation, and the resulting internal displacement amplitude is shown in Fig.4.14. That the position of the maximum displacement amplitude point moves from the convex surface to the horizontal boundary and inside with the increase of the incident angle. Under horizontal incident, it can be clearly seen that the amplitude of surface displacement at the horizontal boundary decreases significantly, and the internal displacement presents a certain vibration.

According to these three groups of figures, the displacement amplitude distribution under the three inhomogeneous parameters has a certain similarity. The maximum displacement amplitude increases with the growth of inhomogeneous parameters. With the gradual increase of the incident angle, the maximum points of displacement amplitude move from the position of the convex surface to the junction with the horizontal boundary and the interior of region.

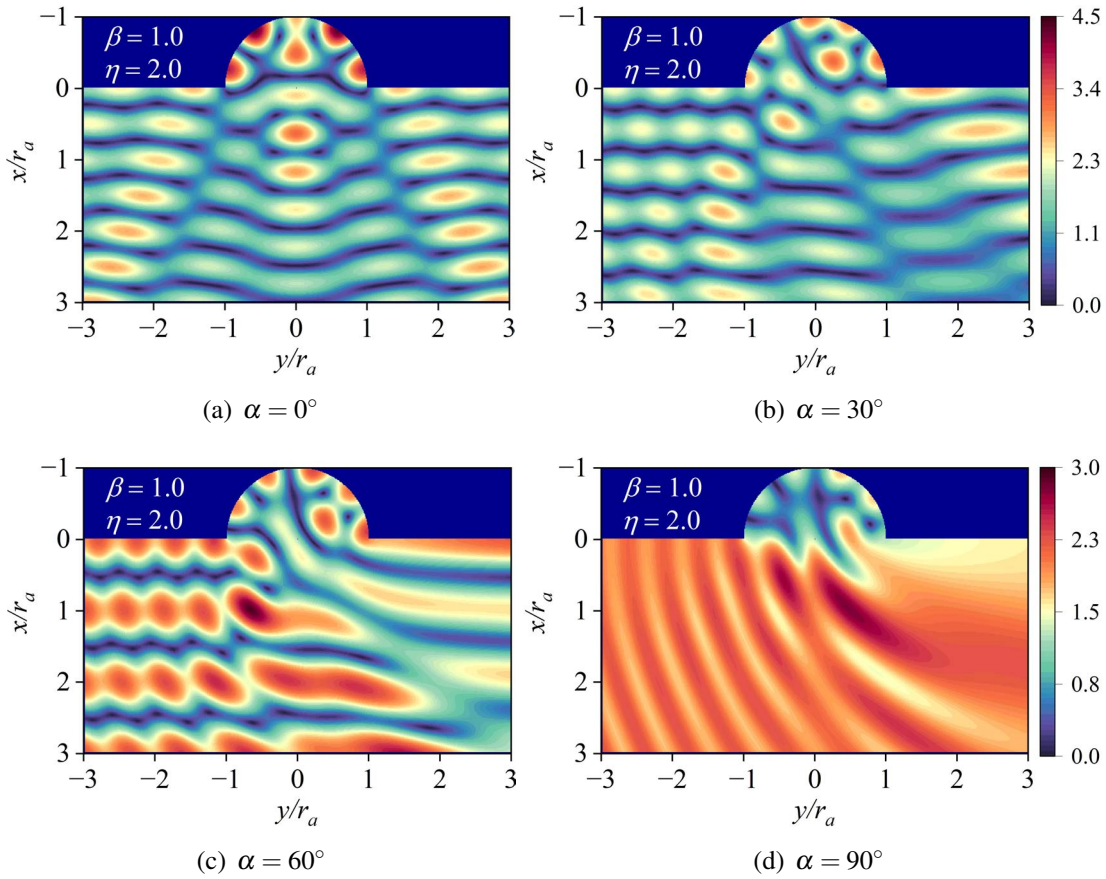

(a) $\alpha = 0°$ (b) $\alpha = 30°$

(c) $\alpha = 60°$ (d) $\alpha = 90°$

Fig. 4.13 Internal displacement amplitude of inhomogeneous parameter $\beta = 1.0$

However, different inhomogeneous parameters still have some influence on the internal displacement distribution. Under vertical incident, the displacement amplitude of the area directly below the surface convex at $\beta = 1.25$ decreases significantly when compared with the other two inhomogeneous parameters. At $\beta = 0.75$ and $\beta = 1.0$, there are areas with large displacement amplitude directly below the surface convex. As the incident angle is $30°$, the internal displacement increases gradually along the negative direction of y/r_a when $\beta = 1.25$ and $\beta = 1.0$, but decreases first and then increases when $\beta = 0.75$. At $60°$ oblique incident, the displacement amplitude on the horizontal interface is larger ($\beta \geq 1.0$), while it is smaller on the horizontal interface ($\beta < 1$). Finally, at horizontal incidence, with the increase of three groups of inhomogeneous parameters, the distribution of displacement amplitude changes significantly. It can be considered that at $\beta < 1$, the internal displacement amplitude is reduced, and at $\beta > 1$, the displacement amplitude at the horizontal boundary is reduced.

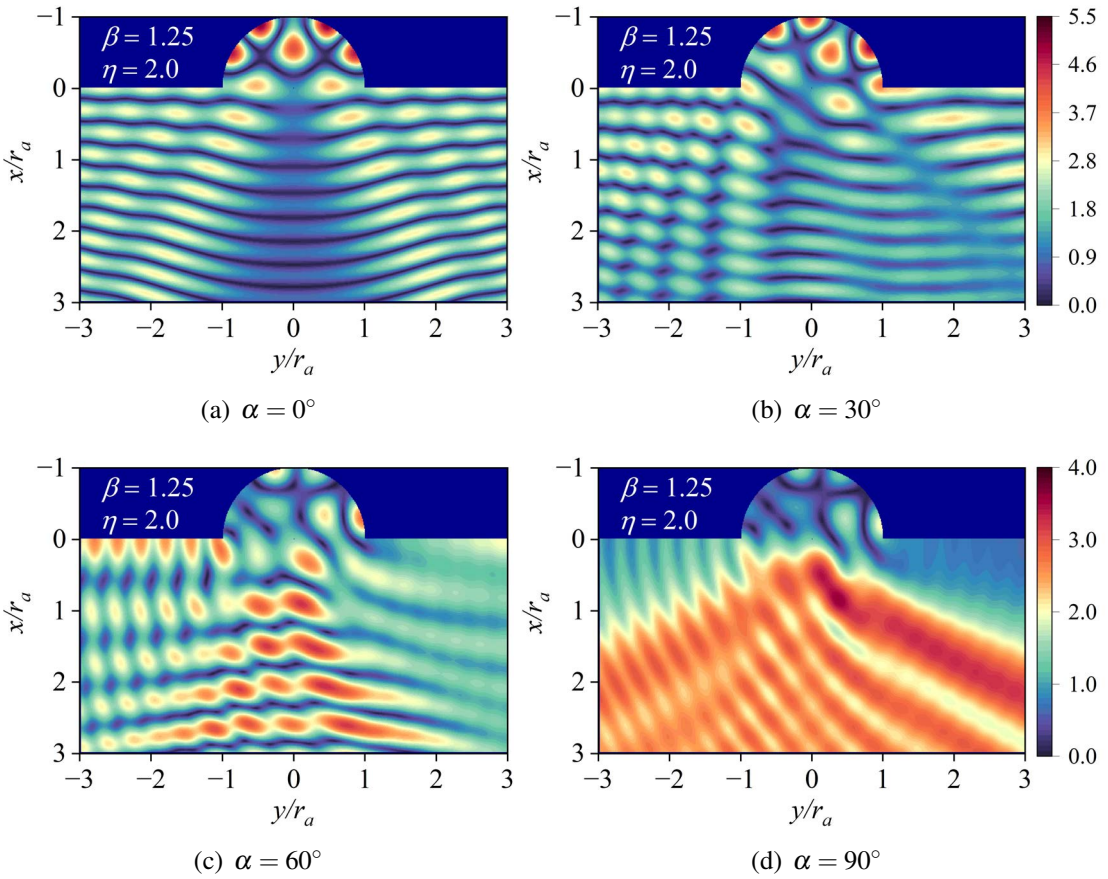

(a) $\alpha = 0°$ (b) $\alpha = 30°$

(c) $\alpha = 60°$ (d) $\alpha = 90°$

Fig. 4.14 Internal displacement amplitude of inhomogeneous parameter $\beta = 1.25$

Compared with the internal displacement amplitude under the surface depression boundary, as given in Fig. 3.12-3.13, the internal displacement distribution under the two surface defects has certain similarity. However, compared with the surface depression, the maximum displacement amplitude of the surface convex occurs at the vertical incident, while the surface depression occurs at the horizontal incident. This can be understood as the energy absorption of SH wave by the convex at horizontal incident, thus weakening the displacement amplitude in the surface convex boundary. While with the vertical incident, the surface convex boundary has a certain converging effect on the SH wave, so the displacement amplitude in this part is larger. In addition, the surface depression boundary has an absorption effect on the SH wave at the wave front with horizontal incident, so that the displacement amplitude of the wave back surface is significantly reduced. However, in the convex boundary, there is no absorption effect, so there is still a large area of the internal displacement amplitude of the wave back surface.

4.2 Scattering of SH waves by surface semi-cylindrical convex with a cylindrical cavity in density inhomogeneous media

The media contains cavities and inclusions, which are common media defects. Under the action of dynamic load, the local dynamic stress concentration around the cavity or inclusion will increase, and will have a greater impact on the distribution of the surrounding displacement amplitude. As a relatively simple model of various defects, cylindrical cavity can be regarded as the basis of other complex models. Meanwhile, in the dynamic analysis of tunnels and reserved pipeline cavities in the project, they can be simplified to cylindrical cavity for research, and the corresponding theoretical basis can be provided by analyzing the dynamic stress concentration and displacement amplitude distribution around them.

4.2.1 Model and wave equation

The model of a surface semi-cylindrical convex with a cylindrical cavity in a density radial inhomogeneous half space under the incidence of SH waves is shown in Fig. 4.15. The coordinate origin o is set at the center of the semi-cylindrical convex with radius r_a. The radius of the cylindrical cavity is r_b. Its center is the same as the center of the semi-cylindrical convex. The x-axis is vertically downward and the y-axis is horizontally right. θ is the angle of r counterclockwise rotation. In order to construct the wave field form in the infinite space subsequently, the model is divided into two regions, and the auxiliary boundary S_a is introduced. Then, Region I is a semi-infinite region with semi-cylindrical boundary S_a, and Region II is a closed cylindrical region with boundary S_a, L and S_b. The function of the media density along the radius is still selected in the same form as in Section 4.1, Eq. (4.1). Thus, the standard Helmholtz equation can be obtained according to the transformation process in Chapter 2, as shown in Eq. (4.2).

4.2.2 Displacement field expression in each region

In order to express the entire wave field in the construction area, the semi-cylindrical convex semi-infinite region with a cylindrical cavity is divided into two regions, a semi-infinite region with a surface semi-cylindrical depression and a closed cylindrical region, as shown in Fig. 4.16. After the corresponding wave field expressions in the two regions are constructed respectively, the final results satisfying the control equation are obtained through the corresponding boundary conditions.

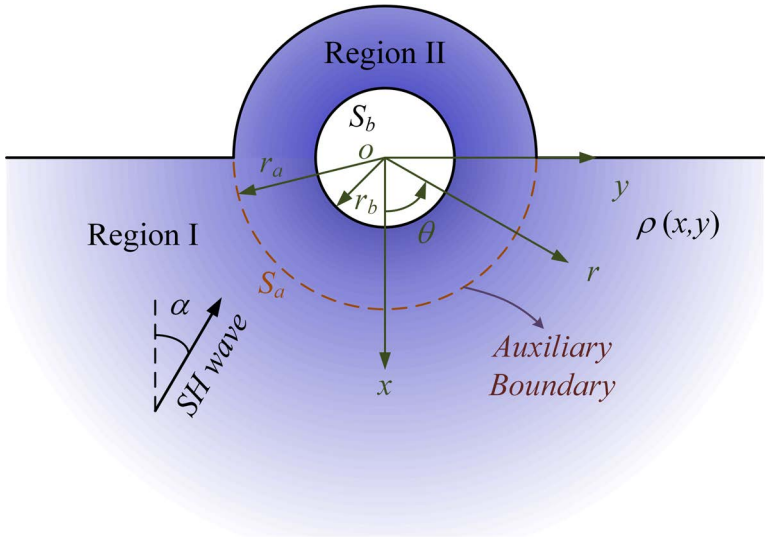

Fig. 4.15 Model of SH wave scattering by a semi-cylindrical convex with a cylindrical cavity in a density radial inhomogeneous media

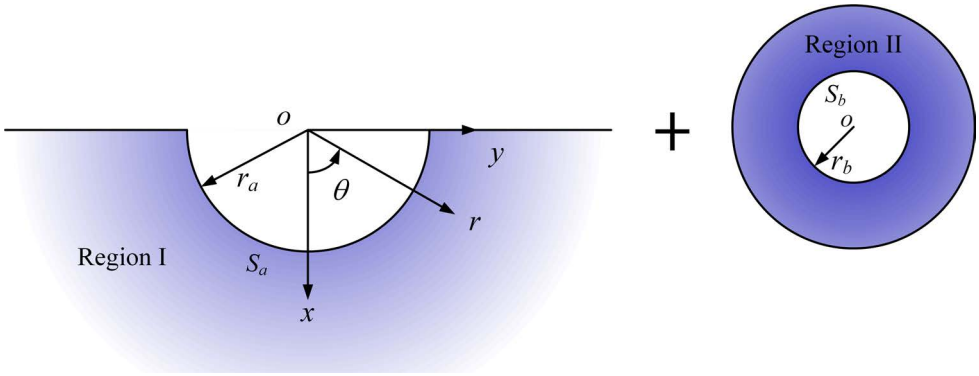

Fig. 4.16 Schematic of semi-cylindrical convex with a cylindrical cavity model division

Displacement field expression in Region I

The wave field $w^{(1)}$ in Region I can be regarded as superposition of free wave field $w^{(f)}$ and scattered wave field $w^{(s)}$:

$$w^{(1)} = w^{(f)} + w^{(s)} \tag{4.16}$$

where the free wave field $w^{(f)}$ is composed of the incident wave and the reflecting wave generated by the semi-infinite interface, which can be written as:

$$\begin{aligned} w^{(f)} = & \sum_{n=0}^{\infty} (-1)^n \varepsilon_n J_{2n/\beta}\left(k_0 |\zeta|\right) \cos 2n\alpha \cdot \left\{ \left(\frac{\zeta}{|\zeta|}\right)^{2n/\beta} + \left(\frac{\zeta}{|\zeta|}\right)^{-2n/\beta} \right\} \\ & + 2\sum_{n=0}^{\infty} (-1)^n J_{(2n+1)/\beta}(k_0 |\zeta|) \sin\left(2n+1\right)\alpha \\ & \cdot \left\{ \left(\frac{\zeta}{|\zeta|}\right)^{(2n+1)/\beta} - \left(\frac{\zeta}{|\zeta|}\right)^{-(2n+1)/\beta} \right\} \end{aligned} \tag{4.17}$$

According to Chapter 3, the scattering field generated by the semi-cylindrical depression can be expressed as:

$$\begin{aligned} w^{(s)}\left(\zeta, \bar{\zeta}\right) = w_0 \sum_{n=0}^{\infty} \Bigg\{ & A_n H_{2n/\beta}^{(1)}\left(k_0 |\zeta|\right) \left[\left(\frac{\zeta}{|\zeta|}\right)^{2n/\beta} + \left(\frac{\zeta}{|\zeta|}\right)^{-2n/\beta} \right] \\ & + B_n H_{(2n+1)/\beta}^{(1)}\left(k_0 |\zeta|\right) \left[\left(\frac{\zeta}{|\zeta|}\right)^{(2n+1)/\beta} - \left(\frac{\zeta}{|\zeta|}\right)^{-(2n+1)/\beta} \right] \Bigg\} \end{aligned} \tag{4.18}$$

where A_n, B_n are unknown coefficients to be solved.

Displacement field expression in Region II

The construction of the annular internal wave field of the inhomogeneous medium in Region II is one of the main works to solve this problem. The standing wave field $w^{(2)}$ in Region II can be seen as a cohesive wave $w^{(a)}$ generated by the auxiliary boundary S_a and a divergent wave $w^{(b)}$ generated when the wave reaches the free boundary S_b.

$$w^{(2)} = w^{(a)} + w^{(b)} \tag{4.19}$$

where $w^{(2)}$ must satisfy the condition of free circular stress at boundary L and S_b.

With the condition that the control equation of inhomogeneous media used in this chapter is satisfied, the constructed convergence wave $w^{(a)}$ can be written as:

$$\begin{aligned} w^{(a)}\left(\zeta,\bar{\zeta}\right) = w_0 \Bigg\{ & \sum_{n=0}^{\infty} C_n J_{2n/\beta}\left(k_0|\zeta|\right)\left[\left(\frac{\zeta}{|\zeta|}\right)^{2n/\beta} + \left(\frac{\zeta}{|\zeta|}\right)^{-2n/\beta}\right] \\ & + \sum_{n=0}^{\infty} D_n J_{(2n+1)/\beta}\left(k_0|\zeta|\right)\left[\left(\frac{\zeta}{|\zeta|}\right)^{(2n+1)/\beta} - \left(\frac{\zeta}{|\zeta|}\right)^{-(2n+1)/\beta}\right] \\ & + \sum_{n=0}^{\infty} E_n J_{(2n+1)/\beta}\left(k_0|\zeta|\right)\left[\left(\frac{\zeta}{|\zeta|}\right)^{(2n+1)/\beta} + \left(\frac{\zeta}{|\zeta|}\right)^{-(2n+1)/\beta}\right] \\ & + \sum_{n=1}^{\infty} F_n J_{2n/\beta}\left(k_0|\zeta|\right)\left[\left(\frac{\zeta}{|\zeta|}\right)^{2n/\beta} - \left(\frac{\zeta}{|\zeta|}\right)^{-2n/\beta}\right]\Bigg\} \end{aligned} \tag{4.20}$$

where C_n, D_n, E_n, F_n are unknown coefficients to be solved.

Similarly, the divergent wave $w^{(b)}$ generated by the free boundary S_b can be expressed as Hankel function of the first kind:

$$\begin{aligned} w^{(b)}\left(\zeta,\bar{\zeta}\right) = w_0 \sum_{n=0}^{\infty} \Bigg\{ & G_n H^{(1)}_{2n/\beta}\left(k_0|\zeta|\right)\left[\left(\frac{\zeta}{|\zeta|}\right)^{2n/\beta} + \left(\frac{\zeta}{|\zeta|}\right)^{-2n/\beta}\right] \\ & + I_n H^{(1)}_{(2n+1)/\beta}\left(k_0|\zeta|\right)\left[\left(\frac{\zeta}{|\zeta|}\right)^{(2n+1)/\beta} - \left(\frac{\zeta}{|\zeta|}\right)^{-(2n+1)/\beta}\right]\Bigg\} \end{aligned} \tag{4.21}$$

where G_n, I_n are unknown coefficients to be solved.

4.2.3 Stress field expression in each region

There are many unknown coefficients to be solved when constructing the wave field, which need to be solved by using the stress boundary condition, so the corresponding expression of the stress field is given. By substituting the wave field expressions in the two regions into Eqs. (2.35) and (2.36), the stress field expressions in each region can be obtained. The stress field in Region I can be expressed as:

$$\begin{aligned} \tau_{rz}^{(1)} = \frac{\beta\mu k_0 w_0}{2} \Bigg[& \sum_{n=0}^{\infty} (-1)^n \varepsilon_n P_{2n/\beta}\left(\zeta\right)\cos 2n\alpha \\ & + \sum_{n=0}^{\infty} (-1)^n Q_{(2n+1)/\beta}\left(\zeta\right)\sin\left(2n+1\right)\alpha \\ & + \sum_{n=0}^{\infty} A_n U_{2n/\beta}\left(\zeta\right) + \sum_{n=0}^{\infty} B_n V_{(2n+1)/\beta}\left(\zeta\right)\Bigg] \end{aligned} \tag{4.22}$$

$$\begin{aligned}\tau_{\theta z}^{(1)} = \frac{\mathrm{i}\beta\mu k_0 w_0}{2}\Bigg[&\sum_{n=0}^{\infty}(-1)^n\varepsilon_n P_{2n/\beta}\,(\zeta)\cos 2n\alpha \\ &-\sum_{n=0}^{\infty}(-1)^n Q_{(2n+1)/\beta}\,(\zeta)\sin(2n+1)\,\alpha \\ &+\sum_{n=0}^{\infty}A_n U_{2n/\beta}\,(\zeta)-\sum_{n=0}^{\infty}B_n V_{(2n+1)/\beta}\,(\zeta)\Bigg]\end{aligned} \tag{4.23}$$

where

$$\begin{aligned}P_t(s) &= J_{t-1}(k_0|s|)\left[\frac{s}{|s|}\right]^{t-1}z^{\beta-1}e^{\mathrm{i}\theta}-J_{t+1}(k_0|s|)\left[\frac{s}{|s|}\right]^{-t-1}z^{\beta-1}e^{\mathrm{i}\theta} \\ &+J_{t-1}(k_0|s|)\left[\frac{s}{|s|}\right]^{1-t}\bar{z}^{\beta-1}e^{-\mathrm{i}\theta}-J_{t+1}(k_0|s|)\left[\frac{s}{|s|}\right]^{-t-1}\bar{z}^{\beta-1}e^{-\mathrm{i}\theta} \\ Q_t(s) &= J_{t-1}(k_0|s|)\left[\frac{s}{|s|}\right]^{t-1}z^{\beta-1}e^{\mathrm{i}\theta}+J_{t+1}(k_0|s|)\left[\frac{s}{|s|}\right]^{-t-1}z^{\beta-1}e^{\mathrm{i}\theta} \\ &-J_{t-1}(k_0|s|)\left[\frac{s}{|s|}\right]^{1-t}\bar{z}^{\beta-1}e^{-\mathrm{i}\theta}-J_{t+1}(k_0|s|)\left[\frac{s}{|s|}\right]^{-t-1}\bar{z}^{\beta-1}e^{-\mathrm{i}\theta} \\ U_t(s) &= H_{t-1}^{(1)}(k_0|s|)\left[\frac{s}{|s|}\right]^{t-1}z^{\beta-1}e^{\mathrm{i}\theta}-H_{t+1}^{(1)}(k_0|s|)\left[\frac{s}{|s|}\right]^{-t-1}z^{\beta-1}e^{\mathrm{i}\theta} \\ &+H_{t-1}^{(1)}(k_0|s|)\left[\frac{s}{|s|}\right]^{1-t}\bar{z}^{\beta-1}e^{-\mathrm{i}\theta}-H_{t+1}^{(1)}(k_0|s|)\left[\frac{s}{|s|}\right]^{-t-1}\bar{z}^{\beta-1}e^{-\mathrm{i}\theta} \\ V_t(s) &= H_{t-1}^{(1)}(k_0|s|)\left[\frac{s}{|s|}\right]^{t-1}z^{\beta-1}e^{\mathrm{i}\theta}+H_{t+1}^{(1)}(k_0|s|)\left[\frac{s}{|s|}\right]^{-t-1}z^{\beta-1}e^{\mathrm{i}\theta} \\ &-H_{t-1}^{(1)}(k_0|s|)\left[\frac{s}{|s|}\right]^{1-t}\bar{z}^{\beta-1}e^{-\mathrm{i}\theta}-H_{t+1}^{(1)}(k_0|s|)\left[\frac{s}{|s|}\right]^{-t-1}\bar{z}^{\beta-1}e^{-\mathrm{i}\theta}\end{aligned}$$

The cohesive wave in Region II is substituted into Eqs. (2.35) and (2.36), and the corresponding stress field is:

$$\begin{aligned}\tau_{rz}^{(a)} = \frac{\beta\mu k_0 w_0}{2}\sum_{n=0}^{\infty}\big[&C_n P_{2n/\beta}(\zeta)+D_n Q_{(2n+1)/\beta}(\zeta) \\ &+E_n P_{(2n+1)/\beta}(\zeta)+F_n Q_{2n/\beta}(\zeta)\big]\end{aligned} \tag{4.24}$$

$$\begin{aligned}\tau_{\theta z}^{(a)} = \frac{i\beta\mu k_0 w_0}{2}\sum_{n=0}^{\infty}\big[&C_n P_{2n/\beta}(\zeta)-D_n Q_{(2n+1)/\beta}(\zeta) \\ &+E_n P_{(2n+1)/\beta}(\zeta)-F_n Q_{2n/\beta}(\zeta)\big]\end{aligned} \tag{4.25}$$

Similarly, the corresponding stress field of divergent wave in Region II can be obtained as:

$$\tau_{rz}^{(b)} = \frac{\beta\mu k_0 w_0}{2} \sum_{n=0}^{\infty} \left[G_n V_{2n/\beta}(\zeta) + I_n U_{(2n+1)/\beta}(\zeta) \right] \tag{4.26}$$

$$\tau_{\theta z}^{(b)} = \frac{i\beta\mu k_0 w_0}{2} \sum_{n=0}^{\infty} \left[G_n V_{2n/\beta}(\zeta) - I_n U_{(2n+1)/\beta}(\zeta) \right] \tag{4.27}$$

Thus, the stress field in Region II can be obtained:

$$\tau_{rz}^{(2)} = \tau_{rz}^{(a)} + \tau_{rz}^{(b)} \tag{4.28}$$

$$\tau_{\theta z}^{(2)} = \tau_{\theta z}^{(a)} + \tau_{\theta z}^{(b)} \tag{4.29}$$

4.2.4 Boundary conditions and solutions

In the process of constructing the wave field, the semi-infinite region is divided into two regions using the auxiliary boundary S_a. Therefore, the equations established for the displacement and stress continuity conditions at the auxiliary boundary S_a are as follows:

$$w_1 = w_1, \qquad r = r_a, \qquad -\pi/2 \le \theta \le \pi/2 \tag{4.30}$$

$$\tau_{rz}^{(1)} = \tau_{rz}^{(2)}, \qquad r = r_a, \qquad -\pi/2 \le \theta \le \pi/2 \tag{4.31}$$

The stress free condition of semi-cylindrical convex:

$$\tau_{rz}^{(2)} = 0, \qquad r = r_a, \qquad \pi/2 \le \theta \le 3\pi/2 \tag{4.32}$$

The stress free condition should be satisfied at the boundary S_b of the cylindrical cavity, which can be expressed as:

$$\tau_{rz}^{(2)} = 0, \qquad r = r_b, \qquad 0 \le \theta \le 2\pi \tag{4.33}$$

In order to solve the equation and obtain the unknown coefficients in the wave field expression in each region, multiply $e^{-\mathrm{i}m\theta}$ and integrate the two ends of Eqs. (4.30) - (4.33)

to obtain the following two sets of infinite algebraic equations:

$$\begin{cases} \sum\limits_{n=0}^{\infty} C_n \beta_{mn}^{(1)} + \sum\limits_{n=0}^{\infty} E_n \lambda_{mn}^{(1)} + \sum\limits_{n=0}^{\infty} G_n \kappa_{mn}^{(1)} = 0 \\ \sum\limits_{n=0}^{\infty} C_n \beta_{mn}^{(2)} + \sum\limits_{n=0}^{\infty} E_n \lambda_{mn}^{(2)} + \sum\limits_{n=0}^{\infty} G_n \kappa_{mn}^{(2)} = 0 \\ -\sum\limits_{n=0}^{\infty} A_n \beta_{mn}^{(3)} + \sum\limits_{n=0}^{\infty} C_n \lambda_{mn}^{(3)} + \sum\limits_{n=0}^{\infty} E_n \varphi_{mn}^{(3)} + \sum\limits_{n=0}^{\infty} G_n \kappa_{mn}^{(3)} = \sum\limits_{n=0}^{\infty} \varsigma_{mn}^{(3)} \\ -\sum\limits_{n=0}^{\infty} A_n \beta_{mn}^{(4)} + \sum\limits_{n=0}^{\infty} C_n \lambda_{mn}^{(4)} + \sum\limits_{n=0}^{\infty} E_n \varphi_{mn}^{(4)} + \sum\limits_{n=0}^{\infty} G_n \kappa_{mn}^{(4)} = \sum\limits_{n=0}^{\infty} \varsigma_{mn}^{(4)} \end{cases} \quad m = 1, 2, 3, ..., \tag{4.34}$$

$$\begin{cases} \sum\limits_{n=0}^{\infty} D_n \beta_{mn}^{(5)} + \sum\limits_{n=0}^{\infty} F_n \lambda_{mn}^{(5)} + \sum\limits_{n=0}^{\infty} I_n \kappa_{mn}^{(5)} = 0 \\ \sum\limits_{n=0}^{\infty} D_n \beta_{mn}^{(6)} + \sum\limits_{n=0}^{\infty} F_n \lambda_{mn}^{(6)} + \sum\limits_{n=0}^{\infty} I_n \kappa_{mn}^{(6)} = 0 \\ -\sum\limits_{n=0}^{\infty} B_n \beta_{mn}^{(7)} + \sum\limits_{n=0}^{\infty} D_n \lambda_{mn}^{(7)} + \sum\limits_{n=0}^{\infty} F_n \varphi_{mn}^{(7)} + \sum\limits_{n=0}^{\infty} I_n \kappa_{mn}^{(7)} = \sum\limits_{n=0}^{\infty} \varsigma_{mn}^{(7)} \\ -\sum\limits_{n=0}^{\infty} B_n \beta_{mn}^{(8)} + \sum\limits_{n=0}^{\infty} D_n \lambda_{mn}^{(8)} + \sum\limits_{n=0}^{\infty} F_n \varphi_{mn}^{(8)} + \sum\limits_{n=0}^{\infty} I_n \kappa_{mn}^{(8)} = \sum\limits_{n=0}^{\infty} \varsigma_{mn}^{(8)} \end{cases} \quad m = 1, 2, 3, ..., \tag{4.35}$$

where $\beta_{mn}^{(\cdot)}$, $\lambda_{mn}^{(\cdot)}$, $\kappa_{mn}^{(\cdot)}$, $\varphi_{mn}^{(\cdot)}$, $\varsigma_{mn}^{(\cdot)}$ is the corresponding expression expanded by Fourier series.

$$\begin{cases} \beta_{mn}^{(1)} = \int_{\pi/2}^{3\pi/2} P_{2n/\beta}\ (\zeta_a)\, \mathrm{e}^{-2mi\theta} d\theta \\ \lambda_{mn}^{(1)} = \int_{\pi/2}^{3\pi/2} P_{(2n+1)/\beta}\ (\zeta_a)\, \mathrm{e}^{-2mi\theta} d\theta \\ \kappa_{mn}^{(1)} = \int_{\pi/2}^{3\pi/2} V_{2n/\beta}\ (\zeta_a)\, \mathrm{e}^{-2mi\theta} d\theta \end{cases}$$

$$\begin{cases} \beta_{mn}^{(2)} = \int_{0}^{2\pi} P_{2n/\beta}\ (\zeta_b)\, \mathrm{e}^{-2mi\theta} d\theta \\ \lambda_{mn}^{(2)} = \int_{0}^{2\pi} P_{(2n+1)/\beta}\ (\zeta_b)\, \mathrm{e}^{-2mi\theta} d\theta \\ \kappa_{mn}^{(2)} = \int_{0}^{2\pi} V_{2n/\beta}\ (\zeta_b)\, \mathrm{e}^{-2mi\theta} d\theta \end{cases}$$

$$\begin{cases}
\beta_{mn}^{(3)} = \int_{-\pi/2}^{\pi/2} H_{2n/\beta}^{(1)}\left(k|\zeta_a|\right)\left[\left(\zeta_a/|\zeta_a|\right)^{2n/\beta} + \left(\zeta_a/|\zeta_a|\right)^{-2n/\beta}\right] \mathrm{e}^{-2m\mathrm{i}\theta} d\theta \\
\lambda_{mn}^{(3)} = \int_{-\pi/2}^{\pi/2} J_{2n/\beta}\left(k|\zeta_a|\right)\left[\left(\zeta_a/|\zeta_a|\right)^{2n/\beta} + \left(\zeta_a/|\zeta_a|\right)^{-2n/\beta}\right] \mathrm{e}^{-2m\mathrm{i}\theta} d\theta \\
\kappa_{mn}^{(3)} = \int_{-\pi/2}^{\pi/2} H_{2n/\beta}^{(1)}\left(k|\zeta_a|\right)\left[\left(\zeta_a/|\zeta_a|\right)^{2n/\beta} + \left(\zeta_a/|\zeta_a|\right)^{-2n/\beta}\right] \mathrm{e}^{-2m\mathrm{i}\theta} d\theta \\
\varphi_{mn}^{(3)} = \int_{-\pi/2}^{\pi/2} J_{(2n+1)/\beta}\left(k|\zeta_a|\right)\left[\left(\zeta_a/|\zeta_a|\right)^{(2n+1)/\beta} + \left(\zeta_a/|\zeta_a|\right)^{-(2n+1)/\beta}\right] \mathrm{e}^{-2m\mathrm{i}\theta} d\theta \\
\zeta_{mn}^{(3)} = \int_{-\pi/2}^{\pi/2} (-1)^n \varepsilon_n J_{2n/\beta}\left(k|\zeta_a|\right)\cos 2n\alpha\left[\left(\zeta_a/|\zeta_a|\right)^{2n/\beta} + \left(\zeta_a/|\zeta_a|\right)^{-2n/\beta}\right] \mathrm{e}^{-2m\mathrm{i}\theta} d\theta
\end{cases}$$

$$\begin{cases}
\beta_{mn}^{(4)} = \int_{-\pi/2}^{\pi/2} U_{2n/\beta}\left(\zeta_a\right) \mathrm{e}^{-2m\mathrm{i}\theta} d\theta \\
\lambda_{mn}^{(4)} = \int_{-\pi/2}^{\pi/2} P_{2n/\beta}\left(\zeta_a\right) \mathrm{e}^{-2m\mathrm{i}\theta} d\theta \\
\kappa_{mn}^{(4)} = \int_{-\pi/2}^{\pi/2} V_{2n/\beta}\left(\zeta_a\right) \mathrm{e}^{-2m\mathrm{i}\theta} d\theta \\
\varphi_{mn}^{(4)} = \int_{-\pi/2}^{\pi/2} P_{(2n+1)/\beta}\left(\zeta_a\right) \mathrm{e}^{-2m\mathrm{i}\theta} d\theta \\
\zeta_{mn}^{(4)} = \int_{-\pi/2}^{\pi/2} (-1)^n \varepsilon_n P_{2n/\beta}\left(\zeta_a\right) \cos 2n\alpha \mathrm{e}^{-2m\mathrm{i}\theta} d\theta
\end{cases}$$

$$\begin{cases}
\beta_{mn}^{(5)} = \int_{\pi/2}^{3\pi/2} Q_{(2n+1)/\beta}\left(\zeta_a\right) \mathrm{e}^{-(2m+1)\mathrm{i}\theta} d\theta \\
\lambda_{mn}^{(5)} = \int_{\pi/2}^{3\pi/2} Q_{2n/\beta}\left(\zeta_a\right) \mathrm{e}^{-(2m+1)\mathrm{i}\theta} d\theta \\
\kappa_{mn}^{(5)} = \int_{\pi/2}^{3\pi/2} U_{2n/\beta}\left(\zeta_a\right) \mathrm{e}^{-(2m+1)\mathrm{i}\theta} d\theta
\end{cases}$$

$$\begin{cases}
\beta_{mn}^{(6)} = \int_{0}^{2\pi} Q_{(2n+1)/\beta}\left(\zeta_b\right) \mathrm{e}^{-(2m+1)\mathrm{i}\theta} d\theta \\
\lambda_{mn}^{(6)} = \int_{0}^{2\pi} Q_{2n/\beta}\left(\zeta_b\right) \mathrm{e}^{-(2m+1)\mathrm{i}\theta} d\theta \\
\kappa_{mn}^{(6)} = \int_{0}^{2\pi} U_{2n/\beta}\left(\zeta_b\right) \mathrm{e}^{-(2m+1)\mathrm{i}\theta} d\theta
\end{cases}$$

$$
\begin{cases}
\beta_{mn}^{(7)} = \int_{-\pi/2}^{\pi/2} H_{(2n+1)/\beta}^{(1)}\left(k|\zeta_a|\right)\left[\left(\zeta_a/|\zeta_a|\right)^{(2n+1)/\beta} - \left(\zeta_a/|\zeta_a|\right)^{-(2n+1)/\beta}\right] \mathrm{e}^{-(2m+1)\mathrm{i}\theta} d\theta \\
\lambda_{mn}^{(7)} = \int_{-\pi/2}^{\pi/2} J_{(2n+1)/\beta}\left(k|\zeta_a|\right)\left[\left(\zeta_a/|\zeta_a|\right)^{(2n+1)/\beta} - \left(\zeta_a/|\zeta_a|\right)^{-(2n+1)/\beta}\right] \mathrm{e}^{-(2m+1)\mathrm{i}\theta} d\theta \\
\kappa_{mn}^{(7)} = \int_{-\pi/2}^{\pi/2} H_{(2n+1)/\beta}^{(1)}\left(k|\zeta_a|\right)\left[\left(\zeta_a/|\zeta|\right)^{(2n+1)/\beta} - \left(\zeta_a/|\zeta_a|\right)^{-(2n+1)/\beta}\right] \mathrm{e}^{-(2m+1)\mathrm{i}\theta} d\theta \\
\varphi_{mn}^{(7)} = \int_{-\pi/2}^{\pi/2} J_{2n/\beta}\left(k|\zeta_a|\right)\left[\left(\zeta_a/|\zeta_a|\right)^{2n/\beta} - \left(\zeta_a/|\zeta_a|\right)^{-2n/\beta}\right] \mathrm{e}^{-(2m+1)\mathrm{i}\theta} d\theta \\
\zeta_{mn}^{(7)} = \int_{-\pi/2}^{\pi/2} 2(-1)^n J_{(2n+1)/\beta}\left(k|\zeta_a|\right)\sin(2n+1)\,\alpha \\
\qquad \left[\left(\zeta_a/|\zeta_a|\right)^{(2n+1)/\beta} - \left(\zeta_a/|\zeta_a|\right)^{-(2n+1)/\beta}\right] \mathrm{e}^{-(2m+1)\mathrm{i}\theta} d\theta
\end{cases}
$$

$$
\begin{cases}
\beta_{mn}^{(8)} = \int_{-\pi/2}^{\pi/2} V_{(2n+1)/\beta}\left(\zeta_a\right) \mathrm{e}^{-(2m+1)\mathrm{i}\theta} d\theta \\
\lambda_{mn}^{(8)} = \int_{-\pi/2}^{\pi/2} Q_{(2n+1)/\beta}\left(\zeta_a\right) \mathrm{e}^{-(2m+1)\mathrm{i}\theta} d\theta \\
\kappa_{mn}^{(8)} = \int_{-\pi/2}^{\pi/2} U_{(2n+1)/\beta}\left(\zeta_a\right) \mathrm{e}^{-(2m+1)\mathrm{i}\theta} d\theta \\
\varphi_{mn}^{(8)} = \int_{-\pi/2}^{\pi/2} Q_{2n/\beta}\left(\zeta_a\right) \mathrm{e}^{-(2m+1)\mathrm{i}\theta} d\theta \\
\zeta_{mn}^{(8)} = \int_{-\pi/2}^{\pi/2} 2(-1)^n Q_{(2n+1)/\beta}\left(\zeta_a\right)\sin(2n+1)\,\alpha \mathrm{e}^{-(2m+1)\mathrm{i}\theta} d\theta
\end{cases}
$$

The model in this section contains a cylindrical cavity, thus its dynamic stress concentration under the incidence of SH wave is considered. Based on the stress field expression and the solved coefficient, the dynamic stress concentration factor (DSCF) around the cylindrical cavity can be expressed as:

$$
\tau_{\theta z}^{*} = \left| \tau_{\theta z}^{(1)} + \tau_{\theta z}^{(2)} / \tau_0 \right| \tag{4.36}
$$

where $\tau_0 = \mu k_0 w_0$.

4.2.5 Convergence analysis

Similarly, the solution method in this section is still based on the use of special functions and Fourier series expansion in the process of solving the equation to convert the equation into infinite algebraic equations. Therefore, it is necessary to truncate the number of infinite terms and conduct convergence analysis to obtain the number of finite terms for deriving the

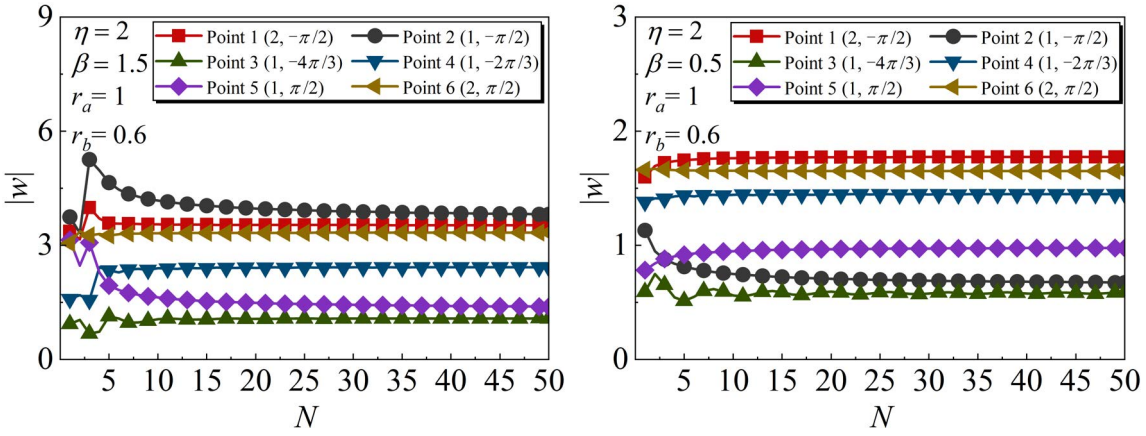

(a) $\beta = 1.5$ (b) $\beta = 0.5$

Fig. 4.17 Convergence analyses of displacement amplitudes at four typical positions with increasing N

unknown coefficient. The truncation term can not only satisfy the convergence requirements, but also save the calculation cost. According to the calculation model, six typical locations are selected to analyze and verify the convergence of free, scattering and standing wave field. In order to ensure the convergence requirements of all the calculation examples in this section, the dimensionless frequency $\eta = 2.0$, incident angle $\alpha = 90^\circ$, inhomogeneous parameters are set to 1.5 and 0.5 respectively, and the ratio of the radius of cylindrical cavity to the radius of the semi-cylindrical convex $r_b/r_a = 0.6$, and the truncation term $N = m = n$ is considered to establish the standard solution matrix. According to a large number of convergence calculations, as shown in Fig. 4.17, as $N = 10$ is taken, the results have converged. Therefore, in the subsequent calculation, the convergence of results can be guaranteed and the calculation time can be saved in $N = 15$.

4.2.6 Validation

Before analyzing the influence of various parameters on displacement amplitude and dynamic stress concentration coefficient, it is still need to verify the validation of the constructed standing wave and scattering wave fields in this section. This section shows the comparison of the results of two groups and two methods in homogeneous media, in Fig. 4.18. In order to ensure the function of the inhomogeneous parameter in the formula and better simulate the homogeneous medium, the inhomogeneous parameter $\beta = 0.99$ is taken. In these figures, the abscissa y/r_a is still used to represent the relative position of the semi-cylindrical convex and the horizontal plane, the position of the convex surface $[-1, 1]$, and the position of

the horizontal plane on both sides $[-3,-1)$ and $(1,3]$. Fig. 4.18 (a) demonstrates the comparison of the surface displacement amplitude under three incident angles when the dimensionless frequency $\eta = 1.25$ and the ratio of the radius between cylindrical cavity and semi-cylindrical convex is 0.2. Fig. 4.18 (b) is a comparison of surface displacement amplitude with dimensionless frequency $\eta = 1$ and the ratio of radius equals to 0.1, 0.2 and 0.5 respectively under horizontal incident. From the two comparison results that the calculation record in this section is in well agreement with the existed results, which can verify the validation of the structural wave field and the calculation method in this section. Fig. 4.19 gives two groups of dynamic stress concentration coefficient (DSCF) comparison. Fig. 4.19 (a) indicates the comparison between the calculated results and the existed results when the inhomogeneous parameter is 0.99. There is a well agreement with the known results. Fig. 4.19 (b) shows a group of inhomogeneous parameters approaching 1.0 and comparing with the existed results. The calculated results are close to the results when the inhomogeneous parameters are 1.0, and have a good consistency with the existed results. The validation of the method is verified by two sets of examples.

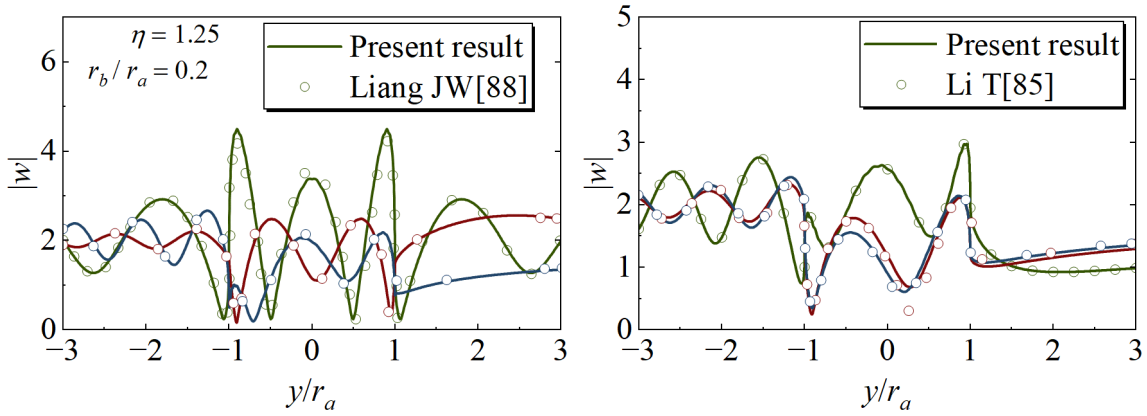

(a) $\eta = 1.25$ (b) $\eta = 1.0$

Fig. 4.18 Results of approximately homogeneous medium for comparison with the existed results

4.2.7 Numerical results and discussion

The model in this section has a cylindrical cavity, so the influence of the ratio of the radius between cavity and convex on the surface displacement amplitude under different inhomogeneous parameters is considered primary. Three kinds of incidence cases (horizontal incidence, oblique incidence and vertical incidence) are calculated under the dimensionless frequency is 1.0. The results are displayed in Figs. 4.20-4.22.

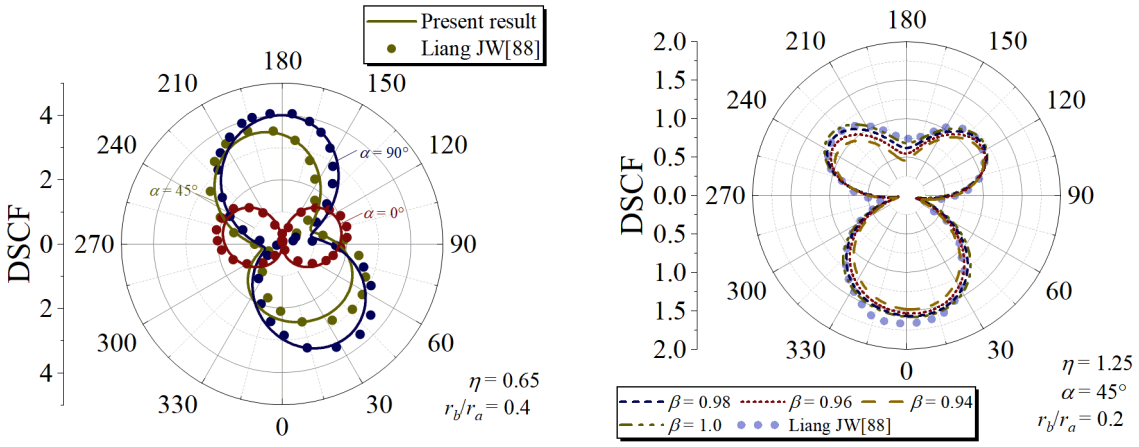

(a) $\eta = 0.625$ (b) $\eta = 1.25$

Fig. 4.19 Comparison of DSCF with existed results

According to the results of Fig. 4.20, under the same radius ratio, the surface displacement amplitude is decreased with the growth of the inhomogeneous parameter as a whole. With $r_b/r_a \leq 0.6$ and $\beta = 0.6$, the surface displacement amplitude at the junction of the convex and the plane ($y/r_a = \pm 1$) has a significant increase effect compared with other inhomogeneous parameters. Meanwhile, with the inhomogeneous parameters increasing, the vibration frequency of surface displacement amplitude rises and the amplitude descends. From the comparison of the radius ratio variation, it indicated that at the radius ratio is $r_b/r_a \leq 0.6$, the value of surface displacement amplitude varies slightly with the increase of radius ratio, while its vibration amplitude grows with the change of position, and the displacement amplitude raises with the increase of radius ratio at $y/r_a = 1$. At the radius ratio is 0.8, the maximum value of surface displacement amplitude advanced obviously at $y/r_a = 1$, and the effect of increasing the displacement amplitude is most obvious at the situation of $\beta = 0.8$. At this dimensionless frequency and horizontal incident, the maximum value of apparent displacement amplitude moves from the left junction point of the convex and horizontal junction to the right junction point with the ascender of radius ratio .

Under SH wave oblique incident, the influence of inhomogeneous parameters on surface displacement amplitude demonstrates different effects at the convex surface and horizontal boundary, as shown in Fig. 4.21. Still, if the radius ratio $r_b/r_a \leq 0.6$, the distribution characteristics of surface displacement amplitude is almost the same. At the semi-cylindrical convex, the surface displacement amplitude of $\beta \neq 1$ is larger than $\beta = 1$, and the displacement amplitude decreases at inhomogeneous parameter approaches to 1. However, the surface displacement on the horizontal plane on both sides is also increasing with β, while the vibration amplitude is inversely proportional to inhomogeneous parameters. When the radius

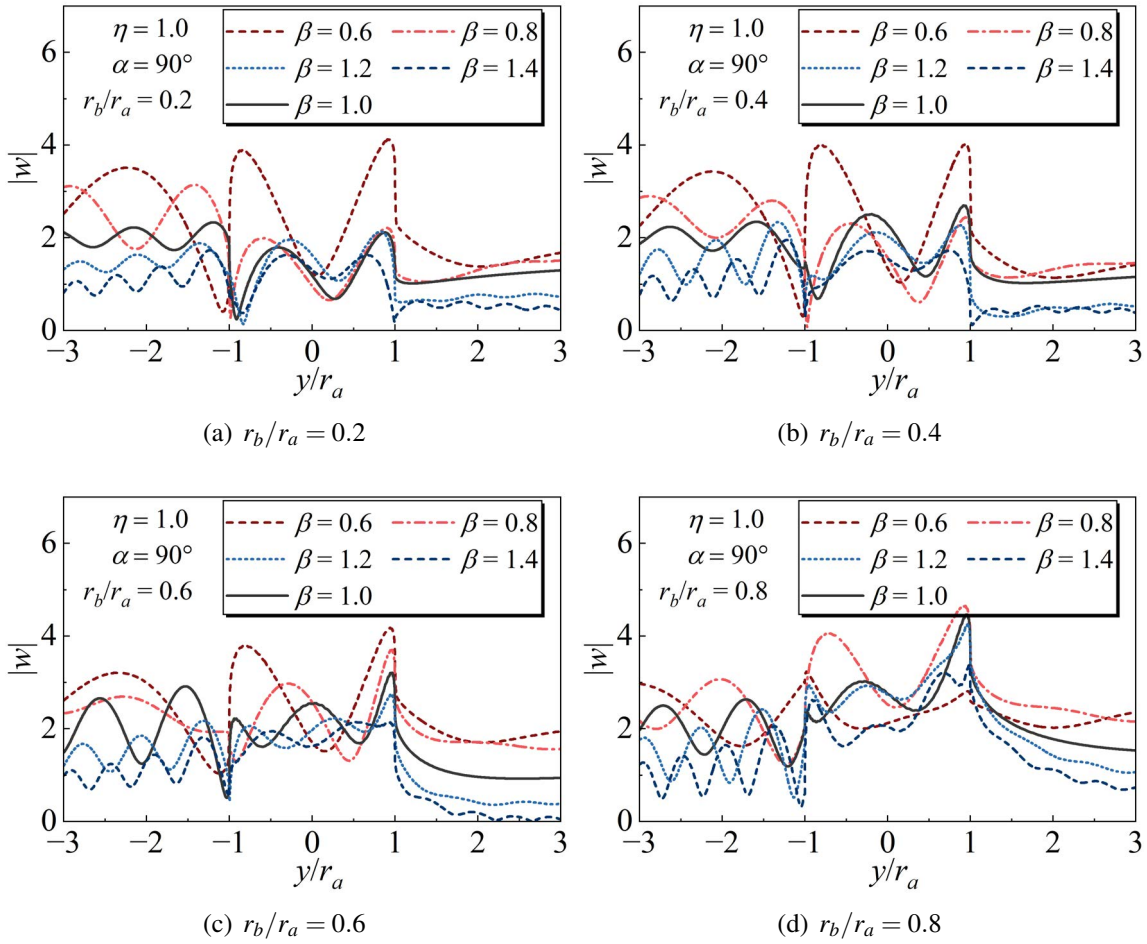

Fig. 4.20 Displacement amplitude distribution with inhomogeneous parameters under four groups of r_b/r_a at horizontal incident and dimensionless frequency is 1.0

ratio reaches to 0.8, the inhomogeneous parameter that has the greatest influence on the surface displacement amplitude of the convex boundary is 0.8. And at the same situation, the surface displacement amplitude on the horizontal plane is proportional to inhomogeneous parameter. At oblique incident, as $\beta < 1$, the surface displacement amplitude of the convex boundary is slightly greater than the displacement amplitude of the two sides plane. While $\beta > 1$, the displacement amplitude of the two sides of the plane is greater than the convex part with the increase of the radius ratio. In particular, from Fig. 4.21 (d), the displacement amplitude of the convex part and the horizontal plane on both sides almost keeps continuous variation under the inhomogeneous parameter is 1.4.

In vertical incident, the surface displacement amplitude with the ascender of inhomogeneous parameters then increases, especially on the two sides of the plane. While, the vibration frequency of displacement amplitude aggravates gradually with inhomogeneous parameters

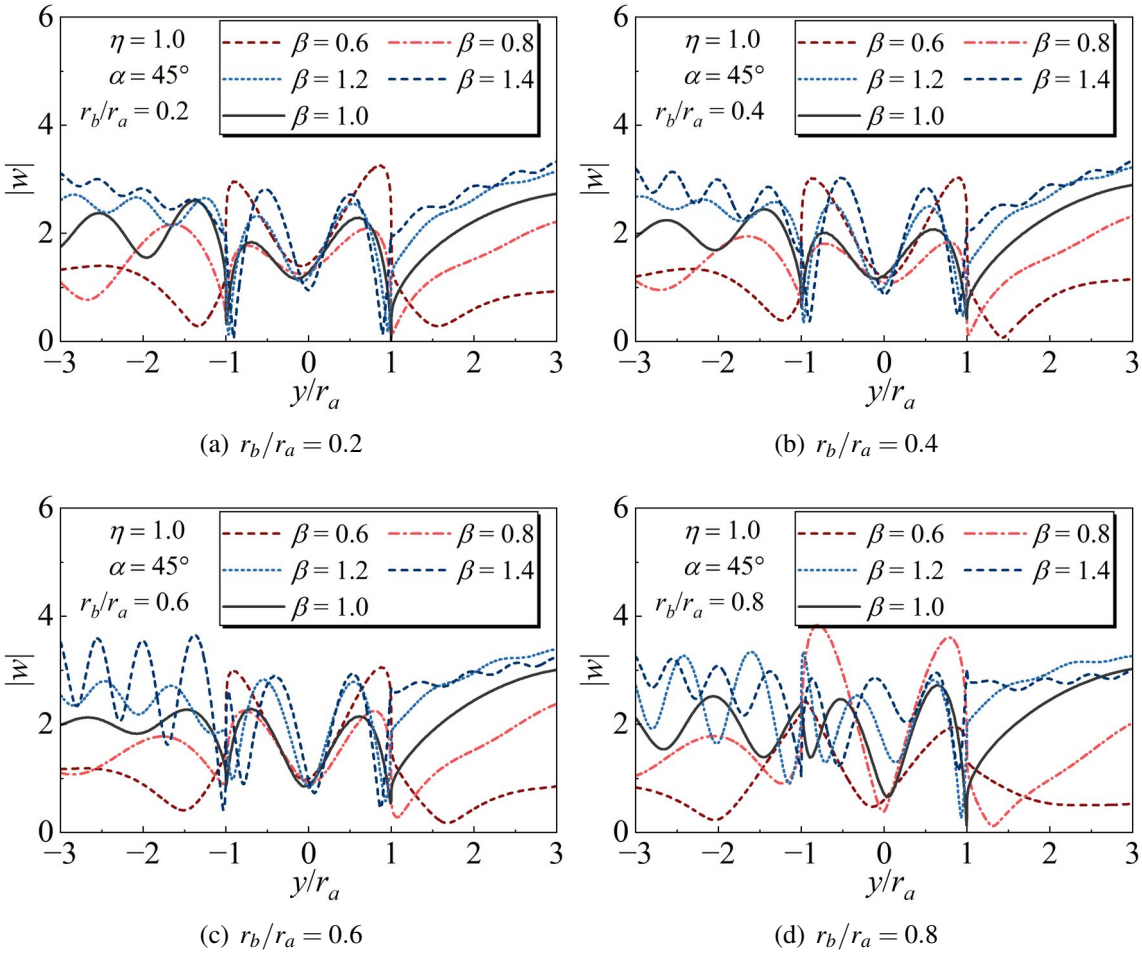

Fig. 4.21 Displacement amplitude distribution with inhomogeneous parameters under four groups of r_b/r_a at oblique incident and dimensionless frequency is 1.0

increasing. Especially at $\beta \neq 1$, the surface displacement amplitude distribution is almost the same on both sides of the plane. It can be observed that the distribution characteristic of surface displacement amplitude under various inhomogeneous parameters is basically the same when the radius ratio is 0.4 and 0.6. The displacement amplitude increases on both sides of the plane is advanced with the growth of inhomogeneous parameter. And the inhomogeneous parameter has a relatively obvious effect on the reduction of the displacement amplitude of the convex vertex to the surface when the inhomogeneous parameter is less than 1. When r_b/r_a is 0.2 and 0.8, the inhomogeneous parameter has a great influence on the surface displacement amplitude of the convex part, while the displacement amplitude of the convex vertex and the junction point on both sides have a great vibration. Based on the above three sets of incident examples, the amplitude of surface displacement is proportional to inhomogeneous parameters.

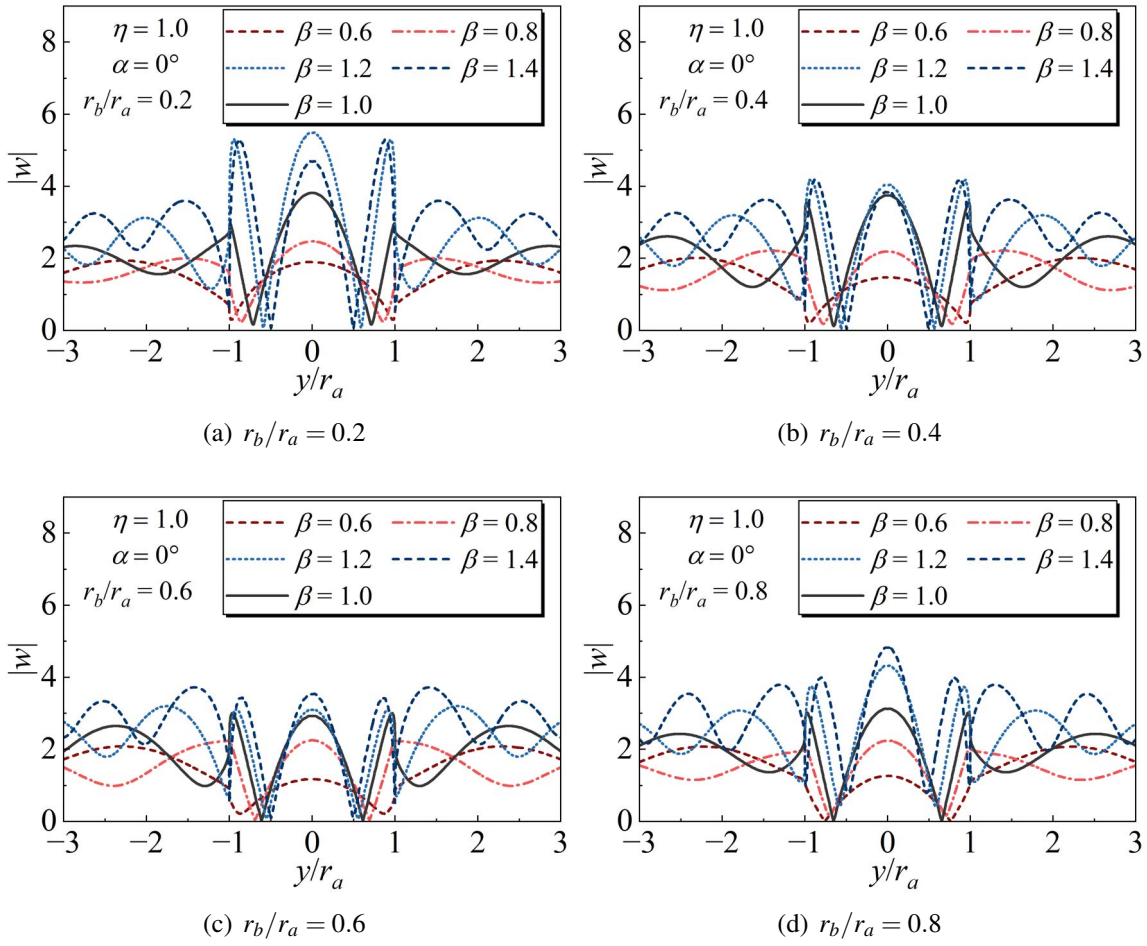

Fig. 4.22 Displacement amplitude distribution with inhomogeneous parameters under four groups of r_b/r_a at vertical incident and dimensionless frequency is 1.0

Then, the 3D surface displacement amplitude distribution with the dimensionless frequency various under the two groups of radius ratios is given as $\beta = 1.2, 0.8$. Figs. 4.23 (a) and (b) illustrate that under SH wave horizontal incident, the surface displacement amplitude under the two radius ratios declines gradually with the dimensionless frequency grows on the whole, and the displacement amplitude under the two radius ratios reaches the maximum value and appears at the convex position at $\eta = 1$. Under oblique incident, as shown in Figs. 4.23 (c) and (d), the radius ratio reaches to 0.4, the position of the maximum displacement amplitude gradually moves from the convex vertex to the junction with the dimensionless frequency rises, and the maximum displacement amplitude has a trend of increasing gradually. While the radius ratio is 0.8, the maximum displacement amplitude appears near $\eta = 0.5$ and declines with the dimensionless frequency increasing. As $\beta = 1.2$, and the radius ratio is 0.4, the smaller dimensionless frequency has a greater impact on the displacement amplitude

under the incident is horizontal, and the larger dimensionless frequency has a greater impact under the incident is vertical. It should be noted that at the radius ratio reaches to 0.4, the amplitude of surface displacement will suddenly expands when the dimensionless frequency is around 1.6. At the radius ratio reaches to 0.8, both horizontal and vertical incident should pay attention to the smaller dimensionless frequency. Moreover, the increase of radius ratio has a greater amplification effect on the amplitude of surface displacement.

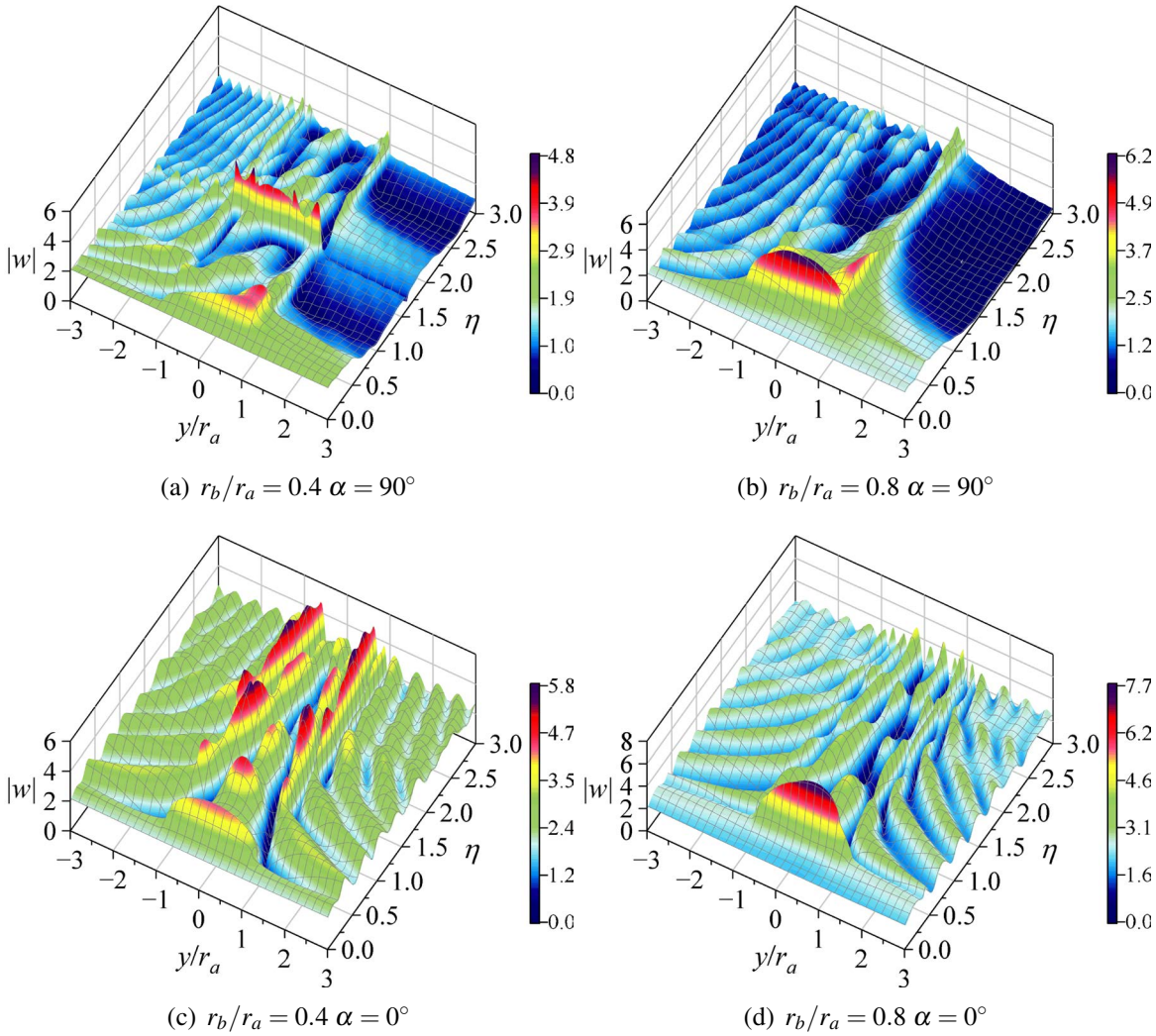

Fig. 4.23 3D displacement of inhomogeneous parameter $\beta = 1.2$

Similar, the 3D displacement distribution under the inhomogeneous parameter set as 0.8 is shown in Fig. 4.24. Figs. 4.24 (a) and (b) demonstrates SH wave horizontal incident the surface displacement under the two groups of radius ratios is proportional to dimensionless frequency, and the effect on left plane displacement increasing is obvious. The surface displacement still has a sudden altering underv this radius ratio when the dimensionless

frequency is near 2. Consider vertical incidence, as shown in Figs. 4.24 (c) and (d), the surface displacement is similar to that of $\beta = 1.2$. The maximum displacement is also proportional to dimensionless frequency, when the radius is relatively small. While, the maximum displacement amplitude appears at the lower frequency, at radius is relatively large. Moreover, the amplification effect of the radius ratio increasing on the displacement amplitude at $\beta = 0.8$ is weaker than $\beta = 1.2$.

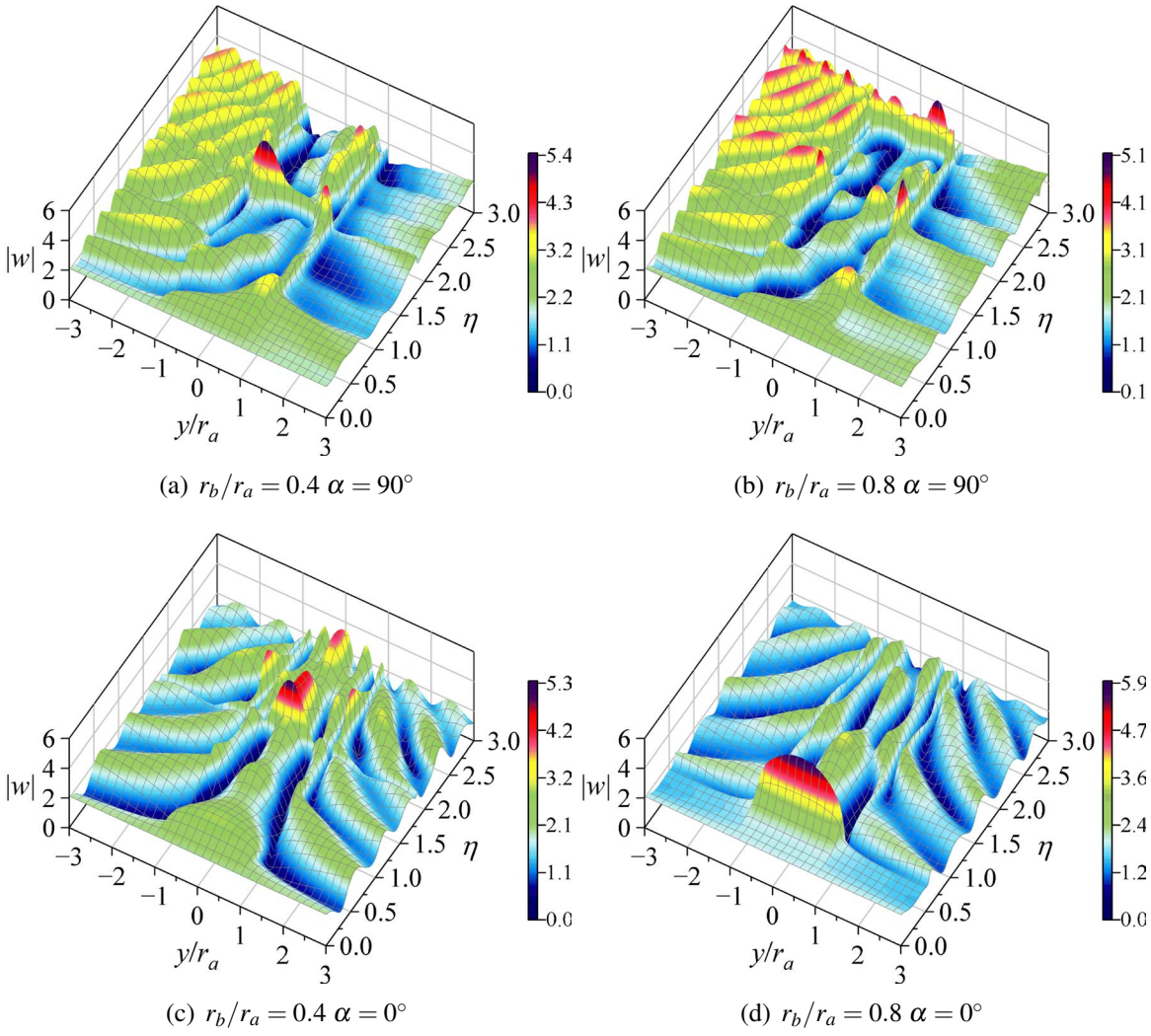

Fig. 4.24 3D displacement of inhomogeneous parameter $\beta = 0.8$

In order to explore the influence of semi-cylindrical convex with a cylindrical cavity on the surface displacement amplitude in inhomogeneous media, six typical observation points 1 $(2, -\pi/2)$, 2 $(1, -\pi/2)$, 3 $(1, -5\pi/6)$, 4 $(1,\ 5\pi/6)$, 5 $(1,\ \pi/2)$, 6 $(2,\ \pi/2)$ and two radius ratios $r_b/r_a = 0.4, 0.8$ were selected for calculation under the horizontal incidence conditions with inhomogeneous parameters of 1.2, 1.0 and 0.8 respectively. Figs. 4.25 (a), (c) and (e)

show the radius ratio is 0.4, it can be observed that under three inhomogeneous parameters, six observation points have a sudden growth in the amplification effect of surface displacement within the range of 1.5-2, especially point 3. As $\beta = 0.8, 1.2$, the amplification effect of point 3 and point 4 at the abrupt change of displacement amplitude declines compared with 1.0. The displacement amplitude of each point is inversly proportional to dimensionless frequency on the whole under $\beta > 1$. The displacement amplitude is proportional to dimensionless frequency, while $\beta < 1$. In Figs. 4.25 (b), (d) and (f), the amplification effect of points 3 and 4 under three inhomogeneous parameters on the displacement amplitude grows suddenly in the range where the dimensionless frequency is 0.5. With the inhomogeneous parameter decreasing and the dimensionless frequency increasing, the amplification effect of each point on the displacement amplitude rises, especially at the observation point 1. At $\beta \geq 1$ the displacement of point 1 has been vibrating around 2, the maximum amplification effect reaches 1.25 times. At $\beta < 1$ the displacement of point 1 is gradually increasing and reaches 1.75 times at most. Moreover, the displacement amplification at the four observation points dropped rapidly to 0.5 times after reaching the maximum of 2 times at $\beta = 1.2$, reached 1.75 times at $\beta = 1$, and then still showed a rapid decline to about 0.3 times, while at $\beta = 0.8$, the amplification gradually increased to 1.5 times and then tended to stabilize at around 1.5 times.

Further explore the amplification effect of each point on the surface displacement under different incidence angles, setting the vertical incident for calculation. The numerical results are shown in Fig. 4.26. Figs. 4.26 (a), (c) and (e) indicate the ratio of radius is 0.4, the amplification effect of each observation point on the surface displacement gradually decreases with the reduction of the inhomogeneous parameters. Moreover, the abrupt change of surface displacement amplitude can still be observed in the range of 1.5-2 in the dimensionless frequency. This phenomenon is mainly manifested in points 3 and 4, as the observation points of the convex surface. Meanwhile, this phenomenon is reduced with the ascender of inhomogeneous parameters. Under the action of three inhomogeneous parameters, the displacement amplitude distribution of points 1, 2, 5 and 6 is similar. The amplification effect of the four points on the displacement amplitude decreases slightly with the decrease of the inhomogeneous parameter. When the $\beta = 1.2$, the amplification effect of the four observation points on the displacement amplitude reaches 2 times and decreases gradually with the dimensionless frequency growing. However, when the inhomogeneous parameters set as 1.0 and 0.8, the amplification effect of the four observation points is 1.5 times the maximum, and the vibration mode is displayed at 1.5 times. At the radius ratio is 0.8, in the case of vertical incident, the displacement amplitude still rises sharply at points 3 and 4 under dimensionless frequency is 0.5, and this sudden advanced with the growth of inhomogeneous

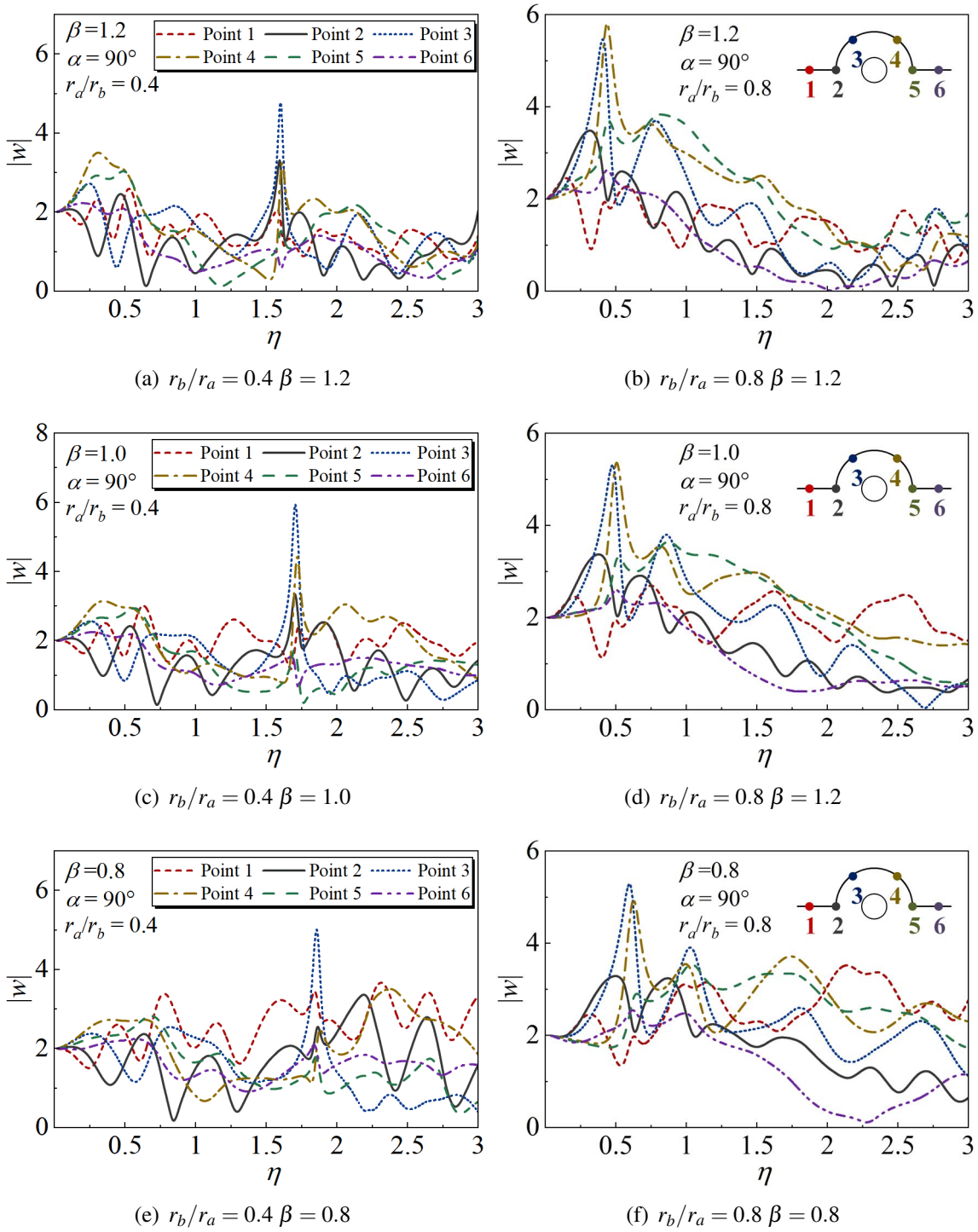

(a) $r_b/r_a = 0.4\ \beta = 1.2$ (b) $r_b/r_a = 0.8\ \beta = 1.2$

(c) $r_b/r_a = 0.4\ \beta = 1.0$ (d) $r_b/r_a = 0.8\ \beta = 1.2$

(e) $r_b/r_a = 0.4\ \beta = 0.8$ (f) $r_b/r_a = 0.8\ \beta = 0.8$

Fig. 4.25 Six selection observation points displacement amplitude with dimensionless frequency varies under the radius ratio r_b/r_a=0.4, 0.8 and horizontal incident

parameters. The amplification effect of the other four points on the displacement amplitude still shows an proportional trend to inhomogeneous parameters, and the vibration frequency has a slight proportional trend. Moreover, it can be seen that when the radius ratio is 0.8, the displacement amplitude amplification effect at the abrupt change is significantly greater than when the radius ratio is 0.4.

Continue to explore the influence of semi-cylindrical convex with cylindrical cavity on the internal displacement amplitude distribution in inhomogeneous media. Two typical radius ratios and incident angles are calculated under the action of three inhomogeneous parameters. The results of internal displacement amplitude are shown in Figs. 4.27-4.29. Fig. 4.27 illustrates the distribution of internal displacement under horizontal and vertical incident when the inhomogeneous parameter is 1.2 and the radius ratio is 0.4 and 0.8, respectively, under dimensionless frequency is 2.0. Under horizontal incident , the displacement below the cylindrical cavity is larger at situation of the radius ratio is 0.8 than 0.4, and the distribution area of the larger displacement is also significantly increased. However, the displacement amplitude at the right side of the cylindrical cavity and near the right plane has significantly decreased. In the case of vertical incident, as shown in Figs. 4.27 (c) and (d), the displacement amplitude under the cylindrical cavity with a large radius is significantly larger than that with a small radius, and a strip-shaped area with an increased displacement amplitude appears directly below the cylindrical cavity with a large radius. The vibration of displacement amplitude around the cylindrical cavity and the convex is intensified. In the case of vertical incident, the maximum displacement amplitude at the radius ratio of 0.4 is greater than that at the radius ratio of 0.8, while in the case of horizontal incident, it is greater at the radius ratio of 0.8.

The internal displacement amplitude distribution under the condition of $\beta = 1.0$ is calculated, as shown in Fig. 4.28. From the figure under horizontal incident, there is still a larger area of displacement amplitude at the lower part of the radius ratio of 0.8 compared with that at the radius ratio of 0.4, and the displacement amplitude is significantly reduced at the right plane and its lower part. Meanwhile, there is a certain weakening effect on the displacement amplitude at the lower left part of the cylindrical cavity. Compared with the calculation results that only have semi-cylindrical convex on the surface, given in Fig. 4.13, the existence of a cylindrical cavity makes the internal displacement amplitude distribution offset to a certain extent, and the area of offset with ascender of the radius ratio then increase. At this time, the maximum displacement amplitude occurs when the radius ratio is 0.8. The maximum displacement amplitude occurs at the radius ratio of 0.4 at vertical incident. As the radius ratio is 0.8, the internal displacement amplitude is smaller than that when the radius ratio is 0.4. However, directly below the cylindrical cavity, the displacement amplitude is

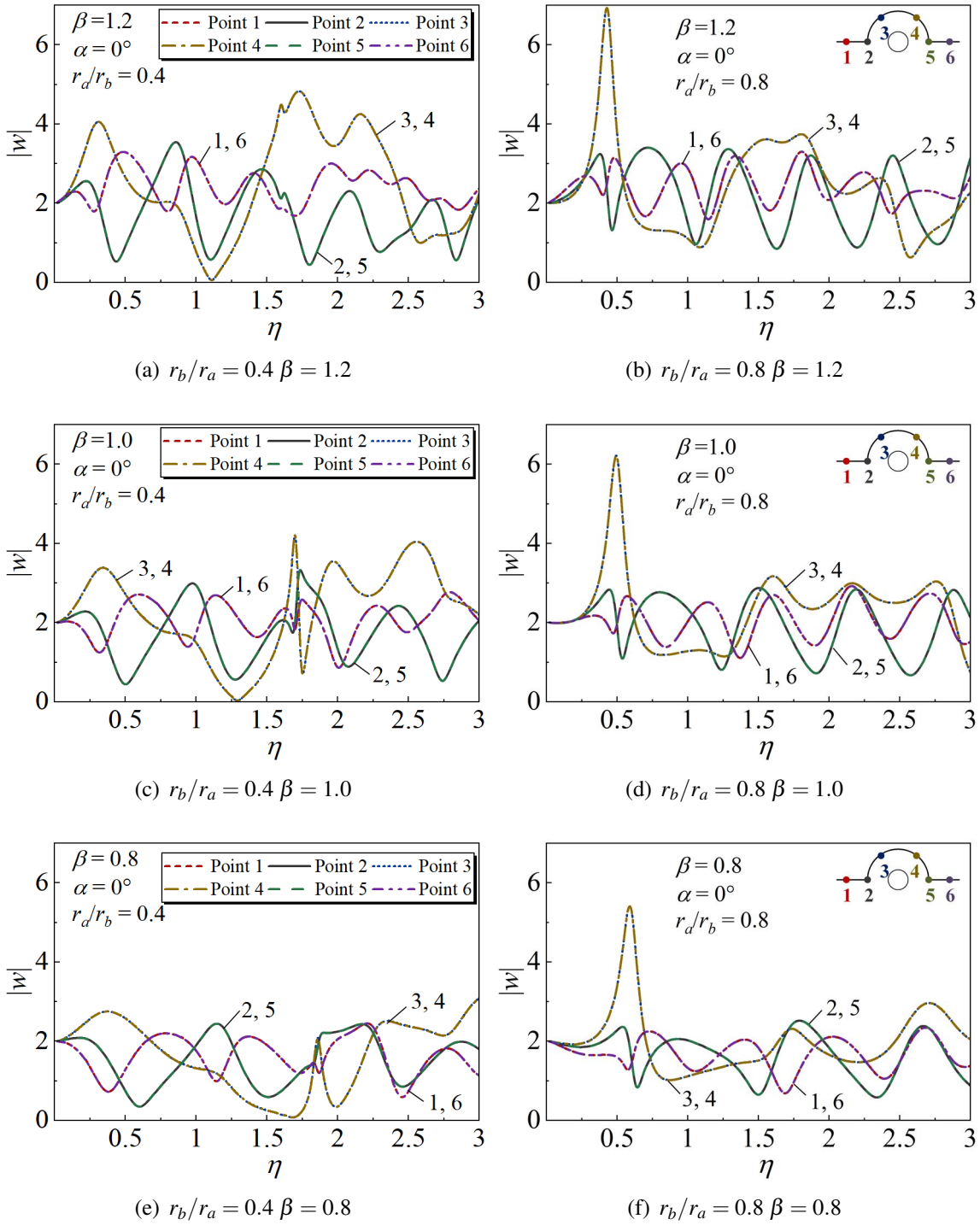

Fig. 4.26 Six selection observation points displacement amplitude with dimensionless frequency varies under the radius ratio r_b/r_a=0.4, 0.8 and vertical incident

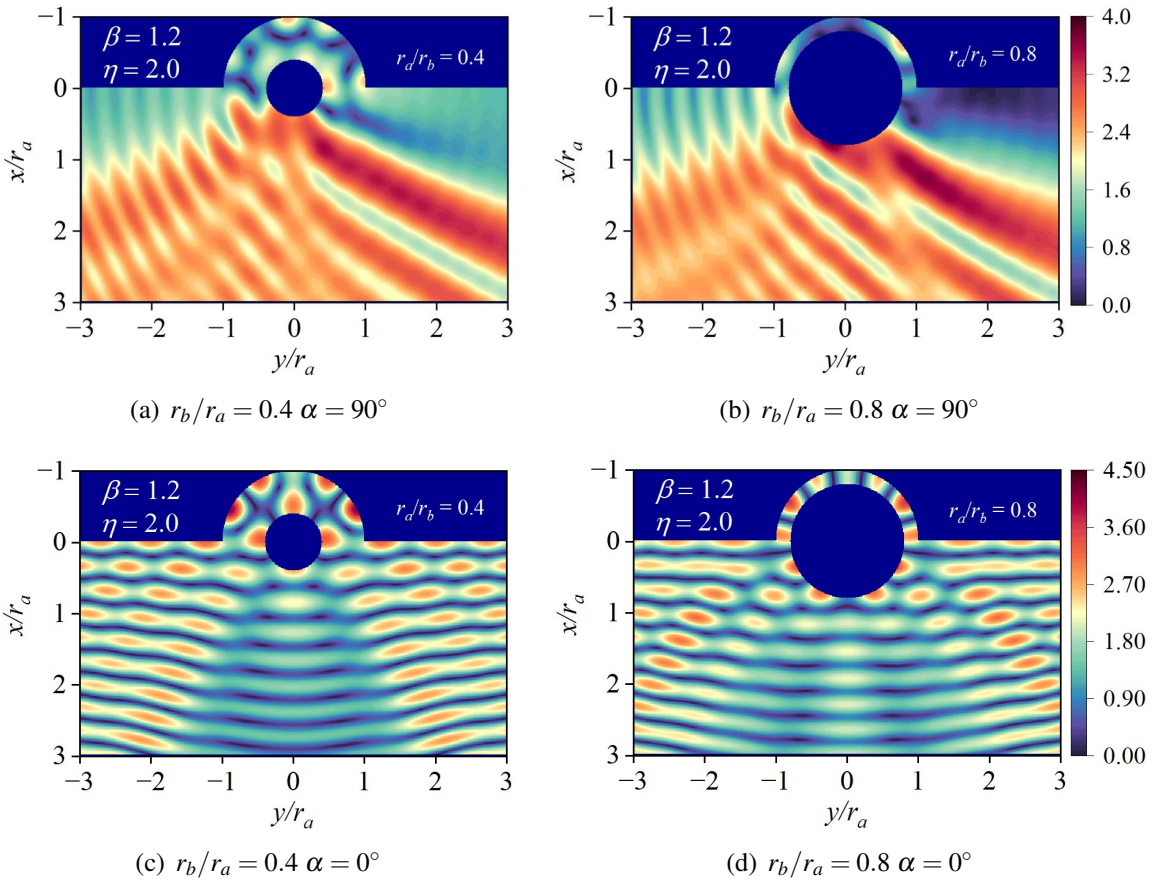

(a) $r_b/r_a = 0.4$ $\alpha = 90°$ (b) $r_b/r_a = 0.8$ $\alpha = 90°$

(c) $r_b/r_a = 0.4$ $\alpha = 0°$ (d) $r_b/r_a = 0.8$ $\alpha = 0°$

Fig. 4.27 Internal displacement amplitude of inhomogeneous parameter $\beta = 1.2$

still a larger area with a radius ratio of 0.4 when the radius ratio is 0.8. It can be seen that the displacement amplitude of vertical incidence is significantly higher than that of horizontal incident.

Consequently, the inhomogeneous parameter is less than 1 is considered, as shown in Fig. 4.29. Similar to the above two sets of numerical examples, in the case of horizontal incident, the displacement amplitude distribution of the two sets of radius ratio is compared. The lower part of the cylindrical cavity shows a larger value area, and the right horizontal surface and its lower part show a distribution trend of decreasing displacement amplitude, as the radius ratio becomes to 0.8. Comparing with the radius ratio is 0.4, as the value reaches to 0.8, the displacement amplitude under the cylindrical cavity increases obviously, and the maximum displacement amplitude still occurs.

Through the comparison of three calculation groups results, the distribution frequency of internal displacement amplitude is advanced with the growth of inhomogeneous parameter. The maximum displacement amplitude region appears when the radius ratio is 0.8, and the

larger radius ratio has a significant weakening effect on the displacement amplitude near the right plane under horizontal incident. However, in the case of vertical incident, it occurs when the radius ratio is 0.4, and there is a large displacement amplitude distribution zone directly below the cylindrical cavity with a large radius ratio, and the value of this displacement amplitude zone will be inversly proportional to inhomogeneous parameter.

Based on the cylindrical cavity in the model, the dynamic stress concentration factor (DSCF) around the cylindrical cavity under different inhomogeneous parameters is calculated in this part. Figs. 4.30 and 4.31 present the distribution of DSCF around the cylindrical cavity when the dimensionless frequency is 1.0 and 2.0 respectively. The parameters are set to be inhomogeneous, β taking 0.6, 0.8, 1.0, 1.2 and 1.4. The incidence angle α is horizontal incident, 45° oblique incident and vertical incident, and the radius ratio r_a/r_b is 0.4 and 0.8 respectively. As can be observed from Fig. 4.30, the DSCF is proportional to inhomogeneous parameters, especially in large radius. Under horizontal incident, the larger values of the two groups of radius ratio DSCF appear near 0° (the bottom position of the cylindrical cavity) and 145° (the upper right position of the cylindrical cavity). Compared with the calculated results of the radius ratio is 0.4, the DSCF at the radius ratio of 0.8 is significantly increased. In oblique incident, the displacement of the larger value changes to 120° and 240° at $r_a/r_b = 0.4$, while the larger value gradually moves from 270° to 60° at $r_a/r_b = 0.8$ with inhomogeneous parameter increasing. Compared with horizontal incident, inhomogeneous parameters variation under oblique incident has greater impact on DSCF. In contrast, in vertical incident, the result are presented in Figs. 4.30 (e) and (f), the maximum DSCF value appears at $\beta = 1.0$ when the radius is relatively small. The DSCF distribution presents a horizontal and vertical symmetrical distribution. The maximum DSCF value gradually moves from the upper half to the lower half of the cylindrical cavity, with the inhomogeneous parameter increasing. As the radius is relatively large, the maximum value of DSCF appears at 150° and 210°. DSCF is symmetrical in the vertical direction, and the maximum value of DSCF moves from the lower half of the cylindrical cavity to the upper part of the cylindrical cavity with inhomogeneous parameter growing.

The DSCF distribution around the cylindrical cavity becomes more complex at $\eta = 2.0$, especially when the radius is relatively large, as displayed in Fig. 4.31. The maximum value of DSCF appears at 0° under horizontal incident and radius ratio is 0.4, and if the $\beta = 1.0$ DSCF is almost symmetrically distributed along the horizontal. While the radius ratio is 0.8, the maximum appears at 120° if $\beta < 1$, otherwise appears at 0°. In the case of oblique incident, when the radius ratio is 0.4 and $\beta \leq 1.0$, the maximum value of DSCF appears in the range of 30° to 60°, while if $\beta > 1$, it occurs in the range of 240°. And this phenomenon is the opposite when the radius ratio is 0.8. At the situation of radius ratio is 0.8

and $\beta \leq 1.0$, the maximum value of DSCF appears between 210° and 240°, while at $\beta > 1$ it appears between 30° and 60°. Under vertical incident and two radius ratios, the maximum value of DSCF is concentrated in the upper half of the cylindrical cavity, and the maximum value of DSCF tends to growth with inhomogeneous parameter. Compared with that if the dimensionless frequency is 1.0, the increase of dimensionless frequency has little effect on the distribution of DSCF when the radius is smaller. When the radius is large, the change of dimensionless frequency has a great impact on the DSCF distribution. With the incident angle from horizontal to vertical, the DSCF extreme points gradually rises.

4.3 Summary

Based on the complex function and auxiliary function method, this chapter investigated the dynamic response of surface semi-cylindrical convex and semi-cylindrical convex with cylindrical cavity in density radial inhomogeneous media under SH wave incident. The model is divided into regions by region matching technique (RMT). With the help of the solution of the control equation in the density inhomogeneous media in Chapter 2, the wave field expressions in the sub-regions are constructed, and the analytical solutions of the displacement and stress fields are given by using the boundary conditions at the auxiliary boundary and the free boundary. By comparing with the existed results and analyzing the convergence, the validity of the wave field expression in this chapter is verified. Furthermore, the effects of different parameters on the displacement field on the surface of the media, the displacement field inside the media and the dynamic stress concentration distribution around the cylindrical cavity are discussed. Meanwhile, compare the calculated results of the surface depression boundary with the results of surface concave boundary, and analyze the influence of different surface boundary on the dynamic response under SH wave incident.

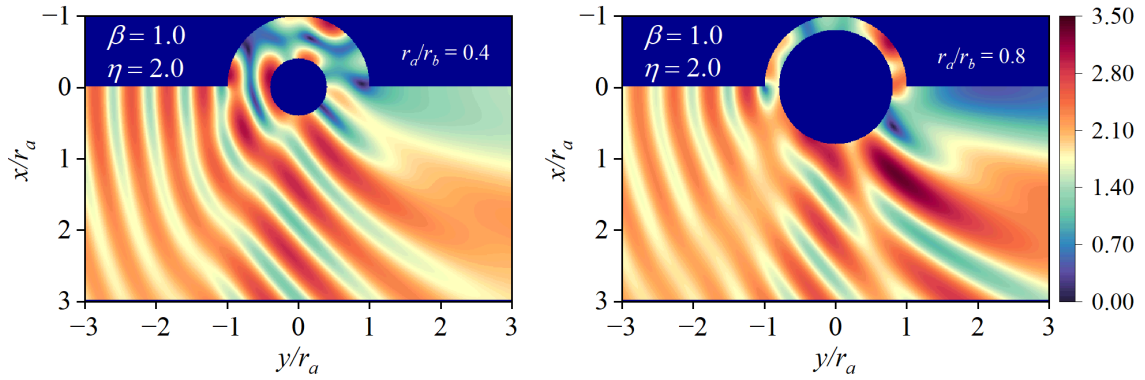

(a) $r_b/r_a = 0.4$ $\alpha = 90°$

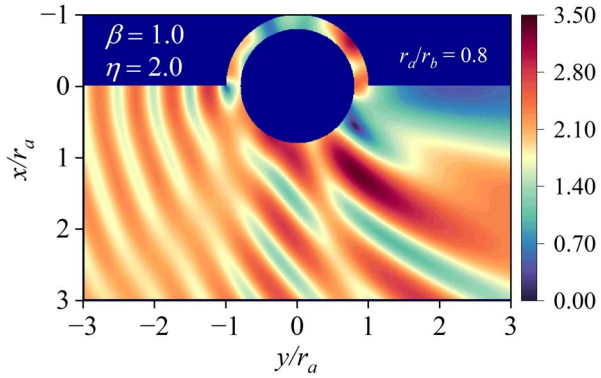

(b) $r_b/r_a = 0.8$ $\alpha = 90°$

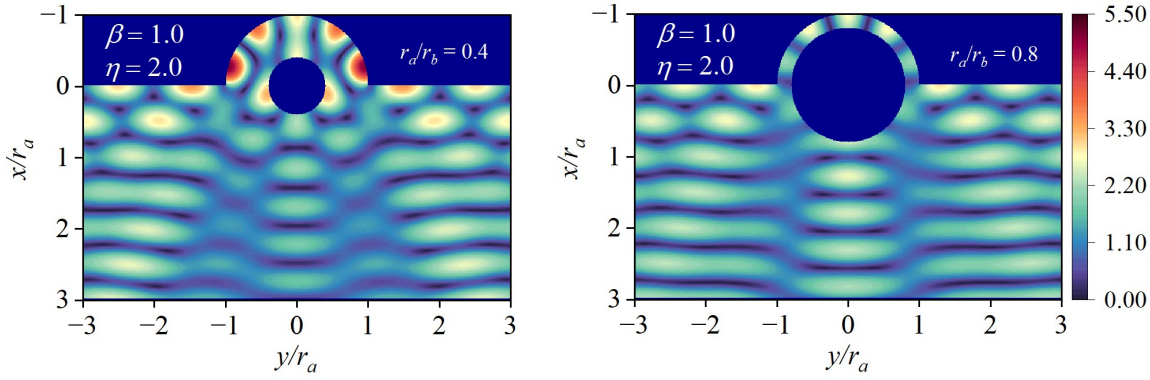

(c) $r_b/r_a = 0.4$ $\alpha = 0°$

(d) $r_b/r_a = 0.8$ $\alpha = 0°$

Fig. 4.28 Internal displacement amplitude of inhomogeneous parameter $\beta = 1.0$

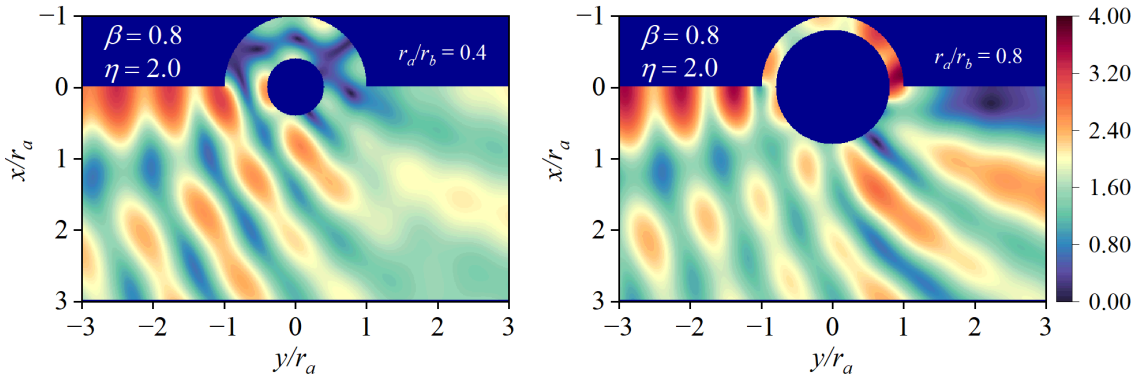

(a) $r_b/r_a = 0.4$ $\alpha = 90°$

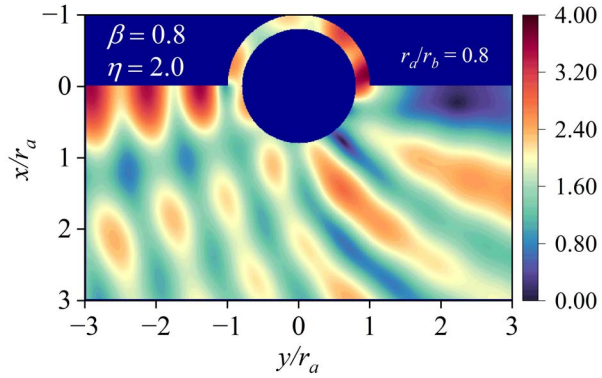

(b) $r_b/r_a = 0.8$ $\alpha = 90°$

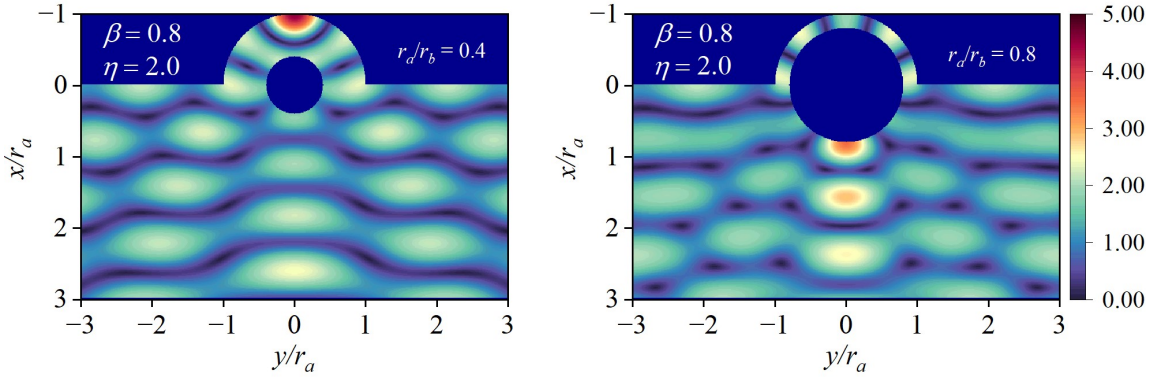

(c) $r_b/r_a = 0.4$ $\alpha = 0°$

(d) $r_b/r_a = 0.8$ $\alpha = 0°$

Fig. 4.29 Internal displacement amplitude of inhomogeneous parameter $\beta = 0.8$

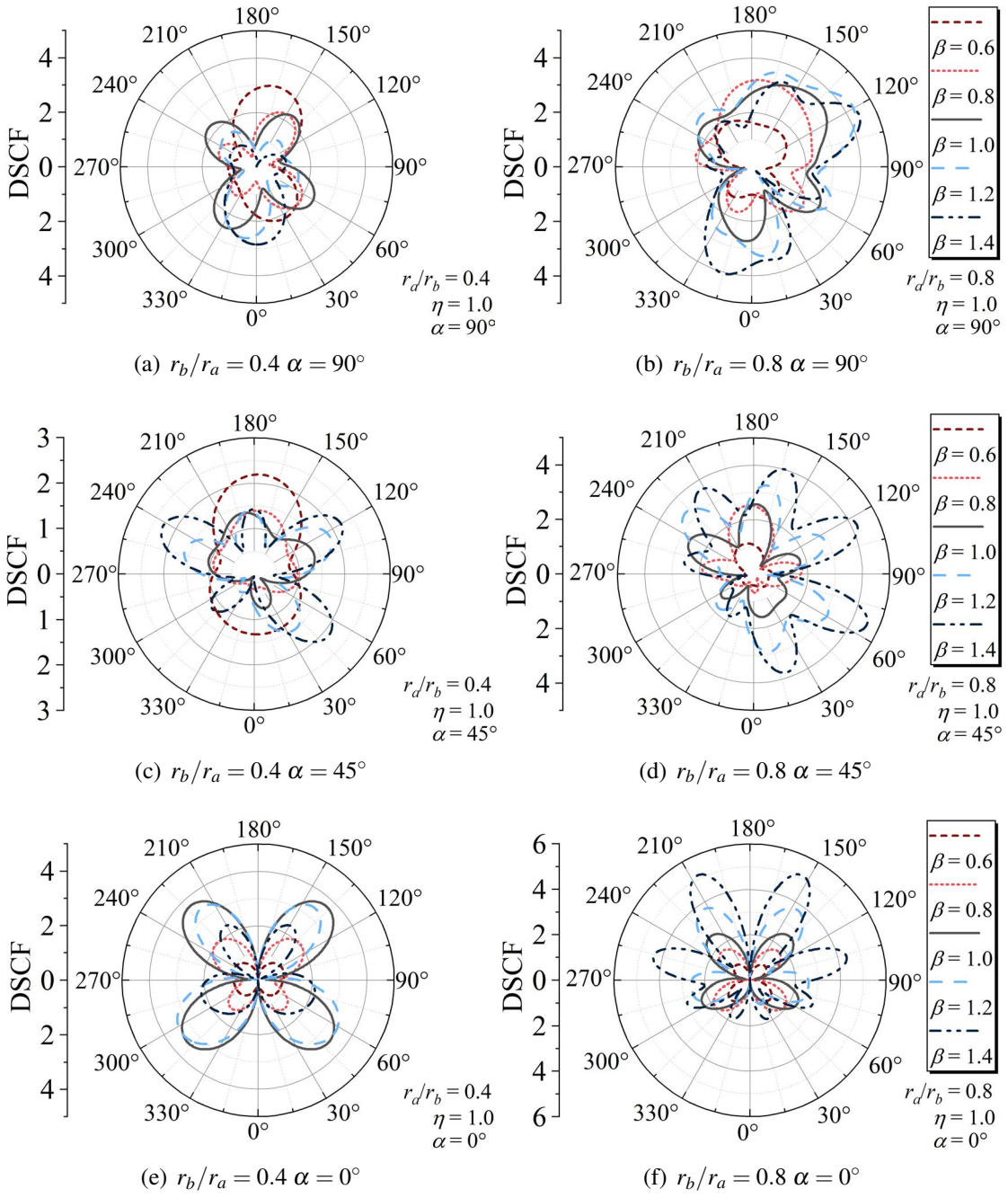

(a) $r_b/r_a = 0.4\ \alpha = 90°$ (b) $r_b/r_a = 0.8\ \alpha = 90°$

(c) $r_b/r_a = 0.4\ \alpha = 45°$ (d) $r_b/r_a = 0.8\ \alpha = 45°$

(e) $r_b/r_a = 0.4\ \alpha = 0°$ (f) $r_b/r_a = 0.8\ \alpha = 0°$

Fig. 4.30 Distribution of DSCF around the circular cavity with different inhomogeneous parameter under $r_a/r_b = 0.4, 0.8$ respectively $\eta = 1$

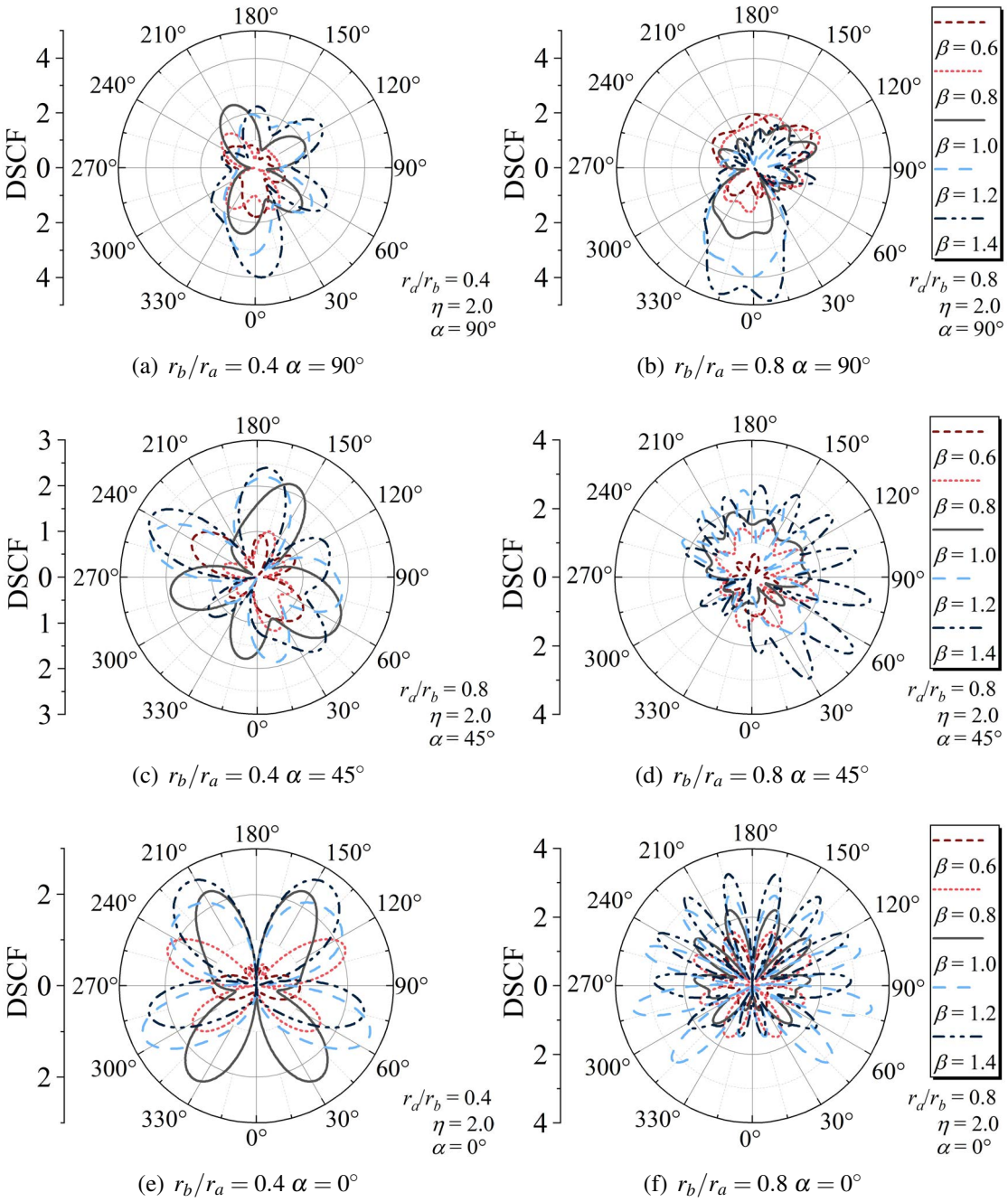

(a) $r_b/r_a = 0.4\ \alpha = 90°$ (b) $r_b/r_a = 0.8\ \alpha = 90°$

(c) $r_b/r_a = 0.4\ \alpha = 45°$ (d) $r_b/r_a = 0.8\ \alpha = 45°$

(e) $r_b/r_a = 0.4\ \alpha = 0°$ (f) $r_b/r_a = 0.8\ \alpha = 0°$

Fig. 4.31 Distribution of DSCF around the circular cavity with different inhomogeneous parameter under $r_a/r_b = 0.4, 0.8$ respectively $\eta = 2$

Chapter 5

Dynamic response of inhomogeneous wedge space under SH wave incident

The propagation characteristics of elastic waves in inhomogeneous media can be applied to nondestructive testing, wave control and composite material performance research, et al. Meanwhile, the progress of composite production technology makes it possible to design and produce composite materials specific elastic wave propagation characteristics . Therefore, the propagation characteristics of elastic waves in complex media is still a hot topic. At present, the researches on the analytical solutions of the wave problem in inhomogeneous media have explored the infinite space, semi-infinite space and right-angle space, but the researches on the wave problem in the wedge space are less. The change of wedge vertex angle can flexibly simulate various regional shapes. Moreover, according to the research, the boundary has a significant impact on the propagation of elastic waves, so it is necessary to discuss the characteristics of elastic wave propagation in the inhomogeneous wedge space under arbitrary vertex angle. Therefore, this chapter demonstrates the dynamic response of SH waves in inhomogeneous wedge space.

5.1 SH wave propagation in wedge space inhomogeneous media

This section mainly gives the research process of the propagation characteristics of SH wave in wedge space inhomogeneous media. This model is relatively simple because it only contains inhomogeneous wedge space. As the basis for other problems in the wedge space, it can provide a basis for the subsequent more complex models.

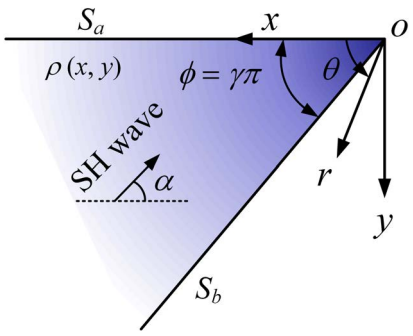

Fig. 5.1 Model of inhomogeneous wedge space under SH wave incident

5.1.1 Model and wave equation

Model of inhomogeneous wedge space with radial density variation under SH wave incidence is shown in Fig. 5.1. The coordinate origin o is set at the wedge vertex. Setting the coordinate origin at the wedge vertex can reduce the stress singularity when the top angle is too large. The x-axis is horizontally to the left, the y-axis is vertically downward, and the wedge vertex angle is $\phi = \gamma\pi\,(0 < \gamma \leq 2)$. S_a and S_b are the two boundaries of the wedge space. The wedge vertex angle varying can simulate the sharp angle wedge to the infinite space. SH wave is incident at an angle of α from the horizontal direction. In order to show the contrast relationship between the incident wave length and the model size, and to dimensionless the parameters in the subsequent calculation example, select the reference point A $(a,0)$ in the positive direction of the x-axis and its distance from the origin is a. This chapter still mainly considers the influence of variable wave velocity on the propagation characteristics of SH wave in inhomogeneous wedge space. Therefore, in the medium parameter setting, only the media density is set as a function to ensure the condition of variable wave velocity, and its form is still the form used in the previous chapter

$$\rho\,(r,\theta) = \rho_0 \beta^2 r^{2(\beta-1)}, \beta > 0 \tag{5.1}$$

where, ρ_0 is the reference density, β is the inhomogeneous parameter, and when β is 1, it is the case of homogeneous media. The corresponding wave number expression can be obtained by substituting the medium density equation into Eq. (2.34). According to the solution process in Section 3.1.2, the wave equation that can be directly used for solution can be obtained

$$\frac{\partial^2 w}{\partial \zeta \partial \bar{\zeta}} + \frac{1}{4} k_0^2 w = 0 \tag{5.2}$$

5.1.2 Boundary condition and wave field expressions

In this model, after SH wave incident, it will cause reflected waves at the boundary S_a and S_b, that is, there is only free wave field $w^{(f)}$ in the wedge space. The free wave field should satisfy the boundary condition of free circumferential stress at the two boundaries, which can be expressed as

$$\tau_{\theta z} = \mathrm{i}\beta\mu\left(\frac{\partial w}{\partial \zeta}z^{\beta-1}e^{\mathrm{i}\theta} - \frac{\partial w}{\partial \bar{\zeta}}\bar{z}^{\beta-1}e^{-\mathrm{i}\theta}\right) = 0,\ \theta = 0, \theta = \gamma\pi \tag{5.3}$$

Based on the above boundary conditions, we assume that the form of free wave field is

$$w^{(f)} = \sum_{n=0}^{\infty} F_n(\alpha) R_n(|\zeta|)\left[\left(\frac{\zeta}{|\zeta|}\right)^{n\gamma/\beta} + \left(\frac{\zeta}{|\zeta|}\right)^{-n\gamma/\beta}\right] \tag{5.4}$$

where, $F_n(\alpha)$ can be written as

$$F_n(\alpha) = \frac{\varepsilon_n}{\gamma\beta\pi}\cos(n\gamma\beta\alpha) \tag{5.5}$$

Substitute Eqs. (5.4) and (5.5) into the control Eq. (5.2)

$$\begin{aligned}\sum_{n=0}^{\infty}\tfrac{\varepsilon_n}{\gamma\beta\pi}\cos(n\gamma\beta\alpha)\Big\{\partial^2 R_n(|\zeta|)\left[(\zeta/|\zeta|)^{n\gamma/\beta} + (\zeta/|\zeta|)^{-n\gamma/\beta}\right]/\partial\zeta\partial\bar{\zeta}\\ +\tfrac{1}{4}k_0^2 R_n(|\zeta|)\left[(\zeta/|\zeta|)^{n\gamma/\beta} + (\zeta/|\zeta|)^{-n\gamma/\beta}\right]\Big\} = 0\end{aligned} \tag{5.6}$$

It can be obtained by rewriting the equation into cylindrical coordinates and simplifying it

$$\left(\frac{\partial}{\partial r^2} + \frac{1}{r}\frac{\partial}{\partial r} - \frac{(n/\gamma\beta)^2}{r^2} + k_0^2\right)R_n = 0 \tag{5.7}$$

According to Eq. (5.7), the corresponding solution of R_n is

$$R_n = \frac{\mathrm{i}\pi}{2}J_{n/\gamma\beta}(kr_<)H^{(1)}_{n/\gamma\beta}(kr_>) \tag{5.8}$$

where, $r_<$ is the minimum distance between r and the initial position of incident wave r_0 , and $r_>$ is the maximum distance between r and the incident wave initial position r_0. Substitute Eqs. (5.5) and (5.8) into Eq. (5.5), and the expression under the series expression can be obtained

$$w^{(f)} = \frac{\mathrm{i}}{2\gamma}\sum_{n=0}^{\infty}\varepsilon_n\cos\left(\frac{n\theta}{\gamma\beta} + \frac{n\pi}{2}\right)\cos(n\gamma\alpha)S_{n/\gamma\beta} \tag{5.9}$$

where $S_{n/\gamma\beta} = J_{n/\gamma\beta}(kr_<) H^{(1)}_{n/\gamma\beta}(kr_>)$.

In ζ coordinates, Eq. (5.9) can be written as

$$w^{(f)} = \frac{\mathrm{i}}{2\gamma} \sum_{n=0}^{\infty} \varepsilon_n \left[\left(\frac{\zeta}{|\zeta|} \right)^{n\nu} + \left(\frac{\zeta}{|\zeta|} \right)^{-n\nu} \right] \cos(n\gamma\alpha) S_{n/\gamma\beta} \tag{5.10}$$

This chapter considers the incident condition of incident wave as two-dimensional plane SH wave. According to Sommerfeld radiation condition, the displacement field is

$$w^{(i)} = \frac{\mathrm{i}}{4\mu} H_0^{(1)}(k_0 |\zeta|) \tag{5.11}$$

Normalize Eq. (5.12) to make $w_0 = w^{(i)}$ have

$$\frac{w^{(f)}}{w_0} = \frac{2}{\gamma} \sum_{n=0}^{\infty} \varepsilon_n \left[\left(\frac{\zeta}{|\zeta|} \right)^{n\nu} + \left(\frac{\zeta}{|\zeta|} \right)^{-n\nu} \right] \cos(n\gamma\alpha) S_{n/\gamma} \tag{5.12}$$

Based on the plane SH wave incident considered in this chapter, there is $r_0 \to \infty$. According to the progressive expression of Hankel function, $S_{n/\gamma\beta}$ can be simplified as

$$S_{n/\gamma\beta} = e^{-\frac{\mathrm{i}n\pi}{2\gamma\beta}} J_{n/\gamma\beta}(kr) \tag{5.13}$$

According to the above equation, the free wave field $w^{(f)}$ in the inhomogeneous wedge space can be constructed as follows

$$w^{(f)} = 2pw_0 \sum_{n=0}^{\infty} \varepsilon_n e^{-\frac{\mathrm{i}n\nu\pi}{2}} J_{n\nu}(k_0 |\zeta|) \left[\left(\frac{\zeta}{|\zeta|} \right)^{n\nu} + \left(\frac{\zeta}{|\zeta|} \right)^{-n\nu} \right] \cos(np\alpha) \tag{5.14}$$

where $\nu = p/\beta$, $p = 1/\gamma$, $J_{n\nu}(\cdot)$ is a fractional Bessel function. The constructed free wave field $w^{(f)}$ does not contain unknown coefficients and can be directly analyzed and calculated. It can also be obtained from the equation that the displacement amplitude of the wedge tip is only related to the wedge tip angle, and its value is $2/\gamma$.

In order to facilitate the subsequent parameter representation to dimensionless parameters, in this section, the dimensionless frequency $\eta^{(1)}$ can be expressed as

$$\eta^{(1)} = k_0 a/\pi = 2a/\lambda \tag{5.15}$$

where, a is the distance from the reference point to the origin, and $\eta^{(1)}$ used to represent the ratio of the reference distance to the half wavelength, and also represent the amplitude of the reference wave number.

5.1.3 Convergence analysis

The special function is used for the displacement amplitude in the region constructed in this section. It is necessary to carry out the convergence analysis to obtain the number of infinite terms. According to the model, this section selects two typical points, point 1 $(1.5,0)$ and point 2 $(1.5,\gamma\pi)$, to analyze the convergence of the free wave field under four top angles. In order to ensure the convergence requirements of all the examples in this section, the dimensionless frequency $\eta^{(1)}=1.2$, the incident angle $\alpha=0^{\circ}$, and the inhomogeneous parameter $\beta=1.5$ are set, and the truncation term $N=m=n$ is considered to establish the standard solution matrix. According to a large number of convergence calculations, as shown in Fig. 5.2, when 20 items are taken, the results have converged. Therefore, in subsequent calculations, taking $N=25$ ensure the convergence of the results and save calculation time.

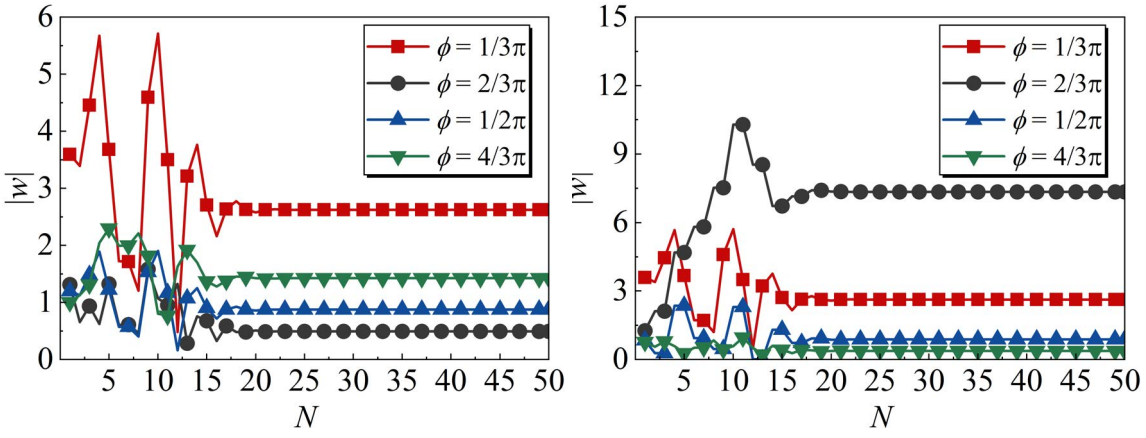

(a) $\beta=1.5$ (b) $\beta=0.5$

Fig. 5.2 Convergence analyses of displacement amplitudes at four typical positions with increasing N

5.1.4 Validation

Before discussing the inhomogeneous parameter influence on SH wave propagation in wedge space, the constructed free wave field in the space is verified. In order to make the calculation results dimensionless, the horizontal coordinates are normalized here, and the

surface displacement amplitude is given in the form of x/a relative to the displacement amplitude of the free zone. Fig.5.3 indicates the comparison between the present results in this section and the existed result in homogeneous media. Taking inhomogeneous parameters not only ensures the existence of inhomogeneous parameters in the formula, but also can better simulate the situation of homogeneous media. The displacement amplitude under three angles of incidence at the top angle ϕ=$2\pi/3$ in Fig. 5.3 (a) and under four angles of incidence at the top angle ϕ=$3\pi/2$ in Fig. 5.3 (b). From the two figures, present results in this section are in well agreement with the existed results, which can verify validation of the wave field and calculation method constructed in this section. Fig. 5.4 displays the displacement of symmetrical and horizontal incident under two wedge vertex angles when the values of two groups of inhomogeneous parameters are approximate to and the dimensionless frequency is 1.0. Fig. 5.4 (a), wedge vertex angle $\phi = 2\pi/3$, the result of reaching 1.0 when the inhomogeneous parameter is less than 1 under symmetrical incident, and Fig. 5.4 (b) is the calculation result of wedge vertex angle $\phi = 4\pi/3$, reaching 1.0 when the horizontal incident is greater than 1. The two groups of results show a continuous close to the value of 1, which verifies the continuity of the calculation results and thus reflects the validation of the results.

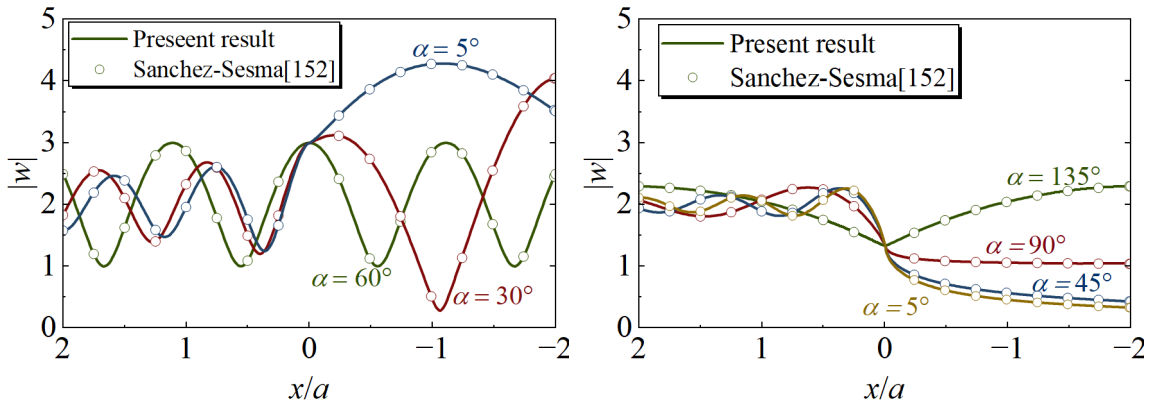

(a) $\phi = 2\pi/3$ (b) $\phi = 3\pi/2$

Fig. 5.3 Results of approximately homogeneous medium for comparison with the existed displacement results

5.1.5 Numerical results and discussion

In this section, the influence of inhomogeneous parameters on SH wave in the wedge region with different apex angles is first discussed. Figs. 5.5-5.7 shows the surface displacement

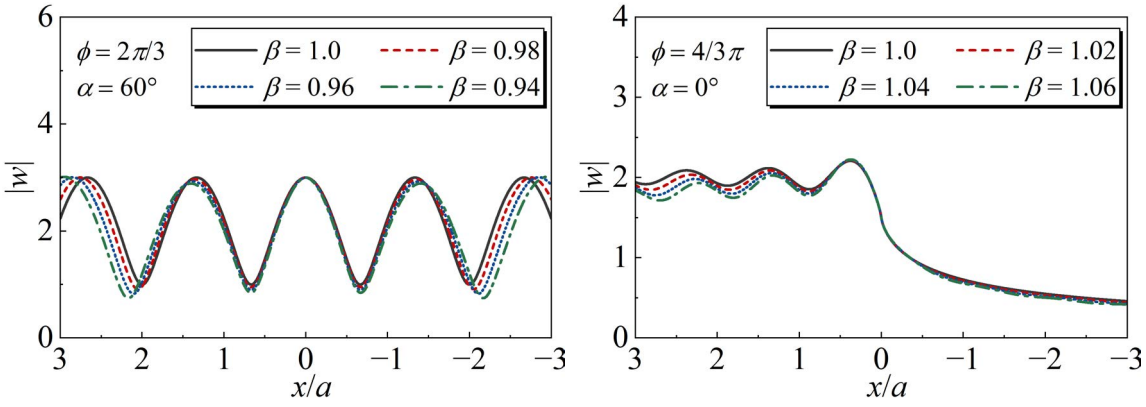

(a) $\phi = 2\pi/3$ (b) $\phi = 4\pi/3$

Fig. 5.4 Displacement distribution corresponding to different inhomogeneous parameters

amplitude when the inhomogeneous parameters $\beta = 0.5, 0.75, 1.0, 1.25, 1.5$, the wedge vertex angle $\phi = \pi/3, 2\pi/3, 4\pi/3, 5\pi/3$, respectively, and the incident angle is horizontal, symmetric and oblique.

The displacement amplitude of wedge surface under horizontal incident is given in Fig. 5.5. From the figure that under different inhomogeneous parameters, the wedge vertex displacement is the same value and the value is $2/\gamma$, which is consistent with the results obtained by the equation. The surface displacement amplitude at $\phi = \pi/3$, is symmetrically distributed under horizontal incident, in Fig. 5.5 (a). The displacement with the ascender of inhomogeneous parameters then increases. With wedge vertex angle increasing, the displacement amplitude decreases as a whole. Moreover, the displacement amplitude near the vertex has an obvious trend of declining first and then growing, and the minimum value of displacement amplitude appears at the horizontal axis of 0.5. As the vertex angle reaches to $2\pi/3$, the wedge left plane displacement is inversely proportional to the inhomogeneous parameter in the horizontal incident. While on the right plane, the displacement amplitude is also proportional to inhomogeneous parameter. And, it can be clearly seen that the displacement amplitude of the right plane of the wedge is larger than that of the left plane as a whole at horizontal incidence, and this phenomenon is more obvious with the increase of inhomogeneous parameters, and the amplification factor of the right plane is about 2 β. Considered the situation of $\phi > \pi$, as $4\pi/3$ and $5\pi/3$, under horizontal incident, the displacement amplitude of the right plane is significantly reduced compared with that of the left plane, and the wave absorption is proportional to the wedge space. However, compared with Figs. 5.5 (a) and (b), as $\phi > \pi$ the displacement amplitude of the two planes is almost

constant under horizontal incident, and only slightly declines in the right plane, especially when the inhomogeneous parameter is less than 1.

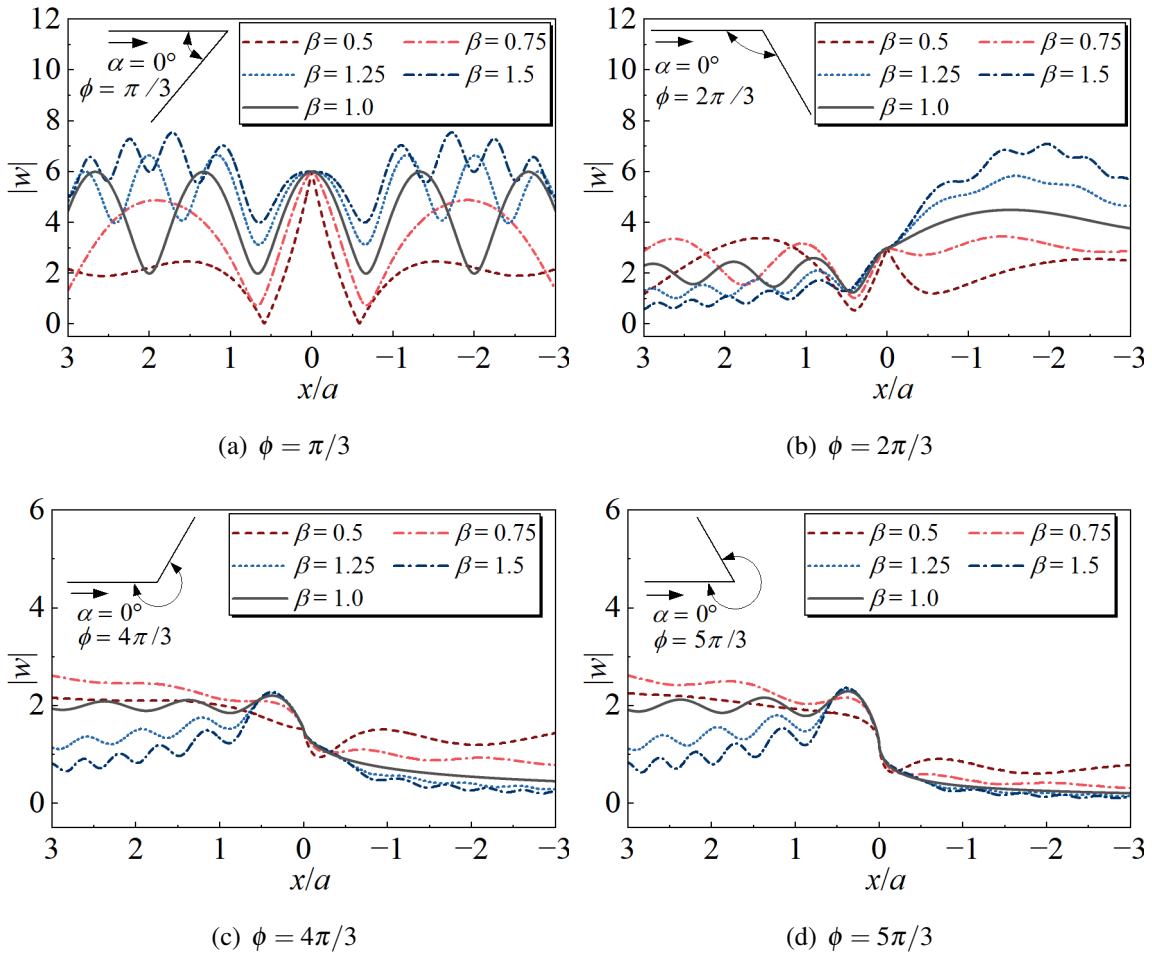

(a) $\phi = \pi/3$ (b) $\phi = 2\pi/3$

(c) $\phi = 4\pi/3$ (d) $\phi = 5\pi/3$

Fig. 5.5 Surface displacement amplitude of different inhomogeneous parameter under four types wedge space vertex angle with SH wave horizontal incident

Change the incident angle to symmetrical incident, $\alpha = 2/\phi$. At this time, the plane displacement on both sides of the wedge under different inhomogeneous parameters is shown in Fig. 5.6.The displacement amplitude at the wedge vertex angle is still $2/\gamma$ in various inhomogeneous parameters and top angles. The minimum displacement position at each wedge vertex angle almost occurs at the abscissa of 0.5. The wedge space both side displacement at $\phi = \pi/3$ under symmetrical incident of $\beta \geq 1$ is significantly greater than the value of $\beta < 1$. At $\beta \geq 1$, the impact on the plane displacement on both sides is small, and the impact on the distribution of the surface displacement is large. With the inhomogeneous parameter increasing continuously, the displacement is more obvious with the vibration of the surface position, as shown in Fig. 5.6 (a). The plane displacement presents symmetrical

distribution, and vibration around 2 on the whole, at $\phi = 2\pi/3$. While $\beta \geq 1$, the plane displacement will be slightly greater than the displacement at the vertex position, as shown in Fig. 5.6 (b). The surface displacement under the symmetrical incident of $4\pi/3$ wedge vertex angle is shown in Fig. 5.6 (c). The plane displacement is significantly greater than the vertex displacement amplitude under $\beta \geq 1$. Considering $\phi = 5\pi/3$, the plane displacement is smaller than that of the homogeneous media.

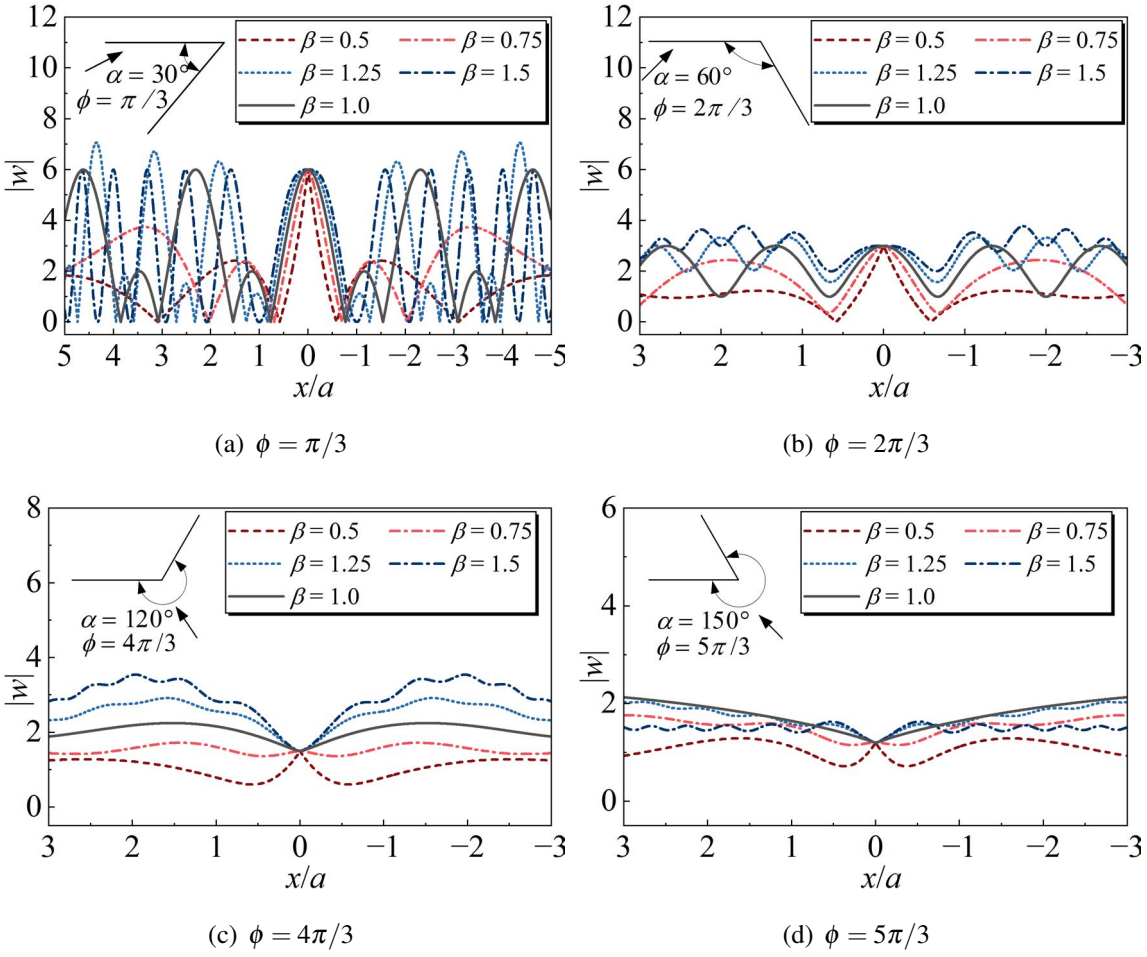

(a) $\phi = \pi/3$ (b) $\phi = 2\pi/3$

(c) $\phi = 4\pi/3$ (d) $\phi = 5\pi/3$

Fig. 5.6 Surface displacement amplitude of different inhomogeneous parameter under four types wedge space vertex angle with SH wave symmetrical incident

For discussing the distribution of plane displacement amplitude on both sides when the incident angle is approximately vertical, Fig. 5.7 illustrates the approximate simulated vertical incident with $\alpha = 85°$. The characteristic of vertex displacement amplitude $2/\gamma$ still exists. Under this incident angle, with wedge vertex angle is $\pi/3$, the plane displacement amplitude on both sides is still symmetrically distributed. Meanwhile, at the situation of $\beta \geq 1$, the influence of the inhomogeneous parameter on the displacement amplitude is

reflected in the vibration distribution that changes with the horizontal ordinate, while at the situation $\beta < 1$ changes to $\beta \geq 1$, the displacement amplitude is significantly increased. The left plane displacement is greater than that of the right plane when the wedge space of other vertex angles is inclined at 85°, and with the wedge vertex angle increasing, the displacement amplitude declines significantly and the vibration with abscissa varying decreases. From Figs. 5.7 (c) and (d), it can be found that the displacement amplitude of the left plane of the two large wedge vertex angles is almost the same when the incident angle is approximately vertical, but the displacement amplitude of the right plane decreases slightly with the ascender of vertex angle.

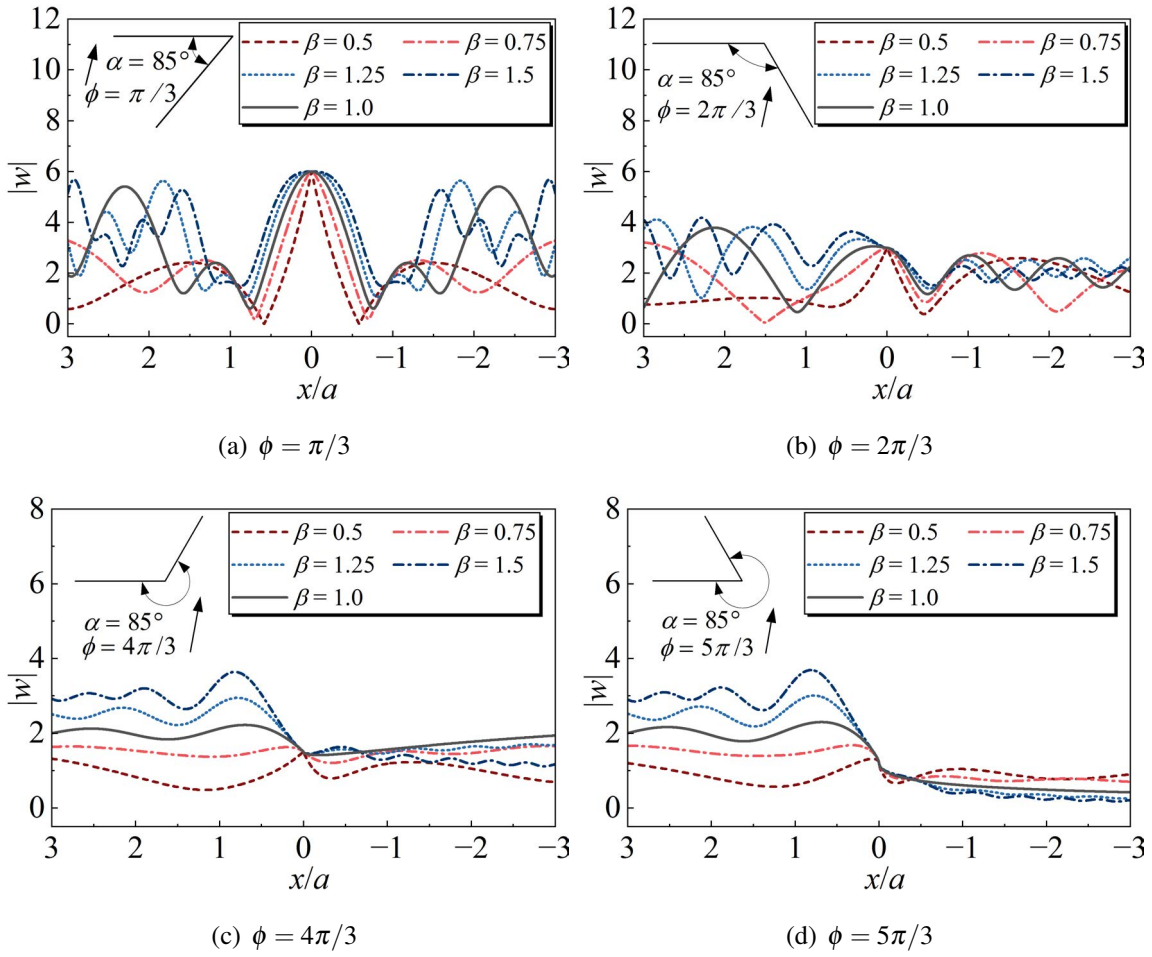

(a) $\phi = \pi/3$ (b) $\phi = 2\pi/3$

(c) $\phi = 4\pi/3$ (d) $\phi = 5\pi/3$

Fig. 5.7 Surface displacement amplitude of different inhomogeneous parameter under four types wedge space vertex angle with SH wave vertical incident

By analyzing and comparing the results of three sets examples, it can be observed that the vertex displacement of $2/\gamma$ still exists in the inhomogeneous media. The surface displacement presents symmetrical distribution at any incident angle with $\phi = \pi/3$. Meanwhile, the

displacement amplitude is proportional to inhomogeneous parameter and the displacement increases with the abscissa vibration, especially when the inhomogeneous parameter changes from less than 1 to greater than or equal to 1, the displacement amplitude increases more obviously. While with incident angle changing from horizontal, symmetrical to nearly vertical, the maximum displacement amplitude distribution ranges from the right plane of the wedge to the left plane at $\phi = 2\pi/3$. At this time, the inhomogeneous parameter has a significant impact on its value on the side with the largest distribution of displacement amplitude, while on the other side, it has a significant impact on the amplitude of displacement vibration with abscissa.

In order to consider the wedge space surface displacement distribution at $\phi > \pi$, the discussion of the wedge vertex angle of $4\pi/3$ and $5\pi/3$ are carried out. From the three sets results that when the incident angle is horizontal, the left plane displacement is inverse proportional in inhomogeneous parameter. However, the left plane displacement amplitude is proportional to inhomogeneous parameter under oblique and symmetric incident. The right plane displacement is small at horizontal and oblique incident. Through three sets of examples, it can be demonstrated that if $\phi < \pi$, the minimum displacement amplitude of the wedge surface generally appears at the $x/a = \pm 0.5$.

Continue to explore the influence of inhomogeneous parameters varying with dimensionless frequency on the wedge surface displacement amplitude. Four groups of typical wedge vertex angles are still selected for calculation, all of which adopt horizontal incident. The surface displacement amplitude distribution is given in Figs. 5.8-5.10 under the condition of $\beta = 1.5, 1.0, 0.5$.The surface displacement vibration with the dimensionless frequency growing at $\beta = 1.5$. Meanwhile, if the wedge vertex angle is less than 180°, the maximum displacement amplitude gradually approaches the wedge vertex with dimensionless frequency increasing. As at $\phi > \pi$, the distribution of surface displacement amplitude with the change of dimensionless frequency is almost the same at the time of horizontal incident, and the displacement amplitude is concentrated at the vertex position, and the plane displacement amplitude on both sides is small.

The inhomogeneous parameter of 1.0, similar to the homogeneous media, is introduced for calculation, and the displacement amplitude distribution diagram with the change of dimensionless frequency under the same conditions is obtained, as shown in Fig. 5.9. The displacement amplitude distribution on both sides is symmetric with the vertex angle is $\pi/3$. The vibration frequency is advanced with the growth of dimensionless frequency, but the oscillation amplitude remains unchanged, and the maximum displacement amplitude is $2/\gamma$. the displacement amplitude still vibration with the dimensionless frequency, with $\phi = 2\pi/3$, and it can be observed that the maximum and minimum values of displacement amplitude

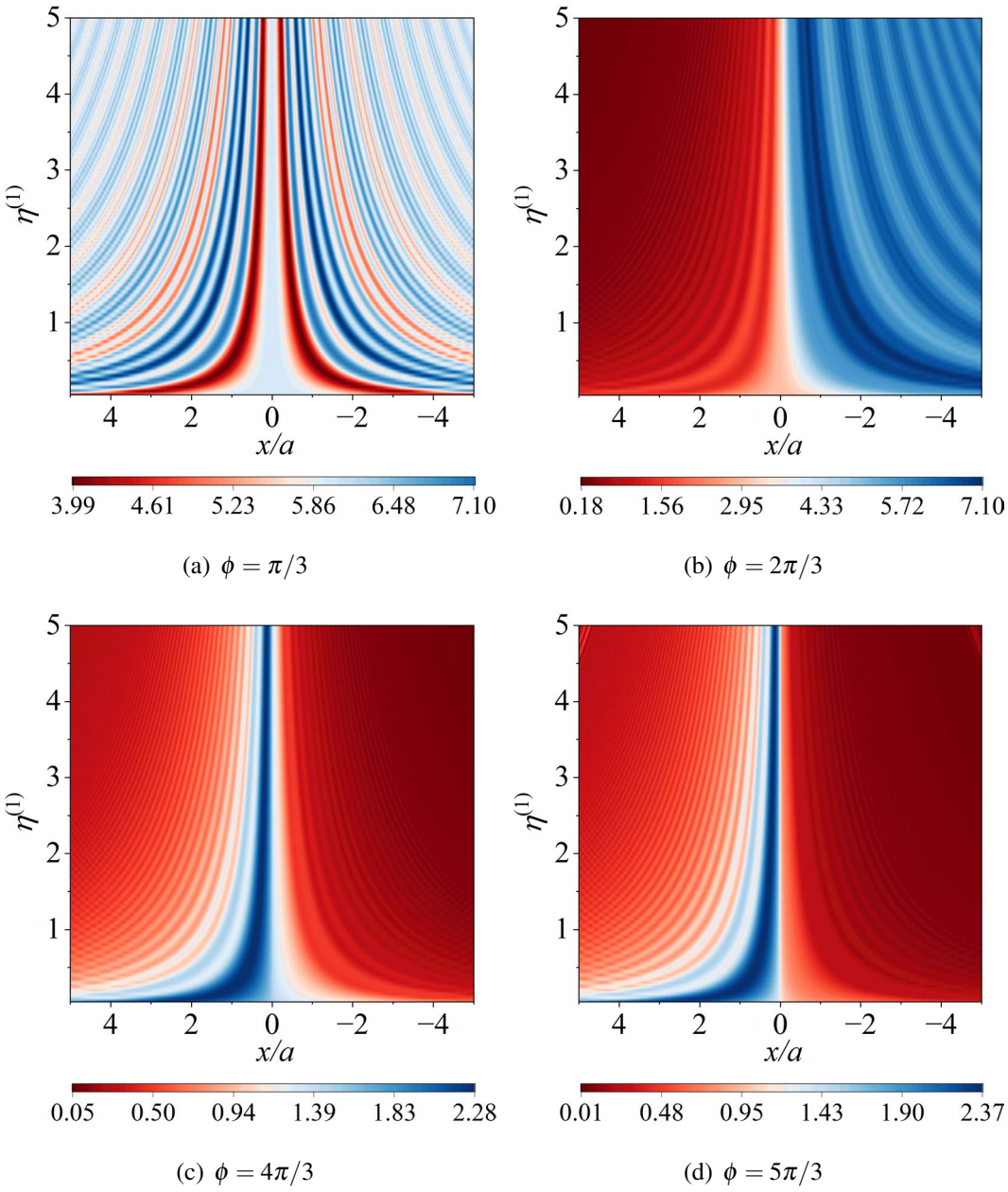

Fig. 5.8 Surface displacement amplitude distribution of four types wedge space vertex angle with the dimensionless frequency varied under horizontal incident and $\beta = 1.5$

appear near both sides of the vertex. If the wedge vertex angle is greater than 180°, the displacement amplitude distribution is similar.

The calculation is carried out as the inhomogeneous parameter is less than 1 as shown in Fig. 5.10 with the displacement amplitude distribution at $\beta = 0.5$. The displacement amplitude is still symmetrically distributed at $\phi = \pi/3$. However, there is a distribution area of larger displacement amplitude on the plane on both sides of the wedge at dimensionless frequency is 2.5, and gradually moves towards the wedge vertex with dimensionless frequency increasing. When the wedge vertex angle is $2\pi/3$, the amplitude vibration of displacement on both sides is proportional to dimensionless frequency. The right plane displacement amplitude with the ascender of dimensionless frequency then gradually grows at wedge vertex angle is $4\pi/3$ under this inhomogeneous parameter.

From the comparison of three sets of examples that the wedge surface displacement amplitude vibration is intensified while the inhomogeneous parameter is increasing. The displacement amplitude of wedge space both sides decreases from left to right with the inhomogeneous parameter rises, as $\phi > \pi$. At $\phi < \pi$, with the inhomogeneous parameter increasing, the vibration frequency of displacement is proportion in dimensionless frequency while the amplitude of displacement is inverse proportional.

The above calculation examples are the wedge surface displacement amplitude distribution of the plane on both sides. Considering the influence of inhomogeneous parameters on the internal displacement amplitude distribution, Figs. 5.11-5.13 illustrate the internal displacement distribution of the horizontal and symmetrical incident of the three wedge vertex angles with a dimensionless frequency of 1.0.

From Fig. 5.11, as the wedge top angle is $\pi/3$, the internal displacement amplitude shows symmetrical distribution along $\phi = 30^\circ$ under various inhomogeneous parameters and incident angle. With the inhomogeneous parameters varying, not only the surface displacement amplitude distribution, but also the internal displacement both changes greatly. It can be observed from Figs. 5.11 (a) and (c) that if $\beta > 1$, the internal displacement amplitude vibration obviously and the maximum value of the displacement will not only appear on the two sides of the plane, but also exist in the area with large displacement amplitude, and the larger value linear area is basically parallel to the radius of $\phi = 30^\circ$. Otherwise if $\beta < 1$, the internal displacement amplitude vibration is weakened, and the minimum band region of internal displacement appears in the circumferential direction near the vertex. While symmetrical incident, if $\beta > 1$, the internal displacement amplitude vibration is still obvious and the radial vibration frequency gradually increases, else, the maximum displacement appears at the vertex, and there are two annular regions with almost zero circumferential displacement.

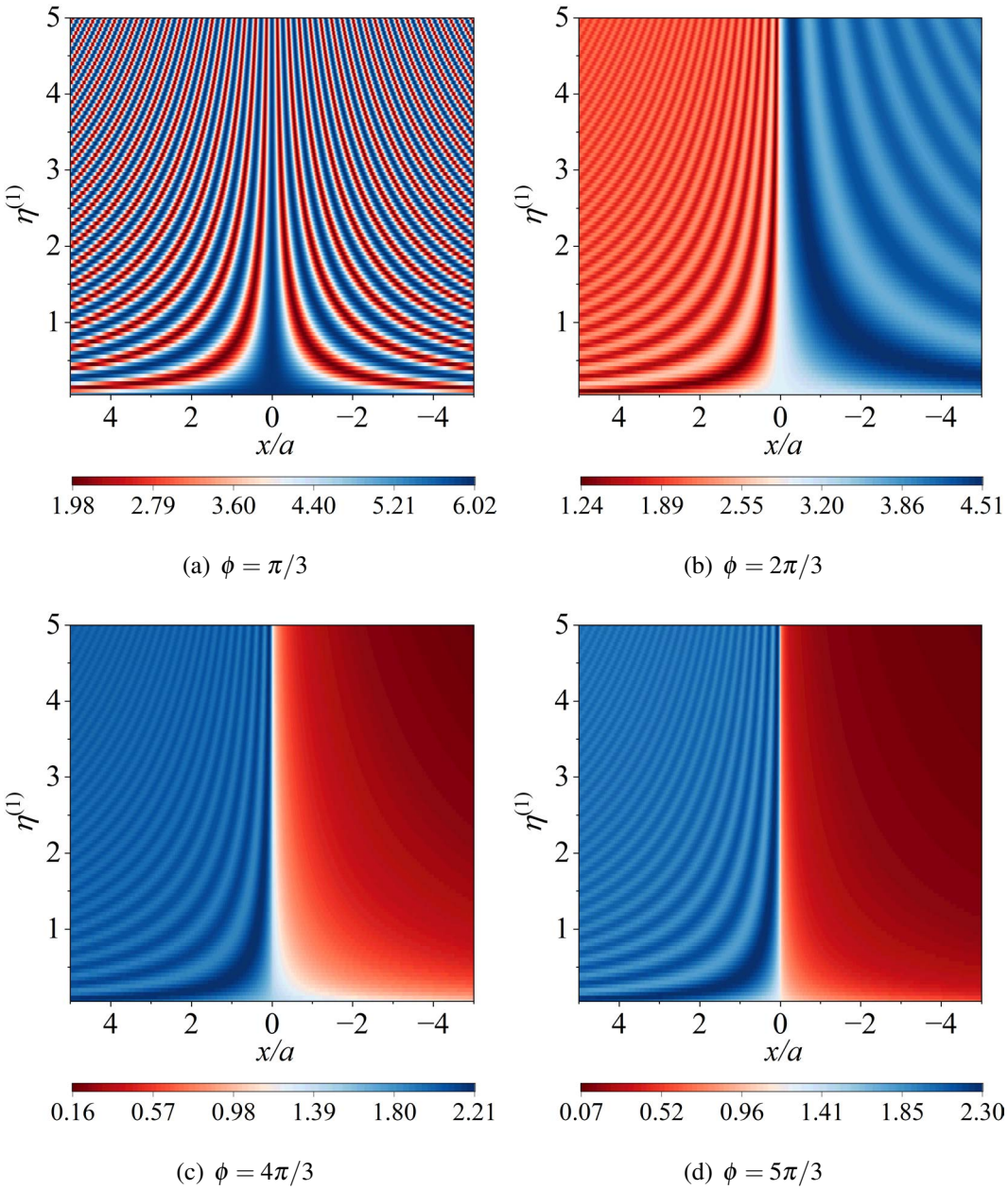

Fig. 5.9 Surface displacement amplitude distribution of four types wedge space vertex angle with the dimensionless frequency varied under horizontal incident and $\beta = 1.0$

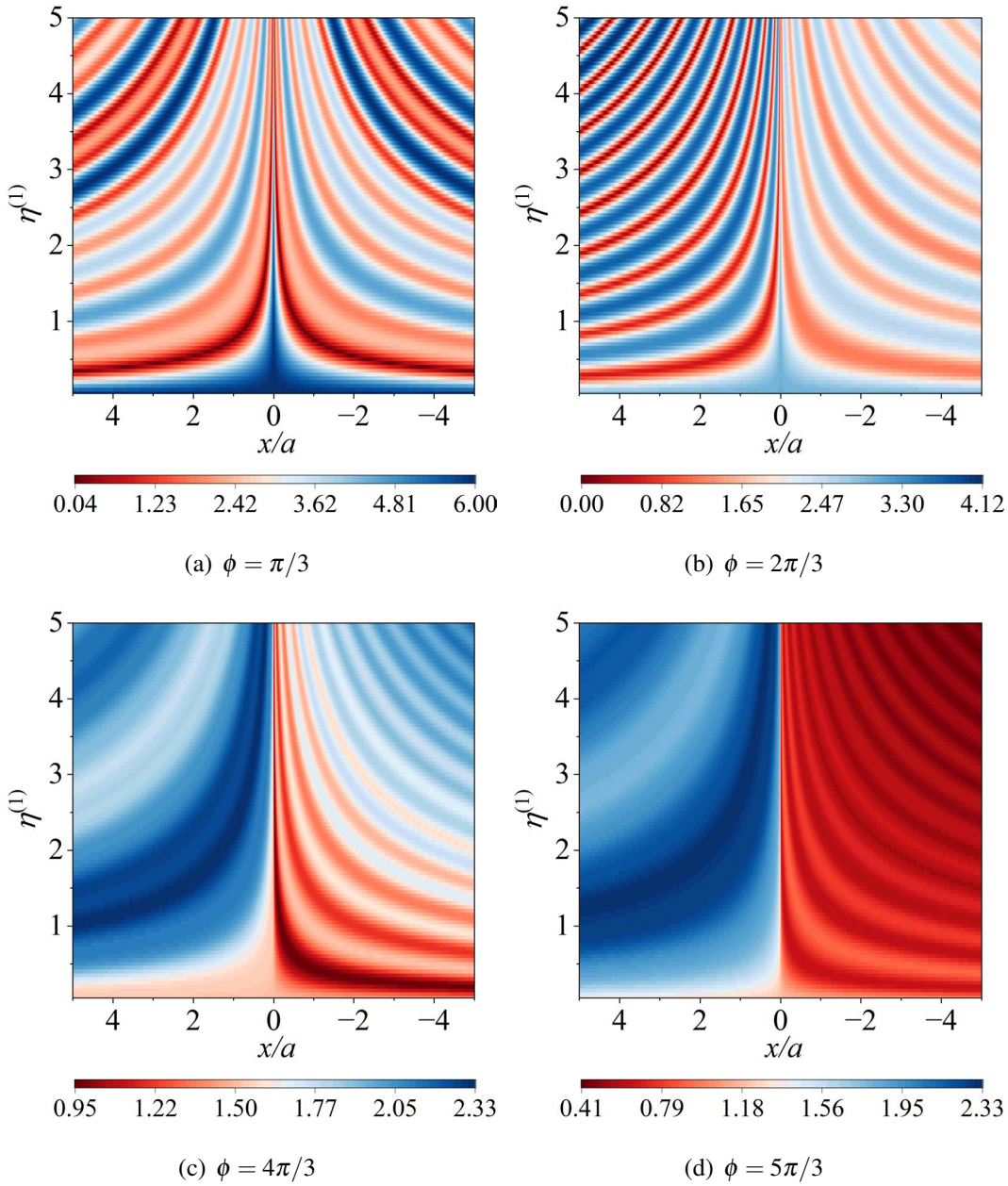

(a) $\phi = \pi/3$ (b) $\phi = 2\pi/3$

(c) $\phi = 4\pi/3$ (d) $\phi = 5\pi/3$

Fig. 5.10 Surface displacement amplitude distribution of four types wedge space vertex angle with the dimensionless frequency varied under horizontal incident and $\beta = 0.5$

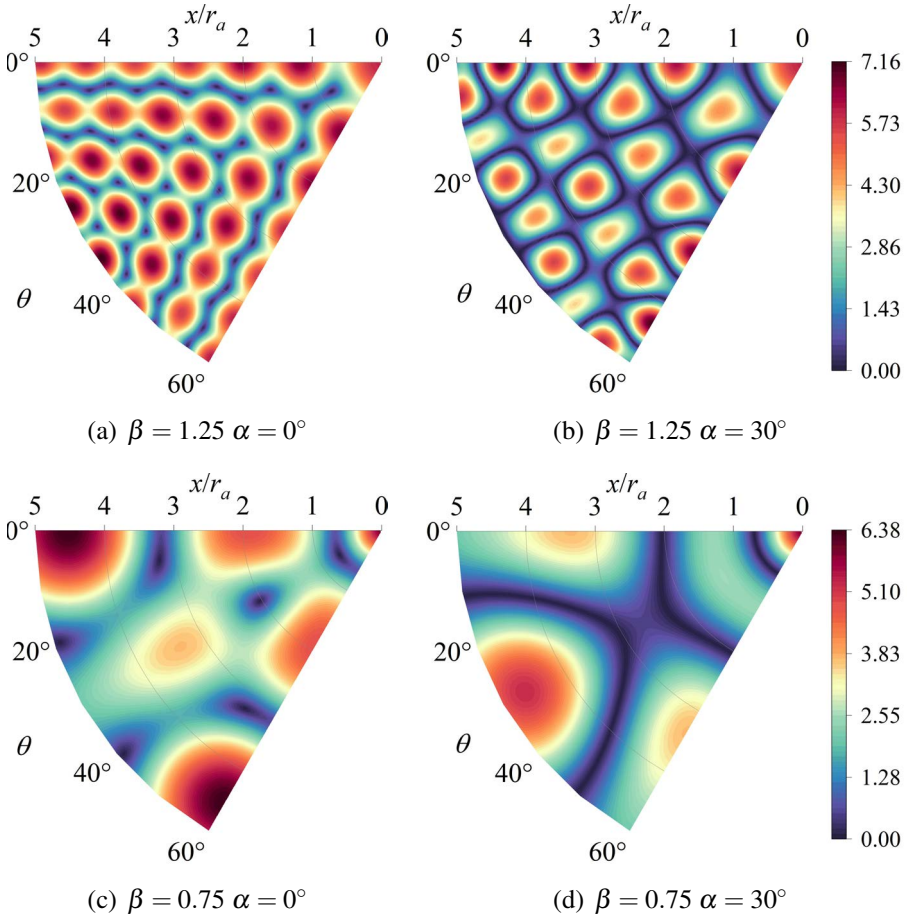

(a) $\beta = 1.25$ $\alpha = 0°$ (b) $\beta = 1.25$ $\alpha = 30°$

(c) $\beta = 0.75$ $\alpha = 0°$ (d) $\beta = 0.75$ $\alpha = 30°$

Fig. 5.11 Internal displacement amplitude distribution of vertex angle $\pi/3$ under two inhomogeneous parameters and incident angles

While the wedge vertex angle arrives to $2\pi/3$ under horizontal incident, the maximum displacement amplitude is almost not reduced since $\beta > 1$, compared with the maximum displacement amplitude at the wedge vertex angle over $\pi/3$, and the internal displacement distribution has varied greatly. The larger value area of internal displacement amplitude under horizontal incident appears near the right plane, the θ-axis is between 90° and 120°, and its linear is parallel to the right plane. However, if $\beta < 1$, the maximum displacement occurs near the left plane, θ-axis is between 0° and 30°, and the maximum value appears at the wedge boundary while the internal displacement amplitude is small, in Figs. 5.12 (a) and (c). In the case of symmetrical incident, the displacement amplitude decreases obviously. The maximum displacement amplitude appears on both sides of the wedge, and the internal displacement vibrates violently, and its vibration frequency increases radially, while $\beta > 1$. For $\beta < 1$, the maximum displacement amplitude appears at the vertex, and a circular region

with almost zero circumferential displacement amplitude also appears near the vertex, and the displacement amplitude in the middle of wedge is small.

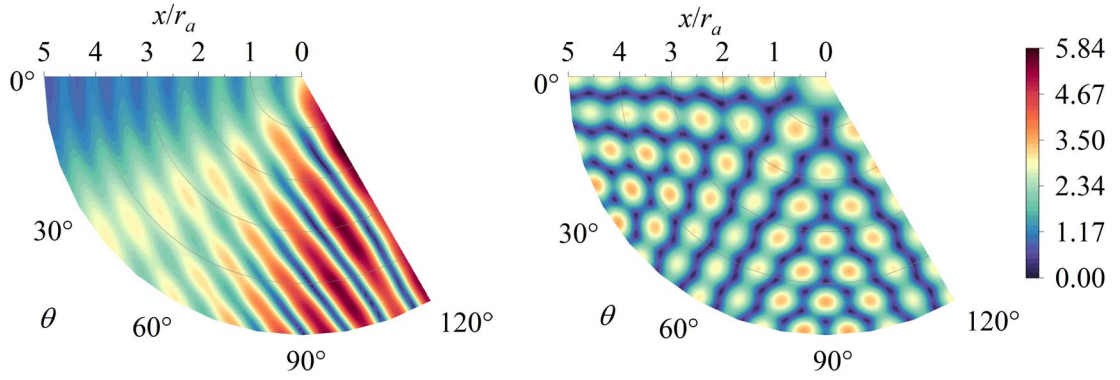

(a) $\beta = 1.25$ $\alpha = 0°$ (b) $\beta = 1.25$ $\alpha = 30°$

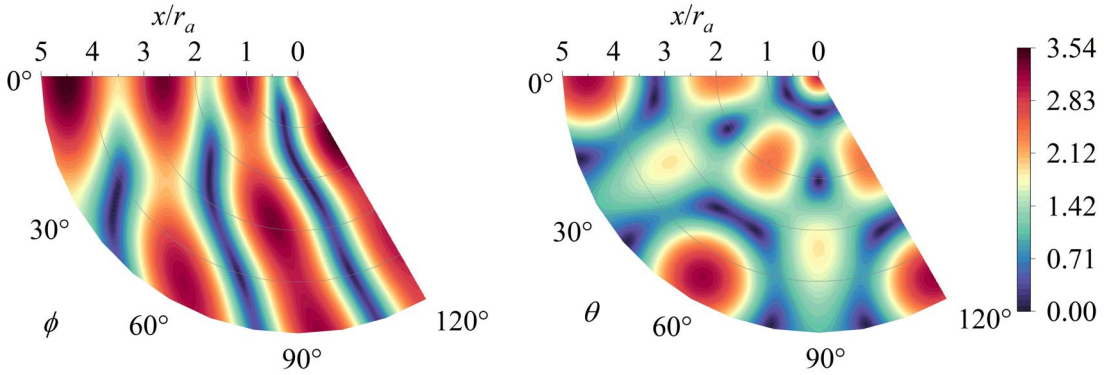

(c) $\beta = 0.75$ $\alpha = 0°$ (d) $\beta = 0.75$ $\alpha = 30°$

Fig. 5.12 Internal displacement amplitude distribution of vertex angle $2\pi/3$ under two inhomogeneous parameters and incident angles

Considering that $\phi > \pi$, this sub example gives the internal displacement distribution when the top angle is $4\pi/3$. It can be illustrated from Fig. 5.13 while $\beta > 1$, the maximum displacement amplitude appears in the internal region radially distribution with θ-axis of $35°$ and $135°$, and the larger value of the internal displacement is distributed between θ-axis of $30°$ and $150°$. In other regions, the displacement amplitude is small, and the minimum value of the displacement amplitude appears in the right plane. However, if $\beta < 1$, the maximum displacement amplitude appears on the left plane of the wedge, and gradually increases along the radial direction. The right plane displacement is relatively high, and the minimum displacement amplitude appears in the internal region with θ-axis of $50°$. In the case of symmetrical incident, in Figs. 5.13 (b) and (d), the displacement amplitude is smaller near the incident angle while $\beta > 1$ and larger while $\beta < 1$, relative to other displacement amplitudes in the region.

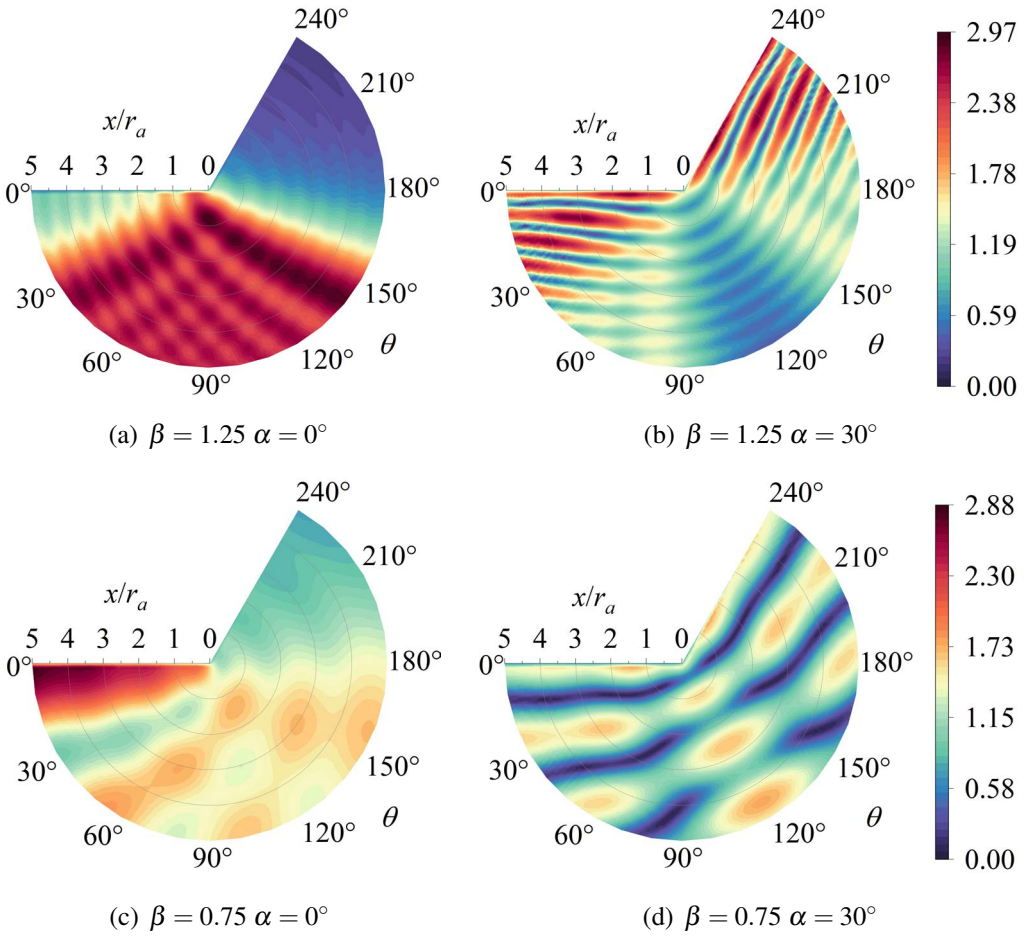

(a) $\beta = 1.25$ $\alpha = 0°$ (b) $\beta = 1.25$ $\alpha = 30°$

(c) $\beta = 0.75$ $\alpha = 0°$ (d) $\beta = 0.75$ $\alpha = 30°$

Fig. 5.13 Internal displacement amplitude distribution of vertex angle $4\pi/3$ under two inhomogeneous parameters and incident angles

From the above three sets of examples indicated that the inhomogeneous parameters have a great influence on the displacement distribution, and different inhomogeneous parameters cause the diametrically opposite phenomenon of displacement distribution in the internal region. When the wedge vertex angle is $2\pi/3$ and $4\pi/3$, if $\beta > 1$, the smaller value of displacement amplitude appears in the area near the incident angle. Otherwise, the maximum displacement amplitude appears in the area near the incident angle.

5.2 Scattering of SH wave around cylindrical depression in inhomogeneous wedge space

According to the research on the SH wave propagation characteristics in the inhomogeneous wedge space in the previous section, this section investigates the scattering of SH wave around cylindrical depression in inhomogeneous wedge space. Due to the flexibility of the wedge vertex angle, the vertex angle ϕ can be taken as 0 to 2π, so it can simulate a variety of shape space, such as rectangular space and semi-infinite space. The wedge vertex has a cylindrical depression, which has certain engineering significance. Cylindrical treatment of the wedge vertex can reduce the displacement and stress concentration at its vertex. At the same time, the foundation of the building structure built on the ridge can be modeled as a cylindrical depression at the wedge vertex. And taking the cylindrical depression as the wedge surface defect as the basis of research, more complex surface defects can be explored.

5.2.1 Model and wave equation

The model of the scattering of SH waves by the cylindrical depression in density radial inhomogeneous wedge space is shown in Fig. 5.14. The radius of the cylindrical depression is r_a, its center is the wedge vertex, and it is set as the coordinate origin o, the x-axis is horizontal to the left, y-axis is vertical to the right, and the wedge vertex angle is $\phi = \gamma\pi\,(0 < \gamma \leq 2)$. Setting $\phi = \pi/2$, the model simulates the right angle space with a cylindrical depression, and setting $\phi = \pi$, it simulates the semi-infinite space with a semi-cylindrical depression. SH wave is incident at an angle α with the horizontal direction. Owing to this section still mainly considers the influence of variable wave velocity on the propagation characteristics of SH wave in wedge inhomogeneous media. Therefore, the density form is shown in Eq. (5.1). Through the transformation method in Chapter 2, the control equation shown in Eq. (5.2) can be directly solved.

5.2.2 Displacement field and stress field in the model

In this model, the total wave field is composed of free wave field $w^{(f)}$ and scattering wave $w^{(s)}$ caused by cylindrical depression, $w = w^{(f)} + w^{(s)}$, according to the above section, the free wave field $w^{(f)}$ satisfying the control equation and free boundary conditions on both sides of the wedge can be shown as

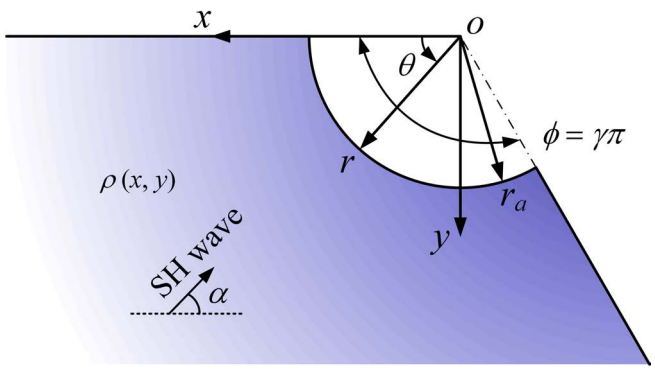

Fig. 5.14 Model scattering of SH wave around cylindrical depression in inhomogeneous wedge space

$$w^{(f)} = 2pw_0 \sum_{n=0}^{\infty} \varepsilon_n e^{-\frac{in\nu\pi}{2}} J_{n\nu}(k_0|\zeta|) \left[\left(\frac{\zeta}{|\zeta|} \right)^{n\nu} + \left(\frac{\zeta}{|\zeta|} \right)^{-n\nu} \right] \cos(np\alpha) \tag{5.16}$$

where, $\nu = p/\beta$, $p = 1/\gamma$, $J_{n\nu}(\cdot)$ is a fractional Bessel function.

The scattering wave field $w^{(s)}$ excited by the cylindrical depression can be constructed by Hankel function, and the scattering wave excited by it must satisfy the condition of free hoop stress at the two wedge boundaries,

$$\tau_{\theta z}^{(s)} = 0, \theta = 0, \theta = \gamma\pi \tag{5.17}$$

According to the above requirements, the fractional Hankel function is still used to satisfy the stress free conditions at different angles, and the scattering wave field in the following form is constructed

$$w^{(s)} = w_0 \sum_{n=0}^{\infty} A_n H_{n\nu}^{(1)}(k|\zeta|) \left[\left(\frac{\zeta}{|\zeta|} \right)^{n\nu} + \left(\frac{\zeta}{|\zeta|} \right)^{-n\nu} \right] \tag{5.18}$$

where, A_n is the unknown coefficient to be solved.

In order to solve the coefficient A_n, the free condition of radial stress at the cylindrical depression is needed, so the expression of free wave field and scattered wave field is given

$$\tau_{rz}^{(f)} = pw_0 \beta\mu k_0 \sum_{n=0}^{\infty} \varepsilon_n e^{-\frac{in\nu\pi}{2}} P_{n\nu}(\zeta) \cos(np\alpha) \tag{5.19}$$

$$\tau_{rz}^{(s)} = \frac{pw_0\beta\mu k_0}{2}\sum_{n=0}^{\infty} A_{(n)}P_{nv}(\zeta) \tag{5.20}$$

where,

$$P_t(s) = J_{t-1}(k_0|s|)\left[\frac{s}{|s|}\right]^{t-1} z^{\beta-1}e^{\mathrm{i}\theta} - J_{t+1}(k_0|s|)\left[\frac{s}{|s|}\right]^{-t-1} z^{\beta-1}e^{\mathrm{i}\theta}$$
$$+ J_{t-1}(k_0|s|)\left[\frac{s}{|s|}\right]^{1-t} \bar{z}^{\beta-1}e^{\text{-i}\theta} - J_{t+1}(k_0|s|)\left[\frac{s}{|s|}\right]^{-t-1} \bar{z}^{\beta-1}e^{\text{-i}\theta}$$

5.2.3 Boundary conditions

According to this model, the free wave field and scattered wave field constructed have automatically satisfied the free condition of hoop stress at the boundary of both sides of the wedge. The boundary condition of zero radial stress shall be satisfied at the cylindrical depression,

$$\tau_{rz}^{(f)} + \tau_{rz}^{(s)} = 0, r = a \tag{5.21}$$

Substituting Eqs. (5.19) and (5.20) into Eq. (5.21)

$$\sum_{n=0}^{\infty} A_n E_n = -\sum_{n=0}^{\infty} F_n \tag{5.22}$$

where, $E_n = P_{nv}(\zeta)$, $F_n = \varepsilon_n e^{-\frac{\mathrm{i}n\nu\pi}{2}} P_{nv}(\zeta)\cos(np\alpha)$.

And multiply $e^{-\mathrm{i}m\theta}$ on both sides of the equation to expand it into Fourier series in the range of $[0, \gamma\pi]$

$$\sum_{m=0}^{\infty}\sum_{n=0}^{\infty} A_n E_{mn} = -\sum_{m=0}^{\infty}\sum_{n=0}^{\infty} F_{mn} \tag{5.23}$$

where, $E_{mn} = \int_0^{\gamma\pi} E_n e^{-\mathrm{i}m\theta} d\theta$, $F_{mn} = \int_0^{\gamma\pi} F_n e^{-\mathrm{i}m\theta} d\theta$.

According to the above equation, the unknown coefficient A_n can be obtained to acquire the wave field in the whole space.

In the calculation of this section, the dimensionless frequency $\eta^{(2)}$ is defined to represent the relationship between the incident wave length and the model size, and to facilitate the dimensionless representation of the parameters in calculation example analysis

$$\eta^{(2)} = 2r_a/\lambda \ = k_0 r_a/\pi \tag{5.24}$$

5.2.4 Convergence analysis

Based on this section, the special function is also used to construct the wave field expression and the Fourier integral method is used to solve the unknown coefficient. Therefore, the finite term needs to be truncated in the calculation process. The convergence analysis can obtain the limited number of terms. According to the model, five typical location points are selected, point 1 (2,0), point 2 (1,0), point 3 $(1,\phi/2)$, point 4 $(1,\phi)$, and point 5 $(2,\phi)$, to analyze the convergence of free wave field and scattering wave field under two vertex angles. In order to ensure the convergence requirements of all the examples in this section, the dimensionless frequency $\eta^{(2)} = 2.0$, incident angle $\alpha = 0°$ and inhomogeneous parameters $\beta = 1.5$ are set, and the truncation term $N = m = n$ is considered to establish the standard solution matrix. According to a large number of convergence calculations, as shown in Fig. 5.15, when 20 items are taken, the results have converged. Therefore, in subsequent calculations, taking $N = 25$ can ensure the convergence of the results and save calculation time.

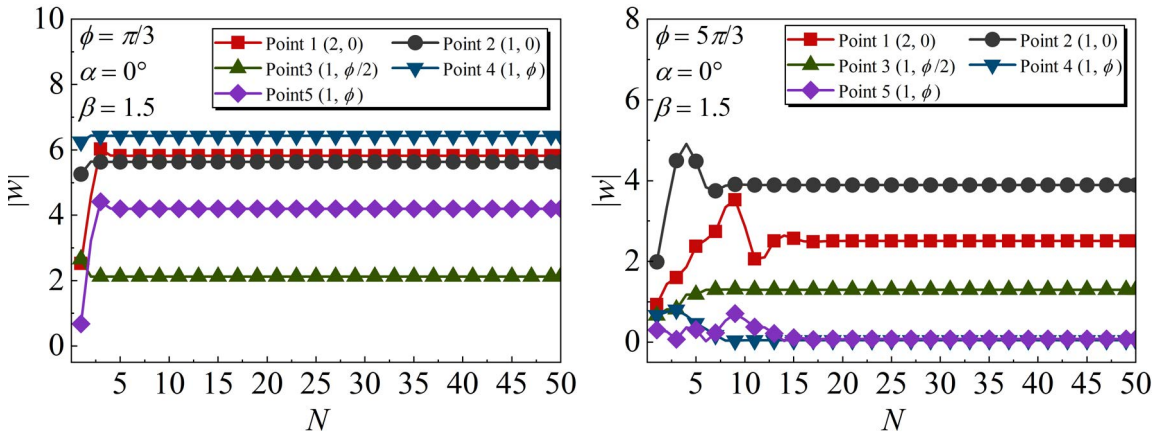

(a) $\phi = \pi/3$ (b) $\phi = 5\pi/3$

Fig. 5.15 Convergence analysis of five typical position displacement amplitudes increasing with truncation term N

5.2.5 Validation

The inhomogeneous parameter is set to 0.99 to simulate the displacement results under homogeneous conditions as above section. Compare the calculated results with the existed results to verify the validation. As shown in Fig. 5.16, set the dimensionless frequency $\eta^{(2)} = 2.0$, three wedge vertex angles $\phi = \pi/2, 2\pi/3, 5\pi/6$, and the two figures are horizontal incident and 30° oblique incident. The horizontal axis x/r_a $[-1,1]$ in the figure corresponds to the position of the cylindrical depression and the position of wedge both sides. The results

calculated by the method in this section are in well agreement with the existed results, thus verifying the effectiveness of the construction of scattered waves in this section. At the same time, two groups of inhomogeneous parameters close to 1.0 are taken for calculation, as shown in Fig. 5.17. The dimensionless frequency is 2.0, and the horizontal incidence and the symmetric incidence. The sacrificial trend of displacement amplitude results also verified this method validation.

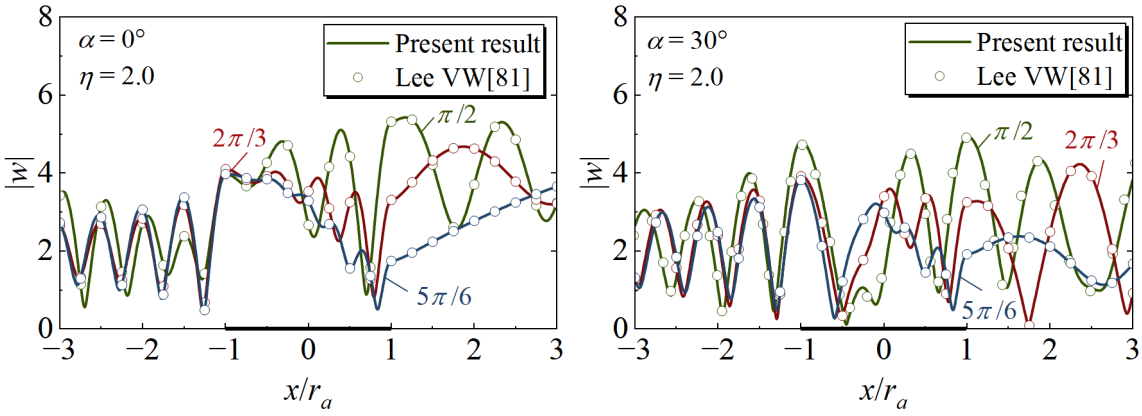

(a) $\alpha = 0°$ (b) $\alpha = 30°$

Fig. 5.16 Results of approximately homogeneous medium for comparison with the existed displacement results

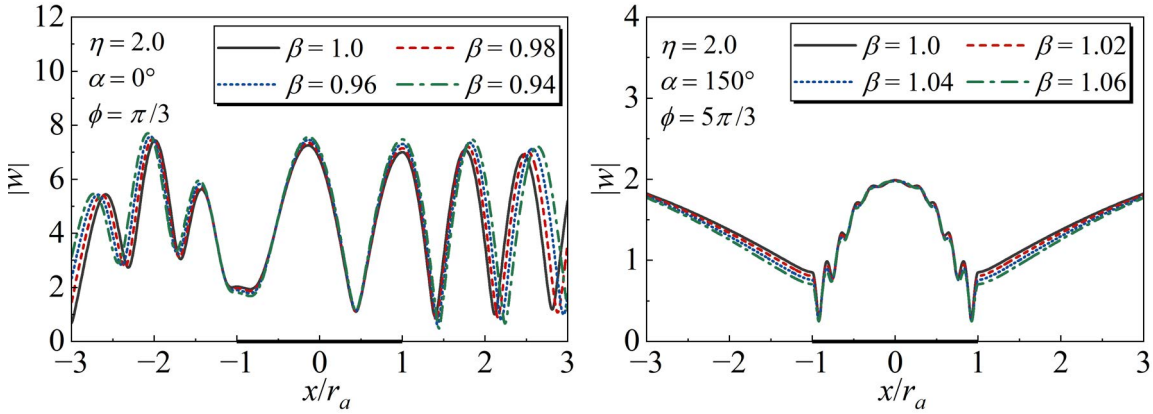

(a) $\phi = \pi/3$ (b) $\phi = 5\pi/3$

Fig. 5.17 Displacement distribution corresponding to different inhomogeneous parameters

5.2.6 Numerical results and discussion

The influence of inhomogeneous parameters on displacement amplitude of wedge space surface with cylindrical depression is primarily explored, and the surface displacement amplitude distribution of inhomogeneous parameters under four wedge vertex angles and three incident angles is calculated, given in Figs. 5.18-5.20.

The displacement amplitude under horizontal incident inverse proportional in inhomogeneous parameters at the junction of the concave and the left plane, and proportional in inhomogeneous parameters at the junction of depression and right plane at $\phi = \pi/3$. And the displacement distribution of the two sides is almost symmetric, as shown in Fig. 5.18 (a). The minimum value of displacement appears at the lowest point of the depression, the maximum value appears at the junction of the right side of the depression while $\beta = 1.5$, and appears at the junction of the left side of the depression under other inhomogeneous parameters. And with the inhomogeneous parameters increasing, the vibration frequency of displacement changes with the position goes further. The displacement amplitude of the left wedge plane declines obviously, and the displacement amplitude of the right wedge plane declines and tends to be stable with the vertex angle growing at $\phi = \pi/2, 2\pi/3$. The displacement at $\beta < 1$ is larger than $\beta > 1$, under these parameter settings. Meanwhile, the maximum point of displacement moves from the depression surface to the right wedge plane. As the wedge vertex angle is $4\pi/3$, the maximum displacement appears at the junction of the depression and the left side. Concurrently, the displacement amplitude of the right side decreases and drops to near zero since inhomogeneous parameter increasing. Compared with the displacement amplitude of wedge space under horizontal incident, Fig. 5.5, it can be seen that the existence of cylindrical depression makes the displacement amplitude of the left side of the wedge rises, while the displacement amplitude of the right side of the wedge declines.

While oblique incident and the wedge vertex angle is $\pi/3$, the amplitude of surface displacement at the depression is inversely proportional to the inhomogeneous parameter. Moreover, the displacement vibrations more obviously at wedge space both sides than at the depression position. The maximum value appears at the junction of the concave and wedge planes if $\beta < 1$, otherwise $\beta \geq 1$,it appears on the wedge plane. For $\phi = \pi/2$, the left plane displacement amplitude at $\beta = 1$ is greater than that of other inhomogeneous parameters, while the maximum displacement occurs in the right plane as $\beta > 1$ are taken. While $\phi = 2\pi/3$, the left place displacement at the incident angle side decreases significantly, and the surface displacement amplitude at $\beta = 1$ is greater than the value of other inhomogeneous parameters, and the maximum value appears at the left junction position. For $4\pi/3$, the left plane displacement is almost the same as that of $2\pi/3$, while on the right side it decreases to near zero.

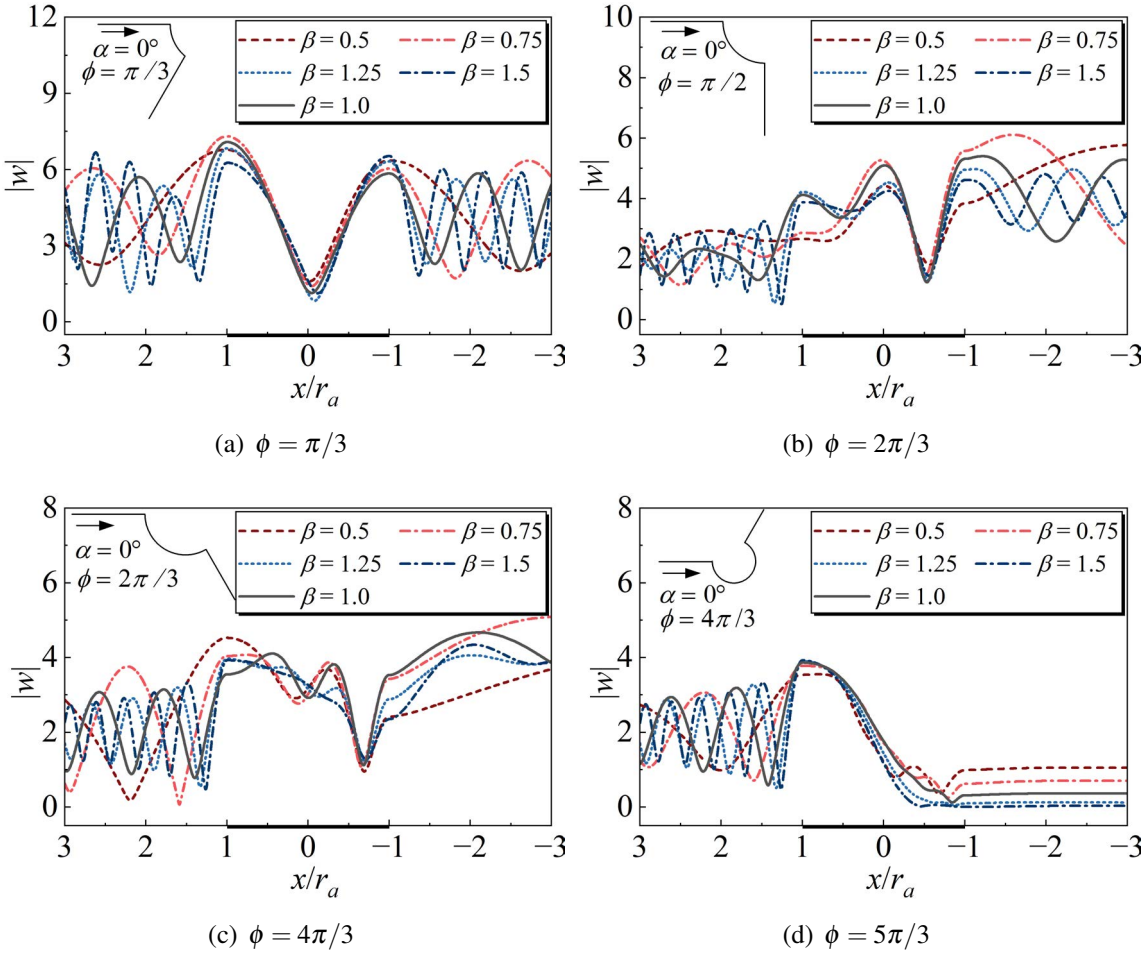

(a) $\phi = \pi/3$ (b) $\phi = 2\pi/3$

(c) $\phi = 4\pi/3$ (d) $\phi = 5\pi/3$

Fig. 5.18 Surface displacement amplitude of different inhomogeneous parameter under four types wedge space vertex angle with SH wave horizontal incident

Similarly, symmetrical incident is given. The surface displacement amplitude under each parameter is symmetrically distributed, as shown in Fig. 5.20. Under the four wedge vertex angles, the inhomogeneous parameters have a great influence on the surface displacement, which vibration with the change of position. At vertex angle setting as $\pi/3$ and $\pi/2$, the plane two sides displacement amplitude tends to reduced with the ascender of inhomogeneous parameters. Compared with the pure wedge Fig. 5.6, the plane displacement with cylindrical depression is reduced under symmetrical incident.

Compared with three sets of numerical examples, under the same wedge vertex angle, the displacement amplitude is inversely proportional to incident angle.The displacement amplitude at the bottom of the depression increases with the incident angle from horizontal to symmetrical, while at the junction of the depression and the two sides of the plane decreases

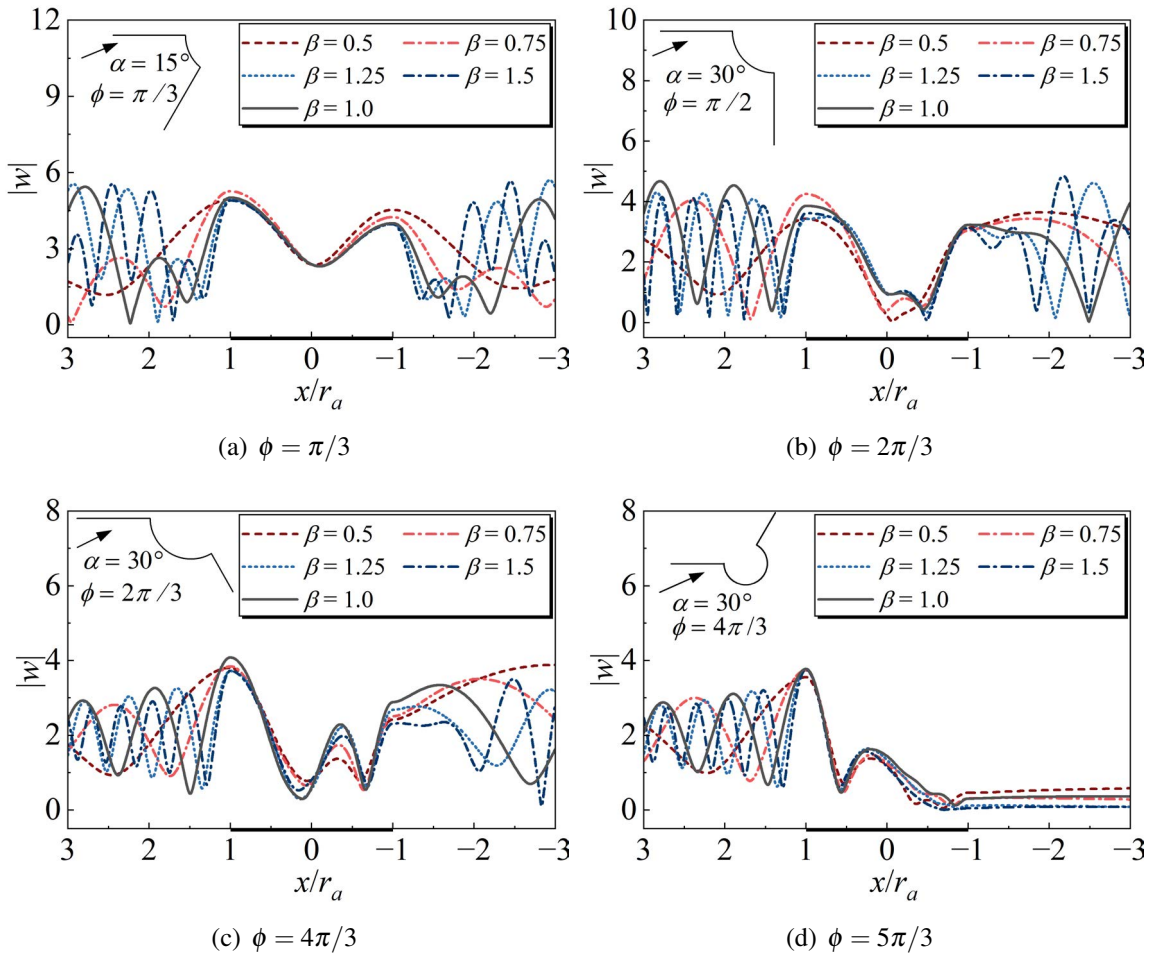

(a) $\phi = \pi/3$ (b) $\phi = 2\pi/3$

(c) $\phi = 4\pi/3$ (d) $\phi = 5\pi/3$

Fig. 5.19 Surface displacement amplitude of different inhomogeneous parameter under four types wedge space vertex angle with SH wave oblique incident

at $\phi = \pi/3, \pi/2$. At the same time, the amplitude of surface displacement tends to vibration at the same incident angle with β growing.

To further investigate the influence of inhomogeneous wedge with cylindrical depression on the surface displacement, six observation points were selected, point 1 (2, 0), point 2 (1, 0), point 3 (1, $\phi/3$), point 4 (1, $2\phi/3$), point 5 (1,ϕ), point 6 (2,ϕ). The displacement of each point was calculated under the different incident angles with the inhomogeneous parameter of 1.25, and the effect of cylindrical depression on surface displacement in the inhomogeneous wedge space was analyzed.

Fig.5.21 shows the displacement amplitude of six observation points with dimensionless frequency under horizontal incident and $\beta = 1.25$. Discussing the situation of $\phi = \pi/3$, the amplification effect of point 5 on the displacement amplitude is about 1.2 times, and the displacement amplitude of point 5 is stable around 7 after the dimensionless frequency

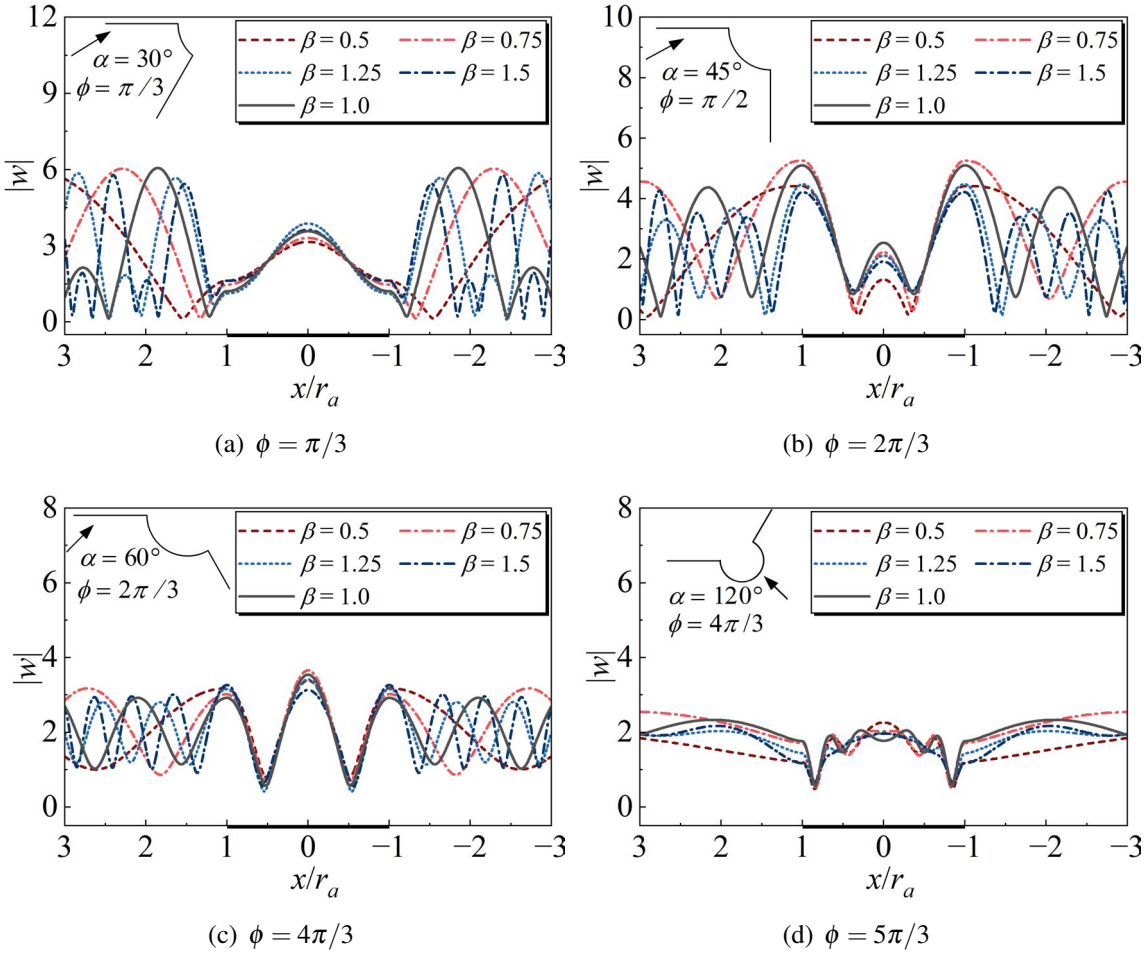

(a) $\phi = \pi/3$ (b) $\phi = 2\pi/3$

(c) $\phi = 4\pi/3$ (d) $\phi = 5\pi/3$

Fig. 5.20 Surface displacement amplitude of different inhomogeneous parameter under four types wedge space vertex angle with SH wave symmetric incident

reaches 1. And the observation point 2 reduces the displacement. The surface displacement of points 3 and 4 at the depression drops obviously, and vibrates at the displacement amplitude of about 3 with dimensionless frequency variation. The displacement amplitudes of points 1 and 6 show a regular vibration mode with dimensionless frequency increasing. Then at $2\pi/3$, the amplification characteristic of points 1, 4, 5 and 6 on the displacement is almost the same as $\phi = \pi/2$. However, points 2 and 3 indicate that the amplitude of surface displacement tends to be stable while the dimensionless frequency reaches to 1.5, as shown in Fig. 5.21 (b). Subsequently, at $2\pi/3$, it can be observed from Fig. 5.21 (c) that the point 6 has the largest amplification effect on the surface displacement amplitude, and the displacement amplitude of points 2, 3, and 6 tends to be stable and almost equal to 4 as the dimensionless frequency reaches 1.5. At point 5, after the dimensionless frequency is greater than 0.25, the displacement gradually decreases as it increases. Point 1 still presents a similar effect to

Figs. 5.21 (a) and (b), and its surrounding vibration value is 2. The displacement of point 4 is stabilized at 3 when the dimensionless frequency is 1.5. Considering the vertex angle as $4\pi/3$, compared with $2\pi/3$, the effect of points 1, 2 and 3 are similar. However, the displacement of points 4, 5 and 6 drops to near zero with dimensionless frequency growing and tends to be stable. From the four figures, the displacement of point 1 vibration with dimensionless frequency variation, and its amplitude is inversely proportional in vertex angle.

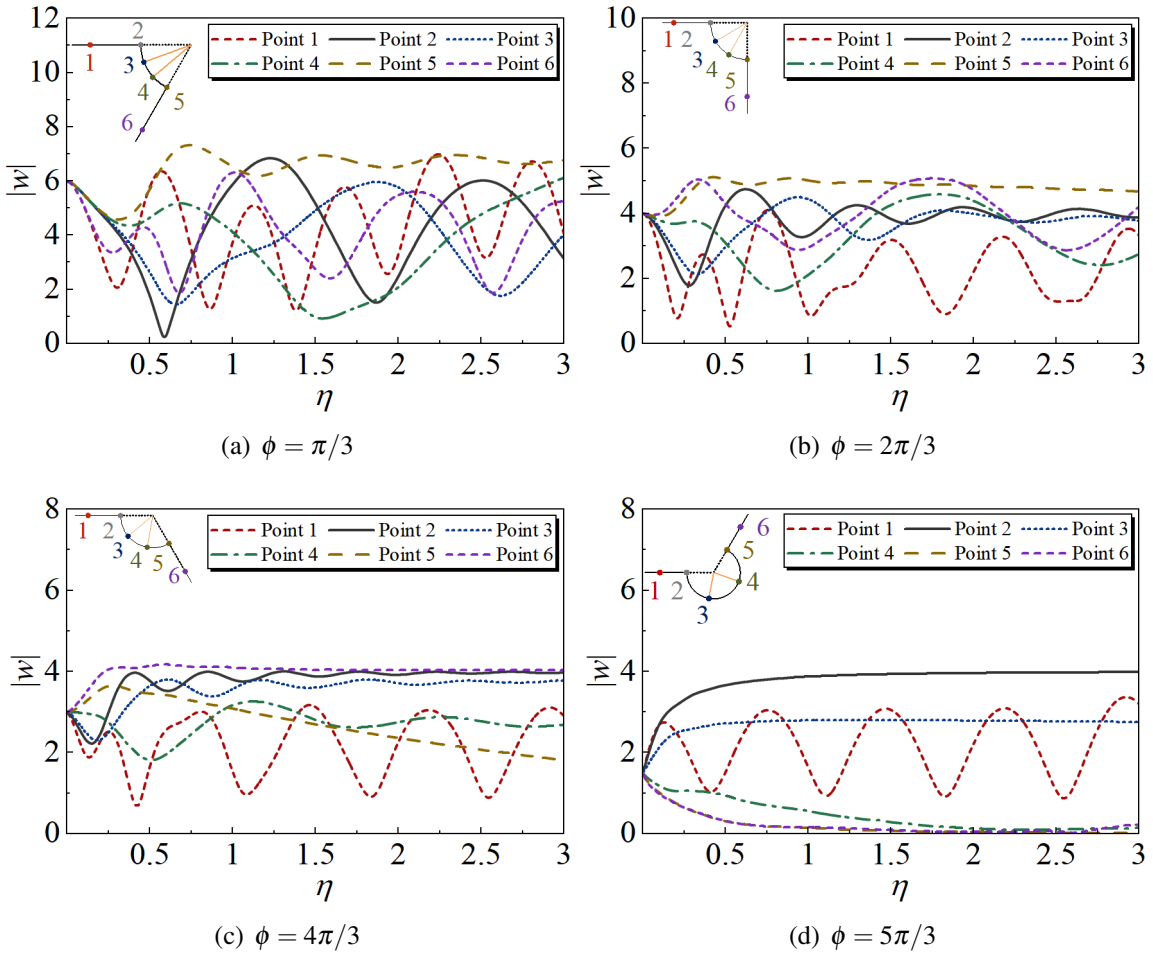

Fig. 5.21 Displacement amplitude of six selection observation points under inhomogeneous parameter $\beta = 1.25$ and horizontal incident

Change the incidence angle to oblique incident. Fig. 5.22 (a) indicates 15° oblique incident, and (b) (c) (d) shows 30° oblique incident. Primarily still discussing $\phi = \pi/3$, the six observation points displacement decreases compared with the horizontal incident, and the maximum amplification is 1 time. Among them, point 1 displacement drops most obviously, and the other points show the same phenomenon as the horizontal incident on

the whole. While $\phi = 2\pi/3$, point 5 displacement vibrates with dimensionless frequency, and the amplification effect on the displacement is 1.1 times. The displacement of points 3 and 6 also declines, while for points 1, 2 and 4 it various with dimensionless frequency in a similar manner to that at horizontal incident. At $\phi = 2\pi/3$, the amplification effect of point 3 and 6 decreases compared with the horizontal incidence, while point 5 shows the form of vibration with dimensionless frequency. The amplification effect of point 2 is still 1.3 times. Under $\phi = 4\pi/3$ and 30° oblique incident, the effect is almost the same as that of horizontal incident.

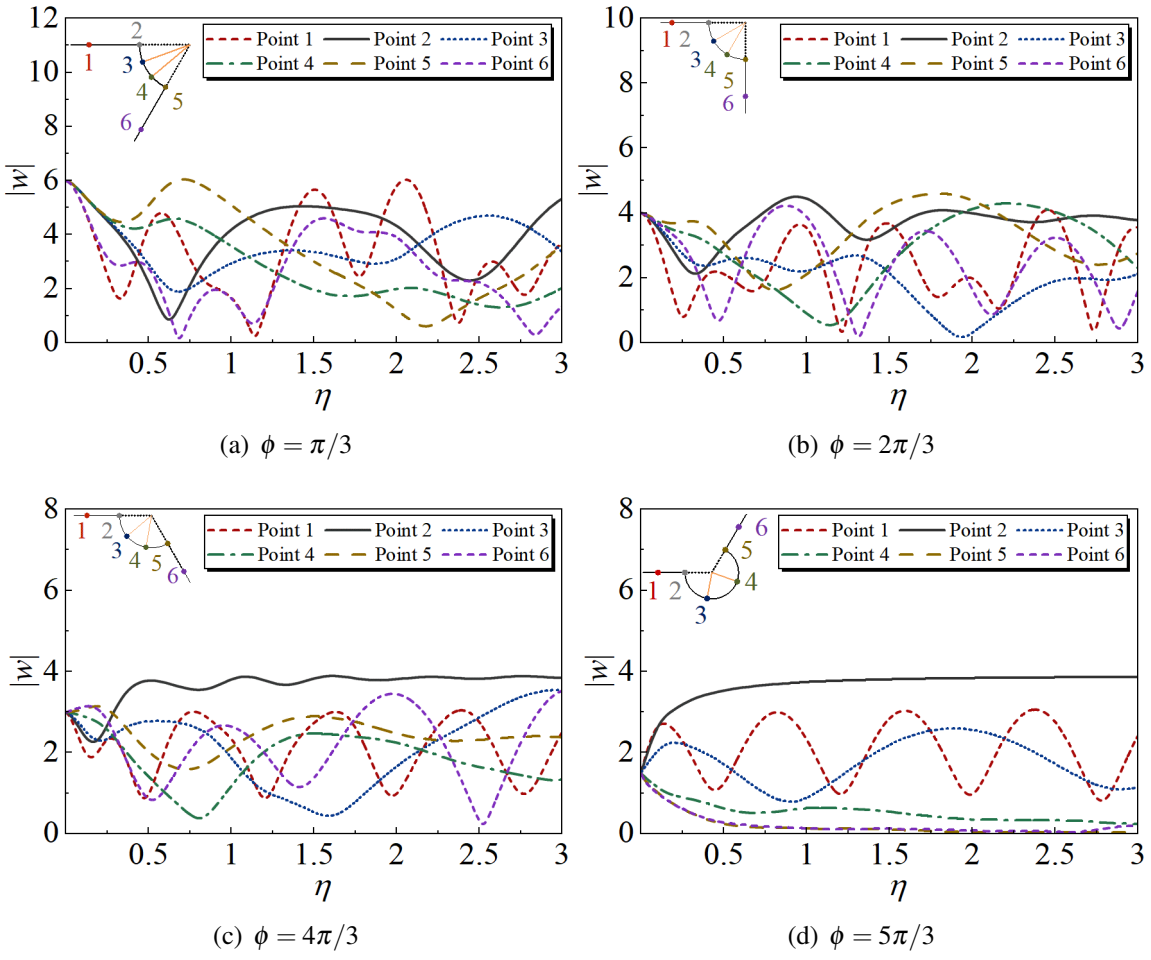

(a) $\phi = \pi/3$ (b) $\phi = 2\pi/3$

(c) $\phi = 4\pi/3$ (d) $\phi = 5\pi/3$

Fig. 5.22 Displacement amplitude of six selection observation points under inhomogeneous parameter $\beta = 1.25$ and oblique incident

Symmetrical incident also taken for investigating the effect, results are given in Fig. 5.23. For the situation of $\pi/3$, the displacement of each point further decreases, and the point displacement tends to zero at a certain dimensionless frequency. The maximum amplification effect is still 1 times, appearing at points 2 and 5. Next for $\pi/2$, and the

maximum amplification effect is 1.25 times. Then is $2\pi/3$, the amplification effect of point 2 only increases to the same as that of point 5 while compared with 30° incident. While the vertex angle is $4\pi/3$, the displacement basically tends to a stable change mode. Among them, points 1, 3, 4, and 6 stabilize around 2 after the dimensionless frequency reaches 0.5, while points 2 and 5 gradually declines to 1 when the dimensionless frequency is over 0.25. In addition, the amplification of displacement amplitude at points 1 and 6 can reach a maximum of 1.4 times under symmetrical incident. The comparison of the four figures illustrates that with the increase of the vertex angle, the displacement amplitude of each point decreases, while the maximum amplification effect on the displacement amplitude gradually increases. If $\phi < \pi$, points 2 and 5 have the greatest amplification effect on the displacement amplitude; else the points 1 and 6 is the largest.

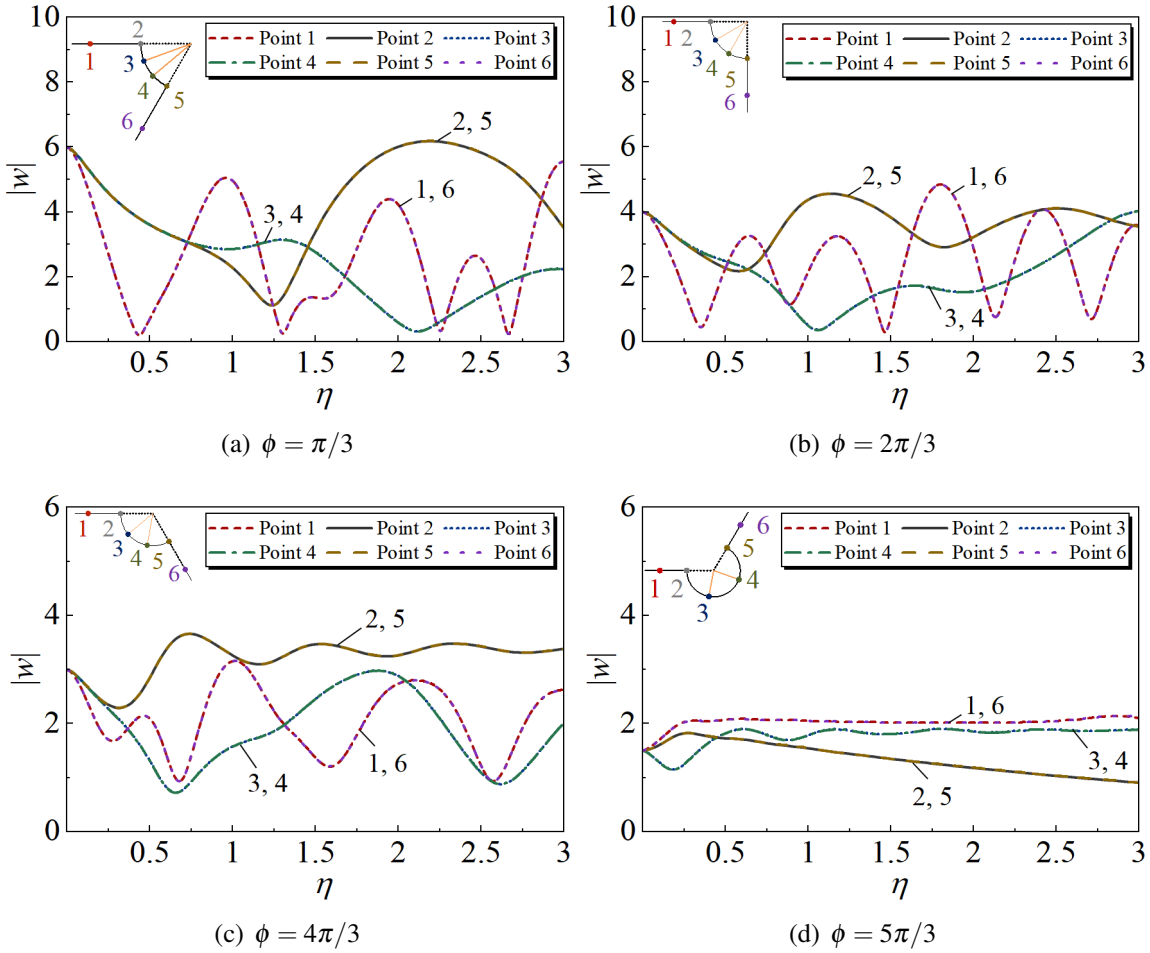

(a) $\phi = \pi/3$ (b) $\phi = 2\pi/3$

(c) $\phi = 4\pi/3$ (d) $\phi = 5\pi/3$

Fig. 5.23 Displacement amplitude of six selection observation points under inhomogeneous parameter $\beta = 1.25$ and symmetrical incident

In order to explore the amplification effect of each point on the displacement amplitude under different inhomogeneous parameters and incident angles, the displacement amplification coefficient w^* of each observation point under different vertex angles and various parameter settings is given, and w^* is given by Eq. (3.25), as shown in Table 5.1-5.4. The inhomogeneous parameters are setting as 0.75, 1.0 and 1.25. w^* corresponding to different dimensionless frequencies under horizontal, oblique and symmetric incident. Table 5.1 exhibits the result for vertex angle at $\pi/3$. From the calculation results, the maximum w^* of each observation point is inversely proportional to inhomogeneous parameters and incident angle. At the same time, the maximum value of w^* generally occurs at points 2 and 5, that is, the junction of the depression and wedge planes. However, w^* of points 3 and 4 in the cylindrical depression are similar under the action of different inhomogeneous parameters, and w^* changes gently with the dimensionless frequency in the case of oblique symmetrical incident. Under the influence of inhomogeneous parameters and incident angle, w^* at points 1 and 6 at two wedge planes presents an vibration mode with dimensionless frequency.

From Table 5.2 as the vertex angle is $\pi/2$, the w^* of the six points still has a decreasing trend with the inhomogeneous parameters rising, and has increasing trend compared with $\pi/3$. Comparing with w^* of each point under different inhomogeneous parameters, the overall value only changes, and the vibration trend with dimensionless frequency is almost the same. Most of w^* still appear at point 5 under various parameter settings, and w^* of point 5 is similar with the action of different dimensionless frequencies under horizontal incident.

Table 5.3 and 5.4 correspond to the calculation results for the wedge vertex angles are $2\pi/3$ and $4\pi/3$. In the two sets of results, the w^* is still inversely proportional to inhomogeneous parameters. At the vertex angle $2\pi/3$ and horizontal incident, w^* of points 2, 3 and 6 under three inhomogeneous parameters are basically stable at these dimensionless frequency. When $\beta = 1$, the w^* of point 5 also remains stable, at $\beta \neq 1$, the maximum value w^* appears at point 6, while $\beta = 1$, the maximum value of w^* appears at point 5. The maximum displacement amplification coefficient moves to observation point 2 under oblique incident. However, since the vertex angle reaches to $4\pi/3$, the w^* appears at point 2 at the maximum level under oblique incident, and at points 1 and 6 under symmetric incident. However, according to the above results, w^* is inversely proportional of inhomogeneous parameters at the same wedge vertex angle. Under the same inhomogeneous parameters, it inverse proportion in incident angle. While under horizontal and oblique incident, the maximum w^* value appears at point 5 under $\phi < \pi$, and appears at point 2 under $\phi > \pi$. For symmetrical incident, the maximum w^* value appears at points 2 and 5 under $\phi < \pi$, and occurs at points 1 and 6 under $\phi > \pi$.

Table 5.1 Displacement amplification coefficient of six points under three inhomogeneous parameters at vertex angle is $\pi/3$

	α	0°						15°						30°		
β	point / η	1	2	3	4	5	6	1	2	3	4	5	6	1,6	2,5	3,4
0.75	0.001	1.00	1.00	1.00	1.00	1.00	1.00	1.00	1.00	1.00	1.00	1.00	1.00	1.00	1.00	1.00
	0.5	0.28	0.42	0.50	0.71	0.82	0.81	0.20	0.47	0.53	0.67	0.75	0.66	0.34	0.60	0.60
	1.0	0.83	1.02	0.50	0.86	1.39	0.51	0.54	0.70	0.43	0.72	1.08	0.46	0.45	0.40	0.46
	1.5	1.06	1.00	0.65	0.24	0.99	0.56	0.34	0.78	0.53	0.35	0.51	0.27	0.92	0.30	0.50
	2.0	0.68	0.10	1.09	0.35	1.42	0.95	0.75	0.80	0.52	0.30	0.34	0.59	0.22	1.15	0.27
	2.5	0.79	1.04	0.55	0.56	1.01	0.72	0.53	0.43	0.72	0.31	0.12	0.47	0.52	0.87	0.17
	3.0	0.75	0.71	0.54	1.22	1.47	1.13	1.08	0.76	0.81	0.40	0.61	0.56	0.18	0.90	0.34
1.0	0.001	1.00	1.00	1.00	1.00	1.00	1.00	1.00	1.00	1.00	1.00	1.00	1.00	1.00	1.00	1.00
	0.5	0.62	0.37	0.48	0.73	0.87	0.80	0.41	0.43	0.51	0.69	0.79	0.60	0.13	0.60	0.60
	1.0	0.23	1.05	0.56	0.74	1.19	0.61	0.32	0.75	0.50	0.63	0.98	0.35	0.83	0.40	0.47
	1.5	0.86	1.04	0.72	0.15	1.12	0.77	0.18	0.83	0.55	0.33	0.51	0.15	0.23	0.43	0.53
	2.0	1.22	0.34	1.06	0.38	1.17	0.60	0.27	0.76	0.49	0.31	0.27	0.59	0.46	1.13	0.14
	2.5	0.79	1.20	0.41	0.79	1.23	0.60	0.73	0.28	0.85	0.37	0.26	0.78	0.84	0.96	0.21
	3.0	0.18	0.54	0.77	1.10	1.16	1.15	0.71	0.97	0.68	0.36	0.58	0.46	0.29	0.74	0.38
1.25	0.001	1.00	1.00	1.00	1.00	1.00	1.00	1.00	1.00	1.00	1.00	1.00	1.00	1.00	1.00	1.00
	0.5	0.97	0.29	0.44	0.77	0.95	0.70	0.71	0.37	0.48	0.72	0.85	0.46	0.71	0.37	0.48
	1.0	0.62	0.98	0.53	0.68	1.09	1.05	0.28	0.70	0.49	0.60	0.96	0.27	0.28	0.70	0.49
	1.5	0.58	0.86	0.82	0.16	1.16	0.46	0.95	0.84	0.56	0.33	0.50	0.75	0.95	0.84	0.56
	2.0	0.55	0.41	0.96	0.35	1.09	0.91	0.94	0.72	0.52	0.33	0.20	0.65	0.97	0.72	0.52
	2.5	0.55	1.00	0.36	0.79	1.14	0.40	0.43	0.40	0.78	0.23	0.27	0.37	0.43	0.40	0.78
	3.0	0.67	0.52	0.67	1.02	1.13	0.87	0.61	0.85	0.56	0.34	0.60	0.23	0.61	0.98	0.56

Table 5.2 Displacement amplification coefficient of six points under three inhomogeneous parameters at vertex angle is $\pi/2$

	α	0°			15°						30°					
β	point / η	1	2	3	4	5	6	1	2	3	4	5	6	1,6	2,5	3,4
0.75	0.001	1.00	1.00	1.00	1.00	1.00	1.00	1.00	1.00	1.00	1.00	1.00	1.00	1.00	1.00	1.00
	0.5	0.84	0.79	0.56	0.89	1.36	1.47	0.56	0.56	0.53	0.75	0.89	0.66	0.28	0.58	0.61
	1.0	0.75	0.83	1.06	0.36	1.23	1.29	0.08	1.06	0.56	0.30	0.36	0.69	0.68	0.92	0.28
	1.5	0.80	1.30	0.76	1.05	1.36	1.18	0.96	0.76	0.64	0.43	1.05	0.52	0.96	1.21	0.45
	2.0	0.05	0.65	1.24	1.31	1.37	1.12	0.85	1.24	0.33	1.16	1.31	0.70	0.63	0.73	0.35
	2.5	0.27	1.23	0.69	0.81	1.24	0.88	0.40	0.69	0.41	0.97	0.81	1.21	0.72	1.15	0.61
	3.0	0.63	0.97	1.24	0.68	1.27	0.57	0.24	1.24	0.60	0.85	0.68	0.42	0.26	0.97	0.97
1.0	0.001	1.00	1.00	1.00	1.00	1.00	1.00	1.00	1.00	1.00	1.00	1.00	1.00	1.00	1.00	1.00
	0.5	0.72	1.02	0.69	0.85	1.37	1.35	0.59	0.69	0.59	0.72	0.85	0.35	0.26	0.57	0.62
	1.0	0.94	0.69	1.15	0.47	1.35	1.00	0.75	1.15	0.53	0.28	0.47	0.92	0.14	1.11	0.19
	1.5	0.39	1.19	0.67	1.10	1.33	0.68	0.01	0.67	0.70	0.56	1.10	0.12	1.08	1.02	0.43
	2.0	0.65	1.01	1.19	1.23	1.33	0.96	0.34	1.19	0.22	1.14	1.23	0.97	0.77	0.67	0.35
	2.5	0.15	0.84	0.82	0.75	1.35	1.32	0.60	0.82	0.42	1.04	0.75	0.36	0.28	1.24	0.72
	3.0	0.54	1.14	1.15	0.66	1.37	1.37	0.59	1.15	0.51	0.73	0.66	1.25	0.74	0.85	0.99
1.25	0.001	1.00	1.00	1.00	1.00	1.00	1.00	1.00	1.00	1.00	1.00	1.00	1.00	1.00	1.00	1.00
	0.5	0.21	1.06	0.74	0.77	1.26	1.07	0.53	0.74	0.63	0.68	0.77	0.22	0.57	0.57	0.62
	1.0	0.22	0.83	1.11	0.53	1.25	0.74	0.89	1.11	0.55	0.23	0.53	0.97	0.54	1.10	0.12
	1.5	0.80	0.96	0.87	1.07	1.23	1.19	0.92	0.87	0.53	0.60	1.07	0.57	0.19	0.96	0.41
	2.0	0.55	1.04	1.00	1.10	1.21	1.18	0.50	1.00	0.08	1.03	1.10	0.41	0.72	0.81	0.39
	2.5	0.32	1.01	0.95	0.71	1.19	0.73	0.99	0.95	0.47	1.01	0.71	0.81	0.93	1.03	0.67
	3.0	0.83	0.97	0.95	0.69	1.17	1.05	0.89	0.95	0.53	0.57	0.69	0.40	0.90	0.89	1.01

Table 5.3 Displacement amplification coefficient of six points under three inhomogeneous parameters at vertex angle is $2\pi/3$

	α	0°						15°						30°		
β	point / η	1	2	3	4	5	6	1	2	3	4	5	6	1,6	2,5	3,4
0.75	0.001	1.00	1.00	1.00	1.00	1.00	1.00	1.00	1.00	1.00	1.00	1.00	1.00	1.00	1.00	1.00
	0.5	0.95	1.50	1.18	0.68	1.33	1.50	1.01	1.31	0.92	0.56	0.87	0.76	0.81	0.82	0.50
	1.0	0.39	1.32	1.13	1.05	1.25	1.57	0.47	1.12	0.73	0.22	0.57	0.83	0.51	1.39	0.50
	1.5	0.94	1.12	1.45	1.28	1.12	1.55	1.06	1.37	0.07	0.95	1.12	1.26	0.56	0.99	0.65
	2.0	0.51	1.18	1.15	0.76	0.98	1.49	0.80	1.35	0.24	0.77	1.15	0.49	0.95	1.42	1.09
	2.5	0.49	1.35	1.34	1.12	0.85	1.42	0.30	1.16	1.03	0.70	0.66	0.76	0.72	1.01	0.55
	3.0	0.89	1.44	1.36	1.25	0.76	1.35	0.84	1.36	1.08	0.51	0.68	0.76	1.13	1.47	0.54
1.0	0.001	1.00	1.00	1.00	1.00	1.00	1.00	1.00	1.00	1.00	1.00	1.00	1.00	1.00	1.00	1.00
	0.5	0.96	1.36	0.92	1.14	1.83	1.42	0.52	1.30	0.93	0.49	0.73	0.48	0.80	0.87	0.48
	1.0	1.25	0.92	1.53	0.63	1.81	1.52	0.88	1.18	0.72	0.29	0.64	0.93	0.61	1.19	0.56
	1.5	0.52	1.59	0.89	1.47	1.77	1.55	0.46	1.18	0.24	0.96	1.15	0.51	0.77	1.12	0.72
	2.0	0.86	1.34	1.59	1.64	1.77	1.53	0.87	1.30	0.49	0.70	1.07	0.88	0.60	1.17	1.06
	2.5	0.20	1.12	1.10	1.00	1.80	1.47	0.73	1.34	0.98	0.60	0.67	1.09	0.60	1.23	0.41
	3.0	0.72	1.52	1.54	0.88	1.83	1.38	0.77	1.29	1.22	0.49	0.88	0.56	1.15	1.16	0.77
1.25	0.001	1.00	1.00	1.00	1.00	1.00	1.00	1.00	1.00	1.00	1.00	1.00	1.00	1.00	1.00	1.00
	0.5	0.55	1.26	1.22	0.61	1.15	1.38	0.32	1.26	0.92	0.47	0.68	0.29	0.70	0.95	0.44
	1.0	0.51	1.27	1.19	1.06	1.03	1.36	0.78	1.27	0.62	0.39	0.71	0.88	1.05	1.09	0.53
	1.5	1.04	1.29	1.20	0.94	0.90	1.35	0.91	1.28	0.18	0.82	0.96	0.46	0.46	1.16	0.82
	2.0	0.76	1.31	1.24	0.92	0.79	1.34	0.33	1.27	0.55	0.75	0.83	1.15	0.91	1.09	0.96
	2.5	0.36	1.32	1.25	0.93	0.69	1.35	0.92	1.27	0.96	0.55	0.77	0.10	0.40	1.14	0.36
	3.0	0.97	1.32	1.26	0.90	0.61	1.35	0.84	1.28	1.18	0.44	0.79	1.17	0.87	1.13	0.67

Table 5.4 Displacement amplification coefficient of six points under three inhomogeneous parameters at vertex angle is $4\pi/3$

	α	0°			15°						30°					
β	point / η	1	2	3	4	5	6	1	2	3	4	5	6	1,6	2,5	3,4
0.75	0.001	1.00	1.00	1.00	1.00	1.00	1.00	1.00	1.00	1.00	1.00	1.00	1.00	1.00	1.00	1.00
	0.5	1.43	2.35	1.79	0.76	0.56	0.56	1.58	2.28	1.22	0.55	0.43	0.44	1.50	1.33	1.18
	1.0	1.05	2.48	1.93	0.67	0.46	0.49	0.74	2.43	0.46	0.29	0.20	0.21	1.57	1.25	1.13
	1.5	2.10	2.55	2.00	0.62	0.37	0.44	1.94	2.53	1.36	0.55	0.26	0.28	1.55	1.12	1.45
	2.0	1.12	2.59	2.04	0.56	0.30	0.38	1.75	2.58	1.87	0.57	0.34	0.41	1.49	0.98	1.15
	2.5	1.26	2.61	2.05	0.60	0.27	0.34	0.58	2.63	1.46	0.52	0.31	0.42	1.42	0.85	1.34
	3.0	2.15	2.62	2.05	0.60	0.25	0.31	1.74	2.65	0.84	0.27	0.22	0.33	1.40	0.76	1.36
1.0	0.001	1.00	1.00	1.00	1.00	1.00	1.00	1.00	1.00	1.00	1.00	1.00	1.00	1.00	1.00	1.00
	0.5	0.74	2.39	1.84	0.76	0.41	0.42	0.91	2.32	1.19	0.50	0.29	0.30	1.42	1.22	1.21
	1.0	2.06	2.55	1.94	0.58	0.25	0.28	1.90	2.48	0.51	0.40	0.18	0.20	1.52	1.18	1.06
	1.5	0.60	2.60	1.99	0.50	0.18	0.22	1.12	2.54	1.49	0.57	0.21	0.26	1.55	1.14	1.25
	2.0	2.09	2.62	2.02	0.46	0.13	0.18	1.72	2.58	1.88	0.52	0.16	0.20	1.53	1.10	1.33
	2.5	0.62	2.64	2.04	0.41	0.11	0.13	1.50	2.60	1.28	0.34	0.09	0.10	1.51	1.06	1.21
	3.0	1.82	2.64	2.06	0.36	0.08	0.06	1.40	2.61	0.64	0.39	0.09	0.27	1.23	1.03	1.27
1.25	0.001	1.00	1.00	1.00	1.00	1.00	1.00	1.00	1.00	1.00	1.00	1.00	1.00	1.00	1.00	1.00
	0.5	1.01	2.44	1.81	0.62	0.21	0.21	0.83	2.35	1.14	0.42	0.17	0.18	1.38	1.15	1.22
	1.0	1.09	2.58	1.86	0.37	0.09	0.10	1.55	2.49	0.59	0.41	0.08	0.08	1.36	1.03	1.19
	1.5	2.04	2.62	1.87	0.19	0.04	0.06	1.89	2.53	1.46	0.36	0.06	0.08	1.35	0.90	1.20
	2.0	1.48	2.64	1.86	0.08	0.03	0.03	0.65	2.56	1.71	0.23	0.02	0.05	1.34	0.79	1.24
	2.5	0.70	2.65	1.85	0.07	0.01	0.03	1.84	2.57	1.15	0.22	0.02	0.03	1.36	0.69	1.25
	3.0	2.13	2.65	1.84	0.09	0.01	0.15	1.62	2.57	0.77	0.16	0.01	0.13	1.40	0.61	1.26

Subsequently, continue to explore the influence of cylindrical depression and various parameters on the internal displacement amplitude of the wedge space, and give the corresponding calculation results, as shown in Figs. 5.24-5.27, the internal displacement amplitude distribution of different inhomogeneous parameters and incident angles under four wedge vertex angles.

Fig. 5.24 indicates the distribution of internal displacement amplitude under horizontal and symmetrical incident with the inhomogeneous parameters of 0.75 and 1.25 respectively under the vertex angle is $\pi/3$. The internal displacement under the action of two groups of inhomogeneous parameters presents an approximate symmetrical distribution compared with that of a simple wedge under the action of a cylindrical depression at horizontal incident. At the same time, the maximum area of the internal displacement is distributed on the right plane of the wedge, in Figs. 5.24 (a) and (c). Moreover, with the escalation of inhomogeneous parameters , the internal displacement becomes more complex, and the vibration frequency aggravates with position. For symmetrical incident situation, the area of maximum displacement is distributed on the symmetry axis as $\beta < 1$, while with $\beta > 1$, the area of maximum displacement is distributed on the planes, as shown in Figs. 5.24 (b) and (d). In addition, the displacement with the ascender of inhomogeneous parameters then rise compared with the upper and lower groups. Comparing with the model where vertex angle is a sharp point, ad Fig. 5.11, that the internal displacement is no longer completely symmetrical under incident horizontally from the depression.

The result of $\pi/2$ are demonstrated in Fig. 5.25, in the same way, horizontal incident is first considered. It can be seen from Figs. 5.25 (a) and (c) that, the maximum displacement is distributed in the left plane of the wedge with $\beta < 1$ and is distributed in the right plane of the wedge with $\beta > 1$. In both cases, the displacement amplitudes show certain vibrations. Moreover, at $\beta = 1.25$, the area with large internal displacement amplitude is distributed in a strip parallel to the right plane between the extreme angle of θ-axis 30° and 90°. In the case of symmetrical incidence, the internal displacement amplitude is symmetrically distributed. There is still a rule that when $\beta < 1$, the maximum displacement amplitude appears on the 45° symmetry axis, and when $\beta > 1$, it appears on the plane on both sides of the wedge, as shown in Figs. 5.25 (b) and (d).

In the case of horizontal incident with $2\pi/3$, the internal displacement amplitude corresponding to the two inhomogeneous parameters presents a strip distribution parallel to the right plane of the wedge. Meanwhile, the area with large displacement is located on the right side of the wedge, as shown in Figs. 5.26 (a) and (c). Since $\beta < 1$, pay attention to the junction between the depression and the left boundary, and its displacement is also in a large range. Under the condition that two inhomogeneous parameters and symmetrically incident,

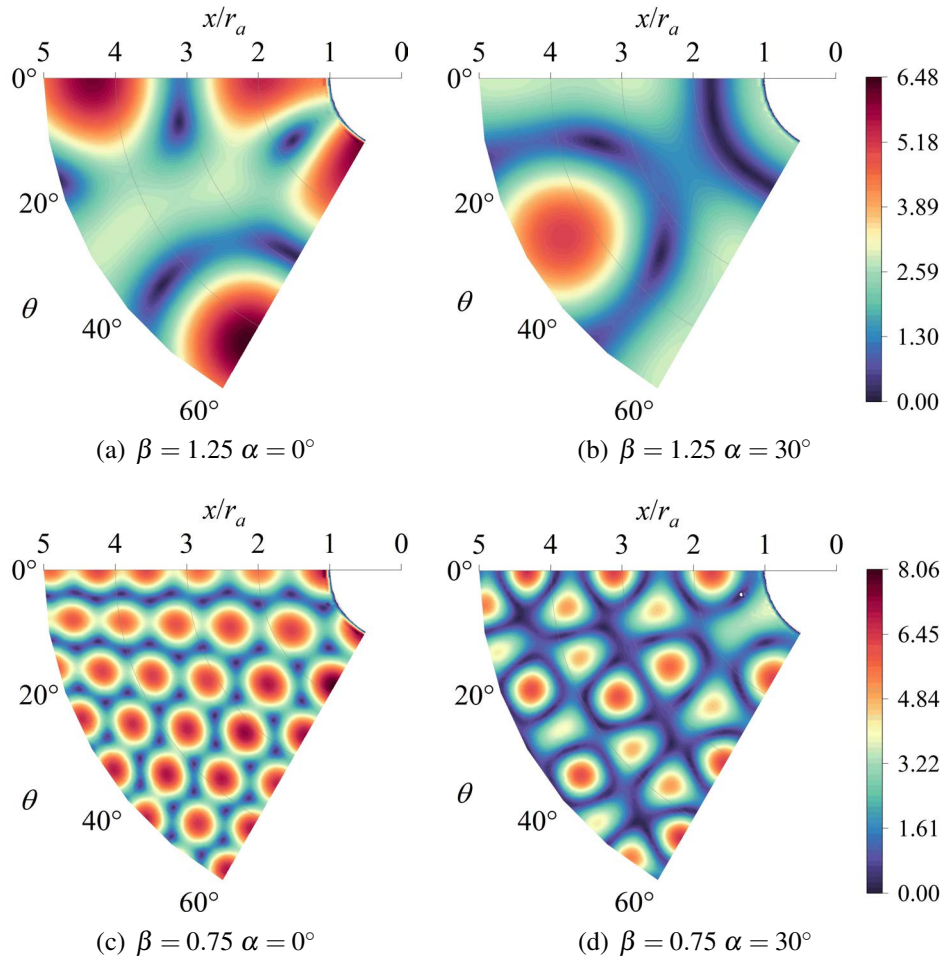

(a) $\beta = 1.25$ $\alpha = 0°$ (b) $\beta = 1.25$ $\alpha = 30°$

(c) $\beta = 0.75$ $\alpha = 0°$ (d) $\beta = 0.75$ $\alpha = 30°$

Fig. 5.24 Internal displacement amplitude distribution of vertex angle $\pi/3$ under two inhomogeneous parameters and incident angles

the maximum displacement is distributed on the plane of both sides of the wedge, still in the form of vibration distribution. As the vertex angle is less than or equal to $\pi/2$, the maximum displacement distribution of symmetrical incidence moves from the symmetry center to the plane on both sides of the wedge as $\beta < 1$. Meanwhile, from the figure that the displacement amplitude distributed below the depression gradually is inversely proportional to incident angle.

The distribution of internal displacement with $4\pi/3$ is shown in Fig. 5.26. It can be observed from the displacement is basically distributed within 180° under the horizontal incident, and the band area of internal displacement distribution is parallel to the radial direction of 150°. Moreover, if $\beta < 1$, the distribution of the larger displacement is located in the left plane, while $\beta > 1$, it is distributed below the left plane. Then, under symmetrical incident, the internal displacement is also distributed in a linear area, and the distribution

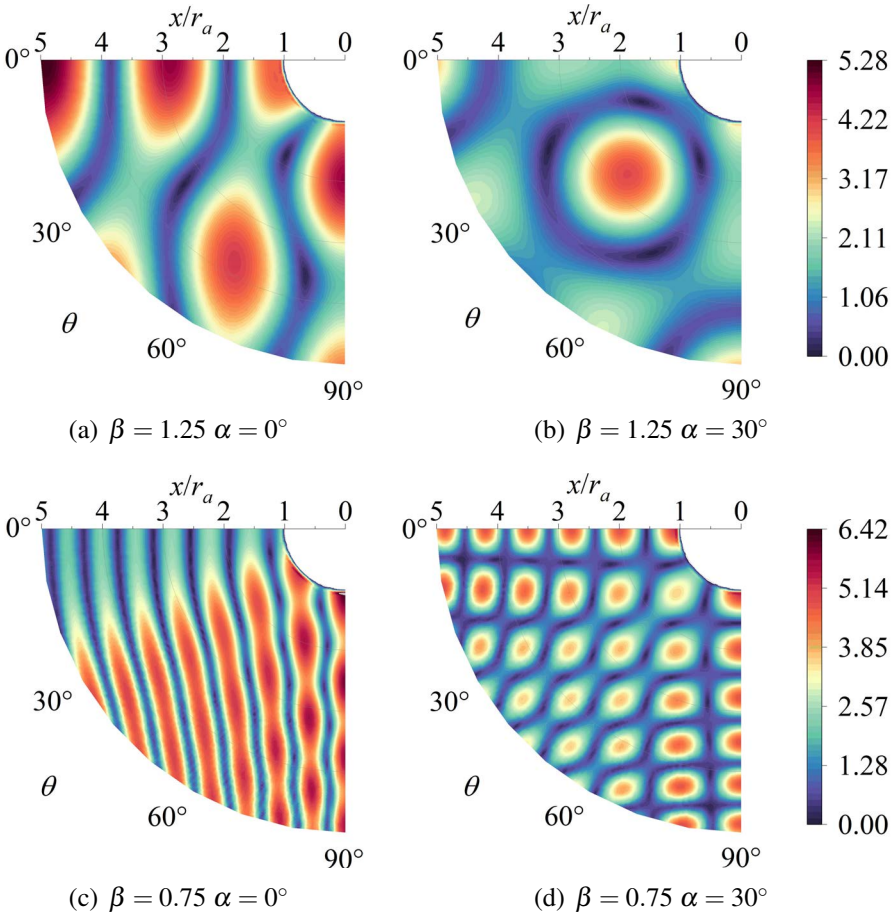

(a) $\beta = 1.25$ $\alpha = 0°$ (b) $\beta = 1.25$ $\alpha = 30°$

(c) $\beta = 0.75$ $\alpha = 0°$ (d) $\beta = 0.75$ $\alpha = 30°$

Fig. 5.25 Internal displacement amplitude distribution of vertex angle $\pi/2$ under two inhomogeneous parameters and incident angles

of the larger displacement under the two inhomogeneous parameters is in the plane on both sides. Compared with the pure wedge (Fig. 5.13), the displacement distribution in the interior is weakened, and the linear distribution is obvious.

Based on the above four sets of calculation examples of internal displacement amplitude distribution under the wedge vertex angle, it can be found that with the wedge vertex angle increasing, the internal displacement amplitude gradually presents a linear distribution parallel to the right plane at horizontal incident, and with the ascender of inhomogeneous parameters, the linear gradually narrows, that is, the vibration frequency of displacement aggravates. If the wedge apex angle is less than π, the internal displacement amplitude is symmetrically distributed in a blocky region, while over π, it is distributed in a linear region. With the ascender of inhomogeneous parameters and wedge angle, the region with large displacement amplitude gradually moves from the internal symmetry axis to the wedge plane on both sides.

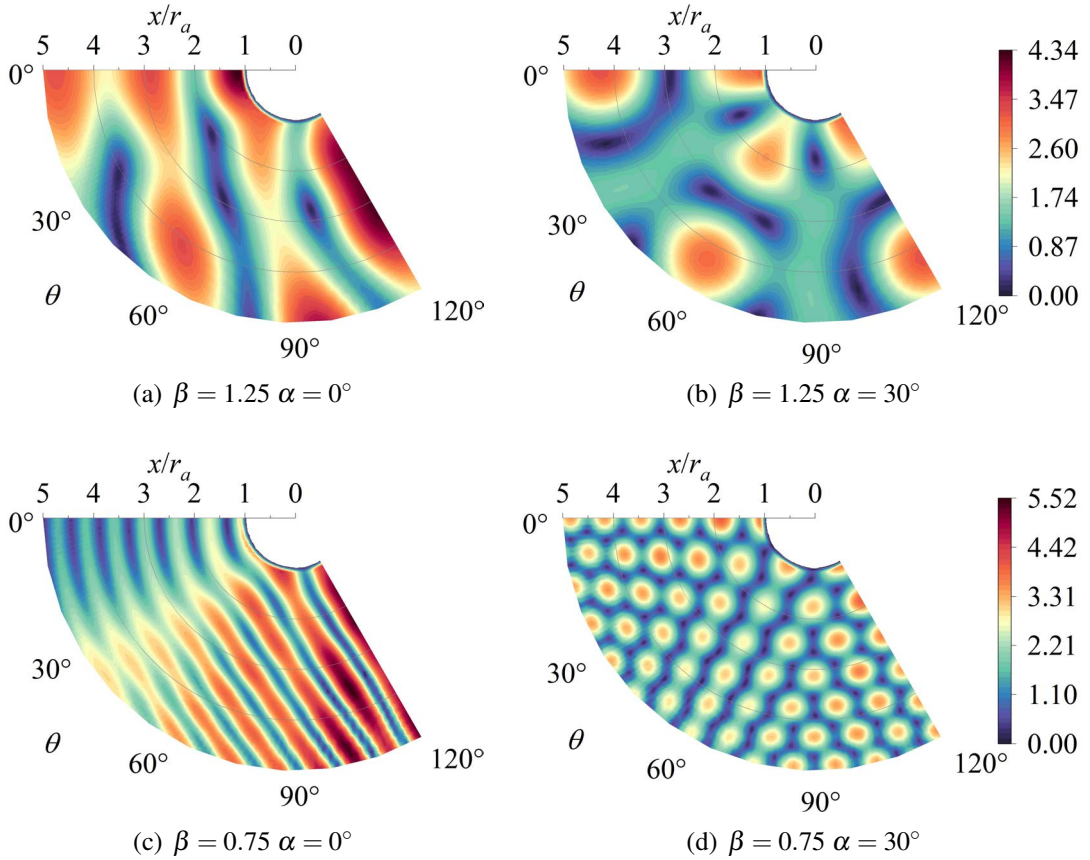

(a) $\beta = 1.25$ $\alpha = 0°$ (b) $\beta = 1.25$ $\alpha = 30°$

(c) $\beta = 0.75$ $\alpha = 0°$ (d) $\beta = 0.75$ $\alpha = 30°$

Fig. 5.26 Internal displacement amplitude distribution of vertex angle $2\pi/3$ under two inhomogeneous parameters and incident angles

5.3 Summary

In this chapter, based on the complex method, the dynamic response in density inhomogeneous wedge space with a cusp and cylindrical depression under SH wave incident is investigated. According to the governing equation obtained after transformation, using the free stress condition and Sommerfeld radiation condition at the boundary of both sides, the expression of free wave field in the density radial inhomogeneous wedge space and the expression of scattering wave field generated by the cylindrical depression are constructed. The validation of this method is verified by setting the medium parameters to be similar to the existing results. Then, the displacement distribution on the surface and inside of the wedge space is calculated, and the influence of various parameters on the displacement distribution is analyzed.

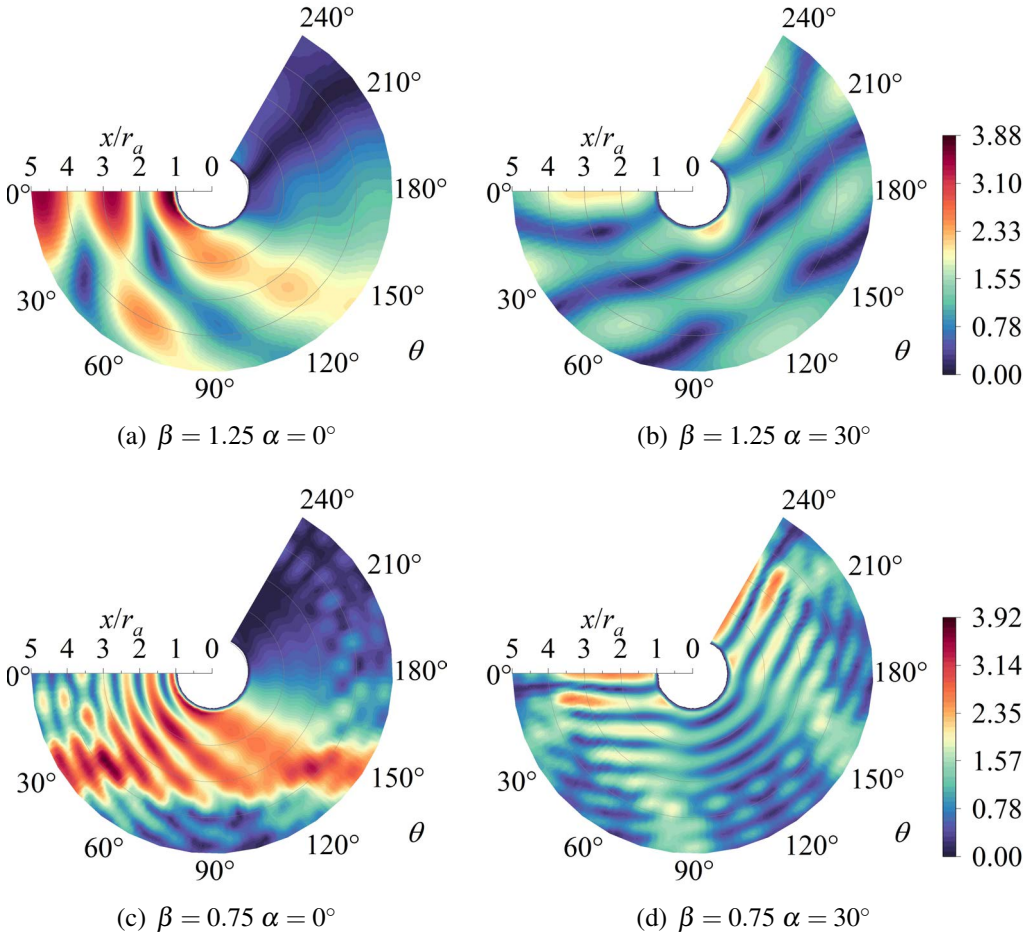

(a) $\beta = 1.25$ $\alpha = 0°$ (b) $\beta = 1.25$ $\alpha = 30°$

(c) $\beta = 0.75$ $\alpha = 0°$ (d) $\beta = 0.75$ $\alpha = 30°$

Fig. 5.27 Internal displacement amplitude distribution of vertex angle $4\pi/3$ under two inhomogeneous parameters and incident angles

Chapter 6

Simulation of 3D wave problems in semi-infinite space based on CUF

Numerical methods have a long-term history of development in wave problems, and the employment of numerical methods for solving complex boundary or large-scale calculations is a cost-effective approach. Research on numerical methods for solving wave problems is also continuously being conducted. The finite element method (FEM) has the advantages of clear physical concepts and accurate representation of complex geometries and material properties; therefore, it has extensive applications and long development in wave problems, especially in scattering problems of irregular shapes and media. FEM based on Carrera Unified Formulation (CUF) has a general framework for higher-order structure theory with variable kinematic description, which derives a three-dimensional description of the field variables by describing the cross section and thickness of the one- and two-dimensional models by the two-dimensional expansion function and the one-dimensional thickness function, respectively, and the results are satisfied the accuracy of the full three-dimensional, but significantly reduce the computational effort. This method is effectively improved the computational speed in large wave propagation problems. During the joint training in MUL2 group, Politecnico di Torino, based on the FEM with CUF framework, an effective absorption boundary and external wave input process are established in the self-developed Fortran program, in this chapter. And then, applying the proposed process simulate and analyze the wave propagation in the superstructure and layered media considering the external wave input.

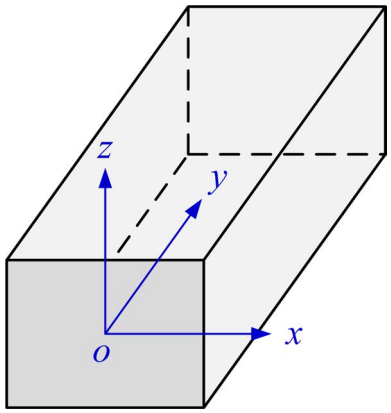

Fig. 6.1 Model of generalized beam element

6.1 Finite element based on CUF framework

6.1.1 CUF theory

In this section we consider a general beam model as shown in Fig. 6.1, with the Cartesian coordinate system (x,y,z), where the $x-z$ plane and y direction represent the cross-section and longitudinal axes of the 3D beam model, respectively, whose displacement vector could be defined as

$$\mathbf{u}(x,y,z) = \begin{Bmatrix} u_x & u_y & u_z \end{Bmatrix}^T \tag{6.1}$$

where u_x, u_y and u_z are the displacement component, the superscript T stands for the transposition operator. Stress σ and strain ε are as follows

$$\begin{aligned} \sigma_p &= [\sigma_{zz} \quad \sigma_{xx} \quad \sigma_{zx}]^T, \varepsilon_p = [\varepsilon_{zz} \quad \varepsilon_{xx} \quad \varepsilon_{zx}]^T \\ \sigma_n &= [\sigma_{zy} \quad \sigma_{xy} \quad \sigma_{yy}]^T, \varepsilon_n = [\varepsilon_{zy} \quad \varepsilon_{xy} \quad \varepsilon_{yy}]^T \end{aligned} \tag{6.2}$$

where the subscript n represents the terms laying on the cross-section and p represents the terms laying on planes which are orthogonal to cross-section ω. Linear strain-displacement relations are used

$$\begin{aligned} \varepsilon_p &= \mathbf{D}_p \mathbf{u} \\ \varepsilon_n &= \mathbf{D}_n \mathbf{u} = (\mathbf{D}_{n\omega} + \mathbf{D}_{ny})\mathbf{u} \end{aligned} \tag{6.3}$$

where

$$\mathbf{D}_p = \begin{bmatrix} 0 & 0 & \partial/\partial z \\ \partial/\partial x & 0 & 0 \\ \partial/\partial z & 0 & \partial/\partial x \end{bmatrix}, \mathbf{D}_{n\omega} = \begin{bmatrix} 0 & \partial/\partial z & 0 \\ 0 & \partial/\partial x & 0 \\ 0 & 0 & 0 \end{bmatrix}, \mathbf{D}_{ny} = \begin{bmatrix} 0 & 0 & \partial/\partial y \\ \partial/\partial y & 0 & 0 \\ 0 & \partial/\partial y & 0 \end{bmatrix}$$

According to Hooke's law

$$\sigma = \mathbf{C}\varepsilon \tag{6.4}$$

Applying Eq. (6.2) to the above equation, can be obtained

$$\sigma_p = \tilde{\mathbf{C}}_{pp}\varepsilon_p + \tilde{\mathbf{C}}_{pn}\varepsilon_n,\ \sigma_n = \tilde{\mathbf{C}}_{np}\varepsilon_p + \tilde{\mathbf{C}}_{nn}\varepsilon_n \tag{6.5}$$

where the coefficient matrices are as follows

$$\tilde{\mathbf{C}}_{pp} = \begin{bmatrix} \tilde{C}_{11} & \tilde{C}_{12} & \tilde{C}_{16} \\ \tilde{C}_{12} & \tilde{C}_{22} & \tilde{C}_{26} \\ \tilde{C}_{16} & \tilde{C}_{26} & \tilde{C}_{66} \end{bmatrix}, \tilde{\mathbf{C}}_{nn} = \begin{bmatrix} \tilde{C}_{55} & \tilde{C}_{45} & 0 \\ \tilde{C}_{45} & \tilde{C}_{44} & 0 \\ 0 & 0 & \tilde{C}_{33} \end{bmatrix} \tilde{\mathbf{C}}_{pn} = \tilde{\mathbf{C}}_{np}^{T} = \begin{bmatrix} 0 & 0 & \tilde{C}_{13} \\ 0 & 0 & \tilde{C}_{23} \\ 0 & 0 & \tilde{C}_{36} \end{bmatrix}$$

Based on the CUF framework, displacement field $\mathbf{u}$ could be defined as

$$\mathbf{u}(x,y,z) = F_\tau(x,z)\,\mathbf{u}_\tau(y)\ \tau = 1,2,...,M \tag{6.6}$$

where $F_\tau(x,z)$ is the cross-sectional expansion function that defines the cross-section kinematics of the numerical model, M denotes the number of terms of the polynomial in the expansion function, and $\mathbf{u}_\tau(y)$ denotes the vector of generalized displacements. The use of the expansion function on the cross-section of a one-dimensional model generates the corresponding three-dimensional displacement field and the relevant three-dimensional strain and stress tensor. The appropriate $F_\tau(x,z)$ and M were selected in order to determine the structural theory used in the model. Various basic functions, such as exponential and trigonometric functions, are available as expansion functions without any modification to the formulas, among which the more used ones are Taylor Expansion and Lagrange Expansion, the specific expressions of these two expansions are given below.

6.1.2 Taylor expansion

The Taylor Expansion (TE) is based on the Taylor (McLaughlin polynomial) series, the cross-sectional expansion function $F_\tau(x,z)$ is expanded to an order of N, and its polynomial expansion can be obtained from Pascal's triangle, as shown in Table **??**.

Then, the second order Taylor expansion ($N = 2$), could be written as

$$\begin{cases} u_x = u_{x1} + xu_{x2} + zu_{x3} + xzu_{x4} + x^2u_{x5} + z^2u_{x6} \\ u_y = u_{y1} + xu_{y2} + zu_{y3} + xzu_{y4} + x^2u_{y5} + z^2u_{y6} \\ u_z = u_{z1} + xu_{z2} + zu_{z3} + xzu_{z4} + x^2u_{z5} + z^2u_{z6} \end{cases} \tag{6.7}$$

Table 6.1 Taylor polynomials

order	number	F_τ
0	1	$F_1 = 1$
1	3	$F_2 = x\ F_3 = z$
2	6	$F_4 = x^2\ F_5 = xz\ F_6 = z^2$
...	...	...
N	$(N+1)(N+2)/2$	$F_{(N^2+N+2)/2} = x^N \ldots F_{(N+1)(N+2)/2} = z^N$

6.1.3 Lagrange expansion

Lagrange Expansion (LE) is the use of Lagrange interpolation polynomials to describe the cross-sectional geometry. In CUF, the LE polynomial is related in cross-section using element form, generally denoted as *Ln*, where *n* denotes the number of nodes in the cross-section element. If a four-node element is used, the displacement field based on the Lagrange polynomial can be expressed as

$$\begin{cases} u_x = \sum_{\tau=1}^{4} F_\tau(x,z) u_{x\tau}(y) \\ u_y = \sum_{\tau=1}^{4} F_\tau(x,z) u_{y\tau}(y) \\ u_z = \sum_{\tau=1}^{4} F_\tau(x,z) u_{z\tau}(y) \end{cases} \tag{6.8}$$

where τ indicates the number of nodes, $u_{x\tau}$,$u_{y\tau}$,$u_{z\tau}$ is the translational degrees of freedom of the nodes. F_τ on the quadrilateral domain defined in the natural coordinate system (r,s), LE as a function of four interpolation points (L4) is

$$F_\tau = \frac{1}{4}(1+rr_\tau)(1+ss_\tau)\ \tau = 1,2,3,4 \tag{6.9}$$

where r and s are defined from -1 to 1, r_τ and s_τ are the coordinates of the nodes τ. If a nine-node element is used, its corresponding Lagrange Expansion function (L9) can be written as

$$\begin{aligned} F_\tau = &\left[\frac{1}{4}rr_\tau(1+rr_\tau) + (1-r^2)(1-r_\tau^2)\right] \\ &\left[\frac{1}{4}ss_\tau(1+ss_\tau) + (1-s^2)(1-s_\tau^2)\right] \qquad \tau = 1,2,3,...,9 \end{aligned} \tag{6.10}$$

By mapping, the functions defined in the natural coordinate system (r,s) could be transformed into the Cartesian coordinate system (x,y) on the cross-sectional definition field,

and the mapping function is as follows

$$\begin{cases} x = x_\tau F_\tau(r,s) \\ z = z_\tau F_\tau(r,s) \end{cases} \tag{6.11}$$

where x_τ and z_τ represent the coordinates of the nodes within the Cartesian coordinate system. The result of the expansion using the LE function is a pure translational degree of freedom in global coordinates, which has an advantage over TE higher order degrees of freedom that do not have physical significance. Moreover, by increasing the number of Lagrange element, the cross section can be locally refined.

6.1.4 Finite element method formulations

Adopting the Finite Element method to discrete the structure along the y axis and interpolating the displacement variables along the y direction by means of the shape functionN_i, Eq. (6.1) could be written as

$$\mathbf{u}(x,y,z) = F_\tau(x,z)N_i(y)\mathbf{q}_{\tau i} \qquad \tau = 1,2,...,M, \qquad i = 1,2,...,n_N \tag{6.12}$$

where $\mathbf{q}_{\tau i}$ for the nodal displacement $\mathbf{q}_{\tau i} = \begin{bmatrix} q_{x_{\tau i}} & q_{y_{\tau i}} & q_{z_{\tau i}} \end{bmatrix}^T$, n_N stands for the order of the shape functions, the repeated subscripts i and τ denote the sum, with a range of one to the number of elemental nodes and functions contained in the kinematic model, respectively. The axial shape function N_i in the y-direction is independent of the choice of the cross-sectional expansion function F_τ, thereby providing flexibility in the modeling process. As the 3D wave propagation problem with damping can be expressed

As the 3D wave propagation problem with damping can be expressed

$$\nabla^2\mathbf{u} + \mathbf{f} = \rho\ddot{\mathbf{u}} + \xi\dot{\mathbf{u}} \tag{6.13}$$

where $\mathbf{f}$ is the body force vector, ρ is the mass density, ξ is the damping coefficient and ∇ is divergence operator.

Given the Principle of Virtual Work (PVK), the internal work δL_{int} could be related to the works of inertial δL_{iner}, damping δL_{damp} and external loads δL_{ext}

$$\delta L_{int} = -\delta L_{iner} - \delta L_{damp} + \delta L_{ext} \tag{6.14}$$

where δ stands for the virtual variation. The substitution of Eqs. (6.3) and (6.12) into Eq. (6.14) leads to the following expressions

$$\begin{aligned}
\delta L_{int} &= \delta \mathbf{q}_{\tau i}^T \mathbf{K}_s^{ij\tau s} \mathbf{q}_{sj} \\
\delta L_{ine} &= \delta \mathbf{q}_{\tau i}^T \mathbf{M}^{ij\tau s} \ddot{\mathbf{q}}_{sj} \\
\delta L_{damp} &= \delta \mathbf{q}_{\tau i}^T \mathbf{C}^{ij\tau s} \dot{\mathbf{q}}_{sj} \\
\delta L_{ext} &= \delta \mathbf{q}_{\tau i}^T \mathbf{F}^{\tau i}
\end{aligned} \tag{6.15}$$

where $\mathbf{K}^{ij\tau s}$, $\mathbf{M}^{ij\tau s}$, $\mathbf{C}^{ij\tau s}$, $\mathbf{F}^{\tau i}$ are called Fundamental Nuclei (FN) of the stiffness matrix, mass matrix, damping matrix, and external load vector, respectively. The additional indexes s and j are used to express the virtual displacement vector in the unified formulation $\delta \mathbf{u}(x,y,z,t) = F_s(x,z) N_j(y) \mathbf{q}_{sj}(t)$ and they have the bounds of τ and i, respectively. The process of assembling the overall stiffness matrix from the FN is given in Fig.6.2. FN is a 3×3 matrix of the following form

$$\mathbf{K}^{ij\tau s} = \begin{bmatrix} K_{\tau sij}^{xx} & K_{\tau sij}^{xy} & K_{\tau sij}^{xz} \\ K_{\tau sij}^{yx} & K_{\tau sij}^{yy} & K_{\tau sij}^{yz} \\ K_{\tau sij}^{zx} & K_{\tau sij}^{zy} & K_{\tau sij}^{zz} \end{bmatrix} \tag{6.16}$$

The expressions of the above matrices are

$$\begin{aligned}
\mathbf{M}^{ij\tau s} &= \int_L \int_\Omega \left(N_i F_\tau \rho \mathbf{I} N_j F_s \right) d\Omega dy \\
\mathbf{C}^{ij\tau s} &= \int_L \int_\Omega \left(N_i F_\tau \xi \mathbf{I} N_j F_s \right) d\Omega dy \\
\mathbf{K}^{ij\tau s} &= \int_L \int_\Omega \left(N_i F_\tau \mathbf{D}^T \mathbf{C} \mathbf{D} N_j F_s \right) d\Omega dy \\
\mathbf{F}^{\tau i} &= \int_L \int_\Omega \left(N_i F_\tau \mathbf{F} \right) d\Omega dy = \int_L \int_\Omega \left(N_i F_\tau \mathbf{f} \right) d\Omega dy + \int_S \left(N_i F_\tau \mathbf{t^n} \right) dS \\
&\quad + \int_l \left(N_i F_\tau \mathbf{Q} \right) dl + \sum_{i=1}^{N} \left(N_i F_\tau \mathbf{F} \right) \mathbf{P}_i
\end{aligned} \tag{6.17}$$

where L, Ω are the length and cross-section area of the element, while S, l are the external surface and line boundaries of the element where the traction vector $\mathbf{t^n}$ and the line force vector $\mathbf{Q}$ is applied, $\mathbf{P}_i$ is point force to the element, $\mathbf{I}$ is the identity matrix. The global FE matrices and vectors related to arbitrary kinematic expansions are automatically obtained by

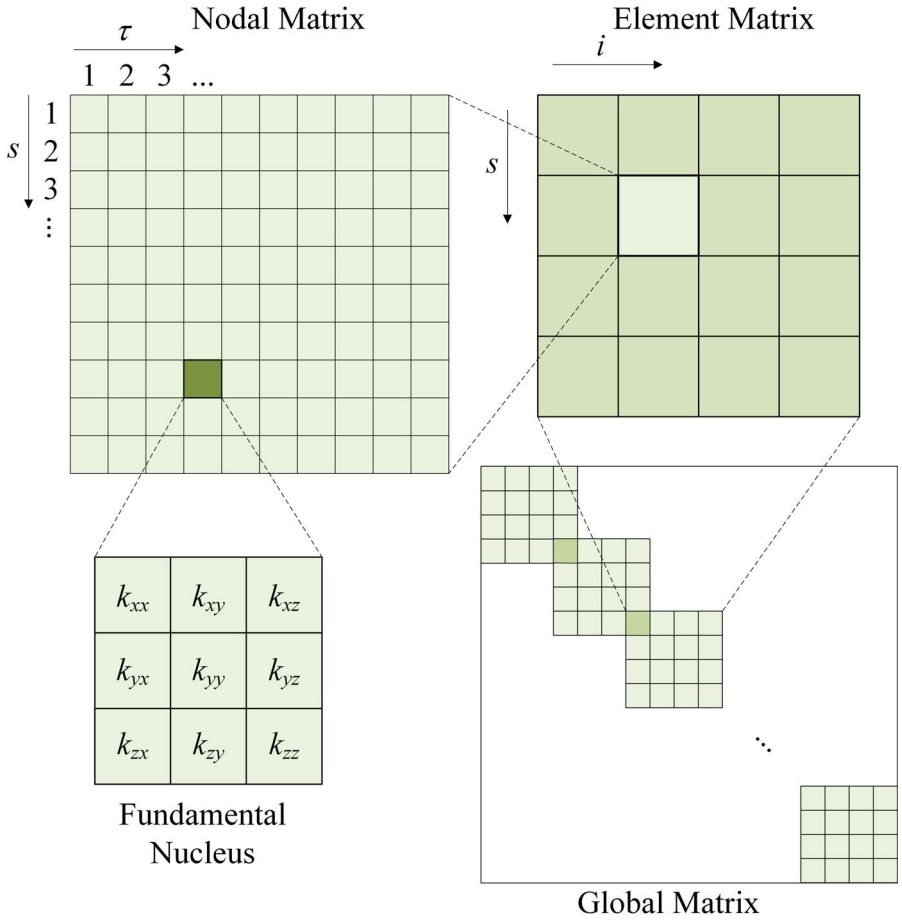

Fig. 6.2 Assembly of the global stiffness matrix from the FN

permuting the four indexes and assembling the FN [18]. Eventually, the equation of motion in the time domain are

$$\mathbf{M\ddot{u}}(t)+\mathbf{C\dot{u}}(t)+\mathbf{Ku}(t)=\mathbf{F}(t) \tag{6.18}$$

The Newmark time integration scheme is employed in this work to resolve the system. For the sake of brevity, readers are referred to [124] for details about this implicit time integration scheme.

6.2 Artificial boundary condition based on CUF framework FEM

6.2.1 The establishment and realization of artificial boundary

Artificial boundaries are usually considered while researching the dynamic response under elastic waves in a local region or intercepting the dynamic response of a partial region under external forces for ensuring the accuracy of the simulation results. The LE approach has two main features: (1) the kinematic field approximation can be varied locally, and (2) the nodal unknowns are the displacements of the sectional nodes. In particular, the second feature is shared with the conventional solid finite element formulations and significantly facilitates the application of the local artificial boundaries. Based on this feature, spring and damping are set at artificial boundary element nodes in combination with traditional finite element formulas to establish a viscous-spring absorbing boundary (VSAB), as shown in Fig. 6.2. The VSAB is a stress type local artificial boundary, which has a well effect on absorbing the scattering wave energy on the boundary. Meanwhile, VSAB is able to simulate the resilience of a semi-infinite space [86, 99, 98]. Moreover, the it also has a good simulation effect and convenient calculation process when inputting external waves. Therefore, the use of viscoelastic artificial boundaries lay a foundation for the subsequent research of the dynamic response under plane elastic wave input from the outer space.

Fig. 6.3 schematically shows a generic 3D domain discretized with cubic elements. A mechanical analog is applied at each node belonging to the five truncated surfaces to ensure the transmitting conditions of an infinite media. K_i and $C_i$values represent the elastic and damping coefficients along the three directions $i=x,y,z$ of the springs and damping of the mechanical analogs and they are defined as follows:

$$\text{In-plane}: \qquad K_N=A_l\cdot\frac{1}{1+A}\frac{\lambda+G}{r},\quad C_N=A_l\cdot B\rho c_p, \tag{6.19}$$

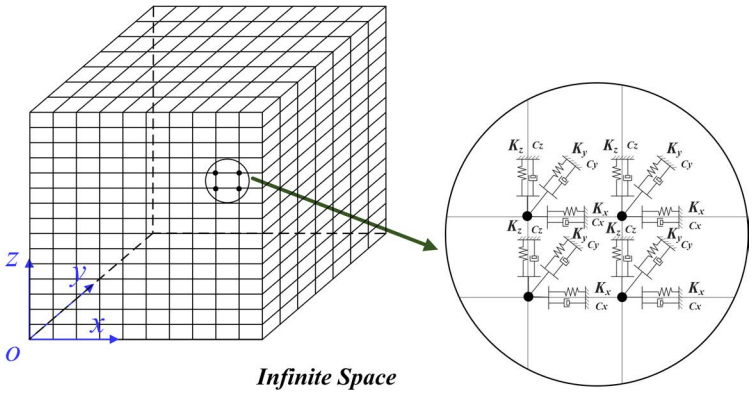

Fig. 6.3 Model for viscous-spring artificial boundary condition

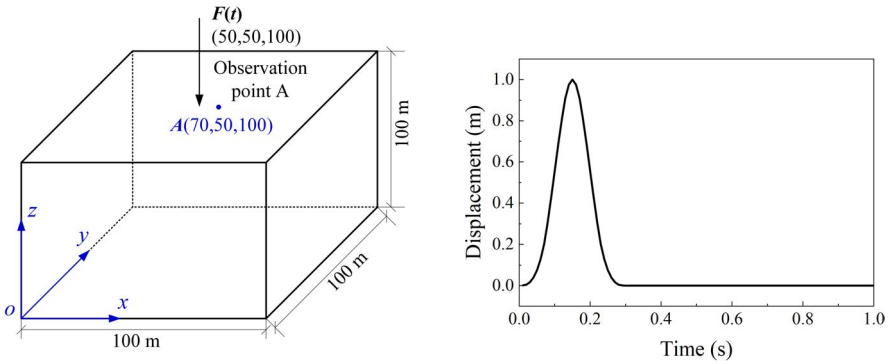

(a) Model (b) Time history

Fig. 6.4 Convergence analysis of five typical position displacement amplitudes increasing with truncation term N

$$\text{Out-of-plane}: \qquad K_T = A_l \cdot \frac{1}{1+A}\frac{G}{r}, \quad C_T = A_l \cdot B\rho c_s, \tag{6.20}$$

where A_l indicates the area of the node l on the artificial boundary in the element, A and B are the modified coefficients with the value of 0.8 and 1.1, λ stands for the lame constant, G represents the shear modulus, r is the distance between the wave source and the artificial boundary, c_p and c_s are the shear wave velocity and compression wave velocity and ρ denotes the density of the media.

6.2.2 Convergence and artificial boundary validity analysis

The finite element solution in the framework of CUF is realized by applying the self-developed Fortran program code of the MUL2 group. In order to verify the validation of establishing artificial boundaries, the Lamb problem with concentrated loads applied to the semi-infinite space surface is analyzed. The computational model is shown in Fig. 6.4 (a),

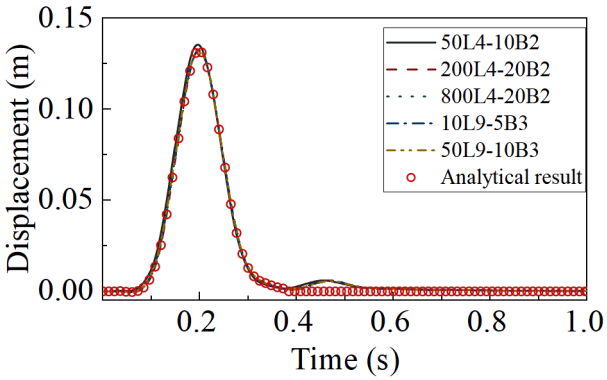

Fig. 6.5 Convergence analysis

the top surface of the model is the free boundary, the other five surfaces are set artificial boundary, the model size is $100m \times 100m \times 100m$, the media parameters are set as follows, density $\rho = 1800\text{kg/m}^3$, Poisson's ratio $\upsilon = 0.25$, shear wave velocity $c_s = 50\text{m/s}$, external concentrated load is a single pulse wave load as Eq. (6.21), where $F_0 = 10\text{KN}$, $T_0 = 0.5\text{s}$, $H(\cdot)$ is the Heaviside step function, the time history is shown in Fig. 6.4 (b)

$$F(t) = 16F_0 \left[\left(\frac{t}{T_0}\right)^3 H\left(\frac{t}{T_0}\right) - 4\left(\frac{t}{T_0} - \frac{1}{4}\right)^3 H\left(\frac{t}{T_0} - \frac{1}{4}\right) + 6\left(\frac{t}{T_0} - \frac{1}{2}\right)^3 H\left(\frac{t}{T_0} - \frac{1}{2}\right) - 4\left(\frac{t}{T_0} - \frac{3}{4}\right)^3 H\left(\frac{t}{T_0} - \frac{3}{4}\right) + \left(\frac{t}{T_0} - 1\right)^3 H\left(\frac{t}{T_0} - 1\right) \right]. \tag{6.21}$$

Observe the displacement distribution of point A with time under the action of point source load, as shown in Fig. 6.5. As can be seen, when the element at section xoz divided using the CUF frame finite element method reaches 64L9, the calculation results converge. Comparing this result with the analytical result, it can be seen that the artificial boundary established based on this method has an effective absorption effect.

6.3 External wave input

6.3.1 General formulation of equivalent load

While considering the influence of external wave source inputs such as earthquakes in the near-field wave analysis, the artificial boundary part needs to be treated. In the case of applying artificial boundary conditions to the response analysis of the external wave source interaction, the wave input is associated with the adopted artificial boundary conditions. For the viscous-spring artificial boundary, the external waves are converted to equivalent nodal

forces at the artificial boundary nodes. The equivalent nodal force f_{li} at node l in direction i is

$$f_{li} = K_{li}u_{li}^{f} + C_{li}\dot{u}_{li}^{f} + A_l\sigma_{li}^{f} \tag{6.22}$$

where K_{li} and C_{li} are the spring and damping coefficient corresponding to the i-direction of node l, respectively. σ_{li}^{f} is the stress of node l in i-direction.

6.3.2 Specific expressions of equivalent nodal force

Elastic waves can be divided into P waves, SV waves, and SH waves, and waveform conversion can occur when P and SV waves propagate to a free surface under incident conditions. Therefore, it is necessary to discuss the equivalent nodal forces for different wave forms of incident. The specific expression of the equivalent nodal force for SV wave incidence is similar to that for P wave incidence. Therefore, this section only gives the specific expression of the equivalent nodal force under the incidence of P and SH waves.

P wave incident

This section takes the oblique incidence of P-wave in isotropic homogeneous media as an example. Fig. 6.6 gives the coordinate system setting and the finite element model of oblique plane P-wave incident $\mathrm{P^i}$. α is the angle between the plane dependent on the incident wave and reflected wave and the x axis, and β is the angle between the $\mathrm{P^i}$ propagation direction and the positive direction of the y axis. The coordinate origin is the wavefront at zero time, and the point A (x_0, y_0, z_0) is the node on the model truncation boundary. The incident wave is oblique in general, so reflected P wave $\mathrm{P^r}$ and reflected SV wave $\mathrm{SV^r}$ would be generated at the free boundary.

The displacement in x, y, z directions on node A for Eq. (6.22) can be expressed as

$$u_x = \left(u_p^i \sin\beta + A_1 u_p^r \sin\beta + A_2 \frac{c_p}{c_s} u_{sv}^r \cos\beta_s\right) \sin\alpha \tag{6.23}$$

$$u_y = \left(u_p^i \sin\beta + A_1 u_p^r \sin\beta + A_2 \frac{c_p}{c_s} u_{sv}^r \cos\beta_s\right) \cos\alpha \tag{6.24}$$

$$u_z = \left(u_p^i - A_1 u_p^r\right) \cos\beta + A_2 \frac{c_p}{c_s} u_{sv}^r \sin\beta_s \tag{6.25}$$

where u_p^i, u_p^r, u_{sv}^r represents the displacement caused by incident P wave, reflected P wave and reflected SV wave, respectively, A_1 is the amplitude ratio of reflected P to incident P waves, A_2 is the amplitude ratio of reflected SV to incident P waves, β_s is the re-

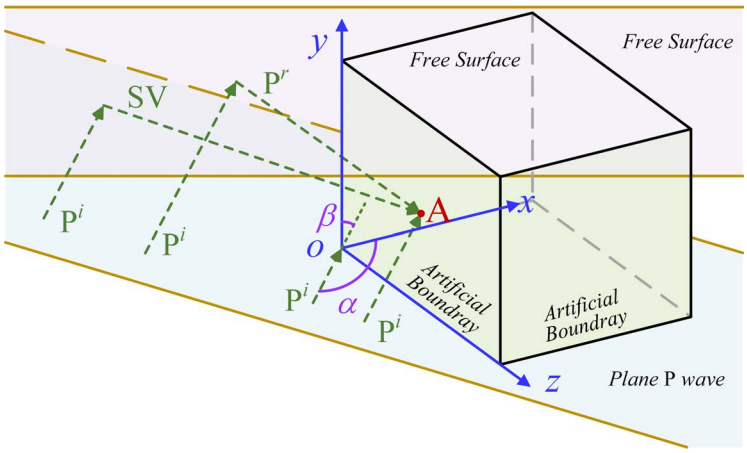

Fig. 6.6 Model for P wave oblique incident

flection angle of the reflected SV wave, according to Snell's law can be derived from, $A_1 = \frac{\sin 2\beta \sin 2\beta_s - (\sin\beta/\sin\beta_s)^2 \cos^2 2\beta_s}{\sin 2\beta \sin 2\beta_s + (\sin\beta/\sin\beta_s)^2 \cos^2 2\beta_s}$, $A_2 = \frac{2\sin 2\beta \cos 2\beta_s}{\sin 2\beta \sin 2\beta_s - (\sin\beta/\sin\beta_s)^2 \cos^2 2\beta_s}$, $\sin\beta_s = \frac{c_s \sin\beta}{c_p}$.

The displacement vectors u_p^i, u_p^r, u_{sv}^r can be describe as

$$u_p^i = U\left(t - \Delta t_1\right) \tag{6.26}$$

$$u_p^r = A_1 U\left(t - \Delta t_2\right) \tag{6.27}$$

$$u_{sv}^r = A_2 U\left(t - \Delta t_3\right), \tag{6.28}$$

where $\Delta t_i \, (i = 1,2,3)$ indicates the time delay between the arrival of the incident P wave, the reflected P wave and the reflected SV wave at node A, the expressions are given as:

$$\begin{aligned}
\Delta t_1 &= [(x_0 - x_1)\sin\beta\cos\alpha + (y_0 - y_1)\sin\beta\sin\alpha + (z_0 - z_1)\cos\beta]/c_p, \\
\Delta t_2 &= [(x_0 - x_1)\sin\beta\cos\alpha + (y_0 - y_1)\sin\beta\sin\alpha + (z_0 - z_1)\cos\beta \\
&\quad + 2(L_z - z_0 + z_1)\cos\beta]/c_p, \\
\Delta t_3 &= [(x_0 - x_1)\sin\beta\cos\alpha + (y_0 - y_1)\sin\beta\sin\alpha + (z_0 - z_1)\cos\beta \\
&\quad + (L_z - z_0 + z_1)\cos(\beta + \beta_s)/\cos\beta_s]/c_p + (L_z - z_0 + z_1)/c_s\cos\beta_s.
\end{aligned}$$

Based on the stress-strain relationship, stresses on each node read

$$\begin{bmatrix} \sigma_{xp}^{i} & \sigma_{xp}^{r} & \sigma_{xsv}^{r} \\ \sigma_{yp}^{i} & \sigma_{yp}^{r} & \sigma_{ysv}^{r} \\ \sigma_{zp}^{i} & \sigma_{zp}^{r} & \sigma_{zsv}^{r} \\ \tau_{xyp}^{i} & \tau_{xyp}^{r} & \tau_{xysv}^{r} \\ \tau_{yzp}^{i} & \tau_{yzp}^{r} & \tau_{yzsv}^{r} \\ \tau_{xzp}^{i} & \tau_{xzp}^{r} & \tau_{xzsv}^{r} \end{bmatrix}$$

$$= \begin{bmatrix} -\frac{\rho c_p\left[\mu+\xi\sin^2\beta\sin^2\alpha\right]}{1-\mu}\cdot\dot{u}_p^i & -\frac{A_1\rho c_p\left[\mu+\xi\sin^2\beta\sin^2\alpha\right]}{1-\mu}\cdot\dot{u}_p^r & -A_2\rho c_p\sin 2\beta_s\sin^2\alpha\cdot\dot{u}_{sv}^r \\ -\frac{\rho c_p\left[\mu+\xi\sin^2\beta\cos^2\alpha\right]}{1-\mu}\cdot\dot{u}_p^i & -\frac{A_1\rho c_p\left[\mu+\xi\sin^2\beta\cos^2\alpha\right]}{1-\mu}\cdot\dot{u}_p^r & -A_2\rho c_p\sin 2\beta_s\cos^2\alpha\cdot\dot{u}_{sv}^r \\ -\frac{\rho c_p\left[\mu+\xi\cos^2\beta\right]}{1-\mu}\cdot\dot{u}_p^i & -\frac{A_1\rho c_p\left[\mu+\xi\cos^2\beta\right]}{1-\mu}\cdot\dot{u}_p^r & A_2\rho c_p\sin 2\beta_s\cdot\dot{u}_{sv}^r \\ -\frac{G\sin^2\beta\sin 2\alpha}{c_p}\cdot\dot{u}_p^i & -\frac{A_1 G\sin^2\beta\sin 2\alpha}{c_p}\cdot\dot{u}_p^r & -\frac{A_2}{2}\rho c_p\sin 2\beta_s\sin 2\alpha\cdot\dot{u}_{sv}^r \\ -\frac{G\sin 2\beta\cos\alpha}{c_p}\cdot\dot{u}_p^i & \frac{A_1 G\sin 2\beta\cos\alpha}{c_p}\cdot\dot{u}_p^r & A_2\rho c_p\cos 2\beta_s\cos\alpha\cdot\dot{u}_{sv}^r \\ -\frac{G\sin 2\beta\sin\alpha}{c_p}\cdot\dot{u}_p^i & \frac{A_1 G\sin 2\beta\sin\alpha}{c_p}\cdot\dot{u}_p^r & A_2\rho c_p\cos 2\beta_s\sin\alpha\cdot\dot{u}_{sv}^r \end{bmatrix}, \tag{6.29}$$

where $\xi = 1-2\mu$.

The presentation of equivalent loads on the boundary nodes at different locations of the VSAB model varies, the equivalent loads on the boundary surface nodes with the outer normal direction of x axis read

$$F_x = K_N u_x + C_N \dot{u}_x - (-1)^k A_l \sigma_x \tag{6.30}$$

$$F_y = K_T u_y + C_T \dot{u}_y - (-1)^k A_l \tau_{xy} \tag{6.31}$$

$$F_z = K_N u_z + C_N \dot{u}_z - (-1)^k A_l \tau_{xz} \tag{6.32}$$

The equivalent loads on the boundary surface nodes with the outer normal direction of y axis read

$$F_x = K_N u_x + C_N \dot{u}_x - (-1)^k A_l \tau_{yx} \tag{6.33}$$

$$F_y = K_T u_y + C_T \dot{u}_y - (-1)^k A_l \sigma_y \tag{6.34}$$

$$F_z = K_N u_z + C_N \dot{u}_z - (-1)^k A_l \tau_{yz} \tag{6.35}$$

The equivalent loads on the boundary surface nodes with the outer normal direction of z axis read

$$F_x = K_N u_x + C_N \dot{u}_x - (-1)^k A_l \tau_{xz} \tag{6.36}$$

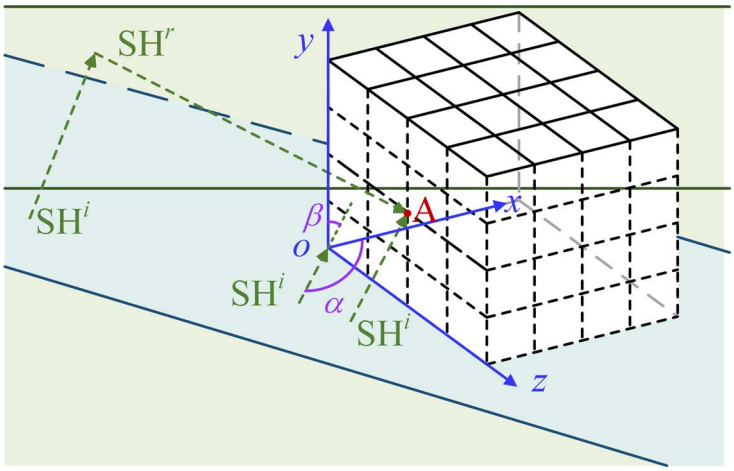

Fig. 6.7 Model for SH wave oblique incident

$$F_y = K_T u_y + C_T \dot{u}_y - (-1)^k A_l \tau_{yz} \tag{6.37}$$

$$F_z = K_N u_z + C_N \dot{u}_z - (-1)^k A_l \sigma_z \tag{6.38}$$

where, if the outer normal direction is positive with axis $k = 1$, else the outer normal direction is negative with axis $k = 0$.

SH wave incident

In the case of incident SH wave, Fig. 6.7 indicates the coordinate system setting and the oblique incident plane SH wave finite element model, α and are β the incident angles, are the included angles between SH^i propagation direction and the y and z axes, respectively. The coordinate origin is the wavefront at zero time, and the point A (x_0, y_0, z_0) is the node on the model truncation boundary. The incident wave is the oblique incident in general, and the displacements expression in the direction x, y, z of node A are

$$u_x = (u_{SH}^i - u_{SH}^r)\cos\alpha \tag{6.39}$$

$$u_y = -\left(u_{SH}^i + u_{SH}^r\right)\sin\beta \tag{6.40}$$

$$u_z = 0 \tag{6.41}$$

where u^i_{SH}, u^r_{SH} represents the displacement caused by incident SH wave, reflected SH wave, respectively. Displacement vector u^i_{SH}, u^r_{SH} are

$$u^i_{SH} = U\left(t - \Delta t_1\right) \tag{6.42}$$

$$u^r_{SH} = U\left(t - \Delta t_2\right) \tag{6.43}$$

where $\Delta t_i\,(i = 1,\ 2)$ indicates the time delay between the arrival of the incident SH wave, the reflected SH wave at node A, the expressions are given as

$$\Delta t_1 = \left[(x_0 - x_1)\sin\beta\sin\alpha + (y_0 - y_1)\sin\beta\cos\alpha + (z_0 - z_1)\cos\beta\right]/c_s$$

$$\begin{aligned}\Delta t_2 = \big[&(x_0 - x_1)\sin\beta\sin\alpha + (y_0 - y_1)\sin\beta\cos\alpha + (z_0 - z_1)\cos\beta \\ &+2\left(L_z - z_0 + z_1\right)\cos\beta\big]/c_s\end{aligned}$$

.

Based on the stress-strain relationship, the stress on the node is as follows

$$\begin{bmatrix} \sigma^i_{xSH} & \sigma^r_{xSH} \\ \sigma^i_{ySH} & \sigma^r_{ySH} \\ \sigma^i_{zSH} & \sigma^r_{zSH} \\ \tau^i_{xySH} & \tau^r_{xySH} \\ \tau^i_{yzSH} & \tau^r_{yzSH} \\ \tau^i_{xzSH} & \tau^r_{xzSH} \end{bmatrix} = \begin{bmatrix} \rho c_s \sin\beta\sin 2\alpha\cdot\dot{u}^i_{SH} & \rho c_s \sin\beta\sin 2\alpha\cdot\dot{u}^r_{SH} \\ -\rho c_s \sin\beta\sin 2\alpha\cdot\dot{u}^i_{SH} & -\rho c_s \sin\beta\sin 2\alpha\cdot\dot{u}^r_{SH} \\ 0 & 0 \\ \rho c_s \sin\beta\cos 2\alpha\cdot\dot{u}^i_{SH} & \rho c_s \sin\beta\cos 2\alpha\cdot\dot{u}^i_{SH} \\ -\rho c_s \cos\beta\sin\alpha\cdot\dot{u}^i_{SH} & \rho c_s \cos\beta\sin\alpha\cdot\dot{u}^i_{SH} \\ \rho c_s \cos\beta\cos\alpha\cdot\dot{u}^i_{SH} & -\rho c_s \cos\beta\cos\alpha\cdot\dot{u}^i_{SH} \end{bmatrix} \tag{6.44}$$

According to Eqs. (6.30)-(6.32), the input load of each node at the boundary could be obtained.

6.3.3 Verification

The implementation process in this section is based on a self-developed FORTRAN program. To verify the validation of the input method and the implementation of program, the semi-infinite elastic space is selected as the model in this section to simulate the propagation process of P-waves. The model size is $0 \le x \le 800$, $0 \le y \le 800$ and $0 \le z \le 600$, its finite element model created by utilizing 16 B2 beam element and 1024 LE4, as shown in Fig. 6.8. Point A $(400, 400, 600)$ is a selected observation point. The properties of elastic half-space is assumed as, elastic modulus E is 1GPa, the Poisson's ratio ν is 0.3, the density ρ is 2000kg/m^3. The pulse function time history equation for P wave input is as Eq. (6.21), $F_0 = 1$kN, $T_0 = 0.5$s.

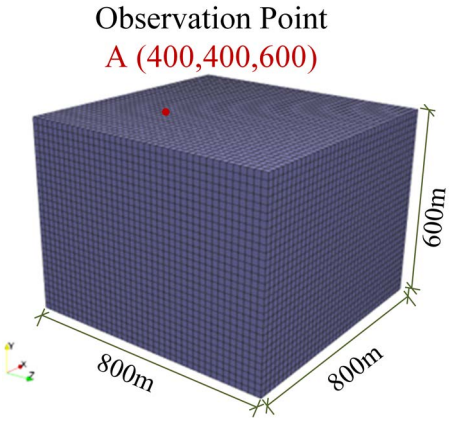

Fig. 6.8 Model for finite element

Fig. 6.9 indicates the displacement distribution in the semi-infinite space when a plane P wave is incident at three incident angles. The reflected P wave and reflected SV wave caused by the incident P wave on the free surface are clearly observed from Figs. 6.9 (b) and (c). Moreover, there is no occurrence of reflected SV waves when vertical incident to the free surface. In addition, under three incident angles, the displacement amplitude at the free surface is twice as the incident displacement amplitude, which conforms to the propagation characteristic of elastic waves. At $t = 2.0$s, the reflected wave basically travels away, and there is no obvious presence of reflected waves caused by truncated boundaries within the model. Moreover, the comparison between the displacement results in the z-direction and the analytical results under the three incident conditions at observation point A is given in Fig. 6.10, which illustrates that the simulation results in this section are in well agreement with the analytical results. The above calculation results indicate that the simulation method used in this section has well simulation accuracy. Comparing with the traditional finite element methods for simulation, finite element methods based on the CUF framework effectively improves computational time, reduces element usage, and reduces computational costs.

6.3.4 Numerical results and discussion

Since analyzing the dynamic response of an external elastic wave under its incidence, it is usually assumed that the elastic external wave is vertically incident for simulation calculations. However, a large number of researches have demonstrated that small changes in the incident angles of elastic waves may have a significant impact on the dynamic response of structures. Therefore, this section mainly investigates the ground motion and dynamic response of the superstructure under the incident of multi-angle external elastic waves. The calculation model and finite element are shown in Fig. 6.11. The semi-infinite space used in the model is sized

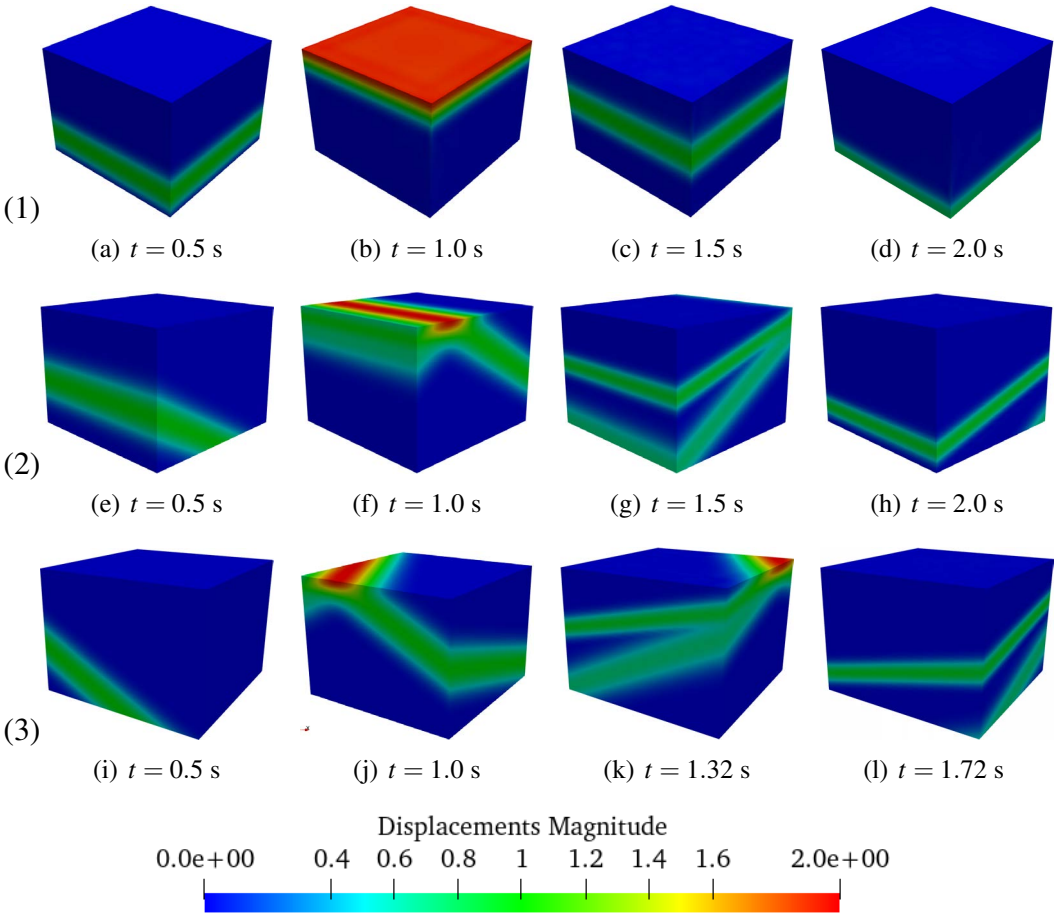

Fig. 6.9 Semi-infinite space displacement contours: case (1), case (2) and case (3).

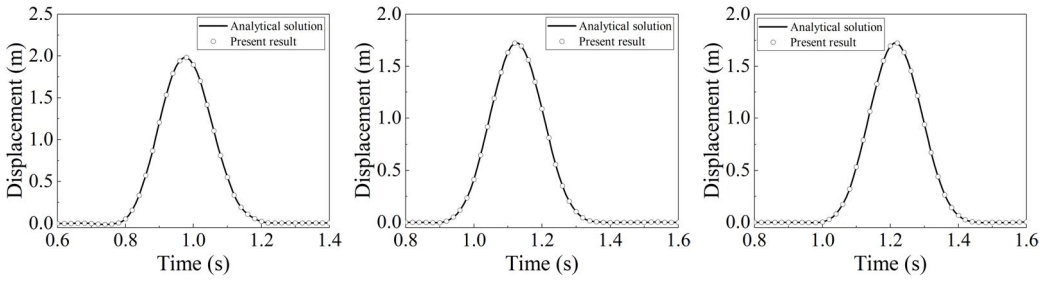

Fig. 6.10 Comparison of displacements of point A in the three cases.

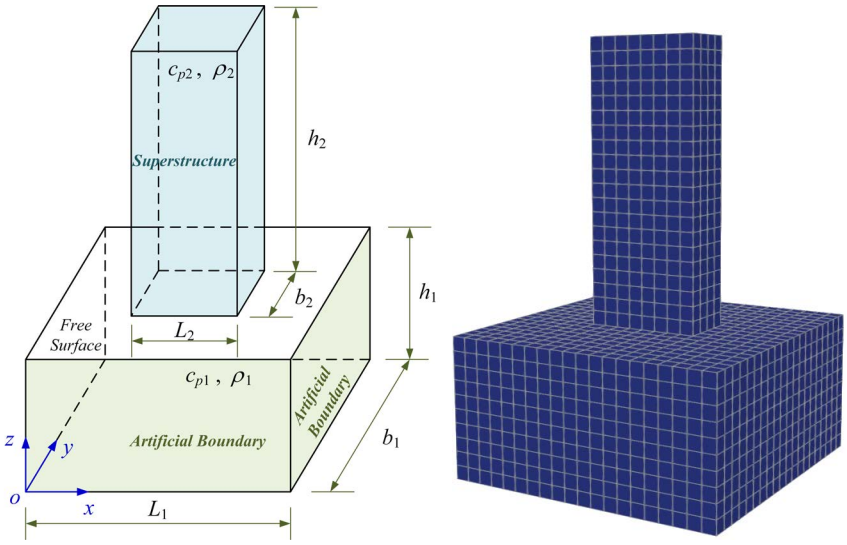

(a) Calculation model (b) Infinite element model

Fig. 6.11 Calculation model for half-space with surface structure

as $L_1 = 50$m, $b_1 = 50$m, $h_1 = 25$m, the ground surface structure is set as $L_2 = 10$m, $b_2 = 20$m, $h_2 = 50$m. For simulate different types of space ground, three types soft, intermediate and stiff are considered, which are characterized by different compressional wave velocities $c_{p1} = 120, 360, 600$m/s, the compressional wave velocity of ground surface structure is set as $c_{p2} = 3.84 \times 10^3$m/s. The selected observation point A is located at (25, 25, 75). The density underground $\rho_1 = 2600\text{kg/m}^{-3}$, surface structure $\rho_2 = 4850\text{kg/m}^{-3}$, Possion's ratio are both $\upsilon = 0.25$, elastic modulus $E = \rho_i {c_{pi}}^2(1+\upsilon)(1-2\upsilon)/2(1-\upsilon)$, $i = 1, 2$.

Convergence analysis

Before performing the calculations, a convergence analysis of the meshing was carried out to allow for more time efficient and accurate subsequent calculations. Fig. 6.12 illustrates the displacement of observation point C (15, 25, 25) under three mesh conditions when a concentrated force $F = 10$GPa is applied at point B (25, 25, 25) and the pulse function time history equation for P wave input is as Eq. (6.21), $F_0 = 0.25$kN, $T_0 = 0.25$s. By comparing the results of the three situation, it is evident that the requirements are satisfied when using 200 LE4-20B2 elements. Therefore, the used calculation model has been consisted of 20 2-node beam elements along the y axis, 200L4 and 80L4 elements have been used to discretize the sections of the space and surface structure, respectively.

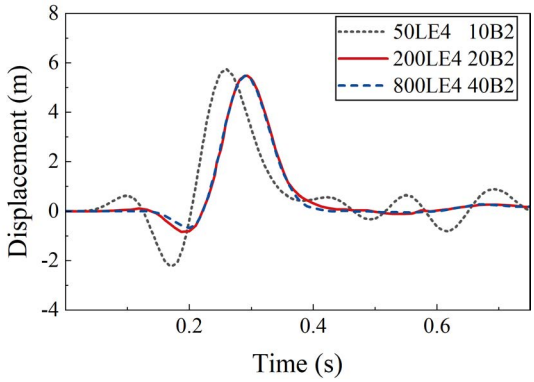

Fig. 6.12 Convergence analysis

P wave incident

In order to explore the influence of different incident angles on the displacement distribution of the superstructure under the incident P wave, three groups of incident angles are given at $c_{p1} = 120$m/s, (a) vertical incident $\alpha = 0°, \beta = 0°$, (b) oblique incidence $\alpha = 0°, \beta = 20°$, (c) oblique incidence $\alpha = 30°, \beta = 20°$, as shown in Fig. 6.13. From the three sets of displacement distribution that at 0.45s, the incident P wave reaches the free surface and produces a reflected wave, which bring a large displacement at the ground free surface. At 0.75s, the incident wave reaches the superstructure, and is reflected at the corresponding position of the superstructure to form a large displacement distribution, and only the reflected wave continues to propagate downward in the underground media. While the time reaches 0.9s, the reflected wave in the underground media gradually disappears, and almost no reflected wave is generated at the artificial boundary, which also verifies the validity of the artificial boundary established in section 6.2. However, the boundary in the upper structure is more complicated, and there are still reflection phenomena, so the displacement distribution is also more complicated. From Fig. 6.13 (a) that in the case of normal incidence of P wave, no reflected S wave is generated, therefore the superstructure only shows compressive deformation. In addition, when the incident wave reaches the superstructure, scattering waves are generated at the corners of the bottom of the structure. As the incident wave becomes obliquely incident, the deformation of the superstructure becomes more complex due to the presence of reflected SV waves, adding shear deformation from the single compression deformation, as shown in Figs. 6.13 (b) and (c). Moreover, under the conditions of the media parameters, when the incident angle β is the same, at the same moment, the displacement distribution and deformation of the superstructure are almost the same.

At the same time, Fig. 6.14 reports the displacement and stress of observation point A changing with time under the above conditions. It can be found that when the incident

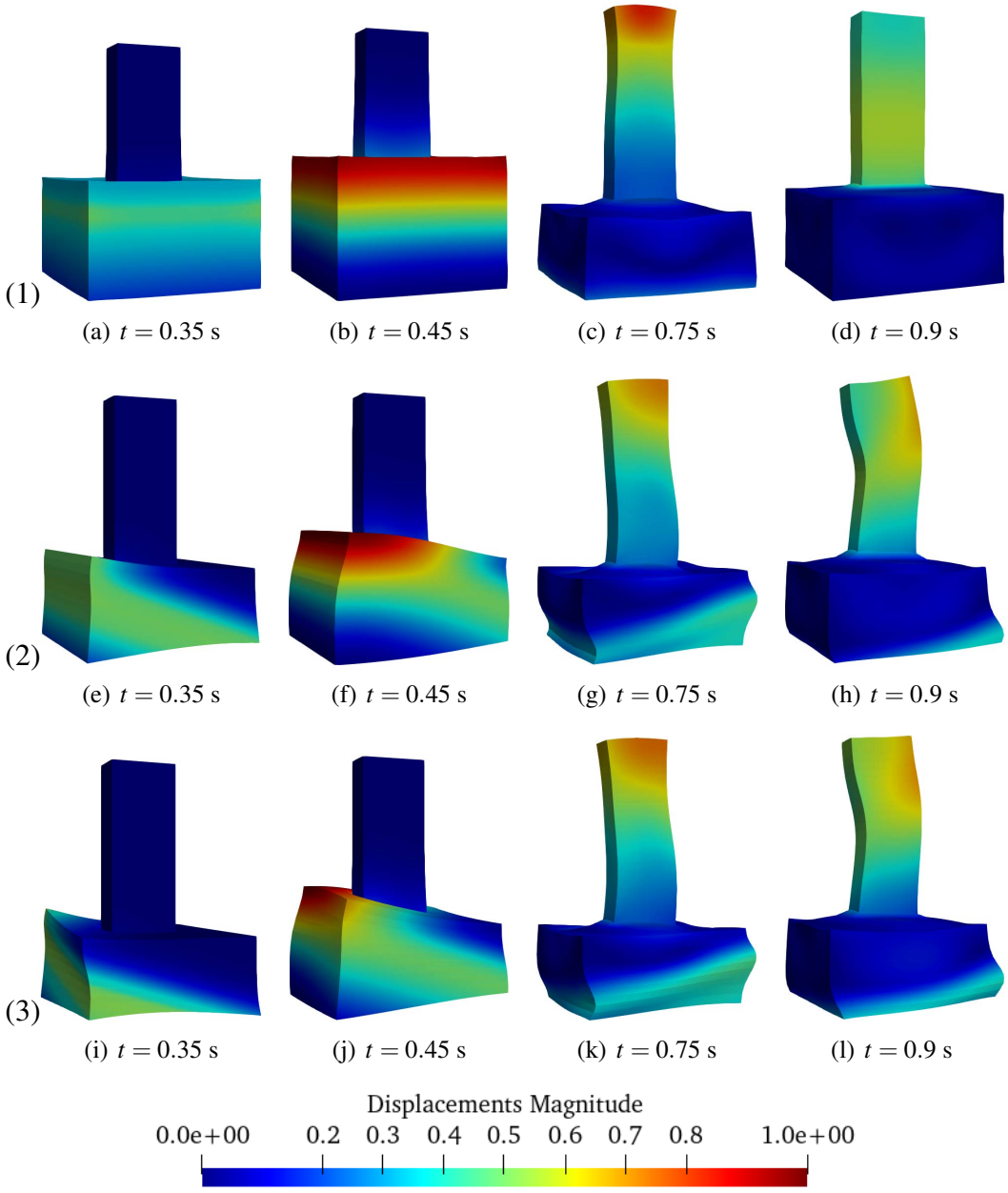

Fig. 6.13 Displacement distribution of underground media with wave velocity $c_{p1} = 120$m/s under three P wave incident angles

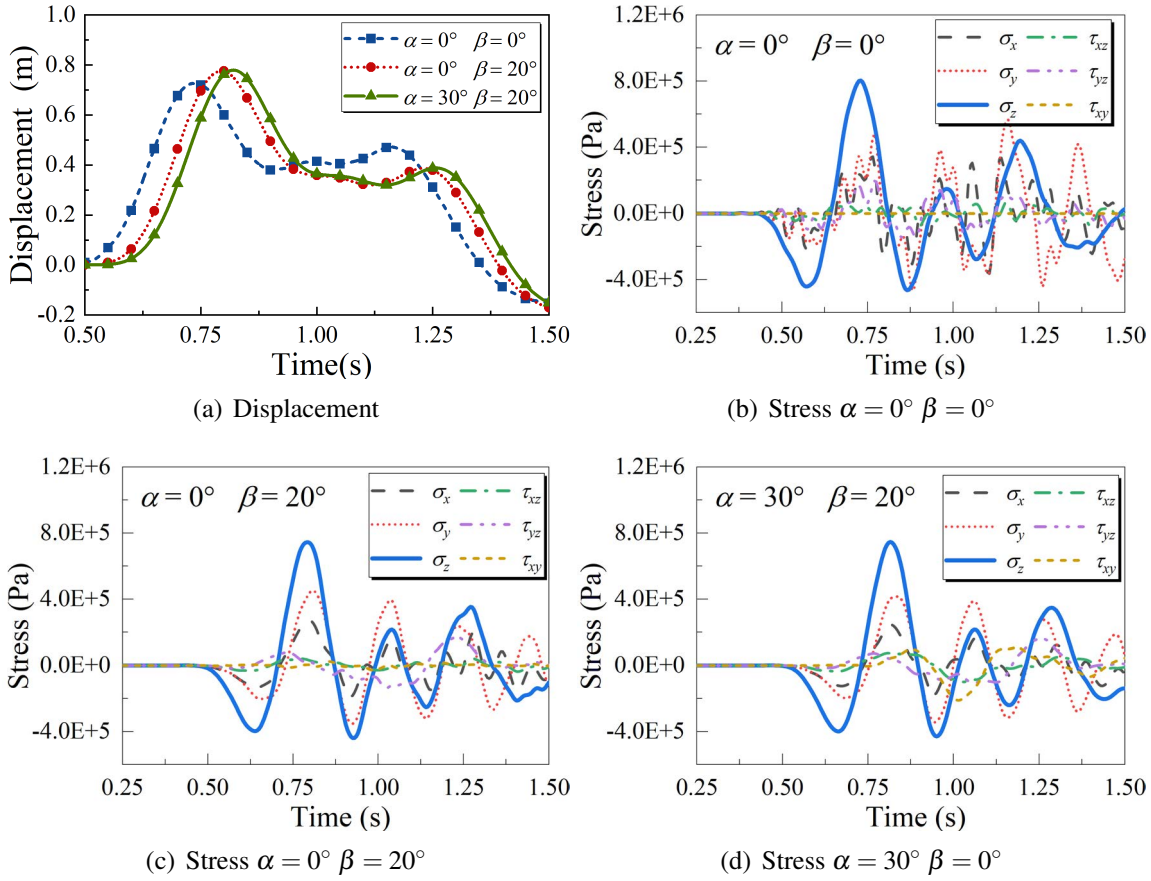

(a) Displacement

(b) Stress $\alpha = 0°$ $\beta = 0°$

(c) Stress $\alpha = 0°$ $\beta = 20°$

(d) Stress $\alpha = 30°$ $\beta = 0°$

Fig. 6.14 Displacement and stress of point A with $c_{p1} = 120$m/s and three incident P wave angle

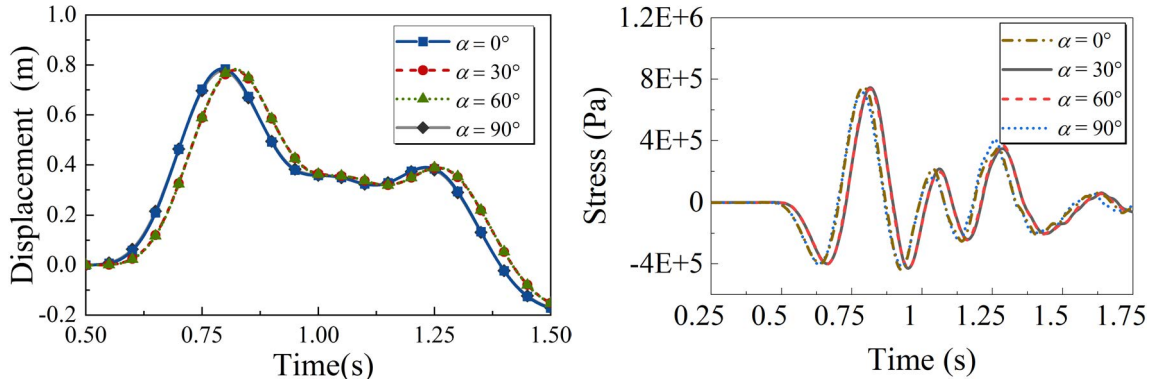

(a) Displacement (b) Stress

Fig. 6.15 Displacement and stress of point A with $c_{p1} = 120$m/s and different α

angle situation is changed, the distribution of displacement is almost the same. As the incident angle β increases, the maximum displacement tends to increase, and the time to reach the maximum displacement is prolonged. However, with the change of the angle α, the displacement distribution hardly changes, as shown in Fig. 6.14. In Figs. 6.14(b)-(d), the stress at observation point A changes with time. Comparison these three figures, it clearly shows that the normal stress σ_z is the maximum stress, and at α equals to 0° the shear stress τ_{xy} and τ_{xz} are almost zero, while when α is changed, the shear stress τ_{xy} and τ_{xz} fluctuates greatly with time, which also verifies that the oblique In the incident case a reflected S wave is generated. And, under the same incident angle β, the stress with time is almost the same. This also further illustrates that in the case of higher rigidity of the superstructure, the change of the angle α has little influence on the displacement and stress distribution of the superstructure under P wave incident.

For further investigation the effect of incident angle α on the distribution of displacement and stress, the displacement and principal stress σ_z at observation point A are calculated for different values of incidence angle $\beta = 0^\circ$, and the results are reported in Fig. 6.15. Under the same incidence angle β, the change of α has less effect on the distribution of displacement, and the overall distribution is almost the same. With α changes from 0° to other angles, the effect of the displacement distribution is reflected in the time delay, and at $\alpha \neq 0^\circ$, the displacement distribution overlaps, as shown in Fig. 6.15(a). The distribution of principal stresses σ_z in response to the change in α is also reflected in the time delay. The above calculation mainly considers the effect of the incident angle on the displacement and stress of the superstructure for a wave velocity $c_{p1} = 120$m/s in the subsurface media. The physical properties of the subsurface media also have a significant effect on the response of the superstructure to incident waves. Therefore, this section investigates the effect of

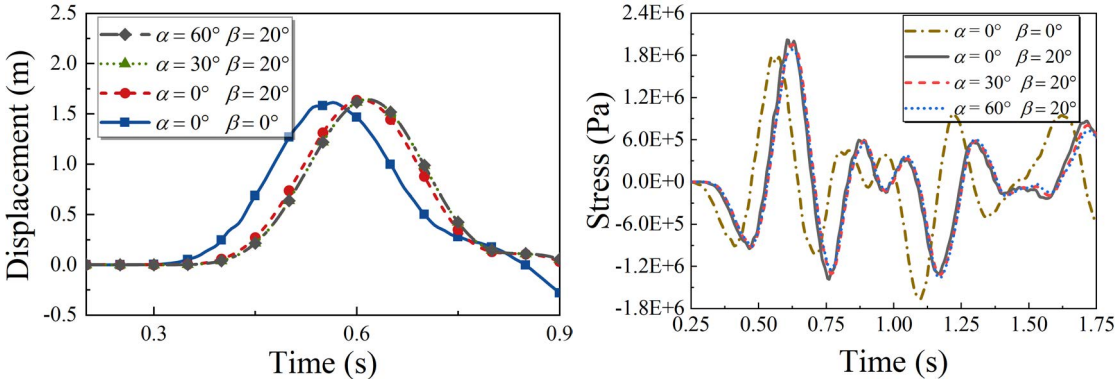

(a) Displacement (b) Stress

Fig. 6.16 Displacement and stress of point A with $c_{p1} = 360$m/s and different α

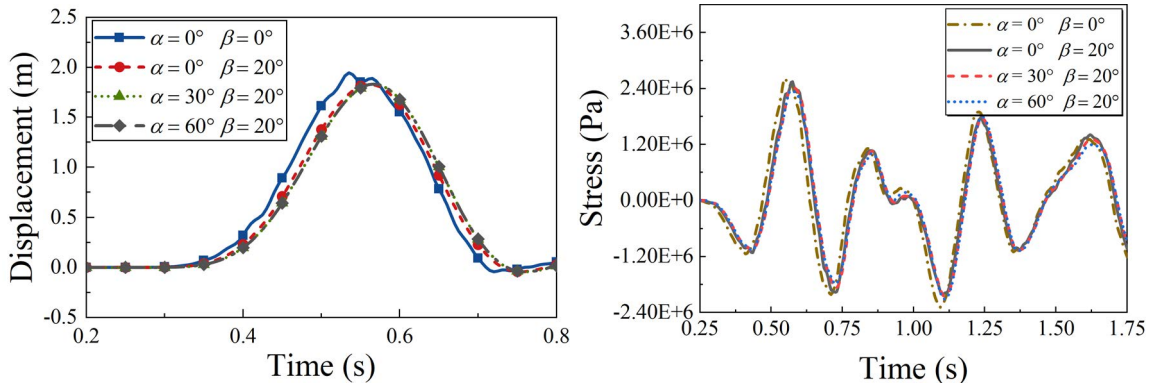

(a) Displacement (b) Stress

Fig. 6.17 Displacement and stress of point A with $c_{p1} = 600$m/s and different α

incident angle on the displacement and stress of the superstructure for different subsurface wave velocities. Compared with Fig. 6.15, there is a significant increase in displacement at observation point A when the wave velocity in the subsurface media reaches 360 m/s. At this wave speed, when the incident angle is 0, the change of a has a small effect on the displacement and stress at point A. The increase of the incident angle β has a small advanced effect on the displacement and stress values, and the more obvious effect is the time rises of the response to wave at the location of point A, under $\alpha = 0°$. At the situation of wave velocity in the subsurface media reaches 600 m/s, there is a further increase in the displacement and stress at point A, as shown in Fig. 6.15. However, at this condition in the subsurface media, the displacement and stress remain almost constant with the variation of the incidence angles α and β, especially the stress. Figs. 6.15- 6.17 clearly demonstrate that the larger the wave velocity in the subsurface media, the larger the elastic modulus

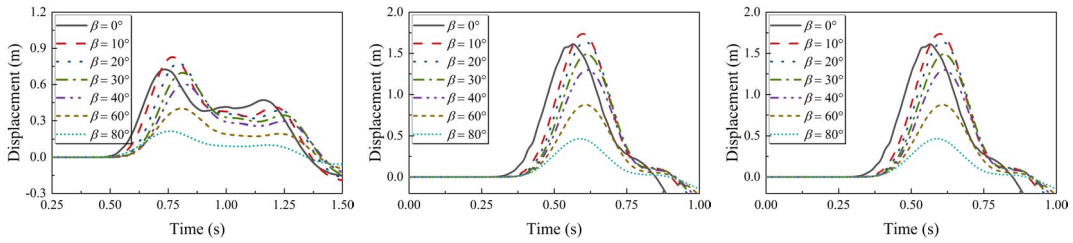

(a) $c_{p1} = 120$m/s (b) $c_{p1} = 360$m/s (c) $c_{p1} = 600$m/s

Fig. 6.18 Displacement under different incident P wave angle with three wave velocity

of the subsurface media, the larger the displacement and stress of the superstructure, and the smaller the effect of the incident angle α. To investigate further the effect of incidence angle on the displacement of the superstructure at different wave velocities in the subsurface media, calculations were performed for different incidence angles β. From Fig.6.18. it can be observed that the displacement tends to decrease gradually with the increasing incidence angle β (from vertical to horizontal incidence) under the conditions of three groups of subsurface media wave velocities. It is noteworthy that the maximum value of displacement occurs at $\beta = 10^\circ$ when the wave velocity is 120m/s and 360m/s, and occurs at $\beta = 0^\circ$ when the wave velocity reaches 600m/s. Therefore, it is necessary to consider the case of oblique incidence in researching the interaction between the subsurface media and the superstructure, especially when the elastic modulus of the subsurface media is small.

SH wave incident

In the process of earthquake wave effects on the superstructure, out plane shear waves, SH waves, propagate to the superstructure with more intense shear damage to the superstructure. Therefore, the dynamic response of the superstructure under SH wave incidence is analyzed in this section. Fig. 6.19 shows the displacement distribution of the SH wave at the same time step under three incidence angles for $c_{p1} = 120$m/s. The superstructure clearly exhibits shear deformation under SH wave incidence. In the case of two oblique incidence, Figs. 6.19 (b) and (c), the incident wave reaches the superstructure at 0.9s, and the displacement distribution as well as deformation are similar at 1.2s and 1.5s for the two incidence angles. Meanwhile, the maximum displacement under SH wave incidence occurs at the top surface of the superstructure compared to P wave incidence, moreover, the maximum value increases compared to P incidence. Similarly, to investigate the effects of incidence angles α and β on the displacement and stress at observation point A under SH-wave incidence, calculations were performed for different incidence angles at $c_{p1} = 120$m/s, the results are shown in Fig. 6.20. With increasing incidence angles, the displacement response to wave is delayed

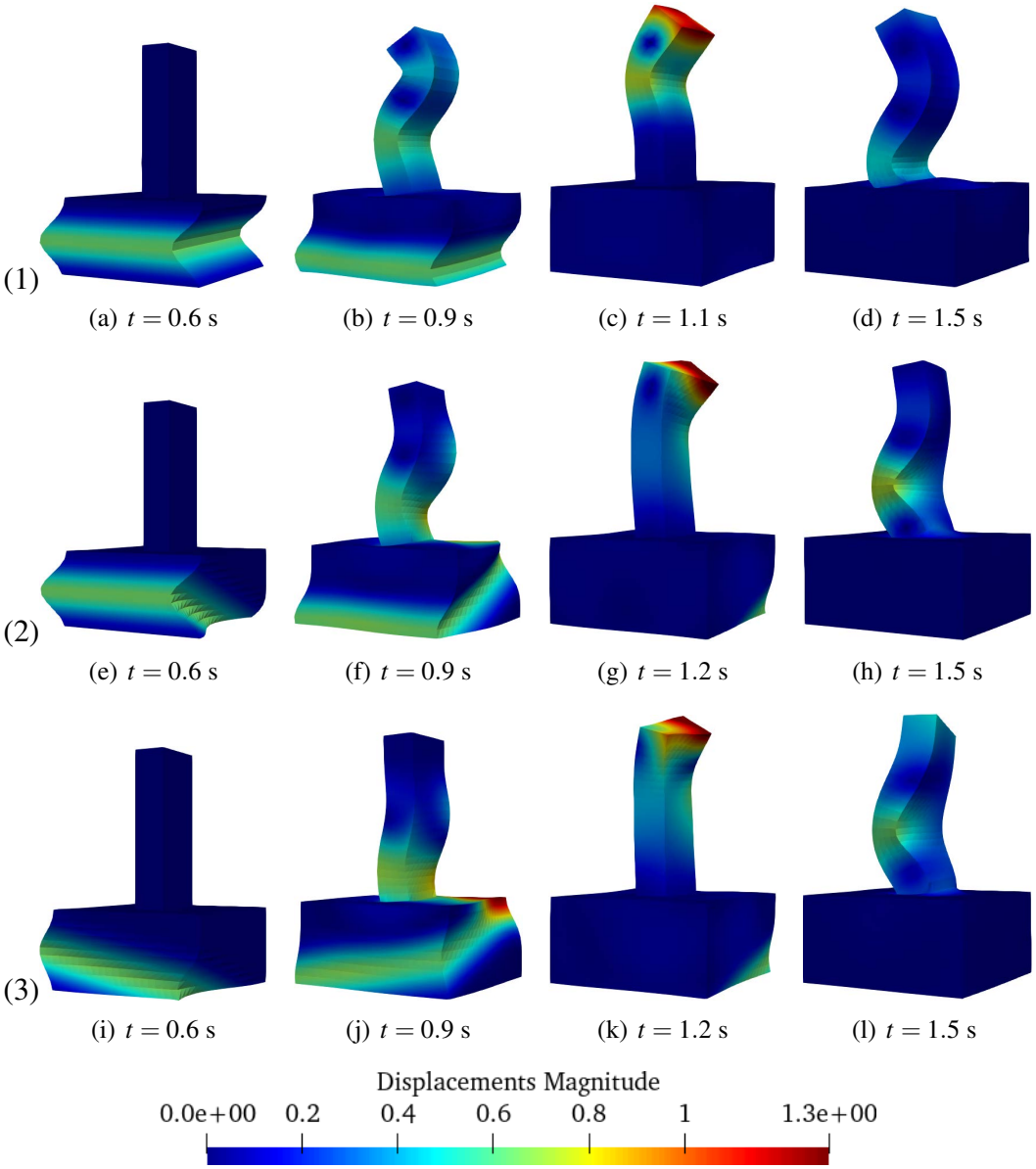

Fig. 6.19 Displacement distribution of underground media with wave velocity $c_{p1} = 120$m/s under three SH wave incident angles

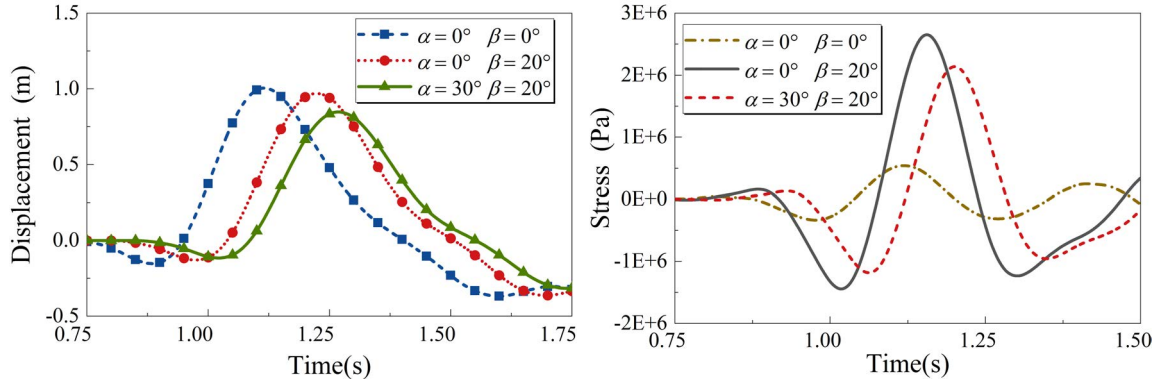

(a) Displacement (b) Stress

Fig. 6.20 Displacement and stress of point A with $c_{p1} = 120$m/s and different incident angle

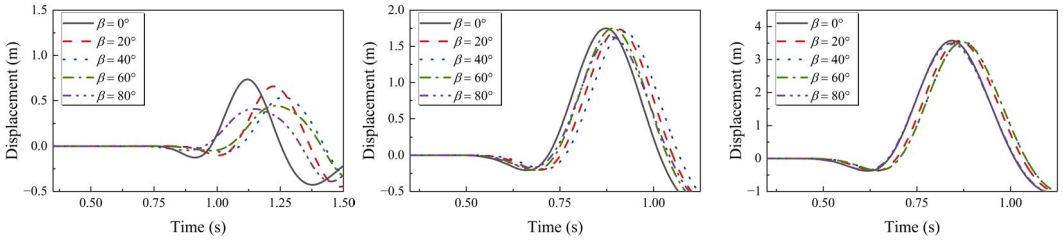

(a) $c_{p1} = 120$m/s (b) $c_{p1} = 360$m/s (c) $c_{p1} = 600$m/s

Fig. 6.21 Displacement under different incident SH wave angle with three wave velocity

significantly, while the stress has a large undulating change. Compared with Fig. 6.15, the displacement and stress at observation point A under the incidence of SH wave are significantly larger than those at the incidence of P wave, and the effects of both the incidence angle α and βon the displacement and stress are more obvious.

Consequently, under the incident angle α =0 of SH wave, the displacement distribution of observation point A with incident angle β variation under three wave velocities is shown in Fig. 6.21. As $c_{p1} = 120$ m/s, the displacement of point A decreases significantly with the increasing of incident angle β (from vertical to horizontal) from Fig. 6.21(a). And when c_{p1} is changed to 360 m/s and 600 m/s, there is a clear increase in displacement. It can be seen from Fig. 6.21 that when β reaches 80°, the displacement response time at point A reduction. However, different from the P-wave incidence, the influence of β on the displacement at point A at the same c_{p1} decreases gradually as the c_{p1} increases. Moreover, compared with incident P-wave, displacement of point A under SH-wave incident is larger at the same wave velocity.

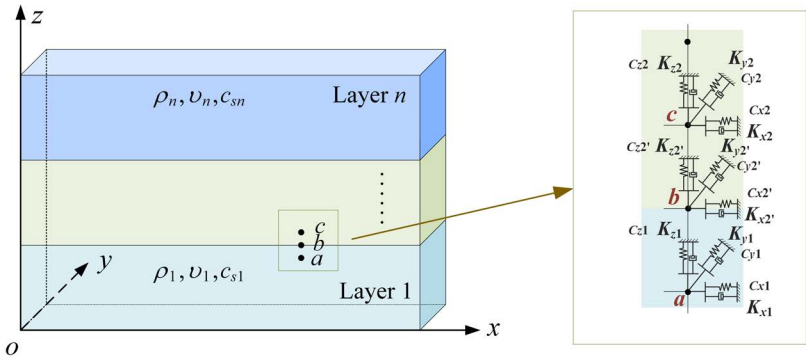

Fig. 6.22 Model for layered media and artificial boundary setting

6.4 External wave input of layered media

It is of vital theoretical and practical engineering significance to investigate the propagation characteristics of elastic waves in layered media. While exploring the character of wave propagation in inhomogeneous media, continuous inhomogeneous media is used to divide into layered media for simulation. In addition, considering practical applications, such as in the field of seismic engineering, layered media is simulated the situation of underground soil media. Therefore, this section researches the input methods of external elastic waves of layered media. By using the FEM under the CUF framework to model the layered model, it is only necessary to change the material properties of the nodes of each layer to complete the establishment of the layered model. Meanwhile, the input of external waves in layered media has always been the key to solving the problem of ground motion response. Thus, this section gives the input method and implementation process of the external domain wave in the layered media. The layered media model and artificial boundary settings are shown in Fig. 6.22.

The corresponding springs and dampers are still set in the three directions of the nodes at the artificial boundary, and the parameters are as Eqs. (6.17) and (6.18). At the nodes of the layer boundary, as shown by node b, the corresponding parameters need to be calculated in each layer respectively. In a layered media, when an elastic wave enters another media from one media, a transmitted wave and a reflected wave will be generated at the interface of the two media, the reflected wave will propagate downward in the incident media layer, and the transmitted wave will continue to propagate upward in the incident media layer. Therefore, it is necessary to calculate the amplitude ratio of the reflected wave and the transmitted wave. Taking P wave vertical incident as an example. When P wave incident from layer $(n-1)$ to layer n, the amplitude ratios of the reflected P wave and the reflected S wave to the incident P wave in layer $(n-1)$ are recorded as $A_{rP(n-1)n}$ and $A_{rSV(n-1)n}$, respectively. And

the amplitude ratios of the transmitted P wave and the transmitted S wave to the incident wave in layer n are recorded as $A_{tP(n-1)n}$ and $A_{tSV(n-1)n}$, respectively. While P wave incident from layer n to layer $(n-1)$, the corresponding amplitude ratios are recorded as $A_{rPn(n-1)}$, $A_{rSVn(n-1)}$, $A_{tPn(n-1)}$, $A_{tSVn(n-1)}$, and the corresponding expressions are as follows

$$A_{rj(n-1)n} = \frac{1-\frac{\rho_n c_{jn}}{\rho_{n-1} c_{j(n-1)}}}{1+\frac{\rho_n c_{jn}}{\rho_{n-1} c_{j(n-1)}}} \tag{6.45}$$

$$A_{tj(n-1)n} = \frac{2}{1+\frac{\rho_n c_{jn}}{\rho_{n-1} c_{j(n-1)}}} \tag{6.46}$$

$$A_{rjn(n-1)} = \frac{\frac{\rho_n c_{jn}}{\rho_{n-1} c_{j(n-1)}}-1}{1+\frac{\rho_n c_{jn}}{\rho_{n-1} c_{j(n-1)}}} \tag{6.47}$$

$$A_{tjn(n-1)} = \frac{2\frac{\rho_n c_{jn}}{\rho_{n-1} c_{j(n-1)}}}{1+\frac{\rho_n c_{jn}}{\rho_{n-1} c_{j(n-1)}}} \tag{6.48}$$

where $j = P,S$, denote the P wave and S wave velocity, ρ_n and ρ_{n-1} denote the layer n and $(n-1)$ density, respectively, c_{jn} and $c_{j(n-1)}$ are the corresponding P wave and S wave velocity in layer n and $(n-1)$.

6.4.1 Plane SH wave input in layered media

This subsection is based on the external wave input method in Section 6.3, and the influence of the parameters of each layer on the SH wave propagation when the SH wave is incident to the double-layer media at an angle β with the positive direction of the z-axis, and the angle α between the incident wave and the plane determined by the reflected wave and the y-axis is used as an example to give the input method and process of the external SH wave in the double-layer media. The calculation model is shown in Fig. 6.23, L_1 and L_2 are the layer heights of the two layers respectively. In layer 1, the total number of waves is W, the media density is ρ_1, and the wave velocity is c_{s1}. In layer 2, the total number of waves is M, the media density is ρ_2, and the wave velocity is c_{s2}. The displacement of random node A (x_0, y_0, z_0) in layer 1 can be expressed as

$$u_x^1 = u_{SH}^i \cos\alpha - A_{rs12} u_{SH}^r \cos\alpha - \sum_{b=3}^{W} (A_{rs21})^{j-3} A_{ts12} A_{ts21} u_{sH}^t \cos\alpha_s \tag{6.49}$$

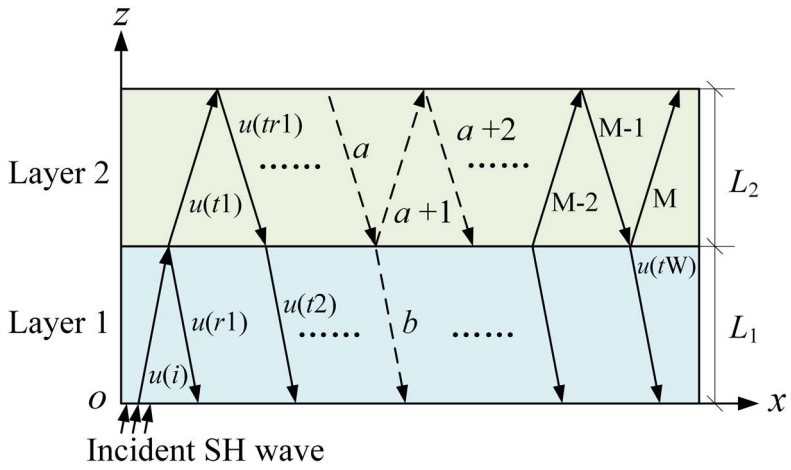

Fig. 6.23 The wave propagation of SH wave incident in the layered media

$$u_y^1 = -u_{SH}^i \sin\alpha - A_{rs12} u_{SH}^r \sin\alpha - \sum_{b=3}^{W} (A_{rs21})^{j-3} A_{ts12} A_{ts21} u_{sH}^t \sin\alpha_s \tag{6.50}$$

$$u_z^1 = 0 \tag{6.51}$$

where $\sin\alpha_s = \sin\alpha$.

In layer 2, the displacement of random node B (x_0, y_0, z_0) are presented as

$$u_x^2 = \sum_{a=3}^{M} (-A_{rs21})^{\varphi(a)} A_{ts12} u_{sH}^{t2} \cos\alpha_t \tag{6.52}$$

$$u_y^2 = \sum_{a=3}^{M} (-A_{rs21})^{\varphi(a)} A_{ts12} u_{sH}^{t2} \sin\alpha_t \tag{6.53}$$

$$u_z^2 = 0 \tag{6.54}$$

where $\sin\alpha_t = c_{s1}/c_{s2} \cdot \sin\alpha$, $\varphi(a) = (2k-3-(-1)^k)/4$, u_{SH}^i, u_{SH}^r, u_{SH}^t denote the displacements caused by incident SH waves, reflected SH waves and transmitted SH waves in layer 1, respectively; u_{SH}^{t2} is the displacements caused by transmitted SH waves in layer 2, and the above displacement vectors can be described as

$$u_{SH}^i = U(t - \Delta t_1) \tag{6.55}$$

$$u_{SH}^r = U(t - \Delta t_2) \tag{6.56}$$

$$u_{SH}^t = U(t - \Delta t_3) \tag{6.57}$$

$$u_{SH}^{t2} = U\left(t - \Delta t_4\right) \tag{6.58}$$

where $\Delta t_i \, (i = 1,2,3,4)$ is indicates that the time delay between the arrival of the incident SH wave and the reflected SH wave at node can be given as

$$\begin{aligned}
\Delta t_1 &= \left[(x_0 - x_1)\sin\beta\sin\alpha + (y_0 - y_1)\sin\beta\cos\alpha + (z_0 - z_1)\cos\beta\right]/c_{s1} \\
\Delta t_2 &= \left[(x_0 - x_1)\sin\beta\sin\alpha + (y_0 - y_1)\sin\beta\cos\alpha + (z_0 - z_1)\cos\beta\right. \\
&\quad \left. + 2\left(L_1 - z_0 + z_1\right)\cos\beta\right]/c_{s1} \\
\Delta t_3 &= \left[(x_0 - x_1)\sin\beta\sin\alpha + (y_0 - y_1)\sin\beta\cos\alpha + (z_0 - z_1)\cos\beta\right. \\
&\quad \left. + 2\left(L_1 - z_0 + z_1\right)\cos\beta\right]/c_{s1} + 2L_2 \cdot (b-2)\cos\beta_t / c_{s2} \\
\Delta t_4 &= \left[(x_0 - x_1)\sin\beta\sin\alpha + (y_0 - y_1)\sin\beta\cos\alpha + L_1\cos\beta\right]/c_{s1} \\
&\quad + \left[(x_0 - x_1)\sin\beta_t\sin\alpha_t + (y_0 - y_1)\sin\beta_t\cos\alpha_t + (L_1 - z_0 + z_1)\cos\beta_t\right]\cdot(-1)^a / c_{s2} \\
&\quad + \left[(x_0 - x_1)\sin\beta_t\sin\alpha_t + (y_0 - y_1)\sin\beta_t\cos\alpha_t + 2L_2\cos\beta\right]\cdot(a - 0.5 + 0.5\cdot(-1)^a)/c_{s2}
\end{aligned}$$

where $\sin\beta_t = c_{s1}/c_{s2} \cdot \sin\beta$.

Depending on the stress-strain relationship, the stress expression of each node can be obtained, and the equivalent load of each node can be obtained by the Eqs. (6.30)-(6.38).

6.4.2 Validation

For verification of the given input method of SH waves in layered media, a two-layer media model is used as an example for calculation, and the calculation model is shown in Fig. 6.24. The model size is $L = 20$m, $b = 20$m and $h_1 = h_2 = 25$m, the finite element model created by using 20 B2 beam element and 64 LE4. Points A $(10, 10, 50)$ and B $(10, 10, 0)$ are the selected observation point. The properties of elastic model is assumed as, elastic modulus E for layer one is 24MPa, for layer 2 is 6MPa, the Poisson's ratio ν is 0.25, the density ρ is 200kg/m^3. The pulse function time history equation for SH wave input is as Eq. (6.21) with $F_0 = 1$, $T_0 = 0.25$.

Fig. 6.25 illustrates the displacement of observation points A and B compared with the existed results. From Fig. 6.25, it can be observed that the transmission and reflection of the wave due to the layered can be reflected in the displacement distribution, and the reflected and transmitted waves gradually weaken with time. The comparison with the analytical results and existed result verifies the validation of the proposed method in this section. Moreover, the method used in this section saves considerable degrees of freedom (DOF) compared with the existed results [13] under the condition that the accuracy is guaranteed. Fig. 6.26

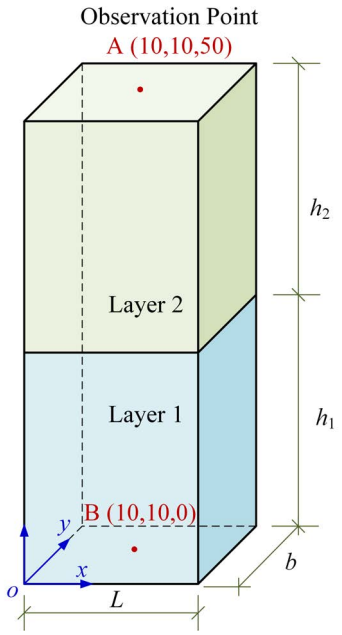

Fig. 6.24 Calculation model for two-layered media under SH wave incident

shows the temporal displacement distribution, and the reflected wave generated by SH wave propagation through stratification can be observed.

6.5 Summary

Based on the FEM of CUF framework, this chapter established the artificial boundary, external P wave and S wave inputs, and the external wave input process for layered media, therefore, the dynamics simulation under the external wave input is available performed for the infinite space or the region with truncated boundary. It is verified that the method and the implementation procedure presented in this chapter are validated and have the advantage of saving model degrees of freedom and improving the computational speed compared to the existing results while maintaining computational accuracy. The proposed method is applied to influence the incident angle at the external wave input on the superstructure dynamics for different wave velocities in the subsurface media. The results indicated that the incident angle has different effects under P wave and S wave incident, hence the analysis of the incident angle on the dynamic response cannot be neglected in the correlation analysis.

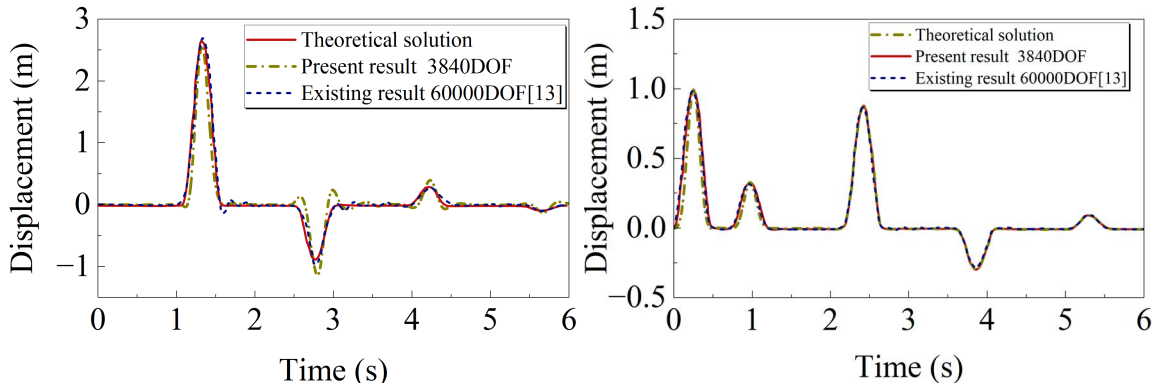

(a) Displacement of Point A (b) Displacement of Point B

Fig. 6.25 Displacement distribution under SH wave input in two-layered media

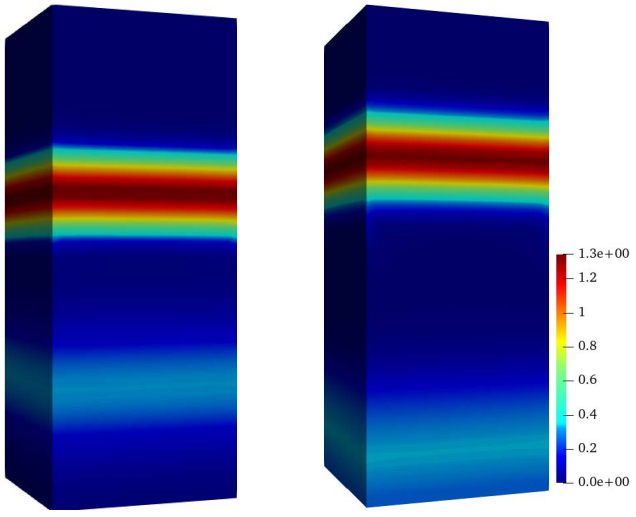

(a) t=0.8s (b) t=0.9s

Fig. 6.26 Displacement distribution under SH wave input at t = 0.8s and t = 0.9s

Chapter 7

Conclusions

7.1 Concluding remarks

Based on the elastic wave theory and the complex function method, SH wave scattering by surface depression and convex in density radial inhomogeneous media with varying wave velocity is investigated in this thesis. Applying the standard Helmholtz equation obtained by transformation function, the analytical solution of SH wave scattering by surface depression is presented. Based on this solution, SH wave scattering problem of surface convex and convex with cylindrical cavity is explored by employing RMT. Subsequently, considering the influence of research range, the dynamic response of the density radial inhomogeneous wedge region under SH wave incident is discussed. Based on the boundary conditions and radiation conditions on both sides of the wedge, the analytical solution of the research region free wave field is proposed. Furthermore, the influence of the wedge space with a cusp and a cylindrical depression on the dynamic response is considered. The effects of incident angle, dimensionless frequency, inhomogeneous parameter and radius ratio of the cylindrical cavity to the convex on the distribution of surface displacement amplitude and DSCF are calculated and discussed. The conclusions are as follows:

1. In the scattering of SH waves by inhomogeneous media surface depression, the inhomogeneous parameters and incident angle have a great influence on the displacement amplitude distribution, and the dimensionless frequency presents a positive correlation with the displacement amplitude. The amplification effect of surface depression on the displacement amplitude is proportional of inhomogeneous parameter. Moreover, the surface depression amplification effect is weaker as inhomogeneous parameter $\beta < 1$ than that of the homogeneous media. As the incident angle varies from horizontal to vertical, the displacement increases on the whole. However, under the joint action of the incident angle and the inhomogeneous parameter, the value range of the inhomogeneous parameter (greater

than 1 or less than 1) at different incident angles may exhibition different effects on the distribution.

2. For the scattering problem of surface semi-cylindrical convex and semi-cylindrical convex containing cylindrical cavity on the in inhomogeneous media, when the dimensionless frequency is about 2, the displacement amplitude distribution will have a sudden change. The inhomogeneous parameter and the incident angle still have different effects on the surface and internal displacement amplitude distribution. In addition, compared with the surface depression amplification coefficient with the same parameters, the displacement amplification coefficient in surface convex is smaller than that in surface depression, especially at horizontal incidence. Meanwhile, the amplification coefficient with the advanced of dimensionless frequency then increases only at the inhomogeneous parameter is less than 1. DSCF around a cylindrical cavity, the ascender of inhomogeneous parameters makes the distribution more complicated.

3. In the inhomogeneous media, the displacement amplitude of the wedge space with a cusp $\gamma/2$ still exists at the vertex, while the maximum displacement amplitude does not necessarily appear at the cusp. Moreover, the inhomogeneous parameter have great influence on the distribution of displacement amplitude. At the vertex angle is cylindrical depression, the displacement amplification coefficient is inversely proportional of inhomogeneous parameter under the same wedge angle. Under the same inhomogeneous parameter, it is proportional of incident angle. By comparing the two types of vertex angle, the scattering wave is generated by the cylindrical depression, which has certain influence on the surface and internal displacement distribution.

4. Applying the FEM based on the CUF framework simulates the dynamic response of the truncated region with superstructure under the input of external elastic wave. Furthermore, the incident angle has obvious influence on the displacement distribution in the research region under the SH wave incident. Compared with the other existing resulting by employing FEM, the total DOF of the element used in this chapter is smaller and the calculation time is faster.

Highlight of this thesis

1. Based on the complex variable function method, the analytical solution to the SH wave scattering caused by semi-cylindrical depressions on the radially inhomogeneous media surface with variable wave velocity and density is derived, and the effect of surface depressions on the displacement amplitude distribution under the action of inhomogeneous parameters is analyzed and discussed.

2. Applying the region matching technique, an analytical solution to the SH wave scattering problem of semi-cylindrical convex on the surface and semi-cylindrical convex with cylindrical cavity in a radially inhomogeneous media with variable wave velocity density is proposed. The corresponding wave field expression is constructed, and the surface and internal displacement amplitude and the dynamic stress concentration factor around the cavity are obtained. The amplifying effects of surface convex and surface depression on the displacement amplitude under inhomogeneous parameters are given.

3. The dynamic response of the dense radial inhomogeneous wedge space under the incident SH wave is investigated. A free wave field expression is constructed for a radially inhomogeneous wedge space with a vertex angle of $(0, 2\pi)$, which satisfies two boundary conditions. Considering two cases where the vertex angle of the wedge is a sharp point and a cylindrical depression, the influence of each parameter on the displacement amplitude of the surface and inside of the media is analyzed and discussed.

4. Based on the FEM under the CUF framework, a viscous-spring artificial boundary is established, which can simulate the dynamic response of infinite or semi-infinite space under the input of external elastic waves.

Future work

Considering the variable wave velocity, this work only investigated the inhomogeneous media with radially varying densities. And for the wedge space exploring, discussed two vertex forms. Scattering problems for other forms of inhomogeneous media, surface depressions and protrusions interacting with internal structures could be further investigated. Furthermore, the application of the CUF in this work is still in the preliminary research stage in the field of seismic waves, and there are still many problems that could be further detected.

1. Further research on surface defects or structural boundaries, while considering the scattering problem in the case of multiple defect combinations.

2. Other forms of inhomogeneous media could be considered. Starting from actual artificial materials, actual material parameters is applying to simulate utilizing reasonable functions, and further research could be conducted.

3. In the application of the finite element method based on CUF framework, through secondary development, the input process of artificial boundary calculation and the setting of artificial boundary node coordinates are automatically matched with the self-developed FORTRAN program, thereby enabling rapid simulation of more complex models.

References

[1] Abd-Alla, A. and Ahmed, S. (1999). Propagation of love waves in a non-homogeneous orthotropic elastic layer under initial stress overlying semi-infinite medium. *Applied Mathematics and Computation*, 106(2-3):265–275.

[2] Achenbach, J. (1973). *Wave propagation in elastic solids*. Elsevier.

[3] Achenbach, J. D. (2002). Modeling for quantitative non-destructive evaluation. *Ultrasonics*, 40:10.

[4] Achenbach, J. D. and Balogun, O. (2010). Anti-plane surface waves on a half-space with depth-dependent properties. *Wave Motion*, 47(1):59–65.

[5] Azis, M. I. (2019). Numerical solutions for the helmholtz boundary value problems of anisotropic homogeneous media. *Journal of Computational Physics*, 381:42–51.

[6] Ba, Z. N., Lee, V. W., Liang, J. W., and Yan, Y. (2017). Scattering of plane qp-and qsv-waves by a canyon in a multi-layered transversely isotropic half-space. *Soil Dynamics and Earthquake Engineering*, 98:120–140.

[7] Ba, Z. N. and Liang, J. W. (2017). Dynamic response analysis of periodic alluvial valleys under incident plane sh-waves. *Journal of Earthquake Engineering*, 21(4):531–550.

[8] Ba, Z. N., Wang, Y., Liang, J. W., and Liu, X. N. (2019). 3d dynamic responses of a 2d hill in a layered half-space subjected to obliquely incident plane p-, sv- and sh-waves. *Engineering Analysis with Boundary Elements*, 105:129–145.

[9] BA, Z. N., Xu, G., and Lee, V. W. (2019). Scattering of plane p-and sv-waves by periodic topography: modeled by a pibem. *Engineering Analysis with Boundary Elements*, 106:320–333.

[10] Balendra, T., Thambiratnam, D. P., Koh, C. G., and Lee, S. L. (1984). Dynamic response of twin circular tunnels due to incident sh-waves. *Earthquake Engineering & Structural Dynamics*, 12(2):182–201.

[11] Balogun, O. and Achenbach, J. D. (2013). Surface waves generated by a line load on a half-space with depth-dependent properties. *Wave Motion*, 50(7):1063–1072.

[12] Bharati, R. B., Filippi, M., Mahato, P. K., and Carrera, E. (2020). Flutter analysis of laminated composite structures using carrera unified formulation. *Composite Structures*, 253:112759.

[13] Bi, Z. H., Cui, B. H., and Zhai, Y. F. (2021). Research on seismic input method of layered ground foundation. *IEEE ACCESS*, 9:54820–54830.

[14] Bobet, A. (2011). Lined circular tunnels in elastic transversely anisotropic rock at depth. *Rock mechanics and rock engineering*, 44:149–167.

[15] Bose, S. K. (1996). Ultrasonic plane sh wave reflection from a uni-directional fibrous composite slab. *Journal of Sound and Vibration*, 193(5):1069–1078.

[16] Boström, A. (2015). Scattering by an anisotropic circle. *Wave Motion*, 57:239–244.

[17] Cao, X. S., Jin, F., and Jeon, I. (2011). Calculation of propagation properties of lamb waves in a functionally graded material (fgm) plate by power series technique. *NDT and E International*, 44(1):84–92.

[18] Carrera, E., Cinefra, M., Petrolo, M., and Zappino, E. (2014). *Finite element analysis of structures through unified formulation*. John Wiley & Sons.

[19] Casadei, F., Rimoli, J., and Ruzzene, M. (2014). Multiscale finite element analysis of elastic wave scattering from localized defects. *Finite Elements in Analysis and Design*, 88:1–15.

[20] Chaki, M. S. and Singh, A. K. (2020). The impact of reinforcement and piezoelectricity on sh wave propagation in irregular imperfectly-bonded layered fgpm structures: an analytical approach. *European Journal of Mechanics-A/Solids*, 80:103872.

[21] Chakraborty, A. and Gopalakrishnan, S. (2004). Wave propagation in inhomogeneous layered media: solution of forward and inverse problems. *Acta Mechanica*, 169(1-4):153–185.

[22] Chang, K. H., Tsaur, D. H., and Wang, J. H. (2013). Scattering of sh waves by a circular sectorial canyon. *Geophysical Journal International*, 195(1):532–543.

[23] Chattopadhyay, A. (1978). On the strong sh motion in a transversely isotropic layer lying over an isotropic elastic material due to a momentary point source. *Indian Journal of Pure and Applied Mathematics*, 9:886–892.

[24] Chen, A. L., Wang, Y. S., Wang, Y. F., Zhou, H. T., and Yuan, S. M. (2022). Design of acoustic/elastic phase gradient metasurfaces: Principles, functional elements, tunability, and coding. *Applied Mechanics Reviews*, 52:1–66.

[25] Chen, W., Wang, H., and Bao, R. (2007). On calculating dispersion curves of waves in a functionally graded elastic plate. *Composite structures*, 81(2):233–242.

[26] Cheng, Y. and Ji, C. Y. (2020). Numerical simulation of violent breaking wave impacts on a moored offshore wind turbine foundation over nonuniform topography. *Physics of Fluids*, 32(10):107106.

[27] Cheng, Z. K. and Liao, R. D. (2015). Effect of surface topography on stress concentration factor. *Chinese Journal of Mechanical Engineering*, 28(6):1141–1148.

[28] Chu, H. C., Zhang, H. Y., Zhang, Y., Peng, R. W., Wang, M., Hao, Y., and Lai, Y. (2021). Invisible surfaces enabled by the coalescence of anti-reflection and wavefront controllability in ultrathin metasurfaces. *Nature Communications*, 12(1):4523.

[29] Craster, R. V. and Guenneau, S. (2012). *Acoustic metamaterials: Negative refraction, imaging, lensing and cloaking*, volume 166. Springer Science and Business Media.

[30] Daros, C. (2008). A fundamental solution for sh-waves in a class of inhomogeneous anisotropic media. *International Journal of Engineering Science*, 46(8):809–817.

[31] Daros, C. (2009). A time-harmonic fundamental solution for a class of inhomogeneous transversely isotropic media. *Wave motion*, 46(4):269–279.

[32] Daros, C. (2010). On modelling sh-waves in a class of inhomogeneous anisotropic media via the boundary element method. *Applied Mathematics and Mechanics*, 90(2):113–121.

[33] Daros, C. (2013). Green's function for sh-waves in inhomogeneous anisotropic elastic solid with power-function velocity variation. *Wave Motion*, 50(2):101–110.

[34] Datta, S. K. and Shah, A. H. (2019). *Elastic waves in composite media and structures: with applications to ultrasonic nondestructive evaluation*. CRC Press.

[35] Dineva, P., Manolis, G., and Rangelov, T. (2006). Sub-surface crack in an inhomogeneous half-plane: Wave scattering phenomena by bem. *Engineering analysis with boundary elements*, 30(5):350–362.

[36] Ding, H. B., Tong, L., Xu, C. J., Cao, Z. G., Wang, R., and Li, S. Y. (2022). On propagation characteristics of rayleigh wave in saturated porous media based on the strain gradient nonlocal biot theory. *Computers and Geotechnics*, 141:104522.

[37] Du, J. K., Jin, X. Y., Wang, J., and Xian, K. (2007). Love wave propagation in functionally graded piezoelectric material layer. *Ultrasonics*, 46(1):13–22.

[38] Du, Y. J., Liu, D. K., Guo, F., Wang, J. D., and Guang, L. J. (2009a). Surface displacement function of two isosceles triangular hills during incidence of sh wave. *Journal of Earthquake Engineering and Engineeering Vibration*, 29(3):1–8 (in Chinese).

[39] Du, Y. J., Liu, D. K., Zhao, Q. C., Qiu, F. Q., and Wang, C. H. (2009b). Ground motion of isosceles triangular and semi-circulaar hill with the sh incident wave. *World Earthquak Engineering*, 25(3):167–174 (in Chinese).

[40] Ducellier, A. and Aochi, H. (2012). Interactions between topographic irregularities and seismic ground motion investigated using a hybrid fd-fe method. *Bulletin of Earthquake Engineering*, 10:773–792.

[41] England, R., Sabina, F. J., and Herrera, I. (1980). Scattering of sh waves by surface cavities of arbitrary shape using boundary methods. *Physics of the Earth and Planetary Interiors*, 21(2):148–157.

[42] Eremin, A. A., Golub, M. V., Fomenko, S. I., Evdokimov, A. A., and Nets, P. A. (2023). Multi-layered and homogenized models for in-plane guided wave excitation, sensing, and scattering in anisotropic laminated composites. *Applied Sciences*, 13(3):1698.

[43] Fares, R. and Deschamps, A. (2019). Soil-structure interaction analysis using a 1dt-3c wave propagation model. *Soil Dynamics and Earthquake Engineering*, 120:200–213.

[44] Feng, H., Yang, W., and Diankui, L. (1995). The interaction of plane sh-waves and circular cavity surfaced with lining in anisotropic media. *Applied Mathematics and Mechanics*, 16:1149–1159.

[45] Fukuhara, M., Kuwano, Y., Saito, K., Hirasawa, T., and Komura, I. (1998). Performance of non-destructive evaluation by diffracted sh ultrasonic waves in predicting degree of fatigue in cyclic bending of ferritic steel. *NDT and E International*, 31(3):211–216.

[46] Gao, L. M., Wang, J., Zhong, Z., and Du, J. K. (2009). An analysis of surface acoustic wave propagation in functionally graded plates with homotopy analysis method. *Acta mechanica*, 208(3-4):249.

[47] Gao, Y. F., Dai, D. H., Zhang, N., Wu, Y. X., and Mahfouz, A. H. (2017). Scattering of plane and cylindrical sh waves by a horseshoe shaped cavity. *Journal of Earthquake and Tsunami*, 11(02).

[48] Gao, Y. F., Zhang, N., Li, D. Y., Liu, H. L., Cai, Y. Q., and Wu, Y. X. (2012). Effects of topographic amplification induced by a u-shaped canyon on seismic waves. *Bulletin of the Seismological Society of America*, 102(4):1748–1763.

[49] Gaur, A. M. and Rana, D. S. (2015). Dispersion relations for sh waves propagation in a porous piezoelectric (pzt–pvdf) composite structure. *Acta Mechanica*, 226:4017–4029.

[50] Gazetas, G., Kallou, P., and Psarropoulos, P. (2002). Topography and soil effects in the ms 5.9 parnitha (athens) earthquake: the case of adámes. *Natural Hazards*, 27:133–169.

[51] Ghafarollahi, A. and Shodja, H. (2018). Scattering of sh-waves by an elliptic cavity/crack beneath the interface between functionally graded and homogeneous half-spaces via multipole expansion method. *Journal of Sound and Vibration*, 435:372–389.

[52] Ghanei Mohammadi, A. R. and Hosseini Tehrani, P. (2019). Interface/interphase effects on scattering of elastic p- and sv-waves from a circular nanoinclusion embedded in a solid viscoelastic matrix. *European Journal of Mechanics - A/Solids*, 73:67–89.

[53] Giurgiutiu, V. and Cuc, A. (2005). Embedded non-destructive evaluation for structural health monitoring, damage detection, and failure prevention. *Shock and Vibration Digest*, 37(2):83.

[54] Graff, K. F. (1975). *Wave motion in elastic solids*. Courier Corporation.

[55] Guidotti, P., Lambers, J. V., and Solna, K. (2006). Analysis of wave propagation in 1d inhomogeneous media. *Numerical Functional Analysis and Optimization*, 27(1):25–55.

[56] Gupta, S., Dutta, R., and Das, S. (2021). Love-type wave propagation in an inhomogeneous cracked porous medium loaded by heterogeneous viscous liquid layer. *Journal of Vibration Engineering and Technologies*, 9:433–448.

[57] Gupta, S., Kundu, S., and Vishwakarma, S. K. (2015). Propagation of torsional surface waves in an inhomogeneous layer over an initially stressed inhomogeneous half-space. *Journal of Vibration and Control*, 21(7):1286–1298.

[58] Guzina, B. and Pak, R. (1996). Elastodynamic green's functions for a smoothly heterogeneous half-space. *International journal of solids and structures*, 33(7):1005–1021.

[59] Han, F., Wang, G. Z., and Kang, C. Y. (2011). Scattering of sh-waves on triangular hill joined by semi-cylindrical canyon. *Applied Mathematics and Mechanics*, 32(3):309–326.

[60] Han, R. P. S., Yeh, K. Y., Liu, G. l., and Liu, D. K. (1992). Scattering of plane sh-waves by a cylindrical canyon of arbitrary shape in anisotropic media. *International Journal of Engineering Science*, 30(12):1773–1787.

[61] Han, X. and Liu, G. (2003). Elastic waves in a functionally graded piezoelectric cylinder. *Smart Materials and Structures*, 12(6):962.

[62] Hayir, A. and Bakirtas, I. (2004). A note on a plate having a circular cavity excited by plane harmonic sh waves. *Journal of Sound and Vibration*, 271(1-2):241–255.

[63] Hei, B. P., Yang, Z. L., Sun, B. T., and Wang, Y. (2015). Modelling and analysis of the dynamic behavior of inhomogeneous continuum containing a circular inclusion. *Applied Mathematical Modelling*, 39(23):7364–7374.

[64] Huang, L., Liu, Z. X., Wu, C. Q., and Liang, J. W. (2019). The scattering of plane p, sv waves by twin lining tunnels with imperfect interfaces embedded in an elastic half-space. *Tunnelling and Underground Space Technology*, 85:319–330.

[65] Jiang, G. X. X., Yang, Z. L., Sun, C., Song, Y. Q., and Yang, Y. (2020a). Analytical study of sh wave scattering by a cylindrical cavity in the two-dimensional and approximately linear inhomogeneous medium. *Waves in Random and Complex Media*, 31(6):1799–1817.

[66] Jiang, X., Shi, C. Z., Li, Z. L., Wang, S. Q., Wang, Y., Yang, S., Louie, S. G., and Zhang, X. (2020b). Direct observation of klein tunneling in phononic crystals. *Science*, 370(6523):1447–1450.

[67] Kara, H. F. (2016a). Diffraction of plane sh waves by a cylindrical cavity in an infinite wedge. *Procedia Engineering*, 161:1601–1607.

[68] Kara, H. F. (2016b). A note on response of tunnels to incident sh-waves near hillsides. *Soil Dynamics and Earthquake Engineering*, 90:138–146.

[69] Kiełczyński, P., Szalewski, M., Balcerzak, A., and Wieja, K. (2016). Propagation of ultrasonic love waves in nonhomogeneous elastic functionally graded materials. *Ultrasonics*, 65:220–227.

[70] Kim, J. H. and Paulino, G. H. (2002). Isoparametric graded finite elements for nonhomogeneous isotropic and orthotropic materials. *Journal of Applied Mechanics*, 69(4):502–514.

[71] Kimoto, K., Ueno, S., and Hirose, S. (2006). Image-based sizing of surface-breaking cracks by sh-wave array ultrasonic testing. *Ultrasonics*, 45(1-4):152–164.

[72] Kong, Y. P., Liu, J. X., and Nie, G. Q. (2015). Propagation characteristics of sh wave in an mm2 piezoelectric layer on an elastic substrate. *AIP Advances*, 5(9):097135.

[73] Koshiba, M., Karakida, S., and Suzuki, M. (1984). Finite-element analysis of lamb wave scattering in an elastic plate waveguide. *IEEE transactions on sonics and ultrasonics*, 31(1):18–24.

[74] Kouretzis, G. P., Andrianopoulos, K. I., Sloan, S. W., and Carter, J. P. (2014). Analysis of circular tunnels due to seismic p-wave propagation, with emphasis on unreinforced concrete liners. *Computers and Geotechnics*, 55:187–194.

[75] Kumar, P., Chattopadhyay, A., and Singh, A. K. (2017). Shear wave propagation due to a point source. *Procedia engineering*, 173:1544–1551.

[76] Kumari, P. and Sharma, V. K. (2019). Dynamics of seismic waves in highly anisotropic triclinic media with intermediate monoclinic layer. *Applied Mathematical Modelling*, 71:375–393.

[77] Lee, J. K., Lee, H. C., and Jeong, H. W. (2016). Numerical analysis of sh wave field calculations for various types of a multilayered anisotropic inclusion. *Engineering Analysis with Boundary Elements*, 64:38–67.

[78] Lee, V. W. (1990). Scattering of plane sh-waves by a semi-parabolic cylindrical canyon in an elastic half-space. *Geophysical Journal International*, 100(1):79–86.

[79] Lee, V. W. and Karl, J. (1992). Diffraction of sv waves by underground, circular, cylindrical cavities. *Soil Dynamics and Earthquake Engineering*, 11(8):445–456.

[80] Lee, V. W. and Manoogian, M. E. (1995). Surface motion above an arbitrary shape underground cavity for incident sh waves. *European Earthquake Engineering*, 1:3–11.

[81] Lee, V. W. and Sherif, R. I. (1996). Diffraction around circular canyon in elastic wedge space by plane sh-waves. *Journal of Engineering Mechanics*, 122(6):539–544.

[82] Lee, V. W. and Trifunac, M. D. (1979). Response of tunnels to incident sh-waves. *Journal of the Engineering Mechanics Division*, 105(4):643–659.

[83] Leung, K., Vardoulakis, I., Beskos, D., and Tassoulas, J. (1991). Vibration isolation by trenches in continuously nonhomogeneous soil by the bem. *Soil Dynamics and Earthquake Engineering*, 10(3):172–179.

[84] Li, S. Y., Jin, X., Ma, Q., and Song, J. D. (2004a). Study on earthquake early warning system and intellegent emergency controling system. *World Earthquak Engineering*, 20(4):21–26 (in Chinese).

[85] Li, T., Wang, G. Q., and Liu, D. K. (2003). Scattering of sh-wave by a semi-cylindrical hill-like protruding with a cavity. *Journal of Earthquake Engineering and Engineeering Vibration*, 23(5):26–31 (in Chinese).

[86] Li, W. H., Liu, Q. H., and Zhao, C. G. (2010). Three-dimensional viscous-spring boundaries in time domain and dynamic analysis using explicit finite element method of saturated porous medium. *Chinese journal of Geophysics*, 53(10):2460–2469.

[87] Li, X., Wang, Z., and Huang, S. (2004b). Love waves in functionally graded piezoelectric materials. *International Journal of Solids and Structures*, 41(26):7309–7328.

[88] Liang, J. W., Luo, H., and Lee, V. W. (2004). Scattering of plane sh waves by a circulararc hill with a circular tunnel. *Acta Seismologica Sinica*, 17(5):549–563.

[89] Liang, J. W., Yan, L. j., and Lee, V. W. (2001). Scattering of plane p waves by circular-arc layered alluvial valleys: An analytical solution. *Acta Seismologica Sinica*, 14(2):176–195.

[90] Liao, K. P. and Hu, C. H. (2013). A coupled fdm–fem method for free surface flow interaction with thin elastic plate. *Journal of marine science and technology*, 18:1–11.

[91] Lin, S. Z., Qiu, F. Q., and Liu, D. K. (2013). Scattering of sh waves by a scalene triangular hill. *Earthquake Engineering and Engineering Vibration*, 9(1):23–38.

[92] Liu, D. K. and Han, F. (1990). Scattering of plane sh-waves on cylindrical canyon of arbitrary shape in anisotropic media. *Acta Mechanica Sinica*, 6(3):256–266.

[93] Liu, D. K. and Han, F. (1993). The scattering of plane sh-waves by noncircular cavity in anisotropic media. *Journal of Applied Mechanics*, 60(3):769–772.

[94] Liu, D. K. and Tian, J. Y. (1999). Scattering and dynamic stress concentration of sh-wave by interface cylindrical elastic inclusion. *Explosion and Shock Waves*, 19(2):20–28 (in Chinese).

[95] Liu, G., Chen, H. T., Liu, D. K., and Khoo, B. C. (2010). Surface motion of a half-space with triangular and semicircular hills under incident sh waves. *Bulletin of the Seismological Society of America*, 100(3):1306–1319.

[96] Liu, G., Ji, B. H., Chen, H. T., and Liu, D. K. (2009). Antiplane harmonic elastodynamic stress analysis of an infinite wedge with a circular cavity. *Journal of Applied Mechanics*, 76(6):061008.

[97] Liu, G. H. and Jiang, D. L. (2020). Layer-effect on variable seismic ground motions of sv-wave scattered by a double-stratified circular-arc crossing by layer-interface. *Soil Dynamics and Earthquake Engineering*, 129:105919.

[98] Liu, J. B. and Li, B. (2005). A unified viscous-spring artificial boundary for 3-d static and dynamic applications. *Science in China Series E Engineering & Materials Science*, 48:570–584.

[99] Liu, J. B. and Lu, Y. D. (1998). *A direct method for analysis of dynamic soil-structure interaction based on interface idea*, volume 83, pages 261–276. Elsevier.

[100] Liu, Q. J., Wu, Z. Y., and Lee, V. W. (2019a). Scattering and reflection of sh waves around a slope on an elastic wedged space. *Earthquake Engineering and Engineering Vibration*, 18(2):255–266.

[101] Liu, Q. J., Zhang, C., and Todorovska, M. I. (2016). Scattering of sh waves by a shallow rectangular cavity in an elastic half space. *Soil Dynamics and Earthquake Engineering*, 90:147–157.

[102] Liu, Q. J., Zhao, M. J., and Liu, Z. X. (2019b). Wave function expansion method for the scattering of sh waves by two symmetrical circular cavities in two bonded exponentially graded half spaces. *Engineering Analysis with Boundary Elements*, 106:389–396.

[103] Liu, Q. J., Zhao, M. J., and Zhang, C. (2014). Antiplane scattering of sh waves by a circular cavity in an exponentially graded half space. *International Journal of Engineering Science*, 78:61–72.

[104] Liu, Z. X., Huang, L., Liang, J. W., and Wu, C. Q. (2019c). A three-dimensional indirect boundary integral equation method for modeling elastic wave scattering in a layered half-space. *International Journal of Solids and Structures*, 169:81–94.

[105] Liu, Z. X. and Liu, L. (2015). An ibem solution to the scattering of plane sh-waves by a lined tunnel in elastic wedge space. *Earthquake Science*, 28(1):71–86.

[106] Liu, Z. X., Zhang, H., Cheng, A., Wu, C. Q., and Yang, G. G. (2019d). Seismic interaction between a lined tunnel and a hill under plane sv waves by ibem. *International Journal of Structural Stability and Dynamics*, 19(02):1950004.

[107] Lou, M. L., Wang, H. F., Chen, X., and Zhai, Y. (2011a). Structure–soil–structure interaction: Literature review. *Soil dynamics and earthquake engineering*, 31(12):1724–1731.

[108] Lou, M. L., Wang, H. F., Chen, X., and Zhai, Y. M. (2011b). Structure–soil–structure interaction: Literature review. *Soil dynamics and earthquake engineering*, 31(12):1724–1731.

[109] Lu, A. Z., Zhang, N., Wang, S. J., and Zhang, X. L. (2017). Analytical solution for a lined tunnel with arbitrary cross sections excavated in orthogonal anisotropic rock mass. *International Journal of Geomechanics*, 17(9):04017044.

[110] Lu, Y. Y. (2010). *Non-destructive evaluation on concrete materials and structures using cement-based piezoelectric sensor*. Thesis.

[111] Manolis, G. and Shaw, R. (1995). Wave motions in stochastic heterogeneous media: a green's function approach. *Engineering analysis with boundary elements*, 15(3):225–234.

[112] Manolis, G. and Shaw, R. (1997a). Harmonic elastic waves in continuously heterogeneous random layers. *Engineering analysis with boundary elements*, 19(3):181–198.

[113] Manolis, G. D., Parvanova, S. L., Makra, K., and Dineva, P. S. (2015). Seismic response of buried metro tunnels by a hybrid fdm-bem approach. *Bulletin of Earthquake Engineering*, 13:1953–1977.

[114] Manolis, G. D. and Shaw, R. P. (1997b). Fundamental solutions to helmholtz's equation for inhomogeneous media by a first-order differential equation system. *Soil Dynamics and Earthquake Engineering*, 16(2):81–94.

[115] Manolis, G. D., Shaw, R. P., and Pavlou, S. (1999). Elastic waves in nonhomogeneous media under 2d conditions: I. fundamental solutions. *Soil Dynamics and Earthquake Engineering*, 18(1):19–30.

[116] Marfurt, K. J. (1984). Accuracy of finite-difference and finite-element modeling of the scalar and elastic wave equations. *Geophysics*, 49(5):533–549.

[117] Medina, C., Álamo, G. M., Aznárez, J. J., Padrón, L. A., and Maeso, O. (2019). Variations in the dynamic response of structures founded on piles induced by obliquely incident sv waves. *Earthquake Engineering and Structural Dynamics*, 48(7):772–791.

[118] Meirbekova, B. and Brun, M. (2020). Control of elastic shear waves by periodic geometric transformation: cloaking, high reflectivity and anomalous resonances. *Journal of the Mechanics and Physics of Solids*, 137:103816.

[119] Mojtabazadeh-Hasanlouei, S., Panji, M., and Kamalian, M. (2022). Attenuated orthotropic time-domain half-space bem for sh-wave scattering problems. *Geophysical Journal International*, 229(3):1881–1913.

[120] Muravskii, G. (1997a). Green functions for a compressible linearly non homogeneous half-space. *Archive of Applied Mechanics*, 67:521–534.

[121] Muravskii, G. (1997b). On time-harmonic problem for non-homogeneous elastic half-space with shear modulus limited at infinite depth. *European journal of mechanics. A. Solids*, 16(2):277–294.

[122] Naderi, A. and Saidi, A. (2011). Exact solution for stability analysis of moderately thick functionally graded sector plates on elastic foundation. *Composite Structures*, 93(2):629–638.

[123] Najafizadeh, J., Kamalian, M., Jafari, M. K., and Khaji, N. (2014). Seismic analysis of rectangular alluvial valleys subjected to incident sv waves by using the spectral finite element method. *International Journal of Civil Engineering*, 12(3):251–263.

[124] Newmark, N. M. (1959). A method of computation for structural dynamics. *Journal of the engineering mechanics division*, 85(3):67–94.

[125] Noginov, M., Li, H., Barnakov, Y. A., Dryden, D., Nataraj, G., Zhu, G., Bonner, C., Mayy, M., Jacob, Z., and Narimanov, E. (2010). Controlling spontaneous emission with metamaterials. *Optics letters*, 35(11):1863–1865.

[126] Pagani, A. and Carrera, E. (2017). Large-deflection and post-buckling analyses of laminated composite beams by carrera unified formulation. *Composite Structures*, 170:40–52.

[127] Pang, Y., Liu, Y. S., Liu, J. X., and Feng, W. J. (2016). Propagation of sh waves in an infinite/semi-infinite piezoelectric/piezomagnetic periodically layered structure. *Ultrasonics*, 67:120–128.

[128] Panji, M. and Ansari, B. (2017). Transient sh-wave scattering by the lined tunnels embedded in an elastic half-plane. *Engineering Analysis with Boundary Elements*, 84:220–230.

[129] Panji, M., Kamalian, M., Asgari Marnani, J., and Jafari, M. K. (2014). Analysing seismic convex topographies by a half-plane time-domain bem. *Geophysical Journal International*, 197(1):591–607.

[130] Pao, Y. H. and Mow, C. C. (1973). *Diffraction of elastic waves and dynamic stress concentration*. Crane and Russak, New York.

[131] Pendry, J. B. (2000). Negative refraction makes a perfect lens. *Physical review letters*, 85(18):3966.

[132] Petcher, P., Burrows, S. E., and Dixon, S. (2014). Shear horizontal (sh) ultrasound wave propagation around smooth corners. *Ultrasonics*, 54(4):997–1004.

[133] Qi, H., Chu, F. Q., Zhang, Y., Yang, R. J., and Guo, J. (2020). Scattering of sh-waves by oblique semi-elliptical notches in half space. *Waves in Random and Complex Media*, pages 1–16.

[134] Qi, H., Guo, J., and Yang, J. (2011). The ground motion of isosceles triangular hill in right-angle plane impacted by sh-wave. *Applied Mechanics and Materials*, 121-126:2363–2366.

[135] Qi, H. and Yang, J. (2012). Dynamic analysis for circular inclusions of arbitrary positions near interfacial crack impacted by sh-wave in half-space. *European Journal of Mechanics - A/Solids*, 36:18–24.

[136] Qian, Z. H., Jin, F., Lu, T. J., and Kishimoto, K. (2009). Transverse surface waves in an fgm layered structure. *Acta mechanica*, 207(3-4):183–193.

[137] Qiu, F. Q. (2006). *Scattering of SH-wave by triangular hill and subsurface cavity*. Thesis.

[138] Qiu, F. Q. and Liu, D. K. (2005). Antiplane response of isosceles triangular hill to incident sh waves. *Earthquake Engineering and Engineering Vibration*, 4(1):37–46.

[139] Qiu, F. Q., Wang, H. W., and Wang, X. (2010). Interaction of scalene triangular structure to soil with incident sh waves. *Journal of Harbin Institute of Technology*, 42(4):634–638 (in Chinese).

[140] Ramos, I., Mantari, J., and Zenkour, A. (2016). Laminated composite plates subject to thermal load using trigonometrical theory based on carrera unified formulation. *Composite Structures*, 143:324–335.

[141] Rangelov, T., Manolis, G., and Dineva, P. (2005). Elastodynamic fundamental solutions for certain families of 2d inhomogeneous anisotropic domains: basic derivations. *European Journal of Mechanics-A/Solids*, 24(5):820–836.

[142] Rokhlin, S. and Wang, L. (2002). Stable recursive algorithm for elastic wave propagation in layered anisotropic media: Stiffness matrix method. *The Journal of the Acoustical Society of America*, 112(3):822–834.

[143] Shaw, R. P. and Manolis, G. D. (2000). A generalized helmholtz equation fundamental solution using a conformal mapping and dependent variable transformation. *Engineering Analysis with Boundary Elements*, 24(2):177–188.

[144] Shekhar, U., Jakobsen, M., Iversen, E., Berre, I., and Radu, F. A. (2023). Integral equation method for microseismic wavefield modelling in anisotropic elastic media. *arXiv preprint arXiv:2301.12836*.

[145] Shelby, R. A., Smith, D. R., and Schultz, S. (2001). Experimental verification of a negative index of refraction. *Science*, 292(5514):77–79.

[146] Smerzini, C., Avilés, J., Paolucci, R., and Sánchez-Sesma, F. J. (2009). Effect of underground cavities on surface earthquake ground motion under sh wave propagation. *Earthquake Engineering and Structural Dynamics*, 38(12):1441–1460.

[147] Smith, W. D. (1975). The application of finite element analysis to body wave propagation problems. *Geophysical Journal International*, 42(2):747–768.

[148] Song, Y. Q., Li, X. Z., Yang, Z. L., Carrera, E., and Yang, Y. (2022a). A series solution for sh wave scattering by irregularly shaped surface topographies. *Journal of Earthquake Engineering*, pages 1–21.

[149] Song, Y. Q., Li, X. Z., Yang, Z. L., Yang, Y., and Sun, M. H. (2022b). Seismic response for an isosceles triangle hill subjected to anti-plane shear waves. *Acta Geotechnica*, 17:275–288.

[150] Sullivan, J. M., Grimes, W. J., and Ludwig, R. (1993). An efficient fem approach for the study of ultrasonic wave propagation in solids. *Review of Progress in Quantitative Nondestructive Evaluation*, 12A and 12B:131–138.

[151] Sun, Q. Q., Dias, D., and Ribeiro e Sousa, L. (2019). Impact of an underlying soft soil layer on tunnel lining in seismic conditions. *Tunnelling and Underground Space Technology*, 90:293–308.

[152] Sánchez-Sesma, F. J. (1985). Diffraction of elastic sh waves by wedges. *Bulletin of the Seismological Society of America*, 75(5):1435–1446.

[153] Sánchez-Sesma, F. J., Herrera, I., and Avilés, J. (1982). A boundary method for elastic wave diffraction: Application to scattering of sh waves by surface irregularities. *Bulletin of the Seismological Society of America*, 72(2):473–490.

[154] Takemiya, H. and Fujiwara, A. (1994). Sh-wave scattering and propagation analyses at irregular sites by time domain bem. *Bulletin of the Seismological Society of America*, 84(5):1443–1455.

[155] Takemura, S., Furumura, T., and Maeda, T. (2015). Scattering of high-frequency seismic waves caused by irregular surface topography and small-scale velocity inhomogeneity. *Geophysical Journal International*, 201(1):459–474.

[156] Tang, X. M. (2011). A unified theory for elastic wave propagation through porous media containing cracks–an extension of biot's poroelastic wave theory. *Science China. Earth Sciences*, 54(9):1441.

[157] Thomson, W. T. (1950). Transmission of elastic waves through a stratified solid medium. *Journal of applied Physics*, 21(2):89–93.

[158] Ting, T. (2010). Existence of anti-plane shear surface waves in anisotropic elastic half-space with depth-dependent material properties. *Wave Motion*, 47(6):350–357.

[159] Trifunac, M. D. (1973). Scattering of plane sh waves by a semi-cylindrical canyon. *Earthquake Engineering and Structural Dynamics*, 1(3):267–281.

[160] Tsaur, D. H. and Chang, K. H. (2008a). An analytical approach for the scattering of sh waves by a symmetrical v-shaped canyon: shallow case. *Geophysical Journal International*, 174(1):255–264.

[161] Tsaur, D. H. and Chang, K. H. (2008b). Sh-waves scattering from a partially filled semi-circular alluvial valley. *Geophysical Journal International*, 173(1):157–167.

[162] Tsaur, D. H. and Chang, K. H. (2009a). Scattering and focusing of sh waves by a convex circular-arc topography. *Geophysical Journal International*, 177(1):222–234.

[163] Tsaur, D. H. and Chang, K. H. (2009b). Scattering of sh waves by truncated semicircular canyon. *Journal of Engineering Mechanics*, 135(8):862–870.

[164] Tsaur, D. H. and Chang, K. H. (2012). Multiple scattering of sh waves by an embedded truncated circular cavity. *Journal of Marine Science and Technology*, 20(1).

[165] Tsaur, D. H. and Chang, K. H. (2018). Exact solution to scattering of sh waves by an elliptic-arc canyon in the corner of an elastic quarter space. *Soil Dynamics and Earthquake Engineering*, 110:137–140.

[166] Tsaur, D. H., Chang, K. H., and Hsu, M. S. (2010). An analytical approach for the scattering of sh waves by a symmetrical v-shaped canyon: deep case. *Geophysical Journal International*, 183(3):1501–1511.

[167] Vrettos, C. (1990a). In-plane vibrations of soil deposits with variable shear modulus: I. surface waves. *International journal for numerical and analytical methods in geomechanics*, 14(3):209–222.

[168] Vrettos, C. (1990b). In-plane vibrations of soil deposits with variable shear modulus: Ii. line load. *International journal for numerical and analytical methods in geomechanics*, 14(9):649–662.

[169] Wang, H., Qin, Q. H., and Kang, Y. L. (2005). A new meshless method for steady-state heat conduction problems in anisotropic and inhomogeneous media. *Archive of Applied Mechanics*, 74(8):563–579.

[170] Wang, J. H., Lu, J. F., and Zhou, X. L. (2009). Complex variable function method for the scattering of plane waves by an arbitrary hole in a porous medium. *European Journal of Mechanics - A/Solids*, 28(3):582–590.

[171] Wang, Y. (2017). *Equivalent relationships and solution methods for wave motion in inhomogeneous media*. Thesis.

[172] Watanabe, K. and Payton, R. G. (2004). Green's function and its non-wave nature for sh-wave in inhomogeneous elastic solid. *International journal of engineering science*, 42(19-20):2087–2106.

[173] Watanabe, K. and Payton, R. G. (2006). Green's function for radially symmetric waves in inhomogeneous anisotropic solids. *Applied Mathematics and Mechanics*, 86(8):642–648.

[174] Wei, X., Rao, C., Chen, S., and Luo, W. (2023). Numerical simulation of anti-plane wave propagation in heterogeneous media. *Applied Mathematics Letters*, 135:108436.

[175] Wen, L. J. and Yan, L. J. (2001). Scattering of plane p wave by circular-arc layered alluvial valleys: an analytical solution. *Acta Seismologica Sinica*, 23(2):167–184 (in Chinese).

[176] Wen, L. J. and Yan, L. J. (2002). Scattering of plane p wave by a circular-arc canyon with a covering layer. *Acta Mechanica Solida Sinica*, 23(4):397–411 (in Chinese).

[177] Wen, L. J. and Yan, L. J. (2003). Scattering of plane sv wave by circular-arc layered alluvial valleys: an analytical solution. *Acta Mechanica Solida Sinica*, 24(2):235–243 (in Chinese).

[178] Wong, H. L. (1975). *Dynamic soil-structure interaction*. Thesis.

[179] Wong, H. L. and Trifunac, M. D. (1974a). Scattering of plane sh waves by a semi-elliptical canyon. *Earthquake Engineering and Structural Dynamics*, 3(2):157–169.

[180] Wong, H. L. and Trifunac, M. D. (1974b). Surface motion of a semi-elliptical alluvial valley for incident plane sh waves. *Bulletin of the Seismological Society of America*, 64(5):1389–1408.

[181] Wu, B., Pagani, A., Chen, W., and Carrera, E. (2021). Geometrically nonlinear refined shell theories by carrera unified formulation. *Mechanics of Advanced Materials and Structures*, 28(16):1721–1741.

[Xiao et al.] Xiao, S., Yang, Z. L., Sun, C., Sun, B. T., Yan, P. L., and Yang, Y. Simulation of wave propagation in cracked elastic medium using fdm-fem. In *2017 Symposium on Piezoelectricity, Acoustic Waves, and Device Applications (SPAWDA)*, pages 174–178. IEEE.

[183] Xu, C., Ding, H., Tong, L., Luo, W., and Wang, N. (2019). Scattering of a plane wave by shallow buried cylindrical lining in a poroelastic half-space. *Applied Mathematical Modelling*, 70:171–189.

[184] Yang, C. H. (2009). Dynamic response of circular-arc-shaped canyon under the incidence of plane sh wave: high-frequency solution. *Technology for Earthquake Disaster Prevention*, 4(2):158–166 (in Chinese).

[185] Yang, J. (2000). Influence of water saturation on horizontal and vertical motion at a porous soil interface induced by incident p wave. *Soil Dynamics and Earthquake Engineering*, 19(8):575–581.

[186] Yang, J. (2005). Rayleigh surface waves in an idealised partially saturated soil. *Geotechnique*, 55(5):409–414.

[187] Yang, Z. L., Jiang, G. X. X., Song, Y. Q., Yang, Y., and Sun, M. H. (2020a). Effect on dynamic stress distribution by the shape of cavity in continuous inhomogeneous medium under sh waves incidence. *Mechanics of Advanced Materials and Structures*, 28(20):2071–2082.

[188] Yang, Z. L., Song, Y. Q., Li, X. Z., Jiang, G. X. X., and Yang, Y. (2020b). Scattering of plane sh waves by an isosceles trapezoidal hill. *Wave Motion*, 92:102415.

[189] Yang, Z. L., Song, Y. Q., Yang, Y., Li, X. Z., and Sun, M. H. (2021). Scattering of sh waves by an isosceles flat-topped hill with multistage slopes. *Waves in Random and Complex Media*.

[190] Yang, Z. L., Wang, Y., and Hei, B. P. (2013). Transient analysis of 1d inhomogeneous media by dynamic inhomogeneous finite element method. *Earthquake Engineering and Engineering Vibration*, 12(4):569–576.

[191] Yang, Z. L., Wang, Y., Hei, B. P., and Li, Z. D. (2016). Analytical solutions to wave motion in a one-dimensional inhomogeneous medium based on an equivalent transformation relationship. *Journal of Vibration and Shock*, 35(6):152–155 (in Chinese).

[192] Yang, Z. L., Zhang, C. Q., Yang, Y., and Sun, B. T. (2017). Scattering of out-plane wave by a circular cavity near the right-angle interface in the exponentially inhomogeneous media. *Wave Motion*, 72:354–362.

[193] Yang, Z. L., Zhu, Y., Ren, H. Q., Yang, Y., Zhao, J., and Chen, Y. C. (2022). Dynamic stress analysis of an elliptical cavity during elastic wave propagation in a density-inhomogeneous medium with the modulus varying as a power function. *European Journal of Mechanics-A/Solids*, 96:104740.

[194] Yazdi, J. T., Valliappan, S., and Zhao, C. (1994). Analytical and numerical solutions for wave propagation in water-saturated porous layered half-space. *Soil Dynamics and Earthquake Engineering*, 13(4):249–257.

[195] Yuan, X. M. (2010). A complete-domain transform formula of cylindrical wave functions for scattering problems. *Journal of Earthquake Engineering and Engineeering Vibration*, 30(4):1–7 (in Chinese).

[196] Yuan, X. M. and Liao, Z. P. (1993). Series solution for scattering of plane sh waves by a canyon of circular-arc cross section. *Journal of Earthquake Engineering and Engineeering Vibration*, 13(2):1–11 (in Chinese).

[197] Yuan, X. M. and Men, F. L. (1992). Scattering of plane sh waves by a semi-cylindrical hill. *Earthquake Engineering and Structural Dynamics*, 21(12):1091–1098.

[198] Zhang, C., Liu, Q. J., and Deng, P. (2015). Antiplane scattering of sh waves by a trapezoidal valley with a circular-arc alluvium in an elastic half space. *Journal of Earthquake and Tsunami*, 9(3):1550008.

[199] Zhang, C., Liu, Q. J., and Deng, P. (2017a). Surface motion of a half-space with a semicylindrical canyon underp,sv, and rayleigh waves. *Bulletin of the Seismological Society of America*, 107(2):809–820.

[200] Zhang, C. H. and Zhao, C. B. (1988). Effects of canyon topography and geological conditions on strong ground motion. *Earthquake Engineering and Structural Dynamics*, 16(1):81–97.

[201] Zhang, D., Wang, G., Feng, X., and Feng, W. B. (2022a). Analytical and numerical investigation of edge waves near a vertical breakwater over a convex bottom. *Ocean Engineering*, 266:112923.

[202] Zhang, H., Yang, G. G., Liu, Z. X., and Wang, X. J. (2017b). An analytical solution to scattering of plane sh waves by a semi-circle lined tunnel in elastic half-space boundary. *Chinese Journal of Applied Mechanics*, 34(2):243–250 (in Chinese).

[203] Zhang, N., Pan, J. S., Gao, Y. F., Chen, X., Dai, D. H., and Zhang, Y. (2022b). Surface motion of an arbitrary number of semi-circular viscoelastic alluvial valleys for incident plane sh waves. *Geophysical Journal International*, 228(3):1607–1620.

[204] Zhang, S. Y. (1987). Inhomogeneous isoparametric elements for stress analysis of composites. *Scientia Sinica Series A-Mathematical Physical Astronomical and Technical Sciences*, 30(8):832–854 (in Chinese).

[205] Zhang, X. F. and Far, H. (2022). Effects of dynamic soil-structure interaction on seismic behaviour of high-rise buildings. *Bulletin of Earthquake Engineering*, 20(7):3443–3467.

[206] Zhao, Y. B., Qi, H., Ding, X. H., and Zhao, D. D. (2016). Dynamic analysis for a shallow buried circular cavity impacted by sh- wave in a soft layered half-space. *Journal of Vibration and Shock*, 35(24):120–127 (in Chinese).

[207] Zhao, Y. B., Qi, H., Ding, X. H., and Zhao, D. D. (2017). Dynamic analysis for shallow buried circular inclusion impacted by sh-wave in a softlayered half-space. *Explosion and Shock Waves*, 37(6):982–989 (in Chinese).

[208] Zhou, C. P., Hu, C., Ma, F., and Liu, D. K. (2014). Elastic wave scattering and dynamic stress concentrations in exponential graded materials with two elliptic holes. *Wave Motion*, 51(3):466–475.

[209] Zhou, J. and Li, L. S. (2018). Metamaterial technology and its application prospects. *Strategic Study of CAE*, 20(6):69–74 (in Chinese).

Appendix A

List of publications

A.1 Journal articles

1 X. Z. Li, Y. Q. Song, Z. L. Yang, E. Carrera (2022), "Scattering of SH waves by a semi-cylindrical bump in an inhomogeneous half-space", International Journal of Applied Mechanics, published online.

2 X. Z. Li, Z. L. Yang, Y. Yang, Y. Q. Song, H. Y. Deng (2022), "Shear horizontal wave propagation in inhomogeneous wedge space", Wave Motion, Vol. 14, pp. 103009.

3 Z. L. Yang, X. Z. Li, Y. Q. Song, G. X. X. Jiang, Y. Yang (2021), "Scattering of SH waves by a semi-cylindrical canyon in a radially inhomogeneous media", Waves in Random and Complex Media, Vol. 31, pp. 1107-1123.

4 Z. L. Yang, X. Z. Li, Y. Q. Song, G. X. X. Jiang, M. H. Sun, Xueqian Fang (2020), "Scattering of SH waves around circular canyon in inhomogeneous wedge space", Geophysical Journal International, Vol. 223, pp. 45-56.

5 Y. Q. Song, X. Z. Li, Y. Yang, M. H. Sun, Z. L. Yang, X. Q. Fang (2022), "Scattering of anti-plane (SH) waves by a hill with complex slopes", Journal of Earthquake Engineering, Vol. 26, pp. 2546-66.

6 Y. Q. Song, X. Z. Li, Z. L. Yang, Y. Yang, M. H. Sun (2022), "Seismic response for an isosceles triangle hill subjected to anti-plane shear waves", Acta Geotechnica, Vol. 17, pp. 275-88.

7 Y. Q. Song, X. Z. Li, Z. L. Yang, E. Carrera, Y . Yang (2022), "A series solution for SH wave scattering by irregularly shaped surface topographies", Journal of Earthquake Engineering, published online.

8 Y. Q. Song, X. Z. Li, J. L. Bian, M. H. Li, Z. L. Yang (2023), "Dynamic analysis for a shallow isosceles trapezoid depression impacted by SH-wave", International Journal of Geomechanics, accepted.

9 Z. L. Yang, Y. Q. Song, X. Z. Li, G. X. X. Jiang, Y. Yang (2022), "Scattering of plane SH waves by an isosceles trapezoidal hill", Wave Motion, Vol. 92, pp.102415.

10 Z. L. Yang, Y. Q. Song, Y. Yang, X. Z. Li, M. H. Sun (2021), "Scattering of SH waves by an isosceles flat-topped hill with multistage slopes", Waves in Random and Complex Media, published online.

11 G. X. X. Jiang, Z. L. Yang, C. Sun, X. Z. Li, Y. Yang (2019), "Dynamic stress concentration of a cylindrical cavity in vertical exponentially inhomogeneous half space under SH wave", Meccanica, Vol. 54, pp. 2411-2420.

A.2 Conference Proceeding

1 X. Z. Li, Y. Q. Song, G. X. X. Jiang, Y. Yang, Z. L. Yang (2019), "Surface Motion of Inhomogeneous Half Space with a Semi-Cylindrical Canyon Under SH Wave", In *The 2019 (13th) Symposium on Piezoelectricity, Acoustic Waves and Device Applications*, Heilongjiang, China, 11 January, 2019.

2 X. Z. Li, Y. Q. Song, G. X. X. Jiang, Y. Yang, Z. L. Yang (2019), "Surface motion of inhomogeneous right-angle space with a circular canyon under SH wave", In *The 2019 (14th) Symposium on Piezoelectricity, Acoustic Waves and Device Applications*, Hebei, China, 1 November, 2019.

3 Y. Q. Song, X. Z. Li, C. Sun, Y. Yang, Z. L. Yang (2019), "Antiplane Response of Isosceles Trapezoidal Hill to Incident SH Waves", In *The 2019 (13th) Symposium on Piezoelectricity, Acoustic Waves and Device Applications*, Heilongjiang, China, 11 January, 2019.

4 Y. Q. Song, X. Z. Li, C. Sun, Y. Yang, Z. L. Yang (2019), "Influence of a steepened hill on the surface displacement amplitudes", In *The 2019 (14th) Symposium on Piezoelectricity, Acoustic Waves and Device Applications*, Heilongjiang, Hebei, China, 1 November, 2019.